**YEAR-END TECHNICAL REPORT**
September 29, 2017 to September 28, 2018

# Environmental Remediation Science and Technology

**Date submitted:**

December 7, 2018

**Principal Investigator:**

Leonel E. Lagos, Ph.D., PMP®

**Florida International University Collaborators:**

Yelena Katsenovich, Ph.D.
Ravi Gudavalli, Ph.D.
Hilary P. Emerson, Ph.D.
Angelique Lawrence, M.S., GISP
Mehrnoosh Mahmoudi, Ph.D.
DOE Fellows

**Submitted to:**

U.S. Department of Energy
Office of Environmental Management
Under Cooperative Agreement # DE-EM0000598

FIU | Applied Research Center
FLORIDA INTERNATIONAL UNIVERSITY

Addendum:

This document represents one (1) of four (4) reports that comprise the Year End Reports for the period of September 29, 2017 to September 28, 2018 prepared by the Applied Research Center at Florida International University for the U.S. Department of Energy Office of Environmental Management (DOE-EM) under Cooperative Agreement No. DE-EM0000598.

The complete set of FIU's Year End Reports for this reporting period includes the following documents:

Project 1: Chemical Process Alternatives for Radioactive Waste
Document number: FIU-ARC-2018-800006470-04b-262

Project 2: Environmental Remediation Science and Technology
Document number: FIU-ARC-2018-800006471-04b-261

Project 3: Waste and D&D Engineering and Technology Development
Document number: FIU-ARC-2018-800006472-04b-251

Project 4: DOE-FIU Science & Technology Workforce Development Initiative
Document number: FIU-ARC-2018-800006473-04b-281

Each document will be submitted to OSTI separately under the respective project title and document number as shown above. In addition, the documents are available at the DOE Research website for the Cooperative Agreement between the U.S. Department of Energy Office of Environmental Management and the Applied Research Center at Florida International University: http://doeresearch.fiu.edu

# TABLE OF CONTENTS

TABLE OF CONTENTS ..... i
LIST OF FIGURES ..... iv
LIST OF TABLES ..... xii
PROJECT 2 OVERVIEW ..... 1
PROJECT ACCOMPLISHEMNTS ..... 4
TASK 1: REMEDIATION RESEARCH AND TECHNICAL SUPPORT FOR THE HANFORD SITE ..... 7
Subtask 1.1: Sequestering Uranium at The Hanford 200 Area By In Situ Subsurface pH Manipulation Using Ammonia ($NH_3$) Gas ..... 7
Subtask 1.1: Introduction ..... 7
Subtask 1.1: Objectives ..... 7
Subtask 1.1: Results and Discussion ..... 7
Subtask 1.1: Future Work ..... 23
Subtask 1.1: Acknowledgements ..... 24
Subtask 1.1: References ..... 24
Subtask 1.3: Investigation of Electrical Geophysical Response to Microbial Activity in the Saturated and Unsaturated Environments ..... 25
Subtask 1.3: Introduction ..... 25
Subtask 1.3: Methodology ..... 26
Subtask 1.3: Results and Discussion ..... 28
Subtask 1.3: Conclusion ..... 40
Subtask 1.3: Acknowledgements ..... 41
Subtask 1.4: Contaminant Fate and Transport under Reducing Conditions ..... 42
Subtask 1.4: Introduction ..... 42
Subtask 1.4: Objectives ..... 43
Subtask 1.4: Methodology ..... 43
Subtask 1.4: Results and Discussion ..... 46
Subtask 1.4: Future Work ..... 53
Subtask 1.4: Acknowledgements ..... 53
Subtask 1.4: References ..... 53
Subtask 1.5: Stability of Contaminants in Carbonate Precipitates ..... 54

Subtask 1.5: Introduction ..... 54
Subtask 1.5: Methodology ..... 56
Subtask 1.5: Results and Discussion ..... 59
Subtask 1.5: Conclusion ..... 66
Subtask 1.5: Acknowledgements ..... 66
Subtask 1.5: References ..... 66
TASK 2: REMEDIATION RESEARCH AND TECHNICAL SUPPORT FOR SAVANNAH RIVER SITE ..... 69
Task 2: Executive Summary ..... 69
Subtask 2.1: Impact of free radicals on the fate of Tc, I, and U in wetlands at SRS ..... 69
Subtask 2.1: Introduction ..... 69
Subtask 2.1: Methodology ..... 70
Subtask 2.1: Results and Discussion ..... 72
Subtask 2.1: Future Work ..... 80
Subtask 2.1: Acknowledgements ..... 80
Subtask 2.1: References ..... 81
Subtask 2.2: The Synergistic Effect of Humic Acid and Colloidal Silica on the Removal of Uranium (VI) ..... 82
Subtask 2.2: Introduction ..... 82
Subtask 2.2: Methodology ..... 83
Subtask 2.2: Results and Discussion ..... 84
Subtask 2.2: Acknowledgements ..... 90
Subtask 2.2: References ..... 91
Subtask 2.3: Humic Acid Batch Sorption and Column Experiments with SRS Soil ..... 92
Subtask 2.3: Introduction ..... 92
Subtask 2.3: Methodology ..... 94
Subtask 2.3: Results and Discussion ..... 100
Subtask 2.3: Future Work ..... 115
Subtask 2.3: Acknowledgements ..... 115
Subtask 2.3: References ..... 115
TASK 3: SURFACE WATER MODELING OF TIMS BRANCH ..... 119
Task 3: Executive Summary ..... 119

Subtask 3.1: Modeling of Surface Water and Sediment Transport in the Tims Branch Ecosystem ..... 119
Subtask 3.1: Introduction ..... 119
Subtask 3.1: Methodology ..... 120
Subtask 3.1: Results and Discussion ..... 121
Subtask 3.1: Conclusion ..... 133
Subtask 3.2: Application of GIS Technologies for Hydrological Modeling Support ..... 133
Subtask 3.2: Introduction ..... 133
Subtask 3.2: Methodology ..... 133
Subtask 3.2: Results and Discussion ..... 134
Subtask 3.2: Conclusion ..... 140
Subtask 3.3: Data Collection, Sampling and Analysis in Tims Branch Watershed ..... 141
Subtask 3.3: Introduction ..... 141
Subtask 3.3: Methodology ..... 141
Subtask 3.3: Results and Discussion ..... 147
Subtask 3.3: Conclusion ..... 153
Task 3: Future Work ..... 155
Task 3: Acknowledgements ..... 155
Task 3: References ..... 155
TASK 5: REMEDIATION RESEARCH AND TECHNICAL SUPPORT FOR THE WASTE ISOLATION PILOT PLANT ..... 158
Task 5: Executive Summary ..... 158
Task 5: Objectives ..... 158
Task 5: Results and Discussion ..... 158
Subtask 5.1: Sorption of neodymium to dolomite in variable ionic strength systems ..... 158
Subtask 5.2: Fate of actinides in the presence of ligands in high ionic strength systems ..... 162
Task 5: Future Work ..... 168
Task 5: Acknowledgements ..... 169
Task 5: References ..... 169
APPENDIX ..... 172

# LIST OF FIGURES

Figure 1. Comparison of U $K_d$ partitioning coefficients (mL/g) for Hanford sediments treated with 5% $NH_3$ + 95% $N_2$ gas for three days in the presence of different electrolyte solutions. Note: error bars are based on triplicate samples. ..... 8

Figure 2. Comparison of U $K_d$ partitioning coefficients (mL/g) for pure minerals and Hanford sediments treated with 5% $NH_3$ + 95% $N_2$ gas for three days with sampling after 15 minutes or three days following the aeration step. Note: error bars are based on triplicate samples. ..... 8

Figure 3. U L3-edge XANES spectra of the reference compounds used for XANES LCA fitting: LCF fit shown in red for $UO_2$ and in black for $UO_3$. ..... 12

Figure 4. U L3-edge XANES spectrum [black] and total LCF fit [red] for Calcite_$NH_3$. Fraction-adjusted standards contributing to the LCF fit shown for $UO_2$ [grey] and $UO_3$ [blue]. ..... 13

Figure 5. U L3-edge XANES spectrum [black] and total LCF fit [red] for Illite_Aerated. Fraction-adjusted standards contributing to the LCF fit shown for $UO_2$ [grey] and $UO_3$ [blue]. ..... 14

Figure 6. U L3-edge XANES spectrum [black] and total LCF fit [red] for Illite_$NH_3$. Fraction-adjusted standards contributing to the LCF fit shown for $UO_2$ [grey] and $UO_3$ [blue]. ..... 14

Figure 7. Diagram of 2:1 layer silicates (Nesse, 2012a). ..... 16

Figure 8. X-ray diffraction (XRD) patterns of illite control (no treatment) showing the five most representative and matched peaks from the phase identification software *Match!*. ..... 18

Figure 9. X-ray diffraction (XRD) patterns of illite for the following conditions: control (no treatment) (orange), ammonia-treated in SGW (red) and aerated-treated in SGW (blue). Note: peak #1 at ~ 8.8 Å is not shown. ..... 19

Figure 10. FTIR spectrum of illite samples before and after $NH_3$ treatment. Major band peaks are labeled below the SGW aerated sample (dark green). ..... 21

Figure 11. FTIR spectrum of muscovite samples before and after NH3 treatment. Major band peaks are labeled below the SGW aerated sample (dark green). ..... 21

Figure 12. FTIR spectrum of montmorillonite samples before and after $NH_3$ treatment. Major band peaks are labeled below the SGW aerated sample (dark green). ..... 22

Figure 13. Experimental ratios of Al to Si from ICP aqueous SGW and NaCl solutions analysis for illite, muscovite and montmorillonite ..... 22

Figure 14. Mini-column prepared for the basic SIP experiments ..... 27

Figure 15. Cole-Cole chargeability for the Fall 2016 column experiment. ..... 28

Figure 16. Cole-Cole DC resistivity (Ohm-m) for the Fall 2016 column experiment. ..... 29

Figure 17. Cole-Cole relaxation time (s) for the Fall 2016 column experiment. ..... 30

Figure 18. Percent RMS error in the phase between Cole-Cole and measured. ..... 30

Figure 19. $Fe^{2+}$ concentrations taken using ferrozine method for mini-column. ..... 31

Figure 20. Fe total concentrations taken using ferrozine for mini-column. ..... 31

Figure 21. Ca concentrations taken using ICP-OES for mini-column. 32

Figure 22. Mg concentrations taken using ICP-OES for mini-column. 32

Figure 23. Phase spectra for mini-column comparing deactivated and live microbes as well as background. 33

Figure 24. Impedance (Ohms) magnitude spectra for mini-column comparing deactivated and live microbes as well as background. 34

Figure 25. Real conductivity spectra for mini-column comparing deactivated and live microbes as well as background. 34

Figure 26. Imaginary conductivity spectra for mini-column comparing deactivated and live microbes as well as background. 35

Figure 27. Real conductivity over time at various frequencies. 36

Figure 28. Phase over time at various frequencies. 36

Figure 29. Imaginary conductivity over time at various frequencies. 37

Figure 30. Phase spectra. Dark blue is start of the experiment. Dark red is end. 38

Figure 31. Imaginary conductivity spectra. Dark blue is start of the experiment. Dark red is end. 38

Figure 32. Cole-Cole chargeability over time for mini-column. 39

Figure 33. Cole-Cole DC resistivity (0hm-m) over time for mini-column. 39

Figure 34. Cole-Cole exponent over time for mini-column. 40

Figure 35. Relaxation time (s) over time for mini-column. 40

Figure 36. Anaerobic glovebox at FIU EC1227 where pertechnetate reduction experiments are currently taking place under 98% $N_2$ : 2% $H_2$ atmosphere. 44

Figure 37. Perkin Elmer TriCarb 2910 TR Liquid Scintillation Counter used throughout the experiments 46

Figure 38. Linear regression (least squares method) for pertechnetate reduction by nano-magnetite at pH 6 and nano- and micro- magnetite at pH 8. 46

Figure 39. Pertechnetate reduction by nano-magnetite at pH 6 and nano- and micro- magnetite at pH 8 doesn't fit to the first order reaction kinetic equation. 47

Figure 40. $Tc(VII)_{aq}$ reduction as a function of time in the presence of 30 mg of nano-magnetite at pH 8. 49

Figure 41. $Tc(VII)_{aq}$ and $Tc(IV)_{aq}$ concentrations, as a function of time, as a result of TcO2 sequestered by nano-magnetite dissolution in the absence of bicarbonates. 49

Figure 42. $Tc(VII)_{aq}$ and $Tc(IV)_{aq}$ as a function of time in the presence of 50 mM bicarbonates at pH 8 for nano- and micro-magnetite. 51

Figure 43. $Tc(VII)_{aq}$ and $Tc(IV)_{aq}$ as a function of time in the presence of 50 mM bicarbonates at pH 8 for nano- and micro-magnetite. 51

Figure 44. $Tc(VII)_{aq}$ as a function of time in the presence of 50 mM bicarbonates at pH 8 for nano- and micro-magnetite. ..... 52

Figure 45. XRD results of 500 mg of nano-magnetite in with 30 mL of DI water under anaerobic conditions. ..... 53

Figure 46. Iodate concentrations measured as total iodine over time. Iodate was mixed with carbonate-forming solutions and measurements were taken after day 1, day 3 and day 7. Concentrations of Si: A) 0 mM, B) 0.5 mM, C) 2 mM, D) 5 mM, F) 20 mM. ..... 59

Figure 47. Iodate concentrations measured as total iodine over time in the "late spike" experiments when iodate was added after mixing of the 0.1 M calcite-forming solutions and precipitation of calcium carbonate solids. Measurements were taken after day 1, day 3 and day 7 after mixing with iodate. Concentrations of Si: A) 0 mM, B) 0.5 mM, C) 2 mM, D) 5 mM, F) 20 mM. ..... 60

Figure 48. Diagrams of carbonate and silicate aqueous species (left) and saturation indices of some of the carbonate and silicate mineral phases (right) plotted as a function of pH. Sample composition includes 0.1M of NaHCO3and CaCl2, 0.5mM silicate and 250ppb of iodine as iodate. ..... 61

Figure 49. Diagrams of carbonate and silicate aqueous species (left) and saturation indices of some of the carbonate and silicate mineral phases (right) plotted as a function of pH. Sample composition includes 0.1M of NaHCO3 and CaCl2, 20mM silicate and 250 ppb of iodine as iodate. ..... 62

Figure 50. Element concentrations in the solution composition with pH: 0.5 mM Si (left) and 20 mM of Si (right). ..... 62

Figure 51. Two different magnifications of calcium carbonate precipitates are reported at pH 7. ..... 65

Figure 52. Precipitate at pH 8 showing rhombohedral calcite crystals covered with amorphous Si floccules. ..... 65

Figure 53. Precipitate formed at pH 10 with an average iodine concentration of 0.19 wt% (left). Silica coating present on the surface of calcium carbonate precipitate at x50,000 magnification (right). ..... 66

Figure 54. ORP measurements for samples following exposure to 18,000 lux in the environmental chamber at 25°C for the first four sample types and natural conditions outside for the last sample, under the following concentrations: 0.5 g/L humic acid at pH 5 (gray), 25 g/L humic acid at pH 3 (blue), 25 g/L humic acid at pH 5 (orange), and 25 g/L humic acid at pH 7 (yellow), solid lines are measured at 71 and 55 days of reaction time for 25 and 0.5 g/L humic acid, respectively, dashed lines are measured at 100 and 84 days for 25 and 0.5 g/L humic acid, respectively. ..... 74

Figure 55. Temperature fluctuations in 0.5 g/L humic acid sample exposed to full sunlight outdoors with respect to time (hours). ..... 74

Figure 56. Fraction dissolved for pH 3 (blue), 5 (orange), and 7 (yellow) at 25 g/L initial humic acid and pH 5 at 0.5 g/L humic acid (gray) with variable treatment conditions as measured after 100 and 84 days of reaction for 25 and 0.5 g/L humic acid concentrations, respectively. ..... 75

Figure 57. E4/E6 ratios for total (solid) and dissolved (diagonal lines) humic acid for pH 3 (blue), 5 (orange), and 7 (yellow) at 25 g/L initial humic acid and pH 5 at 0.5 g/L humic acid (gray) with variable treatment conditions for 100 and 84 days of interaction for 25 and 0.5 g/L humic acid concentrations, respectively. ..... 75

Figure 58. Fraction of humic acid measured at 254 nm as normalized to the control sample in a black tube for 0.5 g/L initial humic acid concentration at pH 5 after 84 days of reaction time under variable conditions. ..... 76

Figure 59. Qualitative comparison of microbial populations in HPC spread plates after five days of incubation at 20°C where (A) is the control plate used to check for contamination during preparation, (B) 0.5 g/L humic acid at pH 5 exposed to the natural environment, (C) 0.5 g/L humic acid at pH 5 in the environmental chamber, (D) 25 g/L humic acid at pH 5 in the environmental chamber, (E) 25 g/L humic acid at pH 3 in the environmental chamber, and (F) 25 g/L humic acid at pH 7 in the environmental chamber. ..... 77

Figure 60. Qualitative comparison of microbial populations in HPC spread plates after seven days of incubation at 21°C where (A) is the control plate used to check for contamination during preparation, (B) 0.5 g/L humic acid at pH 5 exposed to the natural environment, (C-F) 0.5 g/L humic acid at pH 5 in the environmental chamber for all conditions. ..... 79

Figure 61. Experimental setup. ..... 84

Figure 62. Shaker and centrifuge experimental setup. ..... 84

Figure 63. Uranium removal for unfiltered and filtered samples (quartz, Set #1). ..... 86

Figure 64. Uranium removal for unfiltered and filtered samples (kaolinite, Set #2). ..... 87

Figure 65. Uranium removal for unfiltered and filtered samples (quartz and kaolinite, Set #3). . 89

Figure 66. Uranium removal for unfiltered and filtered samples (quartz, kaolinite, and goethite, Set #4). ..... 90

Figure 67. Huma-K ..... 94

Figure 68. Samples with SRS sediment ..... 95

Figure 69. Shaker table with samples ..... 96

Figure 70. Centrifugation ..... 96

Figure 71. Kinetic phosphorescence analyzer ..... 96

Figure 72. Teflon ® adapter with layer of glass wool. ..... 97

Figure 73. Column with SRS sediment post DIW saturation. ..... 97

Figure 74. Mod-HA calibration curve ..... 99

Figure 75. Huma-K calibration curve ..... 100

Figure 76. Kinetic study of U(VI) ($C_i$ = 0.5 mg $L^{-1}$) sorption on (a) SRS sediment and (b) SRS sediment amended with Huma-K (10 g $L^{-1}$ of sediment, pH 4, I = 0.01 M $NaClO_4$, and T = 25°C). ..... 101

Figure 77. Non-linear fit of F data for (a) SRS sediment ($t \leq 0.125$ days) and (b) SRS sediment amended with Huma-K ($t \leq 3$ days). Circle points = experimental data; red line = results of fit with pseudo-first order; blue line = result of fit with pseudo-second order. ..... 101

Figure 78. Sorption isotherm of U(VI) ($C_i$ = 0.025 – 1 mg $L^{-1}$) on SRS sediment with and without Huma-K amendment for 7 days (10 g $L^{-1}$ of sediment, pH 4, I = 0.01 M $NaClO_4$, and T = 25°C). ..... 102

Figure 79. Non-linear fit adsorption isotherm for (a) SRS sediment and (b) SRS sediment amended with Huma-K. Circle points = experimental data; green line = results of fit with Langmuir model; magenta line = result of fit with Freundlich model. ..... 103

Figure 80. %Removal of U(VI) ($C_i$ = 0.5 mg $L^{-1}$) from the aqueous phase as a function of pH (10 g $L^{-1}$ of sediment, 7 days, I = 0.01 M $NaClO_4$, and T = 25°C). ..... 104

Figure 81. (a) Comparison of U(VI) ($C_i$ = 0.5 mg $L^{-1}$) removal for SRS sediment, quartz (100%), quartz/kaolinite (95%:5%), quartz/kaolinite/goethite (94%:5%:1%). (b) Control samples with no sediment (closed circles) and Eh (open circles). (7 days, I = 0.01 M $NaClO_4$, and T = 25°C). . 105

Figure 82. Dissolution of Al and Si from SRS sediment ..... 107

Figure 83. Diagram for U(VI) mineral saturation in the (a) presence and (b) absence of CO2 ($P_{CO2}$ = $10^{-3.5}$ atm) was created in Geochemist's Workbench (thermo-minteq database). ..... 108

Figure 84. (a) Desorption of U(VI) from SRS sediment with and without Huma-K amendment removal (10 g $L^{-1}$ of sediment, 14 days, I = 0.01 M $NaClO_4$, and T = 25°C). (b) Uranium remaining sorbed in SRS sediment after desorption. ..... 109

Figure 85. Concentration of measured rhenium vs collection time ..... 110

Figure 86.Concentration profile of HA in the effluent of the column ..... 112

Figure 87. $C/C_0$ Over Pore Volume ..... 113

Figure 88. $C/C_0$ and Uranium Retained for the Control Column ..... 113

Figure 89. $C/C_0$ and Uranium Retained for the Mod-HA Column ..... 114

Figure 90. $C/C_0$ and Uranium Retained for the Huma-K Column ..... 114

Figure 91. A-014 outfall tributary and model domain. ..... 122

Figure 92. Simulated discharge for 1993 at various cross section locations along A-014 outfall tributary. Each color refers to a cross section location. The locations of the simulated cross sections along A-014 are shown. ..... 124

Figure 93. Daily rainfall data for 1993. The red circles correlate with the peaks seen in the discharge graph (Figure 92). ..... 124

Figure 94. Discharge at cross section 300. The blue line indicates the value of depth of water. 125

Figure 9.: Simulation of water level along A-014. As it shows, cross section 500 is in the proximity of the weir location. ..... 125

Figure 96. DOE Fellow, Mohammed Albassam, with his Master's thesis review committee: (from left to right) Dr. Leonel Lagos (Applied Research Center Director of Research and the DOE Fellows Program Director), Dr. Shonali Laha, Mohammed Albassam and Dr. Walter Tang.... 126

Figure 97. MIKE Hydro tools being used to generate the cross sections and chainages of the modified stream network. ..... 127

Figure 98. Simplification of the stream network into fewer polylines. ..... 128

Figure 99. Simulated water level along Tims Branch. The x axis refers to the distance from the original reference point along Tims Branch and the y axis refers to water level. The blue area indicates how water level varies along Tims Branch. ..... 129

Figure 100.Simulated discharge over time at two locations along Tims Branch. The x axis refers to the time step (month), and the y axis refers to discharge rate (m3/s). ..... 130

Figure 101. Graph depicting raw rainfall and pan evaporation data in 2016 from gauge station neat SRNL. ..... 132

Figure 102. Refined process flow model generated in ArcGIS ModelBuilder for interpolating heavy metal and radionuclide concentrations in water samples collected in June 2017 to show their spatial distribution in the Tims Branch study area. ..... 135

Figure 103. Process flow model generated in ArcGIS ModelBuilder to automate the delineation of the drainage lines and catchments of the smaller A-014 Outfall tributary study area. ..... 136

Figure 104. (1) Delineated drainage line, drainage points and catchments in the Tims Branch watershed generated from a 3m DEM using ArcHydro tools, and (2) the A-014 Outfall tributary study domain. ..... 137

Figure 105. Simplification of the stream network by merging small line segments to generate single polylines. ..... 137

Figure 106. Simplification of the stream network into fewer polylines. ..... 138

Figure 107. Modification of the stream network intersection points using editor tools in ArcMap. ..... 138

Figure 108. Correlation between recurrence time and maximum rainfall for Tims Branch rainfall data. ..... 140

Figure 109.Assembled HOBO RX3000 Remote Monitoring System. ..... 142

Figure 110. DOE Fellows conducting a field test of the HOBO RX3000 Remote Monitoring System. ..... 142

Figure 111. Screen shots of the HOBOlink web-enabled software platform used to access data from the HOBO RX3000 Remote Monitoring System. ..... 143

Figure 112. DOE Fellows installing HOBO RX3000 3G Remote Monitoring Stations in the A-014 Outfall tributary and Tims Branch study areas. ..... 145

Figure 113. (left) FIU graduate student installing the HOBO RX3000 remote monitoring device in Tims Branch at SRS; (right) FIU researcher and student calibrating and testing the device. .... 146

Figure 114. Screenshot of the HOBO Unit 2 device information viewed via the HOBOlink online user interface. ..... 148

Figure 115. Screenshot of HOBOlink interface showing data from Unit 2 for the month of March 2018. ..... 148

Figure 116. Spreadsheet showing some of the data downloaded from Unit 2 on March 5, 2018. Data is recorded in HOBOlink every 15 minutes. (Note: The M-1 Air Stripper located in the SRS A/M Area was turned off at this time). ..... 149

Figure 117. Screenshots of graphs generated in HOBOlink of data collected by Unit 2. Graphs can be generated for recorded data on a daily, weekly or monthly basis. ..... 150

Figure 118. A-014 cross-section taken in February 2018 while installing the HOBO units. As the flow changes, the flow area can be calculated as the cross-section is constant. ..... 151

Figure 119. Recorded and graphed water level data as viewed from the HOBOlink GUI..... 152

Figure 120. Pictures and tabular data showing the difference in water levels in the A-014 outfall tributary when the M-1 air stripper was on versus when it was turned off. ..... 152

Figure 121. Water level data recorded in June 2018 by the HOBO RX3000 stage gauge located downstream in Tim Branch..... 153

Figure 122: Poster presented at the AWRA 2018 Spring Specialty Conference in Orlando, FL. ..... 154

Figure 123. Experimentally determined correction factors (A) by Rai *et al*. (blue circles) and this study (black circles) with the one sigma of a linear regression based on previous work (blue lines). ..... 159

Figure 124. Recovery of rhenium following step injection of 5 ppm $ReO_4^-$ in 0.1 M NaCl mini column (data points) with best fit for constant dispersivity model fit via StanMod software (line) with CXTFIT module. ..... 160

Figure 125. One-dimensional, constant dispersivity (D=0.00014 $cm^2$/sec) prediction of recovery of contaminant following a continuous step injection into mini columns packed with dolomite for $K_d$=0 (solid line) for a conservative tracer and variable $K_d$ based on the range used previously in performance assessment modeling for the WIPP ..... 161

Figure 126. Results for continuous injection column experiments in the presence of 20 ppb Nd at 0.1 and 5.0 M ionic strength (0.003 M $NaHCO_3$ + NaCl), Note: error bars are based on triplicate analyses via ICP-MS..... 161

Figure 127. Comparison of control dolomite (left) not reacted with solutions and dolomite from 5.0 M ionic strength miniature column (right) after approximately one year of exposure..... 162

Figure 128. Measurement of Nd [initial concentration 1000 µg/L] after ten days of equilibration in variable ionic strength solutions of NaCl, $CaCl_2$, or $MgCl_2$ in the presence (diagonal lines) or absence (solid bars) of 5 mg/L of EDTA following settling (green), filtration to remove 450 nm particles (yellow) or <10 nm particles (blue), Note: for $MgCl_2$ and $CaCl_2$ the concentration is 0.033 or 0.33 M to reach 0.1 or 1.0 M ionic strength, respectively..... 164

Figure 129. Measurement of Nd [initial concentration 10 µg/L] after ten days of equilibration in variable ionic strength solutions of NaCl, $CaCl_2$, or $MgCl_2$ in the presence (diagonal lines) or absence (solid bars) of 5 mg/L of EDTA following settling (green), filtration to remove 450 nm particles (yellow) or <10 nm particles (blue), Note: for $MgCl_2$ and $CaCl_2$ the concentration is 0.033 or 0.33 M to reach 0.1 or 1.0 M ionic strength, respectively..... 165

Figure 130. Measurement of U [initial concentration 1000 µg/L] after ten days of equilibration in variable ionic strength solutions of NaCl, $CaCl_2$, or $MgCl_2$ in the presence (diagonal lines) or absence (solid bars) of 5 mg/L of EDTA following settling (green), filtration to remove 450 nm particles (yellow) or <10 nm particles (blue), Note: for $MgCl_2$ and $CaCl_2$ the concentration is 0.033 or 0.33 M to reach 0.1 or 1.0 M ionic strength, respectively..... 166

Figure 131. Measurement of Th [initial concentration 1000 µg/L] after ten days of equilibration in variable ionic strength solutions of NaCl, $CaCl_2$, or $MgCl_2$ in the presence (diagonal lines) or absence (solid bars) of 5 mg/L of EDTA following settling (green), filtration to remove 450 nm

particles (yellow) or <10 nm particles (blue), Note: for $MgCl_2$ and $CaCl_2$ the concentration is 0.033 or 0.33 M to reach 0.1 or 1.0 M ionic strength, respectively. ..... 167

Figure 132. Measurement of Th [initial concentration 10 µg/L] after ten days of equilibration in variable ionic strength solutions of NaCl, $CaCl_2$, or $MgCl_2$ in the presence (diagonal lines) or absence (solid bars) of 5 mg/L of EDTA following settling (green), filtration to remove 450 nm particles (yellow) or <10 nm particles (blue), Note: for $MgCl_2$ and $CaCl_2$ the concentration is 0.033 or 0.33 M to reach 0.1 or 1.0 M ionic strength, respectively. ..... 167

Figure 133. Aqueous Ca (filled) and Mg (open) following reaction of 5 g/L of dolomite with 0.1 M NaCl and 0 (circles) or 5 (triangles) mg/L of EDTA ($1.7 \times 10^{-5}$ M) in batch experiments. .. 168

# LIST OF TABLES

Table 1. Average Concentrations and Standard Deviation (wt %) for Selected Elements Collected via SEM-EDS under the Three Conditions Studied ..... 10

Table 2. Theoretical and Experimental Ratios (X:Si where X is Fe, Al and K) for Muscovite based on Mineral Stoichiometry $KAl_2(Si_3AlO_{10})(OH)_2$ ..... 11

Table 3. XANES U L3-Edge Linear Combination Analysis (LCA) Results in Percentages for Calcite and Illite $NH_3$-gas Treated Samples sent to Argonne National Laboratory ..... 13

Table 4. BET Surface Area for Relevant Minerals for the Hanford Site for Control and Under High pH-(ammonia) and Neutral Condition (aerated) Treatments ..... 16

Table 5. Results from XRD Spectra Showing 2θ Reflection Position and Thickness in Å ..... 18

Table 6. Peak Height Al-Al-OH/Si-O-Si Ratios taken from FTIR Raw Data ..... 22

Table 7 . Experimental FTIR Band Assignments for Treated SGW and NaCl Montmorillonite Samples Compared to Reference Control Band Assignments* ..... 23

Table 8. FTIR major bending and stretching assignments for clays ($cm^{-1}$) ..... 23

Table 9. Kinetic Parameters from Linear Regression of Peretechnetate Reduction by Magnetite at Different pH Values ..... 48

Table 10. Ferrous, ferric and total iron in micro- and nano-magnetite and HS soil ..... 48

Table 11. Dissolution levels in the presence of 0, 5 and 50 mM of bicarbonates at pH 8 ..... 50

Table 12. Reduction Rates in Bicarbonate Free and Bicarbonate Solution. ..... 52

Table 13. Stock Solution Preparations for Calcium Carbonate-Forming Solutions ..... 57

Table 14. Amount of Stock Solutions and DIW to Prepare 20 mL of Mixed Sample ..... 57

Table 15. Summary of HPC Results as Compared with the Conditions in each Batch Sample ..... 78

Table 16. Comparison of E2/E3 Ratios Suggesting Degradation of Natural Organic Matter after 24 hours of Exposure to Full Light or Dark Conditions and 100 mM $NaNO_3$ ..... 80

Table 17. Tracer Test Results ..... 110

Table 18. Column Transport Parameters Determined by Rhenium Tracer Injection ..... 111

Table 19:Soprtion/Desorption of modified humic acid ..... 112

Table 20. Soprtion of Uranium ..... 114

Table 21. Initial Parameter Values Used in the MIKE SHE – ET Module ..... 121

Table 22. Maximum Rainfall Calculations for Different Recurrence Times for SRS Station 700A Data ..... 139

Table 23. Nd speciation in the aqueous phase as predicted by Geochemist's Workbench in variable ionic strength solutions of NaCl, $CaCl_2$, and $MgCl_2$ with 3 mM $NaHCO_3$ and 1000 µg/L Nd at pH 8.5, Note: all similar species aggregated to simplify, i.e. Nd-$CO_3$ represents $Nd(CO_3)^{2-}$ and $NdCO^{3+}$ ..... 163

Table 24. Nd speciation in the aqueous phase as predicted by Geochemist's Workbench in variable ionic strength solutions of NaCl, $CaCl_2$, and $MgCl_2$ with 3 mM $NaHCO_3$ with 5 mg/L of EDTA and 1000 µg/L Nd at pH 8.5, Note: all similar species aggregated to simplify, i.e. Nd-$CO_3$ represents $Nd(CO_3)^{2-}$ and $NdCO^{3+}$ ..... 164

Table 25. Summary of solid phase species forming (moles) as predicted by Geochemist's Workbench in variable ionic strength solutions of NaCl, $CaCl_2$, and $MgCl_2$ with 3 mM $NaHCO_3$ and 1000 µg/L Nd, Th, and U at pH 8.5 ..... 166

# PROJECT 2 OVERVIEW

Florida International University (FIU) is conducting applied research in collaboration with Pacific Northwest National Laboratory (PNNL), Savannah River National Laboratory (SRNL) and Savannah River Ecology Laboratory (SREL) scientists to support environmental remediation efforts at the Hanford Site and Savannah River Site (SRS), which are focused on cleanup technologies for contaminated soil and groundwater and the assessment of the fate and transport of contaminants in the environment. FIU is also teaming with scientists at Los Alamos National Laboratory (LANL) and the DOE Carlsbad Field Office (CBFO) to address potential contamination issues and update risk assessment models associated with the disposal of large quantities of defense-related, transuranic waste at the Waste Isolation Pilot Plant (WIPP). The aim of the Project 2 is to reduce the potential for contaminant mobility or toxicity in the surface and subsurface through the development and application of state-of-the-art scientific and environmental remediation technologies at DOE sites.

During FIU Performance Year 7 (2016-2017), FIU ARC worked on the following tasks:

**Task 1: Remediation Research and Technical Support for the Hanford Site**

Nuclear weapons production and other defense-related activities at the Hanford Site and Savannah River Site (SRS) have resulted in uranium, heavy metal, and radioactive contamination in the surface and subsurface environments. The U.S. Department of Energy's (DOE) Office of Environmental Management faces a number of environmental challenges with tremendous associated cleanup costs. The success of the DOE EM mission requires development and insertion of innovative approaches and novel technologies to address the significant challenges associated with the remaining cleanup of contaminated sites.

There is a need to further investigate the environmental fate of uranium, technetium and iodine under natural conditions and following remediation. For example, a significant residual mass of uranium still resides in the deep vadose zone (VZ) following release of over 200,000 kg of uranium from improper waste disposal and accidental spills. In addition, approximately 703 Ci of $^{99}$Tc have been released to the ground from historical releases, spills and leaks.

During FIU Performance Year 8, ammonia gas injection as a remediation strategy for uranium was investigated further with laboratory-scale experiments. Previous work has shown that the injection of $NH_3$ gas to the vadose zone is a viable method to decrease uranium mobility in the contaminated subsurface via pH manipulation and co-precipitation processes (Szecsody et al. 2012a, Zhong et al. 2015). It is expected that under the alkaline conditions caused by injection of the weak base, mobile uranium species will be transformed to low solubility uranium precipitates and/or additionally coated by non-uranium precipitates that are stable in the natural environment (Szecsody et al. 2012). However, there is a need for a better understanding of the formation processes leading to co-precipitation of uranium and the stability of the U-bearing precipitates. This information is necessary to accurately predict the fate of uranium in post-treated vadose zone soil. Experiments were also focused on solids characterization in order to confirm both mineral transformations and U association via adsorption and co-precipitation processes.

Research continued to investigate geophysical techniques. The spectral induced polarization method (SIP) that has been previously used to distinguish bulk phase changes in subsurface conditions, (e.g., rock/sediment/water, saturation, ionic conductivity) was tested for SIP signatures

of microbial activity using saturated basic column experiment. System complexity was controlled throughout the experimental phase by performing some basic studies for better detection of biofilms and microbial activities affecting ground and porewater quality in order to effectively implement any remediation technique.

Experiments also conducted to investigate for technetium reduction in the presence of magnetite mineral. Hanford groundwater and porewater are rich in bicarbonates. Technetium interactions with Hanford soil and pure minerals present in the Hanford Site were investigated in the presence and absence of bicarbonates. Furthermore, study evaluated the stability of immobilized $TcO_2$, in the presence of bicarbonates to assess for the potential resolubilization of Tc, which is important for designing effective remedial strategies for this contaminant.

The speciation of stable iodine ($^{127}I$) at Hanford sediment has shown that iodate ($IO_3^-$) is the major species followed by organo-iodine species with averages of 71% and 26%, respectively (Zhang et al. 2013). FIU investigated the effect of vadose zone environmental conditions such as pH and porewater constituencies, particularly silica content, on the iodine co-precipitation process with calcium carbonate. The formation of calcium carbonate phases can affect radionuclide concentrations in solution; however, the relationships of silicon and calcium carbonate to the co-precipitation process of radionuclides, and specifically iodine, wasn't investigated in the past.

Three graduate students working on this project 2 graduated this year; Alejandro Garcia graduated with master's degree and DOE Fellows Claudia Cardona and Hansell Gonzalez with PhDs. MS student Robert Lapierre defended his thesis. DOE Fellow Alejandro Hernandez graduated with his bachelor degree in Chemistry.

**Task 2. Remediation Research and Technical Support for Savannah River Site**

Nuclear weapons production and other defense-related activities at the Hanford Site and SRS have resulted in uranium, heavy metals, and radioactive contamination in the surface and subsurface environments.

Humic substances (HS) are complex heterogeneous organic mixtures of polydispersed materials formed by biochemical and chemical reactions during the decay and transformation of plant and microbial remains. Humic substances account for 50-80% of the organic carbon in the soil or sediment and are known for their excellent binding capacity for metals, while being insoluble or partially soluble. This makes HS a strong candidate for remediation efforts to reduce the mobility of uranium (VI) in the subsurface. Humic acid, which carries a large number of functional groups, provides an important function in ion exchange and as a metal complexing ligand with a high complexation capacity being able to affect the mobility of actinides in natural systems. Different types of humic substances such as unrefined humic acid, modified humic acid and commercial humic acid will be used in this research to study the sorption of humic acid on the sediment at different pH and its effect on uranium removal. Huma-K has potential as an amendment in the treatment of uranium in groundwater associated with the SRS F-Area seepage basins plume. In addition, it is thought that elevated silica concentrations in the acidic plume may enhance uranium removal when pH is increased by base injection. Understanding the synergy between humate and silica is important to developing an optimized pH adjustment to treat uranium in groundwater.

Four students were supporting this research in FIU Year 8 including undergraduate research assistants DOE Fellows, Ripley Raubenolt, Katherine Delarosa, Silvia Garcia and PhD student, Hansell Gonzalez, who graduated with his Ph.D. in fall 2018.

### Task 3: Surface Water Modeling of Tims Branch

The principal objective of this task is to develop an integrated hydrology/transport model as a tool to estimate flow and transport parameters and predict the spatial and temporal distribution of contaminants during extreme storm events. Results from this study are key to evaluating the effectiveness of tin(II)-based mercury treatment at the SRS site, and are also relevant to evaluating the potential of using water treatment and novel remediation technologies in other mercury-contaminated streams.

### Task 5: Research and Technical Support for WIPP

FIU ARC collaborated with research scientist Donald Reed of the Actinide Chemistry and Repository Science (ACRSP) team in support of Los Alamos National Laboratory's field office located at the Carlsbad Environmental Monitoring and Research Center (CEMRC) in Carlsbad, New Mexico. The goal is to generate accurate sorption data for the actinides to minerals and under conditions relevant to the Waste Isolation Pilot Plant as previous risk assessment models are based on conservative assumptions.

During FIU Performance Year 8, batch and mini column experiments were finalized to understand sorption of neodymium as an analog for the trivalent actinides at ionic strength from 0.1 - 5.0 M. DOE. In addition, preliminary experiments were conducted investigating the impact of EDTA on sorption of actinides in the WIPP environment. Zengotita also spent ten weeks at LANL CEMRC conducting experiments on the effect of bacteria on transport of relevant radionuclides in the WIPP. This year, two peer-reviewed papers were published and this research was presented in multiple venues including two invited presentations at other universities and an invited presentation as part of the inaugural NAMP webinar for young radiochemists. The project was supported by Fellows Alexis Vento (B.S. Environmental Engineering) and Frances Zengotita (B.S. Chemistry and English).

# PROJECT ACCOMPLISHEMNTS

**Peer-review publications between October 2017 and October 2018**

Emerson, H.P., Di Pietro, S., Katsenovich, Y., and Szecsody, J. (2018) "Uranium immobilization in the presence of minerals following remediation via base treatment with ammonia gas," *Journal of Environmental Management*, **223**, 1, 108-114.

Emerson, H.P., Di Pietro, S., Katsenovich, Y., and Szecsody, J. (2017) "Effect of Ammonium on Uranium Partitioning and Kaolinite Mineral Dissolution." *Journal of Environmental Radioactivity*, **167**, 150-159.

Emerson, H.P., Zengotita, F., Dittrich, T., Richmann, M., Katsenovich, Y., and Reed, D. (2018) "Retention of neodymium by dolomite at variable ionic strength as probed by batch and column experiments," Journal of Environmental Radioactivity. **190-191**, 89-96.

Katsenovich, Y, Cardona, C, Szecsody, J., Lagos L., and W. Tang, 2018. Assessment of Calcium Addition on the Removal of U(VI) in the Alkaline Conditions Created by $NH_3$ Gas. Applied Geochemistry, **92**, 94-103.

Gudavalli R., Katsenovich Y., and D. Wellman. Quantification of kinetic rate law parameters for the dissolution of natural autunite in the presence of aqueous bicarbonate ions at high concentrations, 2018. *Journal of Environmental Radioactivity*, **190-191**, 1-9.

Gonzalez-Raymat, H, Anagnostopoulos, V., Denham, M. Y., Katsenovich, YP, 2018. Unrefined humic substances as a potential low-cost amendment for the management of acidic groundwater contamination. *Journal of Environmental Management*, **212**, 210-218.

Emerson, H.P., Kaplan, D., and Powell, B.A. (2018) "Increased plutonium binding affinity to sediments with exposure up to 32 years," Chemical Geology, accepted.

**Oral presentations between October 2017 and October 2018 (presenter is underlined):**

*Potential impacts to local mineralogy from remediation with ammonia gas*, Silvina Di Pietro, Hilary P. Emerson, and Yelena Katsenovich, 256$^{th}$ American Chemical Society National Meeting, Boston, MA, Aug. 19-23, 2018.

*Uranium sequestration with pH manipulation by ammonia gas*, Yelena Katsenovich, Hilary P. Emerson, Claudia Cardona, Silvina Di Pietro, and Jim Szecsody, Goldschmidt, Boston, MA, Aug. 12-17, 2018.

*Remediation and Disposal of Radionuclides for the U.S. DOE*. Hilary P. Emerson, Green Chemistry Laboratory Seminar (Invited), Lappeenranta University, Mikkeli, Finland, Jun. 13, 2018.

*Actinides in the Environment: Understanding Increasingly Complex Systems*, Hilary P. Emerson, University of Central Florida Chemistry Department Seminar (*Invited*), Orlando, FL, Mar. 30, 2018.

*Base treatment for Uranium immobilization at DOE's Hanford site,* Hilary P. Emerson, Silvina Di Pietro, Yelena Katsenovich, Jim Szecsody, Waste Management Conference, Phoenix, AZ, Mar. 18-27, 2018 (Full paper in conference proceedings).

*Effects of ammonia and variable redox conditions on mineral dissolution*, Silvina Di Pietro, Hilary P. Emerson, Yelena Katsenovich, and James Szecsody, ACS 253rd National Meeting, San Francisco, CA, Apr. 2, 2017.

*The Effect of Biofilm on Spectral Induced Polarization Responses and on Autunite Dissolution in Saturated Hanford sediment.* Garcia, A., Katsenovich, Y., and B. Lee. In the proceeding of the Waste Management Conference (*Paper of Note* Award), March 18 - 22, Phoenix, Arizona, USA, 2018.

*Potential for transport of cesium as biocolloids in a high ionic strength system*, Frances Zengotita, Hilary P. Emerson, Timothy M. Dittrich, Juliet Swanson, Donald T. Reed, and Michael Richmann, FIU McNair Scholars Conference, Miami, FL, Oct. 18-19, 2018.

*Potential for Transport of Cesium and Lanthanides as Biocolloids in a High Ionic Strength System*, Frances Zengotita, Hilary P. Emerson, Timothy M. Dittrich, Juliet S. Swanson, Michael Richmann, and Donald T. Reed, 256th American Chemical Society National Meeting, Boston, MA, Aug. 19-23, 2018.

*Remediation and Disposal of Radionuclides for the U.S. DOE.* Green Chemistry Laboratory Seminar (*Invited*), Lappeenranta University, Mikkeli, Finland, June 13, 2018.

*Neodymium Sorption to WIPP-relevant Minerals*, Frances Zengotita and Hilary Emerson, Young Investigator's Inaugural Webinar in Radiochemistry for the National Analytical Management Program (*Invited*), May 17, 2018.

*Actinides in the Environment: Understanding Increasingly Complex Systems*, University of Central Florida Chemistry Department Seminar (*Invited*), Orlando, FL, Mar. 30, 2018.

*The Role of Chromohalobacter on Transport of Lanthanides and Cesium in the Dolomite Mineral System*, Frances E. Zengotita, Timothy M. Dittrich, Hilary P. Emerson, Michael P. Dugas, Juliet S. Swanson, and Donald T. Reed, FIU McNair Scholars Research Conference, Miami, FL, Oct. 19-20, 2017.

**Poster presentations between October 2017 and October 2018 (presenter is underlined):**

*Effects of alkaline treatment and redox conditions on mineral dissolution for Hanford sediments*, Silvina Di Pietro and Hilary P. Emerson, Waste Management Conference, Phoenix, AZ, Mar. 18-27, 2018.

*Lagos L, Katsenovich Y, Hoffman E, and V. Freedman, 2018.* Florida International University Research on Soil and Groundwater Contamination at DOE's Hanford and Savannah River Sites. In the proceeding of the Waste Management Conference, March 18 - 22, Phoenix, Arizona, USA

*Alejandro Hernandez*, a undergraduate DOE Fellow student presented his poster in the student poster section at WM Symposia 2018, "Interaction of Technetium-99 with Fe(II)-performed minerals in the presence of bicarbonates under reducing conditions", Waste Management Conference, March 18 - 22, Phoenix, Arizona, USA

*Alejandro Garcia*, a graduate DOE Fellow students presented his poster in the professional section at WM Symposia, "*The Effect of Biofilm on Spectral Induced Polarization Responses and on Autunite Dissolution in Saturated Hanford sediment*." This paper was awarded as a "Paper of Note".

*Ximena Lugo, "Iodine Co-precipitation with Calcium Carbonate", FIU McNair Scholars Conference, October* 2018

*Gudavalli, R., Smoot, A., Katsenovich Y, and M. Denham, 2018.* Study of Synergetic Interactions between Uranium, Humic Acid, Silica Colloids and SRS Sediments at Variable pH. In the proceeding of the Waste Management Conference, March 18 - 22, Phoenix, Arizona, USA

*Mahmoudi, M., Lawrence, A., Albassam, M., Hariprashad, R. and J. Morales.* Development of an Integrated Hydrology Model to Monitor Flow in Tims Branch Watershed, SC , American Water Resources Association (AWRA) 2018 Spring Specialty Conference – GIS & Water Resources X: Spatial Analysis of Watersheds: Ecological, Hydrological, and Societal Responses, Orlando, FL, April 2018

*Potential for transport of cesium as biocolloids in a high ionic strength system*, Frances Zengotita, Hilary P. Emerson, Timothy M. Dittrich, Juliet Swanson, Donald T. Reed, and Michael Richmann, FIU McNair Scholars Conference, Miami, FL, Oct. 18-19, 2018. (1st Place Poster Award)

*Fate of Actinides in the Presence of EDTA and Dolomite at Variable Ionic Strength*, Hilary P. Emerson, Frances Zengotita, Yelena Katsenovich, and Donald T. Reed, 256th American Chemical Society National Meeting, Boston, MA, Aug. 19-23, 2018.

*Role of Chromohalobacter on the potential transport of lanthanides and cesium in a dolomite mineral system*, Frances E. Zengotita, Hilary P. Emerson, Timothy M. Dittrich, Michael P. Dugas, Juliet S. Swanson, and Donald T. Reed, Waste Management Conference, Phoenix, AZ, Mar. 18-27, 2018.

*The Role of Chromohalobacter on Transport of Lanthanides and Cesium in the Dolomite Mineral System*, Frances E. Zengotita, Timothy M. Dittrich, Hilary P. Emerson, Michael P. Dugas, Juliet S. Swanson, and Donald T. Reed, FIU McNair Scholars Research Conference, Miami, FL, Oct. 19-20, 2017. (3rd Place Poster Award)

**Student awards**

2018 WM Symposia - best student poster (Hansell Gonzalez)

2018 WM Symposia - young professional award (Cristine Wipfli)

2018 WM Symposia - paper of note (Alejandro Garcia)

2018 Innovations in Nuclear R&D Award for Universities with Less than $600M in 2016 R&D Expenditures (Silvina Di Pietro), 2018.

Innovations in Nuclear R&D Award for Undergraduates (Frances Zengotita) 2018

Cash award for undergrad research symposia at FIU (Ripley Raubenolt) 2018

3rd place poster award at FIU McNair Scholars Conference (Frances Zengotita) 2017

1st place poster award at FIU McNair Scholars Conference (Frances Zengotita) 2018

2st place poster award at FIU McNair Scholars Conference (Ximena Lugo) 2018

# TASK 1: REMEDIATION RESEARCH AND TECHNICAL SUPPORT FOR THE HANFORD SITE

## Subtask 1.1: Sequestering Uranium at The Hanford 200 Area By In Situ Subsurface pH Manipulation Using Ammonia ($NH_3$) Gas

### Subtask 1.1: Introduction

The following task includes research to understand the processes controlling the sequestration of uranium at the 200 Area by *in situ* subsurface pH manipulation using $NH_3$ gas. The major focus for FIU Year 8 was solid phase characterization of mineralogical and sediment samples treated with ammonia gas. This task produced one publication in a peer-reviewed journal, five oral presentations, and one poster presentation during FIU Performance Year 8 (listed below) including two invited seminars at other universities and a proceedings paper for the Waste Management Symposia. The publications were based on results from batch experiments conducted during FIU Year 7. In addition, DOE Fellow Silvina Di Pietro received an award from the Innovations in Nuclear R&D program sponsored by DOE-NE for universities with less than $600M in 2016 R&D expenditures based on her Waste Management proceedings paper from 2017. DOE Fellow Di Pietro also passed her candidacy exam and spent ten weeks as an intern at PNNL studying the potential for reduction and removal of iodine from sediments with dithionite treatment.

### Subtask 1.1: Objectives

The objective of this subtask is to understand the potential impacts of ammonia gas treatment on mineral alterations and U fate in a vadose zone environment. These results will complement the pilot scale testing conducted earlier in 2018. FIU will consider the following research questions:

1. Is there an effect of redox conditions on mineral dissolution processes?
2. How does the solid to liquid ratio affect mineral alterations and U fate?
3. What are the major mineral phases forming following base treatment?
4. Which mechanisms control the fate of U during base treatment? (e.g. adsorption and incorporation)

### Subtask 1.1: Results and Discussion

During FIU Year 8, solid phase analysis was conducted on various mineral samples exposed to ammonia gas via batch experimental conditions. Results are presented below for SEM-EDX, XANES, BET, and FTIR analysis of solid phases as well as preliminary analysis of the aqueous phase via ICP-MS and ICP-OES.

#### Investigation of aged minerals following U and ammonia exposure

Select samples treated with ammonia gas were prepared to confirm short term aging results alongside a subset of samples with variable solid to liquid ratios. Batch samples with 0.5 g/L of the following minerals (kaolinite, muscovite, illite, montmorillonite, and calcite) and Hanford sediments were exposed to ammonia gas for three days in the presence of 1.3 mM $NaHCO_3$ and 1.9 mM $CaCl_2$ (SGW-2). Synthetic groundwater (SGW-2) is further simplified from initial experiments (SGW-1) which included 1.1 mM $NaHCO_3$, 1.4 mM $CaCl_2$, 0.22 mM $KHCO_3$, and 0.6 mM $MgCl_2$. Figure 1 shows comparable results for 3-day treatment with 5% $NH_3$ + 95% $N_2$

gas for Hanford sediments. However, without aging, the results following aeration represent much greater fractions in the aqueous phase with decreased $K_d$ partitioning coefficients (Figure 2). FIU suggests that the aging step increases co-precipitation processes leading to greater incorporation of U into the solid phase. In addition, with greater solid loadings, FIU expects greater removal as there will be more secondary precipitation occurring. However, initial samples were inconclusive due to challenges separating solids.

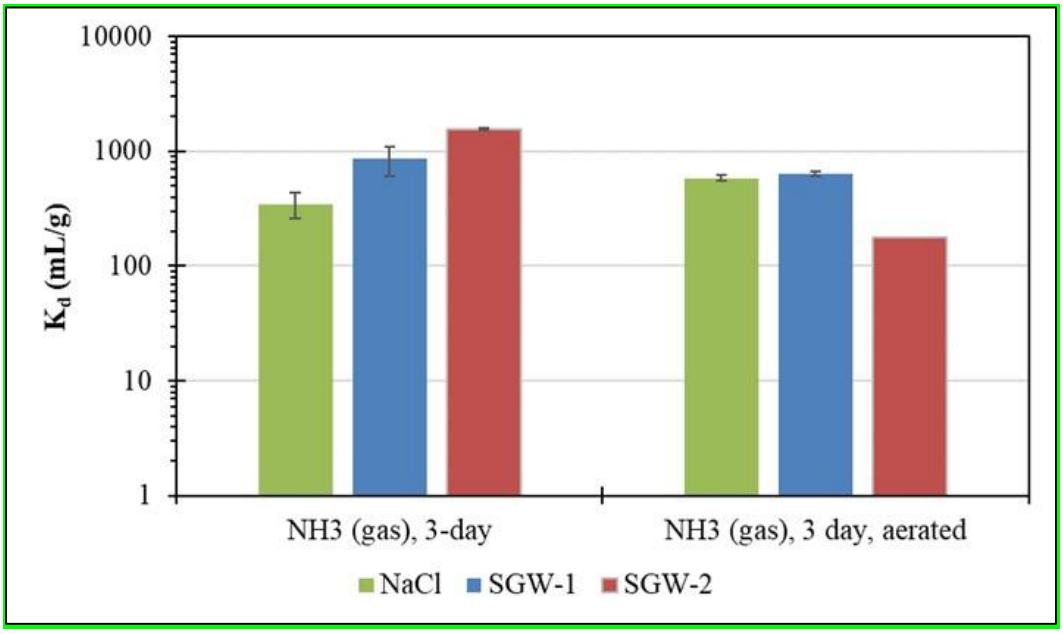


**Figure 1. Comparison of U $K_d$ partitioning coefficients (mL/g) for Hanford sediments treated with 5% $NH_3$ + 95% $N_2$ gas for three days in the presence of different electrolyte solutions. Note: error bars are based on triplicate samples.**

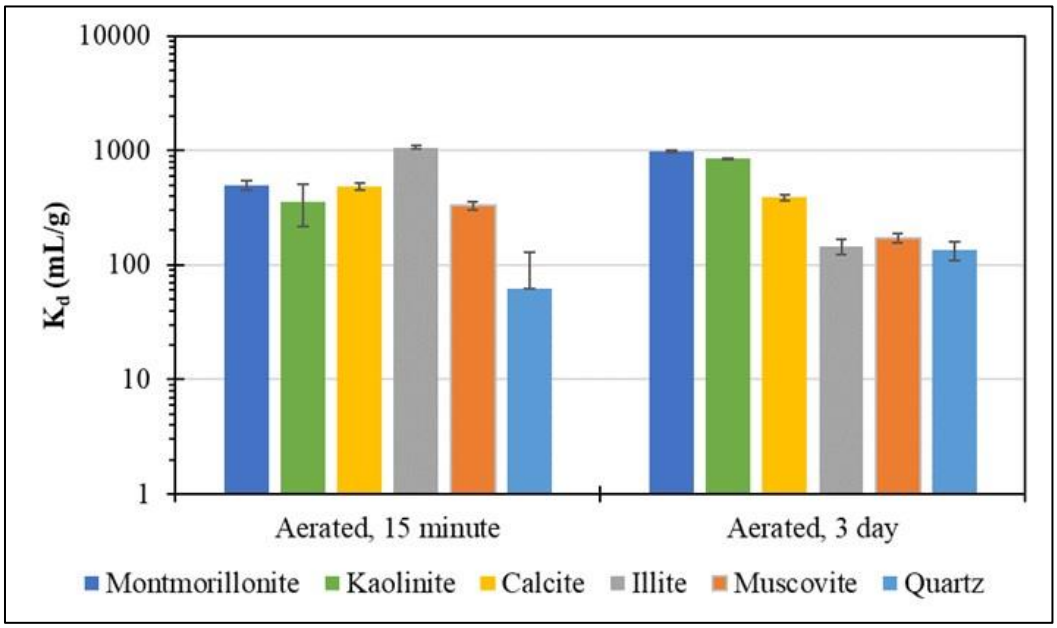


**Figure 2. Comparison of U $K_d$ partitioning coefficients (mL/g) for pure minerals and Hanford sediments treated with 5% $NH_3$ + 95% $N_2$ gas for three days with sampling after 15 minutes or three days following the aeration step. Note: error bars are based on triplicate samples.**

**SEM-EDS analysis of samples exposed to U and treated with $NH_3$ gas**

Scanning electron microscopy (SEM) was conducted at the Florida Center for Analytical Electron Microscopy (FCAEM). A total of nine samples were taken to the facility to examine: 1) morphology, 2) particle size, and 3) elemental composition using a scanning electron microscope with energy dispersive spectroscopy (SEM-EDS). The EDS detector collected data for 20 seconds of live time at 24 Pa vacuum pressure with an X-ray beam, at an incident angle of 35° and energy of 25 keV for the mineral under study (muscovite). Backscatter detection mode was utilized to allow for the heavier elements to appear brighter in order to search for particles and minerals associated with U.

Table 1 summarizes elemental analysis data for muscovite under variable conditions. Muscovite samples underwent three different treatments: 1) dried mineral neither with U addition nor with ammonia gas treatment used as a control, 2) synthetic groundwater solution equilibrated with 5% $NH_3$ gas in the presence 500 ppb U, and 3) 7.2 mM NaCl solution equilibrated with 5% $NH_3$ gas in the presence 500 ppb. Interestingly, from the elements selected, elemental concentrations and ratios (wt %) were consistent across the control and electrolyte solution conditions (Table 2). These results indicate that any transformations in mineralogy due to dissolution and precipitation processes upon base treatment were not detectable within the capabilities of SEM-EDX (on the order of 0.1% by wt.). An effort was made to collect SEM images and EDS data for both bright particles found on the mineral surface and background (i.e., darker surfaces). In addition, elemental analysis was consistent upon comparison of two different magnifications (300x and 1100x) and, therefore, data were combined to estimate an average and standard deviation based on a greater pool of data. As one of the most abundant elements in Earth's crust, Si showed the greatest concentration with a range of 44.9 – 47.1 wt%. The Si > Al > K trend will be discussed below when describing Table 2.

Because the aqueous phase is expected to be oversaturated with respect to calcite following base treatment in SGW, Ca content in solids was also carefully monitored. For this set of results, Ca concentrations are much lower than Na, K, and Mg content. Since Ca concentrations are the same as their standard deviation error, they are likely too near to detection limits to support analysis of secondary precipitates of calcite. Similar Ca content was measured for all three muscovite treatments.

In addition to analysis of potential secondary precipitates from electrolyte solutions and changes in bulk mineralogy via major cations in the mineral structure, SEM-EDS allows for measurement of trace impurities present in the muscovite samples. Ti and Fe are both observed with consistent concentrations and ratios across treatments. These results indicate that Fe and Ti are likely present as impurities, potentially as Fe-Ti oxides, and that minimal removal and transformations are observed with base treatments.

It is important to note that for all three figures, SEM-EDX analysis for U detected 0.0 wt%. This lack of U detection could be either due to: 1) not enough beam energy in kilovolts coming from the instrument for U, or 2) no secondary precipitate was formed under base treatment (control samples are not expected to contain U). The electron binding energies from U's K and L shells are 115.6 kV and 21.8 kV, respectively. The x-rays emitted following ejection of a K-shell electron cannot be detected with this technique as the beam of charged particles is operated at only 25 kV. Because this energy is lower than the binding energy for K shell electrons, they cannot be excited.

However, the L shell electrons may be excited and ejected, leading to emission of an x-ray when the vacancy is filled.

Because there were no locations within the sample above detection limits for U and secondary precipitates were not observed based on the bulk elemental analysis, FIU suggests that U is associated fairly homogenously with the surface. The bulk loading of U with the solid estimated from aqueous phase measurements during batch sorption experiments would be below detection limits for this technique (0.1% or 1000 ppm) if the U was homogenously associated with the surface. However, if U was removed from the aqueous phase via secondary co-precipitation with smaller particles, there may be some areas with high enough U content for detection. Notably, this was not observed, although a lack of detection of U does not demonstrate how U is associated with the solid phase. Future experiments will reach greater U loadings in order to provide unequivocal evidence for removal by either adsorption or co-precipitation or both.

**Table 1. Average Concentrations and Standard Deviation (wt %) for Selected Elements Collected via SEM-EDS under the Three Conditions Studied**

*(Control with neither U addition nor with ammonia gas treatment, SGW and NaCl)*

| | Treatment (wt%) | | |
|---|---|---|---|
| **Element** | **Dry Control*** | **Synthetic Groundwater solution equilibrated with 5% $NH_3$ gas†** | **7.2 mM NaCl solution equilibrated with 5% $NH_3$ gas*** |
| Na | 0.9±0.2 | 0.6±0.1 | 0.8±0.1 |
| Mg | 0.8±0.1 | 1.3±0.7 | 0.7±0.1 |
| Al | 30.4±0.3 | 29.7±0.8 | 30.2±0.2 |
| Si | 46.7±2.0 | 45.5±1.1 | 45.4±0.6 |
| K | 17.1±1.9 | 18.4±1.1 | 18.4±0.5 |
| Ca | 0.1±0.1 | 0.1±0.1 | 0.1±0.1 |
| Ti | 0.4±0.1 | 0.3±0.1 | 0.4±0.1 |
| Fe | 3.6±0.7 | 4.1±0.6 | 4.1±0.4 |
| U | 0.0±0.0 | 0.0±0.0 | 0.0±0.0 |

*Note: * and † represent an average and standard deviation of 7 and 8 measurements, respectively.*

Lastly, Table 2 below confirms muscovite's stoichiometry $KAl_2(Si_3AlO_{10})(OH)_2$ (Miller, *et al*., 1981). X:Si (where X is Fe, Al and K) ratios are similar for all three conditions providing further evidence that the treatments did not significantly affect the mineral phase (within the capabilities of SEM-EDS to detect these changes based on elemental detection limits of ~0.1%). The ratios of Al:Si and K:Si are 0.67 and 0.33, respectively. Experimental results in Table 2 confirm that the mineral is a phyllo-aluminosilicate from the mica group since elemental ratios are similar to theoretical values. Micas (muscovite and biotite) are the main K-containing mineral groups found in the soil as confirmed in Table 1 results (Osman, 2012). However, future work will compare experimentally-determined ratios with other minerals and determine a statistical error on measurements.

**Table 2. Theoretical and Experimental Ratios (X:Si where X is Fe, Al and K) for Muscovite based on Mineral Stoichiometry $KAl_2(Si_3AlO_{10})(OH)_2$**

| Theoretical | | Experimental | | |
|---|---|---|---|---|
| | | Dry Control* | SGW solution equilibrated with $NH_3$ gas† | 7.2 mM NaCl solution equilibrated with 5% $NH_3$ gas* |
| **Fe:Si** | - | 0.08 | 0.09 | 0.09 |
| **Al:Si** | 0.67 | 0.65 | 0.65 | 0.67 |
| **K:Si** | 0.33 | 0.37 | 0.41 | 0.40 |

Note: * and † represent an average and standard deviation of 7 and 8 measurements taken, respectively

## XANES preparation procedure

Three samples were prepared for EXAFS with a target mass of 300 milligrams and at least 500 ppm loading of uranium: 1) calcite co-precipitates from synthetic groundwater, 2) illite exposed to U and treated with $NH_3$ gas, and 3) illite exposed to U and treated with $NH_3$ gas with aeration to return to neutral pH conditions. All $NH_3$ gas treatments were conducted in a glovebag (GlasCol) with approximately 5% $NH_3$/95% $N_2$ with the samples uncapped for 12-16 hours to equilibrate with the gas phase. The initial concentration of 500 ppb of U in the aqueous phase in these experiments is similar to that expected in the subsurface based on previous leaching experiments from contaminated sediments removed from the Hanford site [1]. Approximately two liters of synthetic groundwater with 500 ppb U were treated in order to recover 100 milligrams of solid.

In order to increase the loading of U without precipitating at neutral pH conditions (i.e., before base treatment), sequential treatments were conducted with illite at a concentration of 1 g/L with 500 ppb of U in synthetic groundwater. After each step, the samples were centrifuged and the aqueous phase was decanted and then a fresh solution was added with U for ammonia gas treatment. Samples for illite exposed to U and treated with $NH_3$ gas were loaded and treated twice in series to reach an appropriate loading, but the aerated samples were sequentially loaded three times as some U was expected to be lost during aeration and washing. Following the loading steps, all of the samples were washed twice with pH-adjusted deionized water (> 18 MΩ-cm). The solid phases were recovered and dried at 40°C. The aqueous phase was monitored at each step in order to estimate solid phase loadings of U and will be reported in the December monthly report.

## XANES Results from Argonne National Laboratory (interpreted by Dr. Sarah Saslow – PNNL)

XANES data were obtained at the APS using beamline 12-BM-B for the U L3 edge (17166 eV) at room temperature. XANES spectra were carefully energy calibrated using Zr foil as an energy reference. Two standard spectra were used in the linear combination analysis fitting of the sample XANES spectra: $UO_2$ and $UO_3$. Each standard was diluted in cellulose to minimize the effects of self-absorption. U-XANES standard spectra are provided in Figure 3, while the U-XANES spectra for unknown samples are provided in Figure 4 to Figure 6. The unknown samples are labeled *Calcite_NH3*, *Illite_NH3*, and *Illite_Aerated*. Calcite_$NH_3$ are precipitates formed following $NH_3$ gas treatment of synthetic groundwater solutions with 500 ppb U and should consist mainly of calcite. *Illite_NH3* and *Illite_Aerated* were both exposed to U and treated with $NH_3$ gas, while *Illite_Aerated* was aerated following treatment to return to neutral pH conditions. The estimated

U loadings from KPA measurements of the aqueous phase were 3300, 850 and 350 ppm, respectively.

Table 3 presents the $UO_2$ and $UO_3$ fractions percentage for each sample. For the three samples analyzed, the $UO_3$ fraction or the +6 valence state is most dominant with >74% estimated for all samples. However, there is a significant fraction of U in the +4 oxidation state. It must be noted that the spectra for U associated with the illite mineral following ammonia gas treatment (Figure 5) and ammonia gas treatment and aeration (Figure 6) are not as smooth as the spectra of U co-precipitated with calcite due to the significantly lower concentration of U present. This led to greater error in the fitting as the samples were near detection limits.

Previous data shows that conditions are much more reducing following treatment with ammonia gas ($5\%NH_3/95\%N_2$) as oxidation reduction potential (ORP) measurements under simulated natural conditions are 530±50 mV versus 150±15 mV following gas treatment. It is possible that reduction of U occurred as previous research suggests that reduction of U can occur below 250 mV (McKinley et al., 2007). Further, precipitation of U(IV) would be likely due to its significantly lower solubility than U(VI) (Langmuir, 1997). However, efforts were not made to keep the samples under reducing conditions as they were aerated, washed, and dried in the presence of air. Therefore, it is notable that a significant fraction of U(IV) persists in the solid phase. FIU suggests that a fraction of U(IV) remains due to incorporation into the mineral phase during treatment, although further investigation is ongoing.

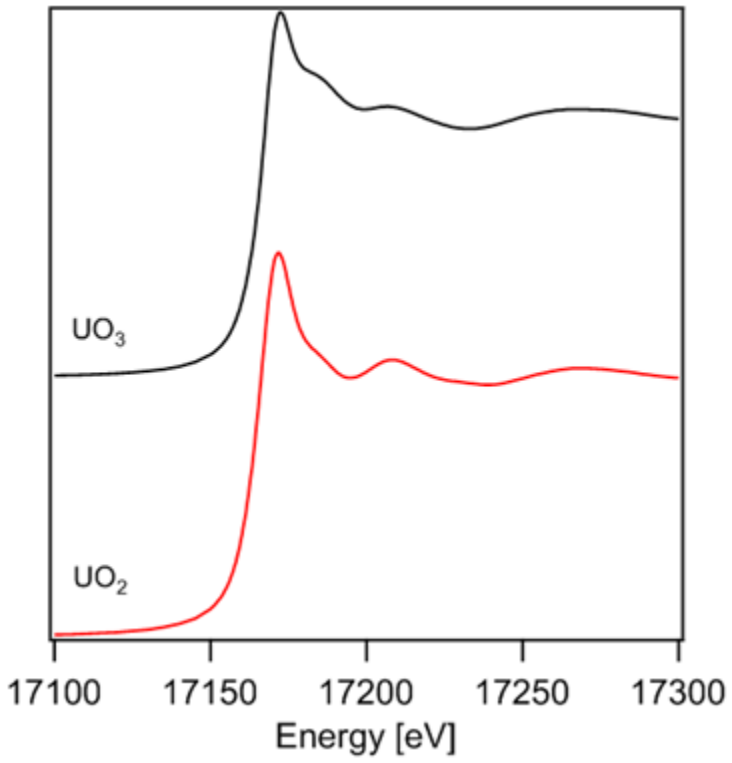


**Figure 3. U L3-edge XANES spectra of the reference compounds used for XANES LCA fitting: LCF fit shown in red for $UO_2$ and in black for $UO_3$.**

**Table 3. XANES U L3-Edge Linear Combination Analysis (LCA) Results in Percentages for Calcite and Illite $NH_3$-gas Treated Samples sent to Argonne National Laboratory**

| Sample | Valence State | Calcite_$NH_3$ | Illite_Aerated | Illite_$NH_3$ |
|---|---|---|---|---|
| $UO_2$ Fraction | U(IV) | 26±4% | 26±11% | 15±8% |
| $UO_3$ Fraction | U(VI) | 77±4% | 74±11% | 91±8% |

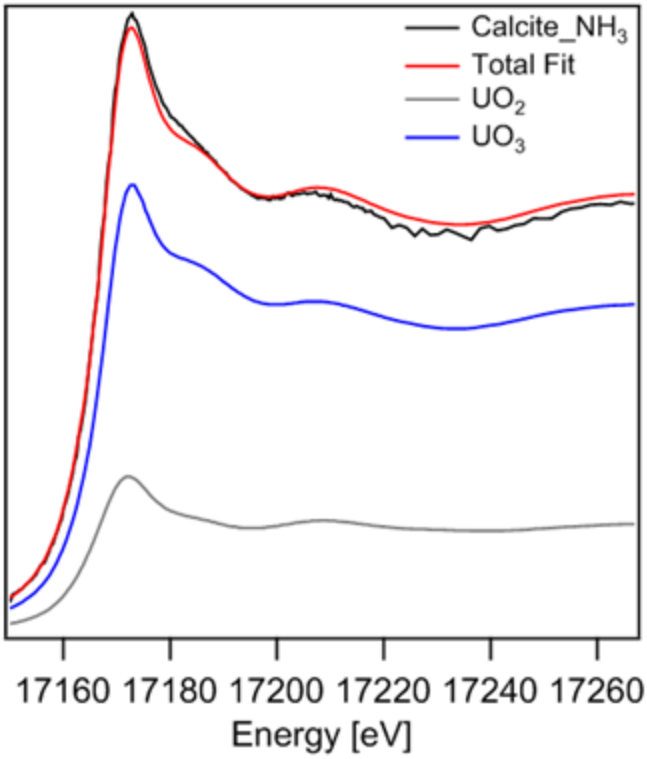


**Figure 4. U L3-edge XANES spectrum [black] and total LCF fit [red] for Calcite_$NH_3$. Fraction-adjusted standards contributing to the LCF fit shown for $UO_2$ [grey] and $UO_3$ [blue].**

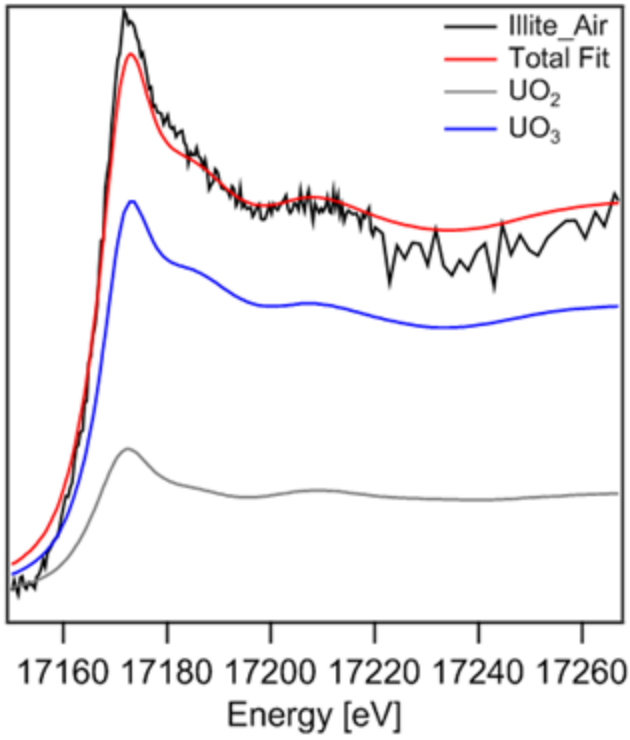


**Figure 5. U L3-edge XANES spectrum [black] and total LCF fit [red] for Illite_Aerated. Fraction-adjusted standards contributing to the LCF fit shown for $UO_2$ [grey] and $UO_3$ [blue].**

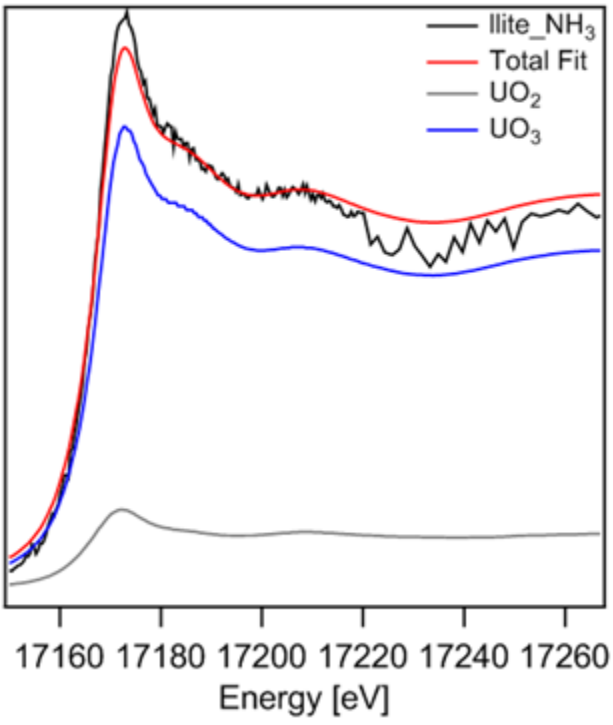


**Figure 6. U L3-edge XANES spectrum [black] and total LCF fit [red] for Illite_$NH_3$. Fraction-adjusted standards contributing to the LCF fit shown for $UO_2$ [grey] and $UO_3$ [blue].**

## BET Analysis of Clean Minerals

Minerals (illite, muscovite, and montmorillonite) that have been aged for one month in the presence of $NH_3$ gas with NaCl and synthetic groundwater (SGW) solutions were analyzed by Brunauer–Emmett–Teller (BET) with the aid of Ebenezer Adelowo from the Department of Mechanical and Materials Engineering at FIU's Engineering Campus (MicroMeritics TriStar II).

Table 4 lists the BET results before (control) and after pH manipulation. Muscovite samples, however, significantly changed after the pH was returned to neutral conditions. An increase of four orders of magnitude is observed for the aerated samples in comparison to ammonia-treated and control samples. This is likely due to breaking of the interlayer phyllosilicate tetrahedral-octahedral-tetrahedral (TOT) sheets. The stacking of the TOT units has a very weak bond and, as a result, provides an excellent cleavage between the units (Hayati-Ashtiani, 2012). Because muscovite samples were aerated, the negative charge of oxygen atoms most likely displaced the cations of the interlayer cation layer, reducing its 9.5-10 Å spacing (Figure 7). Moyes et al. previously reported that "the material (muscovite) is prone to oxidation, making surface area measurements difficult" (Moyes et al., 2000).

For illite and montmorillonite, control BET surface areas are 19.1 and 23.8 $m^2/g$, respectively. Once mineral samples underwent treatment, their surface area did not significantly change. The only exception is montmorillonite in 7.2 mM NaCl solution under aerated treatment. The BET surface area was less than half (7.37 $m^2/g$) compared to the control surface area. However, this is likely an analytical error as there was not adequate mass of solid to place in the instrument due to technical problems while airing stripping the sample. In the case of illite, the cation interlayer spacing is less pronounced due to weathering and its "detrital muscovite" nature, therefore the surface area is not significantly affected (Bailey, 1966; Srodon, 1984). Moreover, the nature of montmorillonite's expanding ~8.0 Å layers is not affected by the oxygen atoms because it is several hydration-layers deep (Hayati-Ashtiani, 2012; Moyes et al., 2000).

**Table 4. BET Surface Area for Relevant Minerals for the Hanford Site for Control and Under High pH-(ammonia) and Neutral Condition (aerated) Treatments**

| Mineral | Solution/Treatment | BET Surface Area ($m^2/g$) |
|---|---|---|
| Illite | $SGW/NH_3$ | 16.2 |
| | $NaCl/NH_3$ | 15.7 |
| | SGW/aerated | 17.1 |
| | NaCl/aerated | 16.6 |
| | control | 19.1 |
| Muscovite | $SGW/NH_3$ | 0.111 |
| | $NaCl/NH_3$ | 0.370 |
| | SGW/aerated | 11.4 |
| | NaCl/aerated | 11.7 |
| | control | 0.096 |
| Montmorillonite | $SGW/NH_3$ | 26.0 |
| | $NaCl/NH_3$ | 24.5 |
| | SGW/aerated | 23.9 |
| | NaCl/aerated | 7.37 |
| | control | 23.8 |

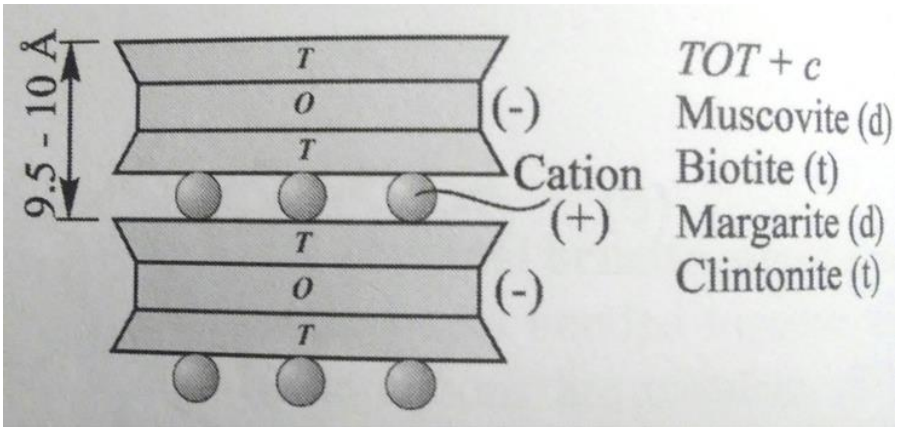


**Figure 7. Diagram of 2:1 layer silicates (Nesse, 2012a).**

## XRD Analysis of Clean Minerals (Illite)

For X-ray diffraction analysis, every crystalline substance has a unique diffraction patterns from with a characteristic set of crystal plane spacings in the crystal lattice (*d*-spacing) which can be measured in Angstroms (Å) and an intensity of reflection at a given diffraction angle $I/I_o$ (where I is an integrated intensity per unit length of diffraction line and $I_o$ is the intensity of the incident beam). Based on Bragg's law (Eq. 1), the scattering angle, $\theta$, can be related to the d-spacing and incident wave ($\lambda$) with *n* representing a positive integer (Lugwisha, 2011).

$$2d\sin\theta = n\lambda \quad \text{Eq. 1}$$

Illite samples were analyzed by an X-ray diffractometer (XRD) (Bruker GADD/D8 X-ray with Apex Smart CCD detector) from the Advanced Materials and Engineering Research Institute (AMERI) at the FIU's engineering campus. XRD measurement of illite samples was conducted at room humidity and temperature. All peak positions were obtained by step-size scanning at 0.02 2θ intervals from 5◦ to 35◦ using CuKα radiation at 40 kV. According to Bruker's CCD detector, the wavelength coming off the copper target is measured to be 1.542 Å. This is in accordance to the wavelength of X-rays used in diffractometers (around 1 or 2 Å) because this is of similar spacing in between atoms of most mineral structures (Nesse, 2012b). Analysis of remaining mineral samples is ongoing. Table 5 summarizes the measured *d* values, or the distance of spacing between planes of atoms, at their reflection wavelength for control (untreated) and ammonia and aerated-treated in synthetic groundwater (SGW) samples. Figure 8 shows diffraction patterns for the three conditions.

Experimental patterns were compared with reference material patterns from the library in the computer program Match! to identify the major minerals present in the illite sample. With a figure-of-merit of 0.93 or 93%, Figure 2-6 was developed. Out of the five major peaks identified, four were matched by the database for the phlogopite mineral. In the spectra shown in Figure 9, pure illite reflected at 10.1, 5.00, and 3.38 Å. These reflections patterns are seen in peak #1, #2 and #5 from experimental patterns in Figure 8. The illite sample is also in accordance with one of the first illite XRD patterns obtained by Reynolds and Hower (1970) and later modified by Reynolds and Moore (1989). Because peaks #3 and #4 are not found in the pure illite literature reference (Figure 2-7), FIU can assume that these peaks do not correspond to illite but instead to a different mineral impurity that was present in the sample. The software report states the following chemical formula: $K(Mg, Fe)_3(Al,Fe)Si_3O_{10}(OH,F)_2$ as the best match for the spectra. However, the Clay Minerals Society previously reported a formula of $Mg_{0.9}Ca_{0.6}K_{1.37}[Al_{2.69}Fe(III)_{0.76}Fe(II)_{0.06}Mn_{(tr)}Mg_{0.43}Ti_{0.06}][Si_{6.77}Al_{1.23}]O_{20}(OH)_4$.

Illite structures are characterized by relatively large layer-to-layer distances (between 9.5 and 10 Å) (Zviagina *et al*., 2015). When comparing the *d* spacings for control and SGW aerated samples, the difference is not significant. Zhen *et al*. analyzed a series of basal $d_{001}$ diffractions peaks (i.e., 10 Å *d* spacing) and found that the position had changed to 11.53 Å when organic solvent DMSO had intercalated in between the interlayer of illite. This was due to the nucleophilic attack of S atom center to $H^+$ ions, as the sample underwent acidification. However, FIU can conclude that no molecules intercalated into the interlayers of treated illite as the *d* spacing did not significantly enlarge (Zhen *et al*., 2017). Interlayer distance, or lateral dimensions, are revealed by peak #2. Because a broad, low-intensity peak appears for $2\theta$ = 17.70-17.74, FIU can conclude that the interlayer of illite was neither occupied nor changed (i.e., *d* spacing remains constant) (Zhen *et al*., 2017; Zviagina *et al*., 2015). Previously, authors concluded that illite is not easily affected by chemical and heat treatments in comparison to kaolinite and thus, it is less subjected to transformation (Lugwisha, 2011). In addition, previous research found that with higher NaOH concentration and longer reaction times, illite peak intensities increased (Mashal *et al*., 2005). Therefore, future analysis will include a comparison of peak intensities in each sample by utilizing peak ratios as done previously by Mashal and team. FIU will also re-measure the illite-SGW-$NH_3$ sample as there is some noise in the spectra.

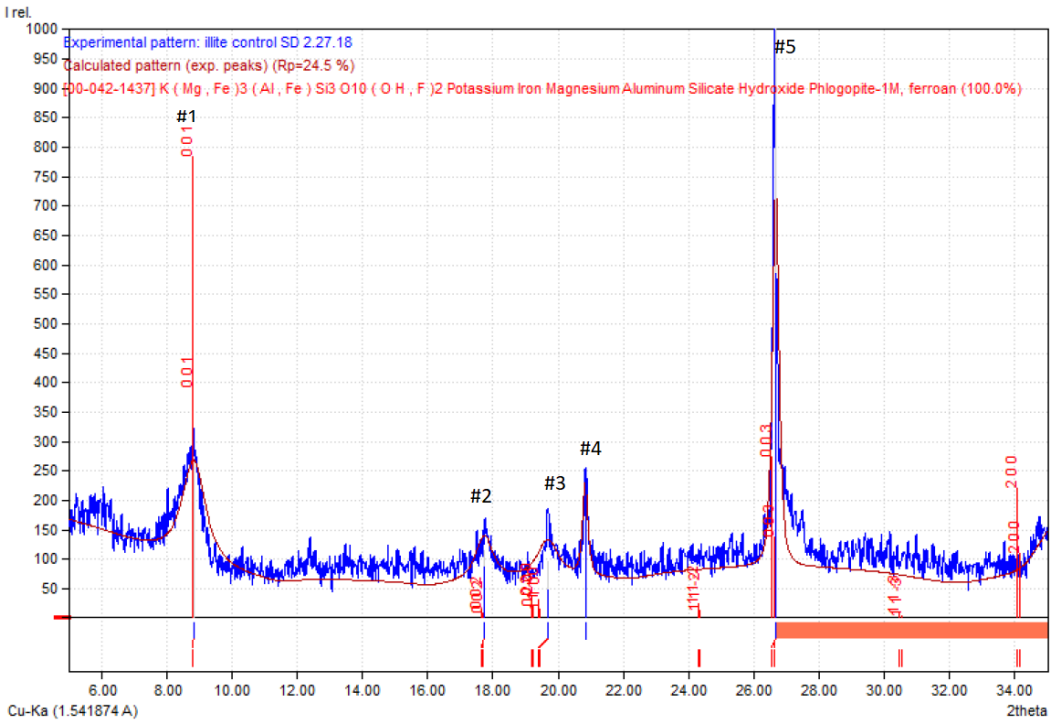


**Figure 8. X-ray diffraction (XRD) patterns of illite control (no treatment) showing the five most representative and matched peaks from the phase identification software *Match!*.**

**Table 5. Results from XRD Spectra Showing 2θ Reflection Position and Thickness in Å**

| | Control | | SGW $NH_3$ | | SGW Aerated | |
|---|---|---|---|---|---|---|
| **Peak** | **2θ [◦]** | **d [Å]** | **2θ [◦]** | **d [Å]** | **2θ [◦]** | **d [Å]** |
| #1 | 8.840 | 10.0 | no available data | | 8.860 | 9.98 |
| #2 | 17.74 | 4.99 | 17.70 | 4.99 | 17.70 | 5.01 |
| #3 | 19.68 | 4.51 | 19.81 | 4.48 | 19.73 | 4.50 |
| #4 | 20.80 | 4.26 | 20.86 | 4.26 | 20.87 | 4.26 |
| #5 | 26.68 | 3.34 | 26.43 | 3.34 | 26.66 | 3.34 |

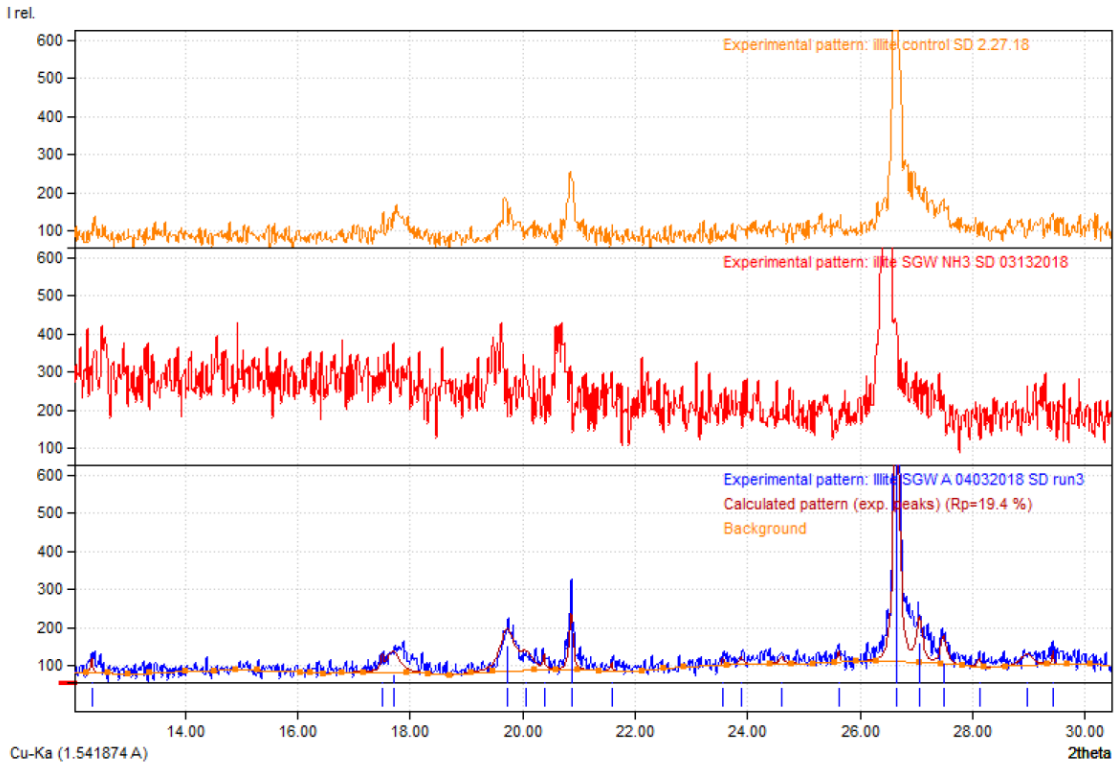


**Figure 9. X-ray diffraction (XRD) patterns of illite for the following conditions: control (no treatment) (orange), ammonia-treated in SGW (red) and aerated-treated in SGW (blue). Note: peak #1 at ~ 8.8 Å is not shown.**

## FTIR Analysis of Clean Minerals

Minerals (illite, muscovite, montmorillonite, calcite, kaolinite, and Hanford sediments) that have been aged for one month in the presence of $NH_3$ gas with NaCl and synthetic groundwater solutions have been analyzed by attenuated total reflectance (ATR) FTIR with the aid of Dr. Ya-Li Hsu from the chemistry department at FIU's main campus.

Prior to FTIR analysis, samples were dried at 30ºC to prevent the OH stretching of hydrogen-bonded water molecules to resonate at wavenumber ~3450 $cm^{-1}$. In the case of treated montmorillonite and Hanford control sediment samples, a mortar and pestle were used to crush the dried solids and thus obtain a homogeneous sample.

The instrument used to obtain IR spectra was an Agilent Model Cary 670 with a PIKE diamond/ZnSe ATR optical crystal used as a reflectance medium. Dry-air is constantly purged through the PIKE detector. Software installed in the FTIR spectrometer was Resolution Pro SW Std version 5.3. Spectra were collected for 4 scans at a resolution of 4 $cm^{-1}$ between 4000 and 600 $cm^{-1}$.

Figure 10 to Figure 12 show the FTIR spectra obtained for illite, muscovite and montmorillonite treated and control samples. In general, all figures contain adsorption peaks in correspondence for smectite and micas. Adsorption bands at 1200-700 $cm^{-1}$ are related to the vibration of typical aluminosilicate structural functions, including strong bonds of Si-O at 1000 $cm^{-1}$ (Busigny, Cartigny, Philippot, and Javoy, 2003; Sedmale, Randers, Rundans, and Seglins, 2017). It is important to note that none of the figures contain broad –OH stretching bands of 3800-3400 $cm^{-1}$,

a strong hydrophilic effect region, due to the drying step (Hayati-Ashtiani, 2012). The –OH bond stretch is most prominent in the 3630-3620 $cm^{-1}$ region (Busigny et al., 2003). Illite spectrum attributes a small peak at 3615 $cm^{-1}$ while both montmorillonite and muscovite spectra display the stretch at 3623 $cm^{-1}$. This peak confirms that the minerals contain a hydroxyl functional group on their surface. Further, the ATR-FTIR spectra in Figure 10 to Figure 12 present the following peak intensity trend in the Si-O strending bands: aerated>control>$NH_3$ treated. This trends suggests that aluminosilicates are: 1) dissolving at elevated pH, and 2) aerated samples are precipitating on the surface. Due to the increase in Si-O bond peak intensity, precipitation of secondary minerals is likely occuring following aeration back to natural pH.

To confirm the aforementioned precipitation, Al:Si ratios were analyzed to track dissolution of the three minerals studied. After the equilibrium step for $NH_3$-treated and aerated samples, the supernatant was acidified in 1% $HNO_3$ for analysis by inductively coupled plasma optical emission spectroscopy (ICP-OES, Perkin Elmer, Optima 7300 DV) for Al and Si. Figure 2-4 shows that muscovite and montmorillonite NaCl samples decrease in Al:Si ratios, suggesting precipitation or, more specifically, incongruent dissolution. In the case of montmorillonite SGW, the trend is less conclusive as minimal aqueous solution was left after the aeration step. The presented incongruent dissolution observed is confirmed by Di Pietro's internship 2016 data as greater leaching of Si than Al occurred for muscovite and montmorillonite samples. In the case of illite, no previous incongruent dissolution data is known. However, while Al:Si ratios may increase as pH returns to neutral conditions, FTIR confirms that SGW and NaCl aerated samples observe a stronger absorbance in the Si-O bands, suggesting greater surface precipitation.

Lastly, to determine if the peak intensity is changing proportionally pertinent to their treatment, peak height ratios of two major aluminosilicate band stretchings were calculated. For the Al-Al-OH and Si-O-Si band stretch, the maxima wavenumber were taken at approximately 914 $cm^{-1}$ and 1000 $cm^{-1}$, respectively. Table 6 shows that indeed all ratios are consistant throughout. Further analysis will be done on other important band stretches. A more detailed study on montmorillonite's absorption peaks in Figure 12 is shown in Table 7. Unlike Figure 10 and Figure 11, Figure 12 shows a broader –OH peak, particularly for montmorillonite in NaCl solution after aeration. The broadness of 3623 $cm^{-1}$ is due to the isomorphic substitution of octahedral $Al^{3+}$ by $Fe^{2+}$ or $Mg^{2+}$ cations. Three bending vibrations of hydroxyl group are associated with these cations in the following band stretches: 915 $cm^{-1}$ (Al-Al-OH), 875 $cm^{-1}$ (Al-Fe-OH) and 836 $cm^{-1}$ (Al-Mg-OH) (Hayati-Ashtiani, 2012). Because Figure 12 shows these stretches, it may prove that isomorphic substitution of $Al^{3+}$ in the octahedral layer is occurring. Octahedral layers are on the inner-planes of the smectite mineral surrounded by tetrahedral sheets consisting of oxygen-silicon. Isomorphic substitution is due to cation exchange capacity of Mg and Al in the central, octahedral plane (Segad, Jonsson, Åkesson, and Cabane, 2010).

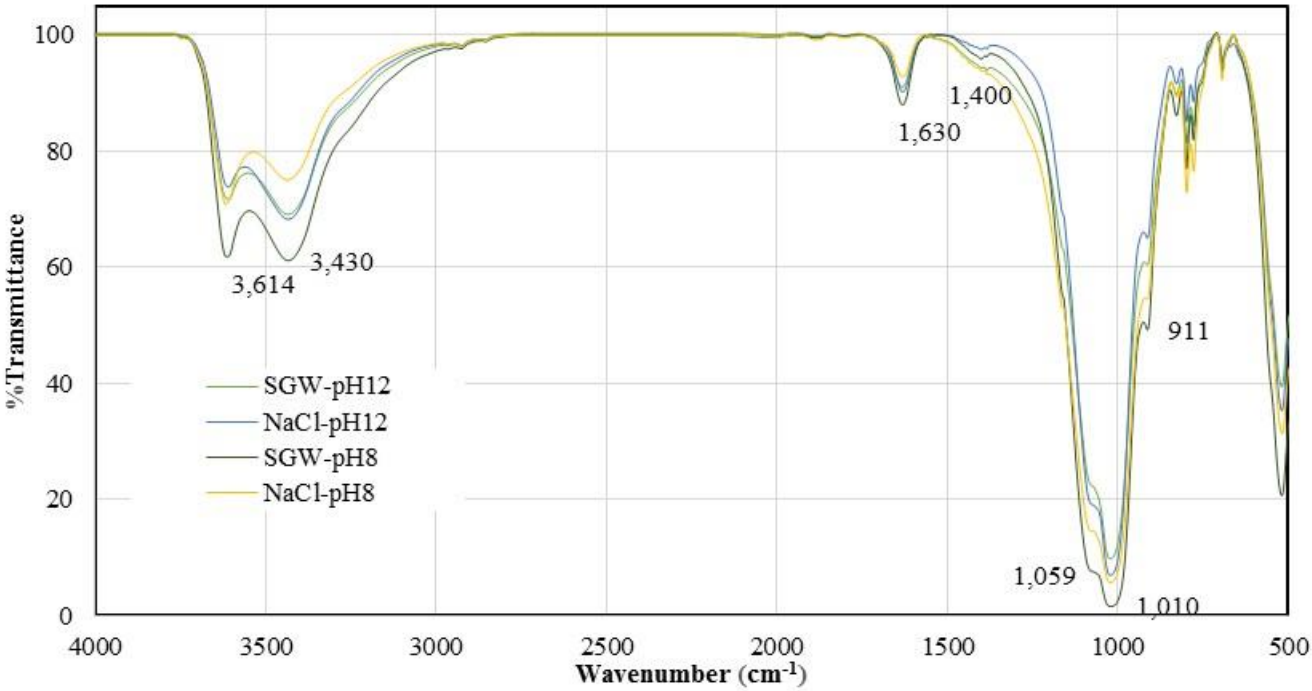


**Figure 10. FTIR spectrum of illite samples before and after $NH_3$ treatment. Major band peaks are labeled below the SGW aerated sample (dark green).**

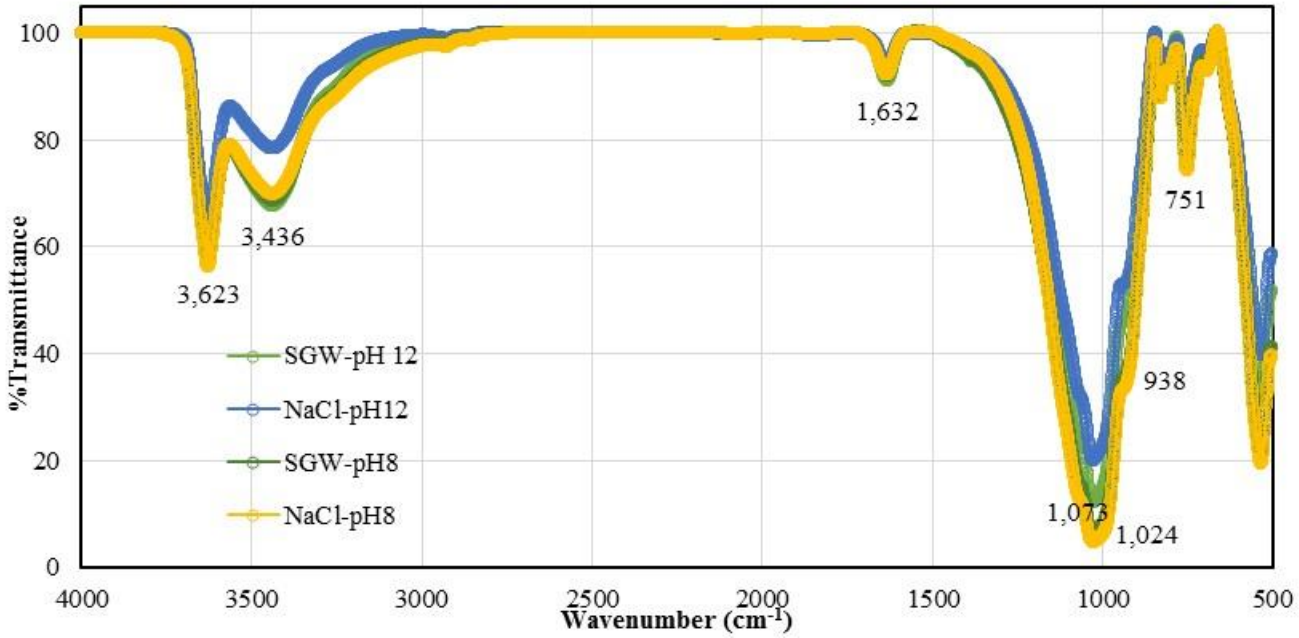


**Figure 11. FTIR spectrum of muscovite samples before and after NH3 treatment. Major band peaks are labeled below the SGW aerated sample (dark green).**

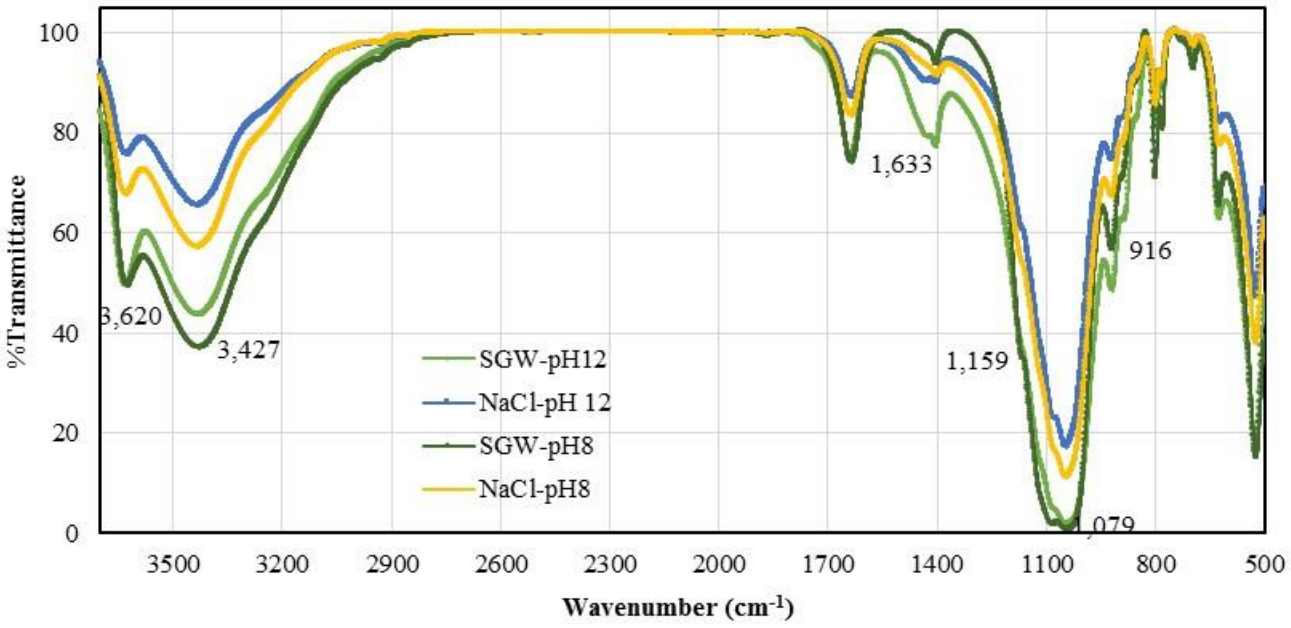


**Figure 12. FTIR spectrum of montmorillonite samples before and after $NH_3$ treatment. Major band peaks are labeled below the SGW aerated sample (dark green).**

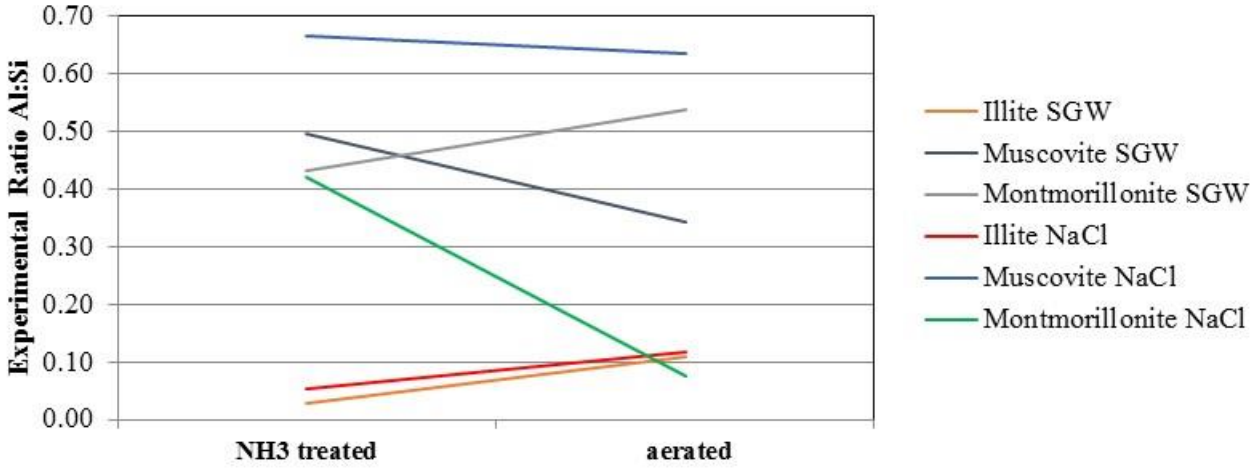


**Figure 13. Experimental ratios of Al to Si from ICP aqueous SGW and NaCl solutions analysis for illite, muscovite and montmorillonite**

**Table 6. Peak Height Al-Al-OH/Si-O-Si Ratios taken from FTIR Raw Data**

| | Illite | Muscovite | Montmorillonite |
|---|---|---|---|
| SGW | 6.64 | 3.74 | 0.036 |
| NaCl | 9.32 | 2.65 | 0.231 |
| SGW-aer | 30.3 | 5.59 | 0.012 |
| NaCl-aer | 9.43 | 7.12 | 0.165 |

**Table 7 . Experimental FTIR Band Assignments for Treated SGW and NaCl Montmorillonite Samples Compared to Reference Control Band Assignments***

| Maxima ($cm^{-1}$) | Assignment (untreated, control sample) | SGW $NH_3$ | NaCl $NH_3$ | SGW aer | NaCl aer |
|---|---|---|---|---|---|
| 3623 | -OH stretching | 3626 | 3624 | 3624 | 3624 |
| 1639 | -OH bending, deformation of water | 1631 | 1631 | 1631 | 1631 |
| 1430-1382 | $CO_3$ stretching of calcite | 1446 | 1448 | 1452 | 1450 |
| 1113 | Si-O stretching, out of plane | 1117 | 1117 | 1117 | 1117 |
| 1040 | Si-O stretching | 999 | 1001 | 1001 | 989 |
| 915 | Al-Al-OH bending | 914 | 916 | 914 | 914 |
| 875 | Al-Fe-OH bending | 883 | 883 | 883 | 883 |
| 836 | Al-Mg-OH bending | 850 | 849 | 845 | 849 |
| 793 | Si-O stretching of quartz | 795 | 796 | 796 | 796 |
| 654 | -OH bending | 683 | 692 | 692 | 692 |

**(Adikary, Ashokcline, & Nirojan, 2015; Hayati-Ashtiani, 2012)*

**Table 8. FTIR major bending and stretching assignments for clays ($cm^{-1}$)**

| Assignments | Illite ($cm^{-1}$) | Montmorillonite ($cm^{-1}$) | Muscovite ($cm^{-1}$) |
|---|---|---|---|
| H bonding to Si-O-Si linkage | *3638* | 3623 | 3622 |
| -OH stretching | 3400 | 3422 | 3440 |
| -OH bending, deformation of $H_2O$ | 1640-1700 | 1639 | 1633 |
| Carbonate impurities | Up to 1400 | 1382-1430 | * |
| Si-O stretching, out of plane | 1123 | 1113 | 1027 |
| Si-O stretching | 1000 | 1040 | 1010 |
| Al-OH-Al bending | *915* | 917 | 935 |
| Fe-Al-OH vibration | 875 | 885 | * |
| Al-OH-Mg bending | 828 | 836 | 828-830 |
| Al-O-Si bending | 693 | 529 | 535 |
| Si-O-Si bending | 478 | 466 | 480 |
| **Reference** | **(Li et al., 2008; Sedmale et al., 2017)** | **(Adikary et al., 2015; Hayati-Ashtiani, 2012; Madejová et al., 1998)** | **(Rashid et al., 2011; Ritz et al., 2011; Wang et al., 2014)** |

*Still searching for appropriate reference

## Subtask 1.1: Future Work

Injection of reactive gases such as $NH_3$ to create alkaline conditions in the vadose zone is an innovative technology that was tested this year at the pilot scale at the Hanford site. This task is improving understanding of the dissolution and secondary product formation of minerals during and after ammonia gas injection. In addition, it is working to identify major uranium phases and investigate the stability of solid phases formed during the remediation process. This will help to predict the long term effectiveness of this potential remediation technique and provide useful parameters for long-term risk assessment models.

These data will particularly complement the applied work at the field scale with contaminated sediments as it will provide a more basic understanding of the dominant mechanisms controlling

U fate through controlled, systematic experiments. Although the treatability study for the U-8 crib has been completed, these studies will provide information that can be used for other sites that may consider ammonia gas injection for uranium sequestration and potentially aid in the interpretation of long-term monitoring of the U-8 crib located in the 200 Area of the Hanford site.

**During FIU Performance Year 9**, FIU will continue measuring mineral dissolution and characterizing solid phases forming from Hanford 200 Area sediments and minerals following exposure to uranium and ammonia gas under saturated and unsaturated conditions. The solid phases will consist of mica minerals (muscovite and illite), montmorillonite, and sediments as their chemistry is not well understood and they are relevant to the 200 Area. The aforementioned minerals represent a significant fraction of the clay-sized minerals at the site (smectites which include montmorillonite represent as much as 35% of the clay-sized fraction and illite represents as much as 40%).

## Subtask 1.1: Acknowledgements

Funding for this research was provided by U.S. DOE Cooperative Agreement DE-EM0000598. We truly appreciate Drs. Jim Szecsody, Timothy Johnson, Nik Quafoku, and Vicky Freedman for their invaluable feedback in the design of these experiments and the time given to training and hosting Silvina Di Pietro as a visiting scientist.

## Subtask 1.1: References

Adikary, S., Ashokcline, M., & Nirojan, K. (2015). Characterization of montmorillonite clay from naturally occurring clay deposits in murunkan area. Proceedings of 8th International Research Conference, KDU, 163-169.

Bailey, S. (1966). "The status of clay mineral structures." 14th Clays and Clay Minerals: Proceedings National Conference, 1-23.

Busigny, V., Cartigny, P., Philippot, P., & Javoy, M. (2003). "Ammonium quantification in muscovite by infrared spectroscopy." *Chemical Geology*, **198**(1-2), 21-31.

Hayati-Ashtiani, M. (2012). "Use of FTIR spectroscopy in the characterization of natural and treated nanostructured bentonites (montmorillonites)." *Particulate Science and Technology*, **30**(6), 553-564.

Langmuir, D., 1997. *Aqueous Environmental Geochemistry*. Prentice Hall, Upper Saddle River, New Jersey.

Lugwisha, E. (2011). "Identification of clay minerals of the eastern southern region of Lake Victoria by ethylene glycol and heat: X-ray diffraction and infrared spectroscopy studies." *Tanzania Journal of Science*, **37**(1).

Mashal, K., Harsh, J. B., & Flury, M. (2005). "Clay mineralogical transformations over time in Hanford sediments reacted with simulated tank waste." *Soil Science Society of America Journal*, **69**(2), 531-538.

McKinley, J. P., Zachara, J. M., Wan, J., McCready, D. E., & Heald, S. M. (2007). "Geochemical controls on contaminant uranium in vadose Hanford formation sediments at the 200 area and 300 area, Hanford Site, Washington." *Vadose Zone Journal*, **6**(4), 1004-1017.

Miller, C. F., Stoddard, E. F., Bradfish, L. J., & Dollase, W. A. (1981). "Composition of plutonic muscovite; genetic implications." *The Canadian Mineralogist*, **19**(1), 25-34.

Moore, D. M., & Reynolds, R. C. (1989). *X-ray diffraction and the identification and analysis of clay minerals*, Oxford University press, New York, NY.

Moyes, L. N., Parkman, R. H., Charnock, J. M., Vaughan, D. J., Livens, F. R., Hughes, C. R., & Braithwaite, A. (2000). "Uranium uptake from aqueous solution by interaction with goethite, lepidocrocite, muscovite, and mackinawite: An X-ray absorption spectroscopy study." *Environmental Science & Technology*, **34**(6), 1062-1068.

Nesse, W. D. (2012). *Introduction to mineralogy*. Oxford University Press, Oxford, UK.

Osman, K. T. (2012). *Soils: Principles, properties and management*, Springer Science & Business Media.

Sedmale, G., Randers, M., Rundans, M., & Seglins, V. (2017). "Application of differently treated illite and illite clay samples for the development of ceramics." *Applied Clay Science*, **146**, 397-403.

Segad, M., Jonsson, B., Åkesson, T., & Cabane, B. (2010). "Ca/na montmorillonite: Structure, forces and swelling properties." *Langmuir*, **26**(8), 5782-5790.

Srodon, J. (1984). "X-ray powder diffraction identification of illitic materials." *Clays and Clay Mineralogy*, **32**(5), 337.

Szecsody, J.E., et al., *Remediation of Uranium in the Hanford Vadose Zone Using Ammonia Gas: FY 2010 Laboratory-Scale Experiments*. 2010, Pacific Northwest National Laboratory (PNNL), Richland, WA (US), Environmental Molecular Sciences Laboratory (EMSL).

Zhen, R., Jiang, Y. S., Li, F. F., & Xue, B. (2017). "A study on the intercalation and exfoliation of illite." *Research on Chemical Intermediates*, **43**(2), 679-692.

Zviagina, B. B., Drits, V. A., Środoń, J., McCarty, D. K., & Dorzhieva, O. V. (2015). "The illite–aluminoceladonite series: Distinguishing features and identification criteria from X-ray diffraction and infrared spectroscopy data." *Clays and Clay Minerals*, **63**(5), 378-394.

## Subtask 1.3: Investigation of Electrical Geophysical Response to Microbial Activity in the Saturated and Unsaturated Environments

### Subtask 1.3: Introduction

Radionuclides contaminants in the VZ such as uranium require *in-situ* remediation to convert aqueous mobile uranyl carbonates to lower solubility precipitates that are stable in the natural environment (Szecsody et al., 2012). A possible solution would be implementation of polyphosphate injections, which would immobilize uranium by forming a low solubility uranyl phosphate mineral, autunite.

Monitoring of contaminant behavior in the subsurface after polyphosphate injections could be accomplished using established geophysical techniques. Of particular interest are electrical techniques, which study the conductive and capacitive properties of the subsurface. Generally, these techniques are sensitive to contrasts in the conductivity of the underlying sediment, allowing the detection of the contaminant plumes as well as amendment injections (Glover, 2015).

The goal of this study is to investigate if biological processes can be detected via geophysical techniques. The formation of an electrical double layer (EDL) around bacterial surfaces, which tend to have a net negative charge, could be exploited to remotely measure microbial growth (Atekwana and Slater, 2009). Electrical geophysical techniques have already been successfully tested in a variety of applications (Johnson et al., 2015b). Electrical resistivity tomography (ERT) has been used to study nitrate plumes (Rucker et al., 2013) as well as river water intrusion and smear zone contamination (Johnson et al., 2015a; Johnson et al., 2012). Nitrogen driven desiccation of the vadose zone has also been tracked successfully using electrical techniques (Truex et al., 2013).

A previous study on calcium and magnesium carbonate precipitation using geophysical techniques found that calcite precipitation on glass beads produced a significant increase in the imaginary conductivity within 9 days of the start of the experiment followed by a gradual decrease (Wu et al., 2010). Wu et al. (2010) attributed the change to the precipitation of micro-calcite crystals, which have a stronger polarization than the larger crystals formed later. Microbial induced carbonate precipitation (MICP) was shown to have an effect on both the elastic properties, measured through shear wave velocities, and electrical properties, measured with spectral induced polarization (SIP) of sediment (Saneiyan et al., 2018).

The objectives of the research were to investigate the ability of geophysical spectral induced polarization (SIP) techniques to remotely determine the microbial effect on the dissolution of Ca autunite in bicarbonate-amended systems incorporating aquifer materials as well as evaluate microbial growth in the same system.

### Research Goals

Primary goals for the 2018 mini-column experiment were as follows:

- Set up a soil-free baseline with simulated groundwater (SGW) solutions with and without bicarbonate for comparison with future experiments.
- Study the SIP response of autoclaved Hanford sediment saturated with SGW solutions aerated with compressed air to simulate aerobic conditions or nitrogen to simulate anaerobic conditions.
- Study the effect of heat-deactivated microbial cells of known titer.
- Study the effect of living cells on the electrical geophysical response.
- Maintain long term monitoring of microbial growth using both geophysical measurements taken continuously and effluent sampling taken once a day.

Secondary goals during 2017-2018 were the reanalysis of existing data:

- Further analyze 2016 and 2017 SIP results by fitting Cole-Cole models to the data.
- Draw further conclusions from the pore-fluid data.

## Subtask 1.3: Methodology

### Continuous Flow Column Set Up

A new mini-column (Figure 14) was constructed in order to further study the effects of microbial growth on the SIP response in Hanford sediment. This column had coiled Ag-AgCl electrodes at either end prepared by dipping a coiled silver wire into a fresh bleach solution for 30 minutes. Two

potential electrodes were placed along the side, centered on the column. These consisted of a straight Ag-AgCl wire in an empty chamber which was then filled with pore-fluid during the saturation step. Flow through the columns was counter gravity at a rate of ~100 mL a day and was powered by an Ismatek peristaltic pump.

**Figure 14. Mini-column prepared for the basic SIP experiments**

SIP measurements for this experiment were taken continuously with 10 minute delays between each measurement using a National Instruments data acquisition card (DAQ). A battery was placed in a circuit to provide the necessary 10 V. The battery was recharged every couple of days which generally produced a gap of one hour in the measurements. On occasion, a short-term loss of power, particularly over weekends, caused a loss of the data for that period of time.

One effluent sample was taken each weekday. Between 10 and 15 mL of effluent was collected and the sample was immediately acidified by adding 50 µL of 8 M nitric acid. The sample was then stored in a refrigerator.

$Fe^{2+}$ and total Fe concentrations were measured using the Ferrozine method while Ca and Mg concentrations were measured using ICP-OES.

The SIP spectra for the previous fall 2016 experiments as well as the new mini-column experiments were fit to Cole-Cole models in order to obtain values for the DC-resistivity ($\rho_0$), the chargeability ($m$), the relaxation time ($\tau$), and the Cole-Cole exponent ($c$). The formula for the Cole-Cole model in terms of the conductivity is:

$$\sigma^*(\omega) = \sigma_0 \left[1 + m\left(\frac{(i\omega\tau)^c}{1 + (i\omega\tau)^c(1-m)}\right)\right].$$

Where $\sigma^*(\omega)$ is the complex conductivity, $\sigma_0$ is the DC-conductivity, $m$ is the chargeability, $\omega$ is the angular frequency ($\omega = f * 2\pi$, where $f$ is the current frequency), $\tau$ is the relaxation time, and $c$ is the Cole-Cole exponent.

The percent RMS error was also calculated for the Fall 20116 spectra. This was calculated as:

$$RMS_{Error} = \sqrt{\frac{\sum(y_2 - y_1)^2}{n}}$$

Where $y_2$ is the modeled value, $y_1$ is the observed value, and $n$ is the total number of values in the spectrum.

## Subtask 1.3: Results and Discussion

### Analysis of Prior Experimental Data Using 6 Columns Set Up

FIU continued assessment of data obtained in FIU performance 7. Cole-Cole fits of SIP spectra were used to calculate the chargeability $m$ (Figure 15), the DC resistivity $\rho_0$ (Figure 16), and the relaxation time $\tau$ (Figure 17).

Chargeability (Figure 15) showed significant variation between columns. C2 (SGW + $HCO_3$) showed the highest chargeability, which can be attributed to increased polarization at the surfaces of the precipitated $CaCO_3$ minerals. The control column C1 showed little change in $m$. The microbial columns all showed decreases, although the decreases in C4 (SGW+$HCO_3$+glucose) seemed more gradual.

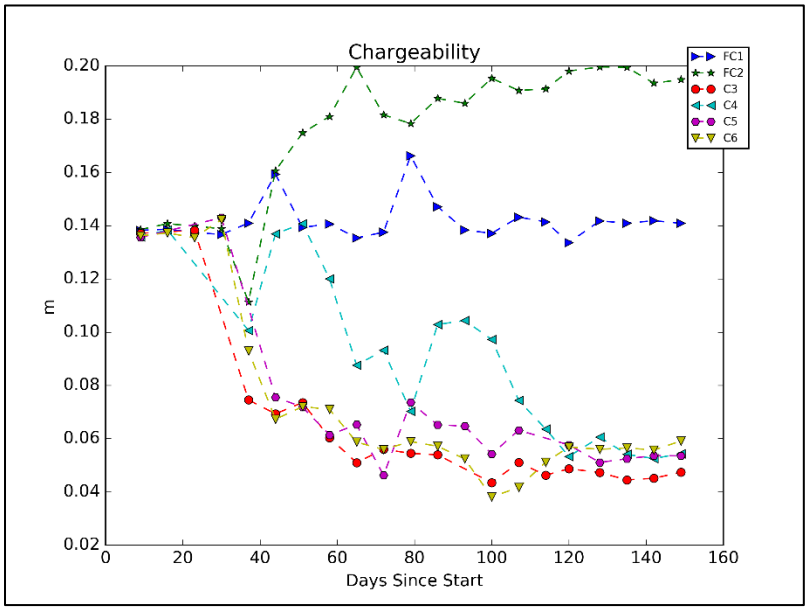


**Figure 15. Cole-Cole chargeability for the fall 2016 column experiment.**

In general, all columns showed decreased resistivity (Figure 16) when compared to the control column. C2 had a lower resistivity due to the addition of 3 mM $HCO_3$. Microbial columns (C3, C4, C5, C6) had higher concentrations of ionic species in solution which leads to them having significantly lower resistivities.

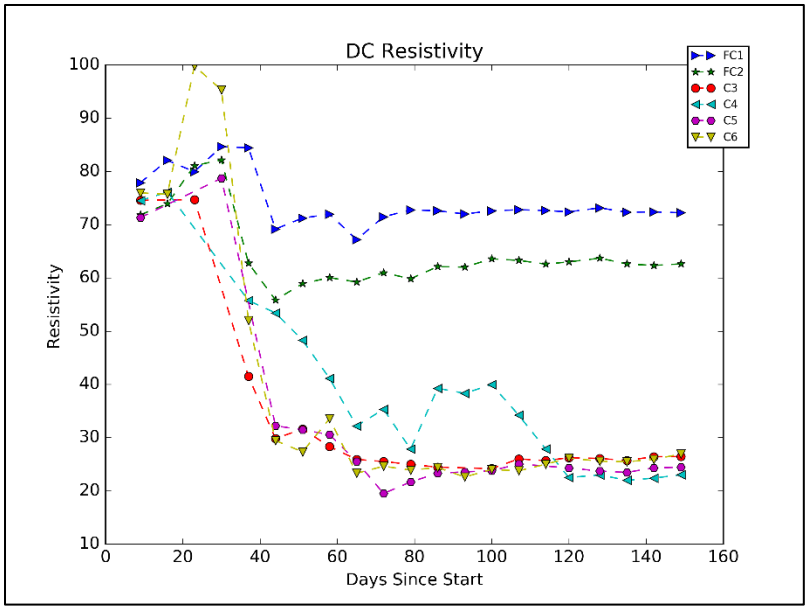


**Figure 16. Cole-Cole DC resistivity (Ohm-m) for the fall 2016 column experiment.**

Differences among the columns were observed in regards to the chargeability (Figure 15, the DC resistivity (Figure 16), and the relaxation time. The elevated chargeability seen in C2 is likely the result of polarization at the surfaces of newly precipitated $CaCO_3$ minerals. C2 also had a lower resistivity than C1, which is the result of the added 3 mM $HCO_3$.

Microbial columns all seemed to equilibrate at a similar resistivity (between 20 and 30 Ωm) regardless of the additional 3 mM $HCO_3$ in the SGW solution. Microbial columns also showed significantly lower chargeability (between 0.04 and 0.06) values than C1. Both microbial columns and C2 showed elevated relaxation times compared to C1. C4 and C6 (microbial with added $HCO_3$) showed higher relaxation times than C3 or C5 (microbial, no added $HCO_3$).

In general Cole-Cole fits were best for C1 and C2 and seem to be worst for C3 and C5. Cole-Cole models work best when there is a distinct peak in the phase spectra which was absent from the microbial column results. The parameter most affected by this is likely the relaxation time as the DC resistivity is mainly controlled by the impedance magnitude and the chargeability by the magnitude of the phase spectra.

Relaxation time (Figure 17) remained mostly constant for C1 but showed variation among the other columns. C4 seemed to show the highest relaxation time while microbial-only columns (C3, C5) showed lower relaxation times that were still higher than C1. The RMS error (Figure 18) showed that the error of the Cole-Cole fit is greatest for columns C3 and C5 which seemed to most affect estimates of the relaxation time.

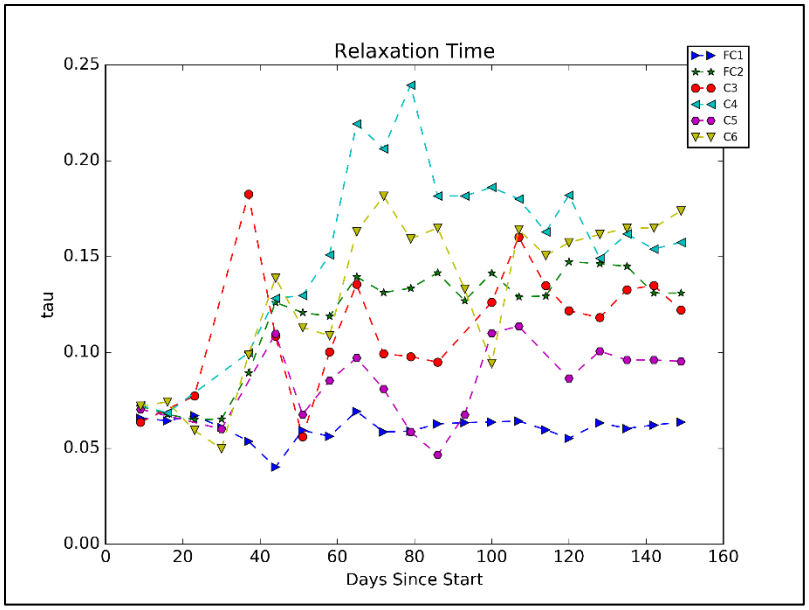


**Figure 17. Cole-Cole relaxation time (s) for the fall 2016 column experiment.**

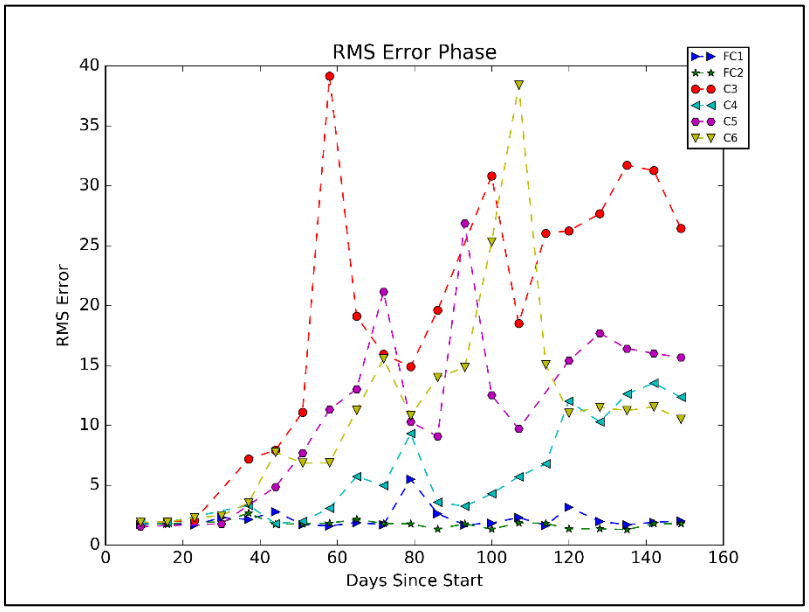


**Figure 18. Percent RMS error in the phase between Cole-Cole and measured.**

## 2018 Mini Column Results

After the initiation of glucose pumping, as well as inoculation with *Shewanella*, increases in total dissolved iron (Figure 20) were observed starting after day 21. After day 40 the amount of reduced iron (Figure 19) began to slowly increase. This steady increase is likely tied to the formation of reducing conditions inside of the columns as was observed in the prior experiments. A sudden increase in total Fe (Figure 20) was observed on day 21 and peaked on day 30. Total iron then trended downward until beginning to rise once again after day 70. It is possible that given enough time total Fe would become dominated primarily by the $Fe^{2+}$ component. Concentrations were lower than those observed in previous experiments. Likely, this is due to a combination of the

lower glucose concentration (200mg/L) and the faster flow rate which flushed the column more quickly.

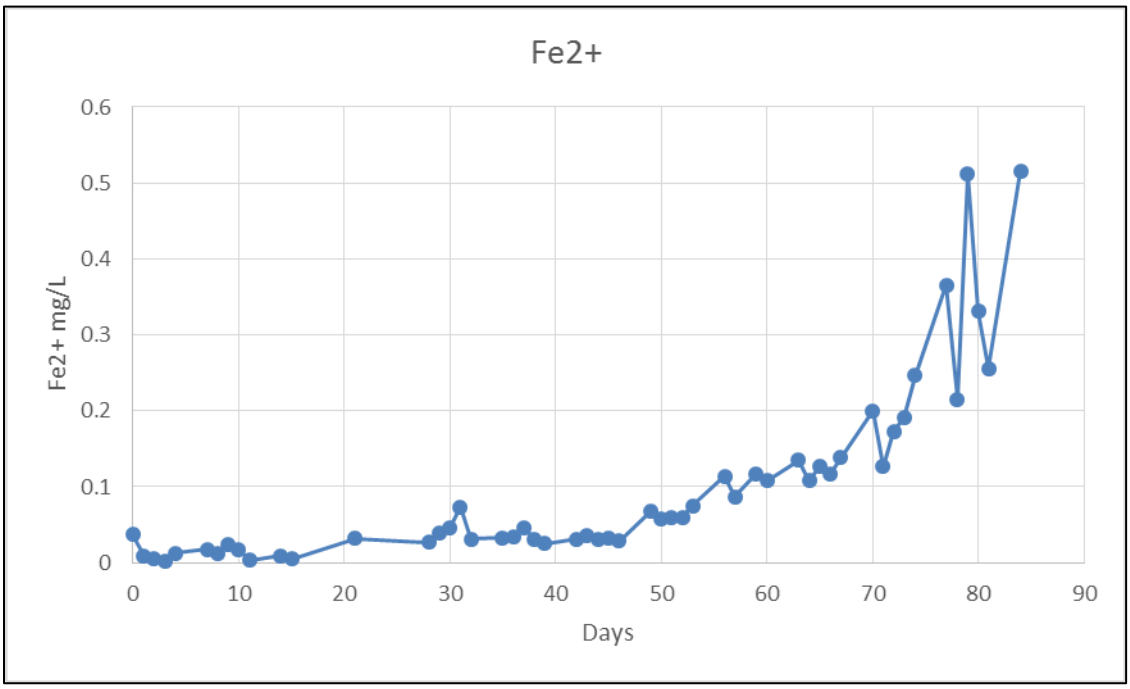


**Figure 19. $Fe^{2+}$ concentrations taken using ferrozine method for mini-column.**

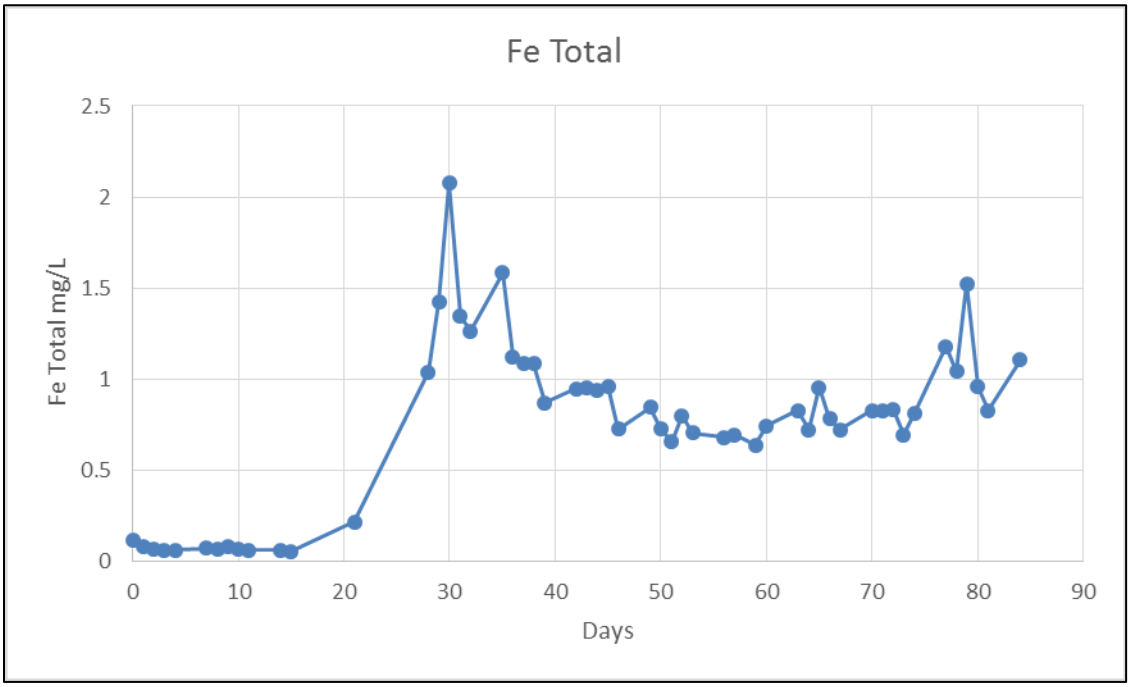


**Figure 20. Fe total concentrations taken using ferrozine for mini-column.**

Similar to previous experiments, changes in concentrations for both Ca (Figure 21) and Mg (Figure 22) showed sudden increases soon after inoculation. Increases in Ca were first observed on day 3, quickly reach maxima on day 21, and then showed a downward trend over time until seeming to

reach an equilibrium concentration of approximately 90 mg/L. Similarly, magnesium (Figure 22) showed a sudden increase on day 5 followed by a second increase on day 21. Magnesium concentrations continued to rise until peaking on day 50 and then slowly trended downward until the end of the experiment.

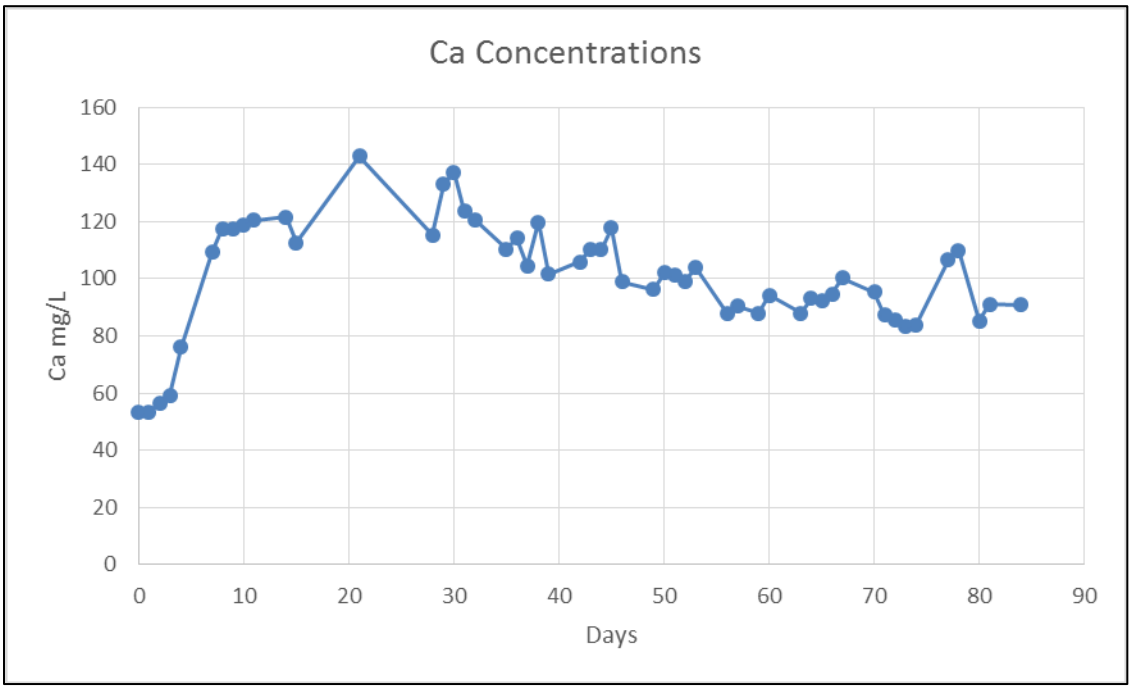


**Figure 21. Ca concentrations taken using ICP-OES for mini-column.**

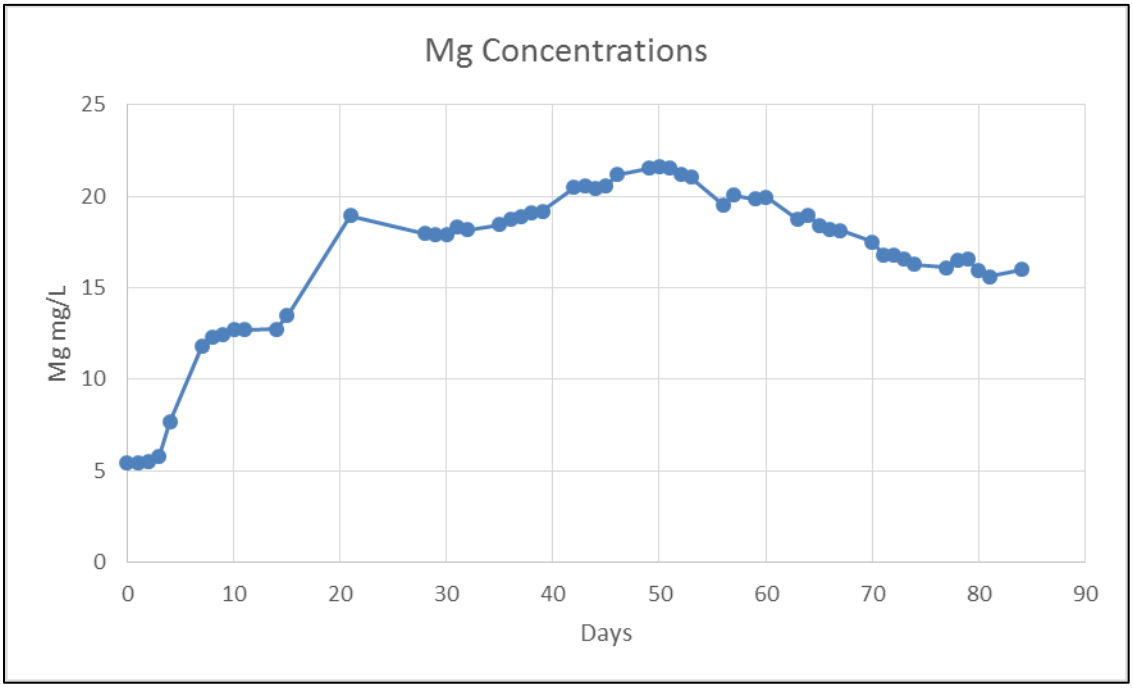


**Figure 22. Mg concentrations taken using ICP-OES for mini-column.**

Results of the experiments using no microbes, dead microbes, and live microbes showed no differences (Figure 23) between no microbes, dead microbes, and live microbes.

Overall, concentrations of Fe, Ca, and Mg were lower than those observed during previous experiments. There are a variety of factors that could contribute to this. This experiment employed a flow rate of ~100 mL/d, which was double that of the flow rate used for previous experiments (~50 mL/d); in addition, the current mini-column was significantly shorter than the larger columns used previously, which would have led to the pore-fluid being in contact with the sediment for a shorter period of time. Finally, 200 mg/L of glucose was used instead of the 1 g/L used previously, which likely led to reduced microbial activity and gas production compared to previous experiments.

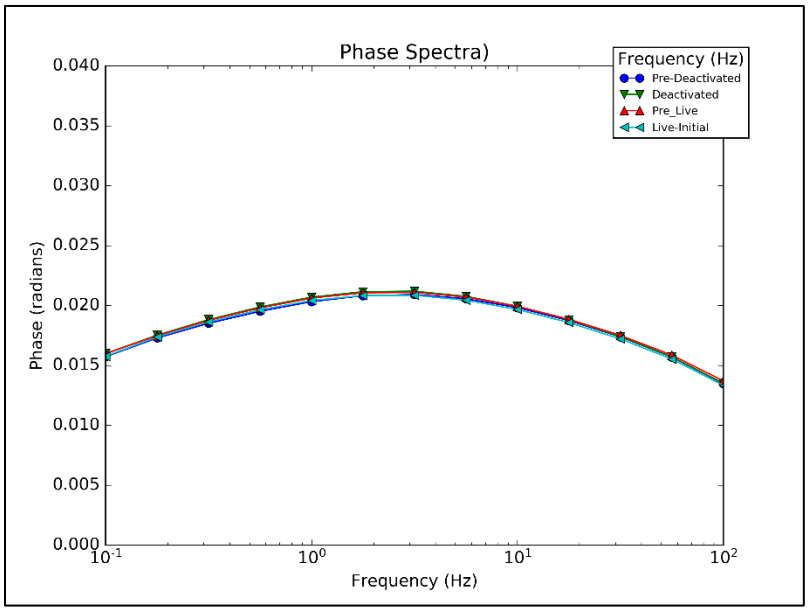


**Figure 23. Phase spectra for mini-column comparing deactivated and live microbes as well as background.**

The injection of microbes seemed to have some effect on the impedance (Figure 24) and conductivity (Figure 25). However, this is likely due to a difference in the conductivity of the injected solution and existing pore fluid. The difference between the two sets of microbes (deactivated and live) is due to equilibrium effects with impedance seemingly increasing over time.

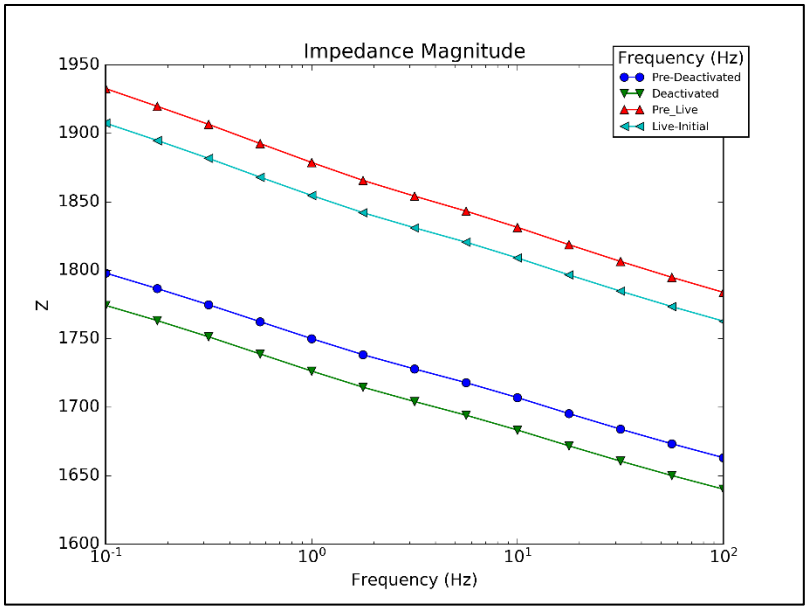


**Figure 24. Impedance (Ohms) magnitude spectra for mini-column comparing deactivated and live microbes as well as background.**

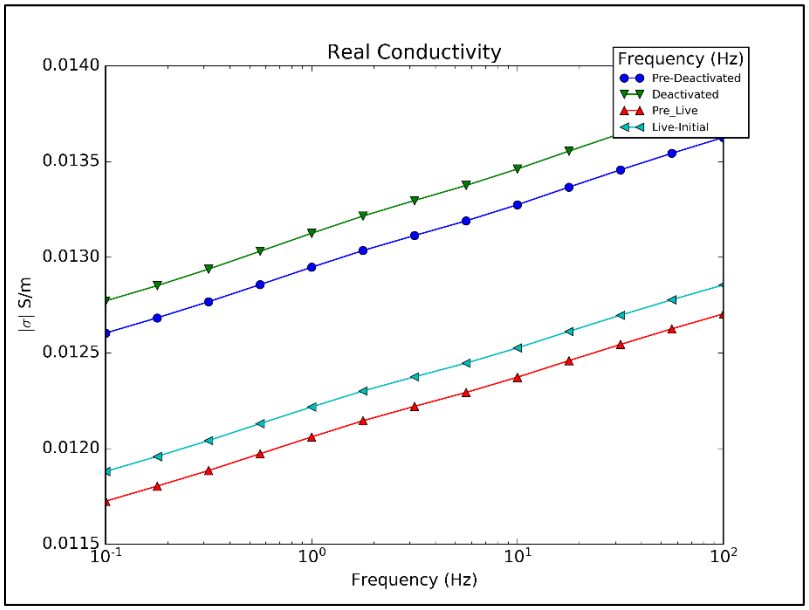


**Figure 25. Real conductivity spectra for mini-column comparing deactivated and live microbes as well as background.**

The imaginary conductivity (Figure 26) showed a minor difference between the experiments with no microbes and the ones with deactivated microbes. No difference was observed between no microbes and live microbes. It is likely that the former difference was due to differences in the conductivity between the injected solution and the pore fluid.

.

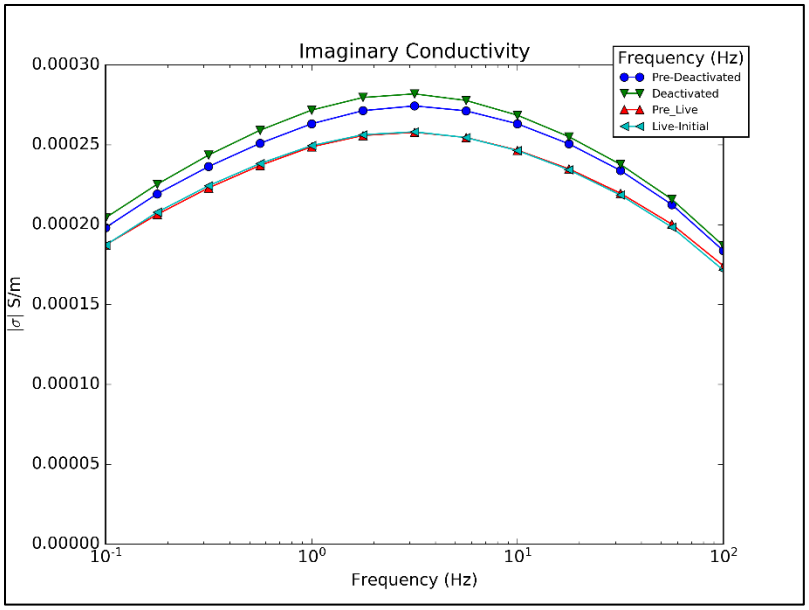


**Figure 26. Imaginary conductivity spectra for mini-column comparing deactivated and live microbes as well as background.**

Measurements of the column inoculated with heat-deactivated microbes and the one inoculated with live microbes (Figure 23, Figure 24, Figure 25, and Figure 26) suggested that microbial injection seems to have a very limited effect on the SIP response.

Phase measurements (Figure 23) were effectively identical between the columns inoculated with no microbes, heat-deactivated microbes, or live-microbes. Deactivated microbes seemed to show a small increase in the imaginary conductivity (Figure 26) when compared to no microbes; however, this increase may be mainly due to differences in conductivity and may not be significant. Both the impedance (Figure 24) and real component of the conductivity (Figure 25) showed some change; however, this is mainly due to differences in conductivity between the injected solution and the existing pore-fluid. This seems to suggest that polarization at microbe surfaces may not be a significant factor affecting the SIP signature in HFS.

Long term tracking showed that the real conductivity (Figure 27) increased rapidly after inoculation with live microbes, similar to previous experiments. There was a period of low conductivity between days 20 and 45. The cause is uncertain but may be due to experimental error such as forgetting to add glucose to the SGW solution being pumped.

.

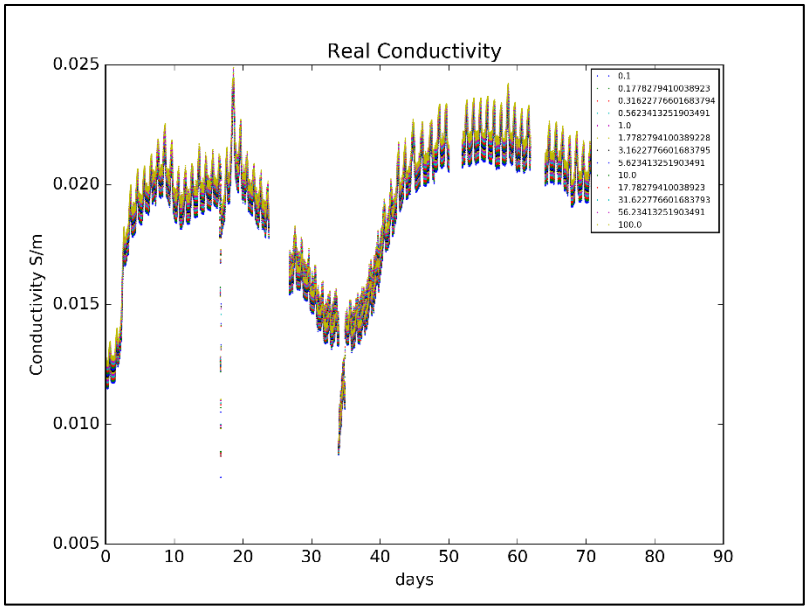


**Figure 27. Real conductivity over time at various frequencies.**

The phases (Figure 28) showed a rapid decrease following microbial growth which is similar to that seen in the previous experiments.

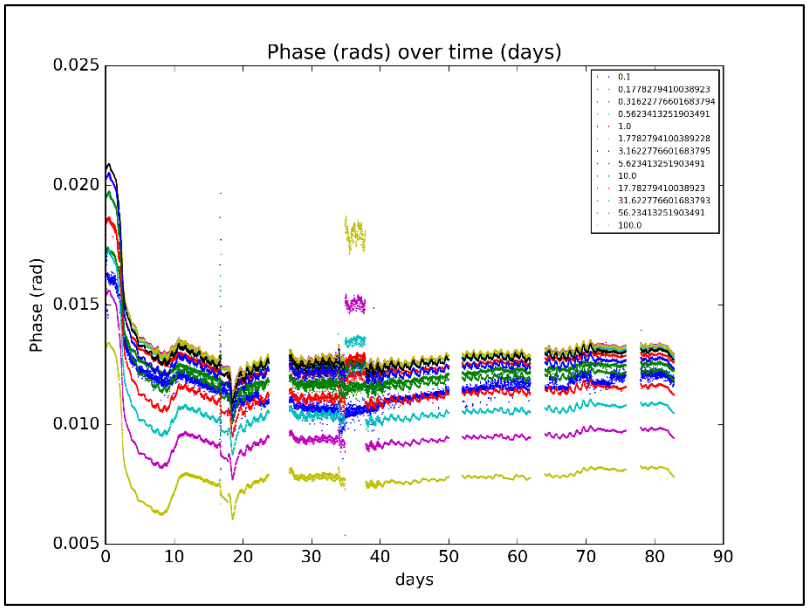


**Figure 28. Phase over time at various frequencies.**

The imaginary conductivity (Figure 29) showed little change after microbial growth; however, it did decrease along with the real component of the conductivity between days 20 and 45. After day 45, the imaginary conductivity seemed to peak at approximately ~day 55 then showed a downward trend.

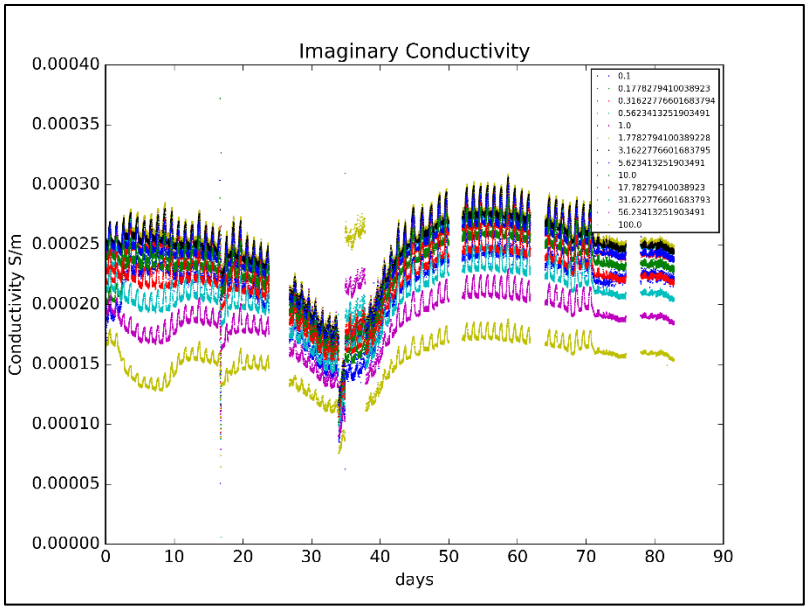


**Figure 29. Imaginary conductivity over time at various frequencies.**

After the injection of live microbes, a sharp increase in the real conductivity was observed (Figure 28) as well as a sharp decrease in the recorded phase (Figure 29). A decrease was observed in the conductivity starting after day 20 and reached a minima at approximately day 35. The start of this decrease occurred at around the same time as total iron concentrations began to quickly increase, and may be connected. The phase remained mostly constant during this time. The imaginary conductivity (Figure 29) decreased during this time period but then reached values greater than those seen at the start of the experiment until eventually decreasing again to initial values.

The phase spectra (Figure 30) show a clear peak at the start of the experiment. This peak was subdued at the end; however, it never flattens out like in previous experiments. Similarly, the imaginary conductivity spectra (Figure 31) showed a clear parabolic shape.

In general the quality of SIP data taken for the mini-column experiment was better than for the previous experiments. This is mainly due to a reduction in the formation of bubbles inside the columns which interfere with the electrical measurements. The primary reason for this improvement is likely the use of 200 mg/L of glucose instead of 1 g/L. Phase spectra for this experiment showed the characteristic peak traditionally found (Figure 30).

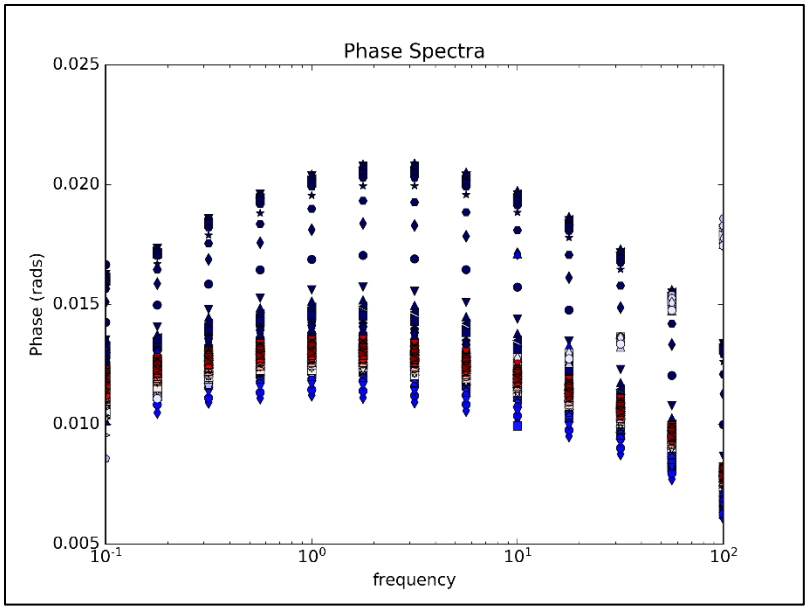


**Figure 30. Phase spectra. Dark blue is start of the experiment. Dark red is end.**

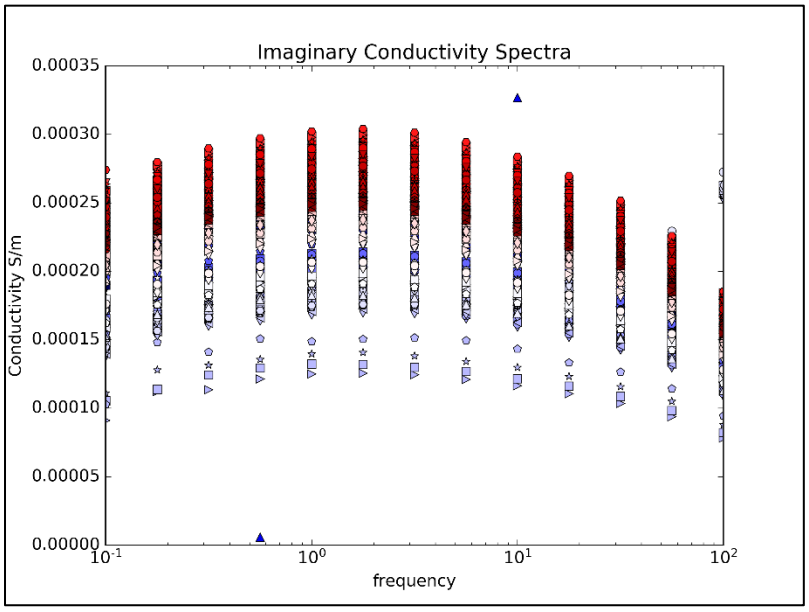


**Figure 31. Imaginary conductivity spectra. Dark blue is start of the experiment. Dark red is end.**

The chargeability (Figure 32) decreased greatly after the start of microbial growth then slowly increases slightly. Analysis of mini-column SIP spectra using Cole-Cole models showed significant decreases in the chargeability (Figure 32).

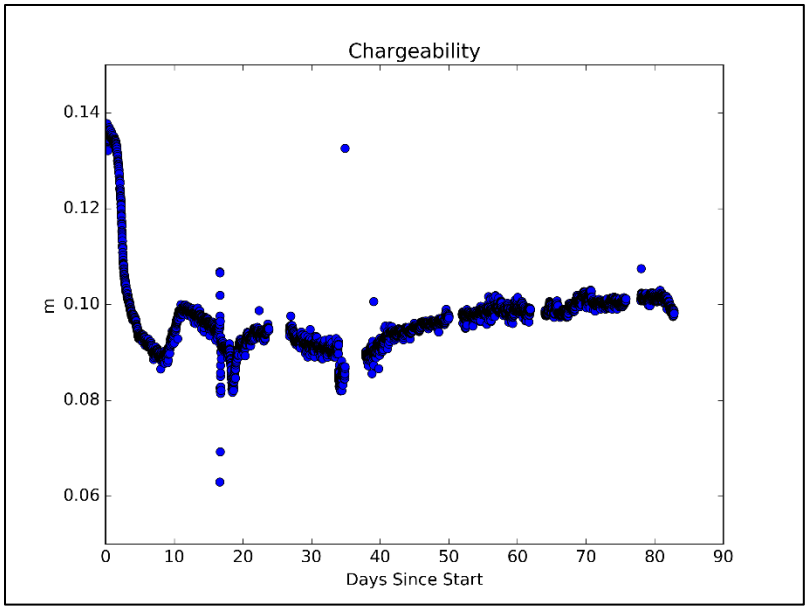


**Figure 32. Cole-Cole chargeability over time for mini-column.**

The DC resistivity (Figure 33) behaved effectively as the inverse of the conductivity. The DC resistivity (Figure 33, inverse of the conductivity) decreased quickly after microbial growth apart from an increase observed between day 20 and 40.

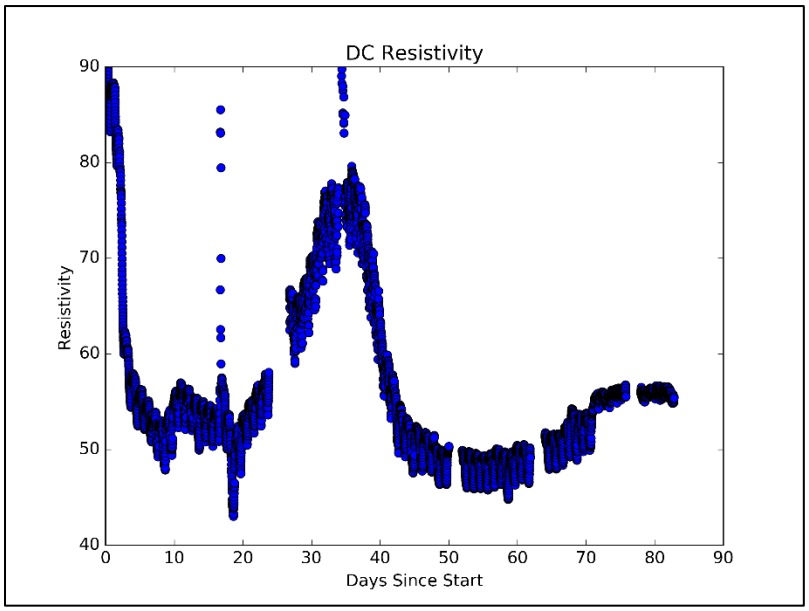


**Figure 33. Cole-Cole DC resistivity (0hm-m) over time for mini-column.**

The Cole-Cole exponent (Figure 34) saw a significant reduction then show a peak, which correlates with the peak in the DC resistivity. The Cole-Cole exponent (Figure 34) seemed to mimic changes in the DC-resistivity.

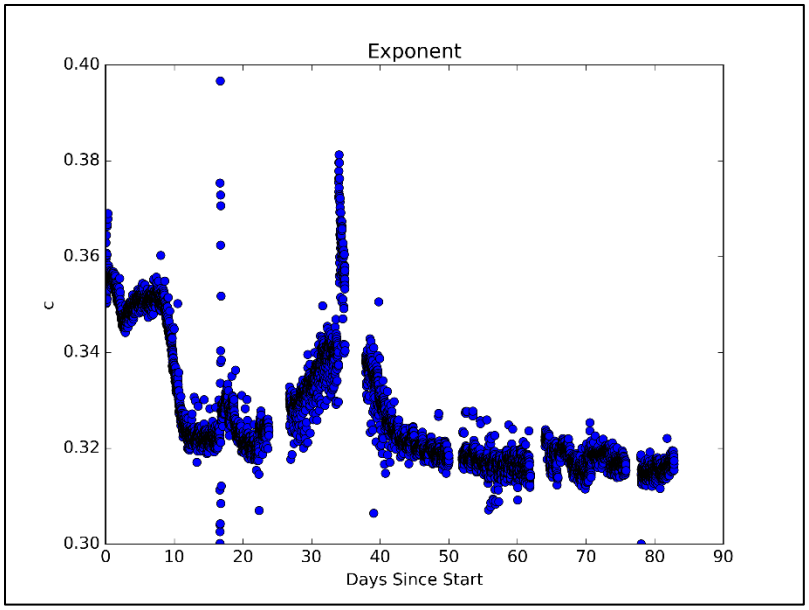


**Figure 34. Cole-Cole exponent over time for mini-column.**

The relaxation time (Figure 35) increased significantly after the start of microbial growth. There was a decrease which correlates with the increase in the DC resistivity which was then followed by a steady increase back to values around 0.023.

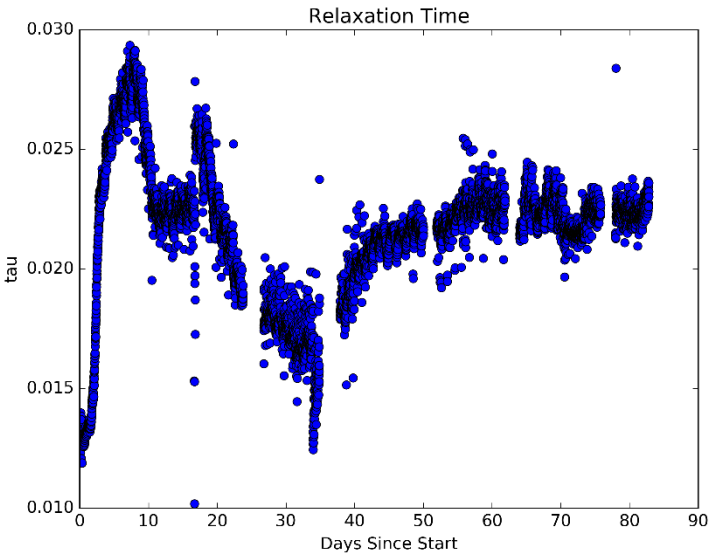


**Figure 35. Relaxation time (s) over time for mini-column.**

The relaxation time increased significantly after microbial growth and then quickly decreased. There was a minima around day 33 which is likely related to the previously observed change in the resistivity around this time and then the values returned to those seen around day 15.

## Subtask 1.3: Conclusion

Mini-column experiment was set up to investigate the influence and corresponding electrical geophysical response of microbial activity in a set of basic experiments without the addition of

autunite minerals. Measurements data of both heat deactivated and live microbes suggested that microbial injection had a very limited effect on the SIP response. Phase measurements were almost identical between no microbe, heat-deactivated microbes, and live-microbes. Deactivated microbes suggested a small increase in the imaginary conductivity when compared to no-microbes; but, this increase was not significant. In general, the quality of SIP data taken for the mini-column experiment was better compared to the previous fall 2016 and spring 2017 experiments. This was mainly due to a reduction of gas bubble formation inside the column, which interfered with electrical measurements. The primary reason for this improvement was likely the use of lower glucose concentration of 200 mg/L instead of 1 g/L.

FIU completed the investigation on the electrical geophysical response to microbial activity in the saturated and unsaturated environments; so, this project will not continue in FIU Performance Year 9. DOE Fellow, Alejandro Garcia, graduated with Master of Science in Geoscience presenting thesis titled, "The effect of microbial growth on the spectral induced polarization response in Hanford vadose zone sediment in the presence of autunite mineral".

## Subtask 1.3: Acknowledgements

Funding for this research was provided by U.S. DOE Cooperative Agreement DE-EM0000598. We truly appreciate Drs. Brady Lee, Edmundo Placencia-Gomez, Christopher Bagwell and Vicky Freedman from PNNL for support on this research.

## Subtask 1.3: References

Atekwana, E. A., and Slater, L. D., 2009, Biogeophysics: A new frontier in Earth science research: Reviews of Geophysics, v. 47, no. 4.

Bernhard, G., Geipel, G., Brendler, V., and Nitsche, H., 1996, Speciation of uranium in seepage waters of a mine tailing pile studied by time-resolved laser-induced fluorescence spectroscopy (TRLFS): Radiochimica Acta, v. 74, no. s1, p. 87-92.

Bernhard, G., Geipel, G., Reich, T., Brendler, V., Amayri, S., and Nitsche, H., 2001, Uranyl (VI) carbonate complex formation: Validation of the Ca2UO2 (CO3) 3 (aq.) species: Radiochimica Acta International journal for chemical aspects of nuclear science and technology, v. 89, no. 8/2001, p. 511.

Cantrell, K. J., Last, G. V., and JEFFREY, R., 2003, Hanford contaminant distribution coefficient database and users guide, United States. Department of Energy.

Glover, P., 2015, Geophysical properties of the near surface Earth: Electrical properties.

Johnson, T., Versteeg, R., Thomle, J., Hammond, G., Chen, X., and Zachara, J., 2015a, Four-dimensional electrical conductivity monitoring of stage-driven river water intrusion: Accounting for water table effects using a transient mesh boundary and conditional inversion constraints: Water Resources Research, v. 51, no. 8, p. 6177-6196.

Johnson, T. C., Rucker, D. F., and Glaser, D. R., 2015b, Near-Surface Geophysics at the Hanford Nuclear Site, the United States: Pacific Northwest National Laboratory (PNNL), Richland, WA (US), Environmental Molecular Sciences Laboratory (EMSL).

Johnson, T. C., Slater, L. D., Ntarlagiannis, D., Day-Lewis, F. D., and Elwaseif, M., 2012, Monitoring groundwater-surface water interaction using time-series and time-frequency analysis

of transient three-dimensional electrical resistivity changes: Water Resources Research, v. 48, no. 7.

Kalmykov, S. N., and Choppin, G. R., 2000, Mixed Ca2+/UO22+/CO32-complex formation at different ionic strengths, Radiochimica Acta International journal for chemical aspects of nuclear science and technology, Volume 88, p. 603.

Peterson, R. A., Buck, E. C., Chun, J., Daniel, R. C., Herting, D. L., Ilton, E. S., Lumetta, G. J., and Clark, S. B., 2018, Review of the scientific understanding of radioactive waste at the US DOE Hanford Site: Environmental science & technology, v. 52, no. 2, p. 381-396.

Rucker, D. F., Myers, D. A., Cubbage, B., Levitt, M. T., Noonan, G. E., McNeill, M., Henderson, C., and Lober, R. W., 2013, Surface geophysical exploration: developing noninvasive tools to monitor past leaks around Hanford's tank farms: Environmental monitoring and assessment, v. 185, no. 1, p. 995-1010.

Saneiyan, S., Ntarlagiannis, D., Werkema Jr, D. D., and Ustra, A., 2018, Geophysical methods for monitoring soil stabilization processes: Journal of applied geophysics, v. 148, p. 234-244.

Szecsody, J. E., Truex, M. J., Zhong, L., Johnson, T. C., Qafoku, N., Williams, M. D., Greenwood, W. J., Wallin, E. L., Bargar, J., and Faurie, D. K., 2012, Geochemical and geophysical changes during ammonia gas treatment of vadose zone sediments for uranium remediation: Vadose Zone Journal, v. 11, no. 4.

Truex, M. J., Johnson, T. C., Strickland, C. E., Peterson, J. E., and Hubbard, S. S., 2013, Monitoring vadose zone desiccation with geophysical methods: Vadose Zone Journal, v. 12, no. 2.

Um, W., Icenhower, J. P., Brown, C. F., Serne, R. J., Wang, Z., Dodge, C. J., and Francis, A. J., 2010, Characterization of uranium-contaminated sediments from beneath a nuclear waste storage tank from Hanford, Washington: Implications for contaminant transport and fate: Geochimica et Cosmochimica Acta, v. 74, no. 4, p. 1363-1380.

Vermeul, V. R., Bjornstad, B. N., Fritz, B. G., Fruchter, J. S., Mackley, R. D., Newcomer, D. R., Mendoza, D. P., Rockhold, M. L., Wellman, D. M., and Williams, M. D., 2009, 300 Area uranium stabilization through polyphosphate injection, PNNL-18529, Pacific Northwest National Laboratory Richland, WA.

Wu, Y., Hubbard, S., Williams, K. H., and Ajo-Franklin, J., 2010, On the complex conductivity signatures of calcite precipitation: Journal of Geophysical Research: Biogeosciences, v. 115, no. G2.

Zachara, J. M., Brown, C., Christensen, J., Davis, J. A., Dresel, E., Liu, C., Kelly, S., McKinley, J., Serne, J., and Um, W., 2007, A site-wide perspective on uranium geochemistry at the Hanford Site.

## Subtask 1.4: Contaminant Fate and Transport under Reducing Conditions

## Subtask 1.4: Introduction

Past practices for waste management activities and disposal operations resulted in leaks of mixed contaminant streams from some of these tanks, ponds, cribs and trenches, causing widespread subsurface contamination. Approximately 703 Ci of $^{99}$Tc have been released to the ground from

historical releases, spills and leaks (Serne, Rapko and Pegg 2014). More specifically, approximately 69 TBq of $^{99}$Tc has been introduced into the vadose zone, either accidentally from leaks from the buried high-level waste tanks or intentionally via direct discharges (Szecsody et al., 2015).

Technetium management is a high-priority activity for the EM complex and there is a need to further investigate the environmental fate of technetium under natural conditions and following remediation. Tc-99 exhibits unique chemistry: when Tc is exposed to the atmosphere or any moderately oxidizing environment, it is found as pertechnetate ($TcO_4^-$) with valence state +7. Pertechnetate is highly soluble, does not sorb onto sediments and migrates at the same velocity as groundwater (Kaplan, Parker and Kutnyakov 1998), whereas under reducing conditions, technetium is found in the +4 valence state. Tc(IV) is expected to either sorb onto the sediments or precipitate as insoluble $TcO_2 \cdot nH_2O$ (Icenhower et al. 2008). Technetium migration is affected by the porewater and groundwater chemical composition and soil mineralogy. Specifically, the presence of bicarbonates in Hanford porewater and iron minerals in Hanford soil may affect technetium's fate in the environment. Recent studies have identified the existence of stable, aqueous Tc(IV) carbonate-hydroxo complexes at circumneutral conditions, such as $Tc(CO_3)(OH)_3^-$ and $Tc(CO_3)(OH)_2$ (Eriksen Trygve et al. 1992, Paquette and Lawrence 1985, Alliot et al. 2009), indicating that despite Tc being reduced, it remains in the aqueous phase. There is very limited data on the effect of bicarbonate on the fate Tc-99 under reducing conditions and technetium interactions with ferrous iron minerals present in the Hanford Site need to be investigated.

## Subtask 1.4: Objectives

The objective of this research is to study the fate of Tc-99 in Hanford sediment and explore the effect of bicarbonates on redox transformations of Tc-99. The reduction of pertechnetate by Hanford sediment such as magnetite was studied in the absence and presence of bicarbonates. The bicarbonate-free experiments aim to establish a "baseline" in pertechnetate reduction rate by magnetite in circumneutral conditions, which were compared to similar experiments in the presence of bicarbonates. Magnetite is an Fe (II,III) oxide found at the Hanford Site (Xie et al. 2003) and due to its high ferrous iron content, it could potentially provide the necessary electrons for the reduction of pertechnetate (+7 oxidation state) to amorphous $TcO_2$ (+4 oxidation state). However, the presence of bicarbonates may significantly affect Tc-99 mobility by facilitating the dissolution of prior-immobilized Tc(IV) in the form of $TcO_2$. The present studies provided new information on Tc(IV)-carbonate complexes as a potential mechanism for technetium migration in reducing geochemical environments by examining Tc-99 fate in Hanford Site sediment.

## Subtask 1.4: Methodology

### 1. Pertechnetate stock and working solutions

Pertechnetate stock solution was provided by Pacific Northwest National Laboratory (PNNL) as an 18-mL solution of $NH_4TcO_4$ with an initial concentration of 1000 mg $L^{-1}$ of Tc-99 (10.2 mM). The stock solution was stored at 4$^o$C and was diluted to the desired final concentration for each experiment using deionized water, which had been degassed with high purity $N_2$ and continuously stirred for 2h. In all experiments, the initial concentration of pertechnetate was 25μM unless stated otherwise.

## 2. Batch experiments

### a. Kinetic analysis of pertechnetate reduction by Hanford sediment and magnetite

Approximately 300 mg of magnetite was weighed out and stored in the anaerobic chamber in 98% $N_2$:2% $H_2$ atmosphere (Figure 36). A stock 250 mL 50 mM bicarbonate solution was prepared and placed in the glovebox. The pH was adjusted for a period of 9 days to the desired pH values (pH 6 and 8±0.2) and Eh levels equilibrated ~-100mV. Eh and pH were monitored periodically by using a Hannah Instruments redox electrode and an Orion 9110D pH electrode, respectively. After the equilibration period, 30 mL of stock 50 mM bicarbonate solution was added to the magnetite samples. The pH of the mixture was monitored and adjusted for a period of 4 days and then the samples were spiked with 74 µL of 10.2 mM $TcO_4^-$ stock solution. The final $TcO_4^-$ concentration in the samples was 25µM.


**Figure 36. Anaerobic glovebox at FIU EC1227 where pertechnetate reduction experiments are currently taking place under 98% $N_2$ : 2% $H_2$ atmosphere.**

### b. Dissolution experiments

In order to determine the concentrations of ferrous and ferric iron in the solids, dissolution of micro- and nano-magnetite was conducted, as well as Hanford soil (mean particle diameter d<300 µm). The purpose of this experiment was to quantitatively identify the amount of ferrous iron in each sample, since ferrous iron in the mineral can act as an electron donor for the reduction of pertechnetate. Approximately 50 mg of micro- and nano-magnetite and HS soil (in triplicate) were weighed in Teflon beakers and a mixture of 4 mL 1:1 $H_2SO_4$: DI water was introduced in each sample. The suspension was then placed on a hot plate and heated to near-boiling. Consequently, 2 mL of concentrated HF acid was added and the beakers were moved to a second hotplate preset to a sufficiently high setting to induce immediate boiling. After 10 minutes of rapid boiling, the samples were allowed to cool at room temperature and 10 mL of saturated boric acid (7.2g $H_3BO_3$ in 120 mL DI $H_2O$) was added. The $H_3BO_3$ complexes with HF, thereby preventing the oxidation of Fe(II) and preventing the reaction of HF with glass (Husler et al., 2010). After digestion, 5 mL of ammonium acetate/acetic acid buffer solution (40g $NH_4C_2H_3O_2$, 24 mL $H_2O$ and 112 mL glacial $HC_2H_3O_3$) was added to each sample to increase the pH within the working pH of ferrozine (3.5-

9). The solution was transferred to a 100 mL volumetric flask and beaker was rinsed the several times to ensure quantitative transfer.

Quantification of ferrous iron and total iron was achieved using the ferrozine method spectrophotometrically. All samples were diluted further as necessary to ensure that their concentrations were within the dynamic range of the UV-VIS. Dissolution experiments of $TcO_2$ sequestered by nano-magnetite at DI water pH 8 (absence of bicarbonates) were performed, in an effort to compare $TcO_2$ dissolution rates in the presence and absence of bicarbonates against similar literature reports.

### c. Pertechnetate reduction in the presence of bicarbonate

Approximately 300 mg of magnetite was weighed out and stored in the anaerobic chamber to prevent the solid magnetite from oxidizing. 30 mL of stock 50 mM bicarbonate solution was added to the magnetite samples. The pH of the mixture was monitored and adjusted for a period of 4 days and then the samples were spiked with 74 µL of 10.2 mM $TcO_4$ stock solution. The final $TcO_4^-$ concentration in the samples was 25µM.

### d. Soil characterization

XRD analysis were conducted on samples containing approximately 500 mg of nanomagnetite in 30 mL of DI water with no pertechnetate. The samples were placed in the rotator for a period of 5 weeks, then after removing the supernatant solution the samples were dried and XRD analysis was performed. Solid characterization of the nano-magnetite was conducted to confirm the secondary mineral formation predicted by Visual MNINTEQ software.

## 3. Tc-99 analysis

The Tc-99 analysis in the aqueous phase was performed by using a Perkin Elmer Tricarb 2910 liquid scintillation counter (Figure 37). The speciation of Tc(IV) and Tc(VII) in the aqueous phase was performed by solvent extraction, using chloroform and tetraphenylphosphonium chloride (TPPC). After extracting an appropriate amount from the aqueous phase, the sample was filtered through a 0.2 µm filter and the appropriate amount of 4 mM TPPC was added to create a final TPPC:$TcO_4^-$ molar ratio higher than 40:1. Chloroform was added to a final volume of 1 mL and the sample was vortexed lightly. Once TPPC is in contact with water, it dissociates to form $Cl^-$ and $(C_6H_5)_4P^+$; which creates very stable complex with Tc(VII). Hence, tetravalent technetium ends up in the aqueous phase and heptavalent technetium ends up in the organic phase (Kopunce et al., 1998; Yalçintaş 2015). The samples were centrifuged at 14,500 rpm for 5 min and the whole amount of each phase (aqueous and organic) was transferred to plastic scintillation vials that contained 5 mL of fluorescent cocktail (Ultima Gold, Perkin Elmer). The samples were measured for 5 min in the liquid scintillation counter.

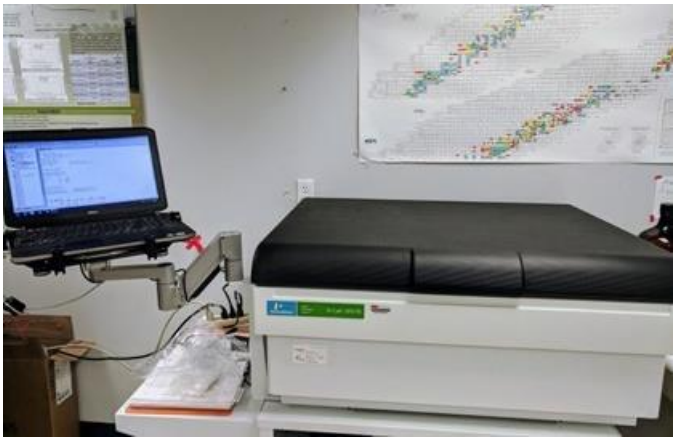

**Figure 37. Perkin Elmer TriCarb 2910 TR Liquid Scintillation Counter used throughout the experiments**

## Subtask 1.4: Results and Discussion

### 1. Kinetic analysis of pertechnetate reduction by Hanford sediment and magnetite

The kinetic results were analyzed by linear regression (least squares method) and were fit to the first order kinetic model, as well. The integrated law of a first order reaction is given by Equation 1:

$$\ln[TcO4^-] = -kt + \ln[TcO4^-_o] \quad \text{(Eq.1)}$$

where, $TcO4^-$ is pertechnetate concentration (µmol) at any given time and $TcO4^-_o$ is the initial pertechnetate concentration (µmol) (Cui and Eriksen, 1996).

The analysis of the reduction kinetics by linear regression and first order kinetics are presented in Figure 38 and Figure 39, respectively.

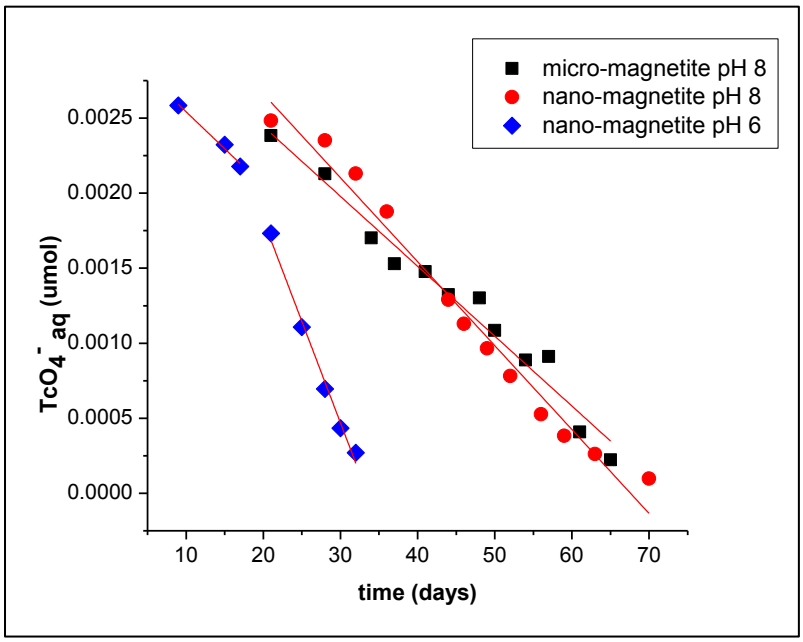


**Figure 38. Linear regression (least squares method) for pertechnetate reduction by nano-magnetite at pH 6 and nano- and micro- magnetite at pH 8.**

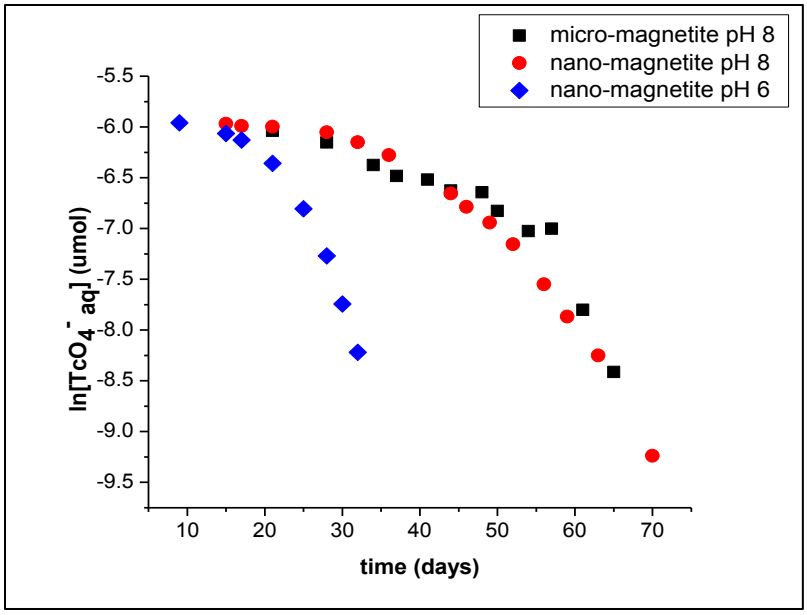


**Figure 39. Pertechnetate reduction by nano-magnetite at pH 6 and nano- and micro- magnetite at pH 8 doesn't fit to the first order reaction kinetic equation.**

As seen in Figure 38, linear regression is fit adequately to the entire range of experimental values for micro- and nano-magnetite at pH 8 ($R^2$=0.97 and $R^2$=0.98, respectively). On the other hand, there is multi-linearity in the case of pertechnetate reduction by nano-magnetite at pH 6: there are two distinct linear regions with different slopes, one at days 9-21 and the other at days 21-36. A similar biphasic trend has been reported by Peretyazhko (Peretyazhko et al., 2012), when studying pertechnetate reduction be ferrous anoxic sediments. Pertechnetate reduction accelerated after a given time point, and it was attributed to the precipitation of a new "active" phase and redistribution of Fe(II). Zachara et al. (Zachara et al., 2007) also observed acceleration of pertechnetate reduction when aqueous Fe(II) was absorbed in freshly precipitated ferrihydrite, as well as Jaisi (Jaisi et al., 2009) who made a similar observation when goethite and hematite were introduced in a Fe(II)-nontronite system. In this case, at pH 6, monitoring of $Fe(II)_{aq}$ and $Fe(III)_{aq}$ in the aqueous phase and speciation studies confirmed the precipitation of Fe(III)-(hydroxy) oxides, such as ferrihydtite and goethite, at day 21. The presence of $Fe(II)_{aq}$ in the system and its potential sorption on the newly formed phases is probably the reason behind pertechnetate reduction acceleration on the exact same day. On the other hand, at pH 8, the reduction rate seems to be constant throughout the time range of studies, despite the prediction of formation of Fe(III)-(hydroxyl) oxide phases at day ~60. This result may be explained by the absence of $Fe(II)_{aq}$ at pH 8, that could sorb on the newly formed species, since Fe(III) oxides and hydroxyl-oxides have little to no reactivity towards pertechnetate. At circumneutral pH, the couples in order of redox potential (lowest to highest) were classified as:

$$Fe^{2+}{}_{aq}/Fe_2O_{3(s)} < Fe^{2+}{}_{aq}/FeOOH_{(s)} < {=}Fe^{III}OFe^{II}OH^{o}/{=}Fe^{III}OH,\ FeOOH_{(s)} \text{ or } Fe_2O_{3(s)}$$

where $=Fe^{III}OH$ is a surface site and $= Fe^{III}OFe^{II}OH^{o}$ is a ferrous iron surface complex (Peretyazhko et al., 2009; Silvester at al., 2005), indicating that sorbed Fe(II) on Fe(III) (hydroxyl)-oxide phases is more reactive against $Fe(II)_{aq}$.

Mineral-associated Fe(II) is an effective heterogeneous reductant of pertechnetate under anoxic conditions, but sorbed Fe(II) on Fe(III) phases is a more rapid heterogeneous reductant compared to structural Fe(II). Reduction rates for all cases studied are summarized in Table 9.

**Table 9. Kinetic Parameters from Linear Regression of Peretechnetate Reduction by Magnetite at Different pH Values**

| Mineral phase | pH | k (nmol $d^{-1}$) | $R^2$ |
|---|---|---|---|
| Micro - magnetite | 8 | 0.046 ± 0.002 | 0.97 |
| Nano - magnetite | 8 | 0.058 ± 0.003 | 0.98 |
| Nano - magnetite | 6 | 0.049 ± 0.003[a] | 0.97 |
| | | 0.15 ± 0.004[b] | 0.99 |

[a] For the first linear phase, days 9-21

[b] For the second linear phase, days 21-36

At pH 6, pertechnetate reduction rate after day 21 almost triples, compared to the rates at days 9-21. Furthermore, at pH 8 nano-magnetite shows higher reduction rate than micro-magnetite, a fact that may be attributed to the higher amount of ferrous iron per mass contained in nano-magnetite. Despite the reduction rate, k, for nano-magnetite being ~26% higher when compared to micro-magnetite, both values are in the same order of magnitude. Finally, the first order reaction kinetic model does not apply to the experimental data (absence of linearity in Figure 39) and no kinetic parameters were calculated.

## 2. Dissolution experiments

The recovery of total iron for micro- and nano-magnetite was 91±2% and 95±2% of the theoretical values, respectively. A summary of the results are shown in Table 10.

**Table 10. Ferrous, ferric and total iron in micro- and nano-magnetite and HS soil**

| | Fe (II) * | Fe (III)* | % Fe(II) in the soil | Fe(III)/Fe(II) |
|---|---|---|---|---|
| Nano Magnetite | 10 ±0.3 | 23±2 | 20±0.7 | 2.3 |
| Micro Magnetite | 3.4 ±0.05 | 26±4 | 7±0.1 | 8 |
| HS Soil (d<300) | 0.06 ±0.02 | 1.6±0.4 | 0.14±0.03 | 29 |

**(mg in 50 mg of solid)*

Dissolution results revealed a significant difference in Fe(II) in magnetite and the soil. 20% of nano-magnetite's mass is ferrous iron, whereas micro-magnetite and Hanford soil contain only 7% and 0.2% of ferrous iron respectively. It is clear that the amount of ferrous iron in the soil affects dramatically its capacity to reduce pertechnetate: at pH 8, nano-magnetite reduced the same amount of pertechnetate faster than micro-magneitite. On the other hand, Hanford sediment did not reduce pertechnetate at all in 90 days, which may be due to the very small amount of ferrous iron in the soil. The results imply the necessity of a minimum amount of ferrous iron in a solid substrate for pertechnetate reduction to take place under the conditions studied. Due to the mineral composition of magnetite (sometimes formulated as $FeO{\cdot}Fe_2O_3$), specific surface area can be affected/correlated by the Fe(II)/Fe(III) ratio in the mineral (Cornell and Schwertmann, 2003).

Along with the above mention investigations, a new experiment to further investigate if there is a minimal mass of Fe(II) needed in the Hanford sediments for the reduction of Tc(VII) to occur was started. The presence of these secondary Fe minerals (iron oxides) was predicted by Visual MINTEQ software. Samples were created using 30 mg of nano-magnetite, containing comparable

Fe (II) content present in 4 g of Hanford sediments. The samples were then taken to a total volume of 30 mL and spiked with 25 µM of Tc (VII), and the results obtained are displayed in Figure 40. There was no observable reduction of pertechnetate in samples containing 30 mg of magnetite. This might be attributed to insufficient ferrous iron present in the magnetite as ($TcO_4^-$ + 4H+ + $3Fe^{-2}$ ↔ $TcO_{2(s)}$ + $2H_2O$ + $3Fe^{-3}$) ferrous iron acts as the electron donor for the reduction of pertechnetate. The ferrous iron content of the sediment sample might be insufficient for the Tc(VII) reduction to occur and this might help to explain the absence of pertechnetate reduction in the Hanford Site (HS) sediments previously reported.

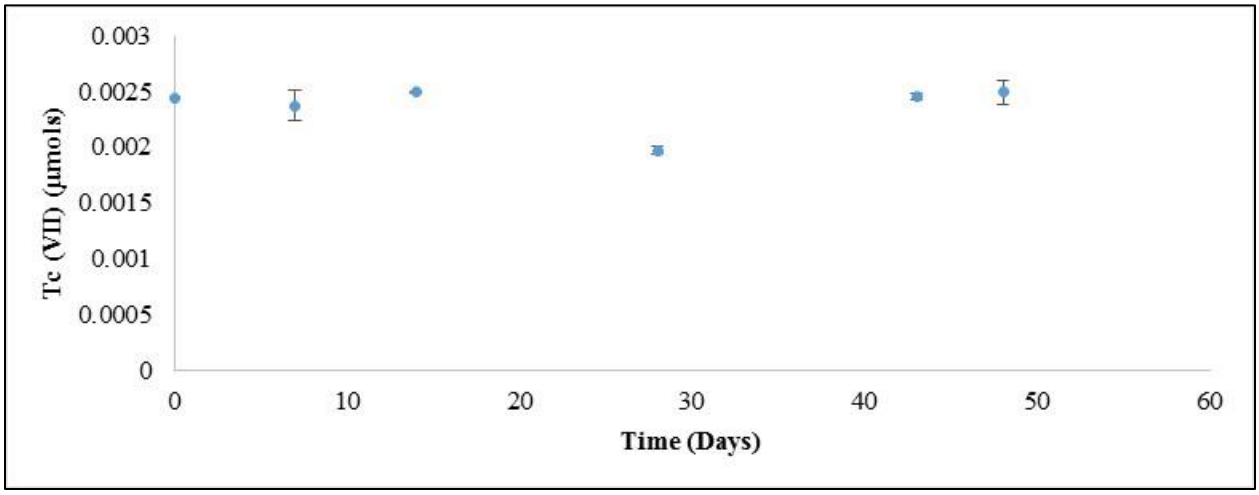


**Figure 40. $Tc(VII)_{aq}$ reduction as a function of time in the presence of 30 mg of nano-magnetite at pH 8.**

Dissolution experiments of $TcO_2$ sequestered by nano-magnetite at DI water pH 8 (absent of bicarbonate) were initiated and monitor in an effort to compare $TcO_2$ dissolution rates in the presence and absence of bicarbonates and to compare those values with similar literature reports. This experiment was carried through to completion and analyzed the dissolution of $TcO_2$ sequestered by nano-magnetite without the presence of bicarbonate in the aqueous solution, at circumenutral pH (pH 8) and in anoxic conditions. The final experimental results are presented in Figure 41.

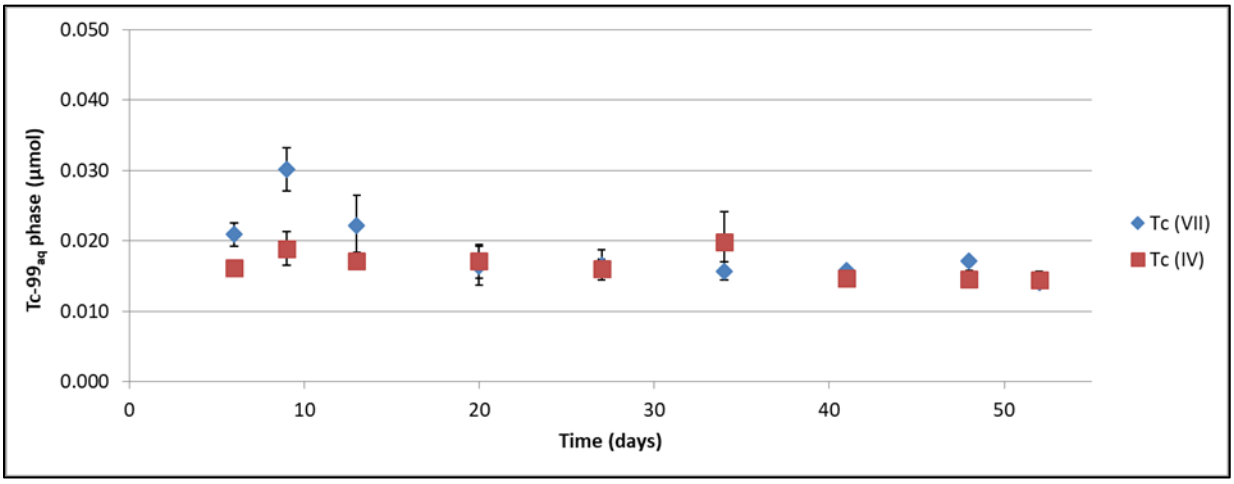


**Figure 41. $Tc(VII)_{aq}$ and $Tc(IV)_{aq}$ concentrations, as a function of time, as a result of TcO2 sequestered by nano-magnetite dissolution in the absence of bicarbonates.**

As anticipated, the results indicate that there has been no change in the dissolution rates over time. The data also reveals that there is no change in the dissolution of $TcO_2$ in the absence of bicarbonate.

The results of the final dissolution rates are presented in Table 11. These results are also in agreement with literature of dissolution values of amorphous $TcO_2$ recorded under anoxic conditions at circumneutral pH conditions ($10^{-7}$ – $10^{-6}$ M) (Peretyazhko T., et al., 2008). Trace amounts of Tc(VII) were determined despite the reducing conditions, that may be attributed to radiolytic phenomena in the solid:liquid interface, which needs to be taken into account in environmental conditions.

**Table 11. Dissolution levels in the presence of 0, 5 and 50 mM of bicarbonates at pH 8**

| **Bicarbonate concentration (mM)** | **0** | **5** | **50** |
|---|---|---|---|
| **Dissolution concentration (M)** | $4.1 \cdot 10^{-7} \pm 0.1 \cdot 10^{-7}$ | $3.8 \cdot 10^{-7} \pm 0.3 \cdot 10^{-7}$ | $3.9 \cdot 10^{-7} \pm 0.3 \cdot 10^{-7}$ |

The results and data collected support the conclusion that bicarbonates, a major ion in Hanford's groundwater composition, do not facilitate $TcO_2$ dissolution due to their chemical affinity to form stable, soluble Tc (IV)-carbonate complexes at circumneutral conditions.

## 3. Pertechnetate reduction in the presence of bicarbonate

Pertechnetate reduction in the presence of nano-, micro-magnetite and 50 mM bicarbonate was monitored. Under the conditions studied, no formation of soluble Tc (IV) was observed, as the Tc(IV) recorded values correspond to roughly 5% of the initial value (well within the experimental error). This could be due to either no formation of Tc(IV)-bicarbonate complex or incorporation/retention of reduced Tc(IV) into magnetite (Marshall et al, 2014). The reduction rate of Tc (VII) seems to be affected by the presence of bicarbonate since after 67 days, only 20% of the initial Tc-99 in the solution has been eliminated, whereas in experiments with bicarbonate-free samples, more than 70% of Tc (VII) was reduced within 70 days. It has been proposed that pertechnetate reduction takes place through a three electron transfer schematic process, as follows: $Tc(VII)O_4^- \rightarrow Tc(VI)O_4^{2-} \rightarrow Tc(V) \rightarrow TcO_2 \cdot nH_2O$ (Cui and Eriksen, 1996; Rard, 1999; Peretyazhko et al., 2009). Therefore, the presence of bicarbonates causing a slowing down/hindering of the reduction of pertechnetate can be speculated due to bicarbonates interfering at some stage of the above process most probably instabilities in pH. After 60 days, the pH of the samples was measured and found to be approximately 9.5. As can be seen from Figure 42, as the pH of the samples increased, pertechnetate reduction slowed down. An effort was made to readjust the pH to the initial pH of 8; unfortunately, due to extensive sampling over more than 90 days, the sample volume was severely depleted and the results showed significantly variability. This experiment was restarted from scratch and the pH was closely monitored.

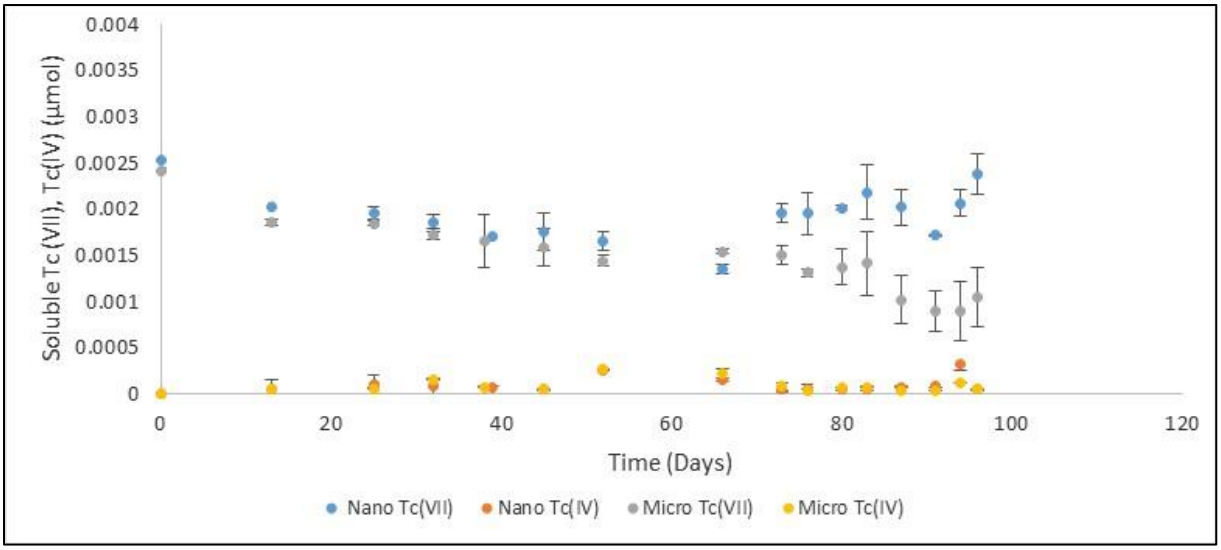


**Figure 42. $Tc(VII)_{aq}$ and $Tc(IV)_{aq}$ as a function of time in the presence of 50 mM bicarbonates at pH 8 for nano- and micro-magnetite.**

Reduction of pertechnetate in the presence of bicarbonate was slower in comparison to similar experiments conducted as bicarbonate-free Figure 43. The previously reported result for nano-magnetite showed a slightly higher reduction of Tc over micro-magnetite in the bicarbonate-free experiments. Whereas, in the presence of 50 mM bicarbonate, there was no observable reduction to date, suggesting that bicarbonate hinders the reduction of pertechnetate in nano-magnetite at pH 8. Tc reduction with micro-magnetite has also slowed as compared to bicarbonate-free samples, but not as drastically as with nano-magnetite. The formation of soluble Tc(IV)bicarbonate has not been observed in this investigation, which suggests a lack of complexation altogether or incorporation of complexes to the magnetite at a faster rate. The experiment was repeated and the results are shown in Figure 44.

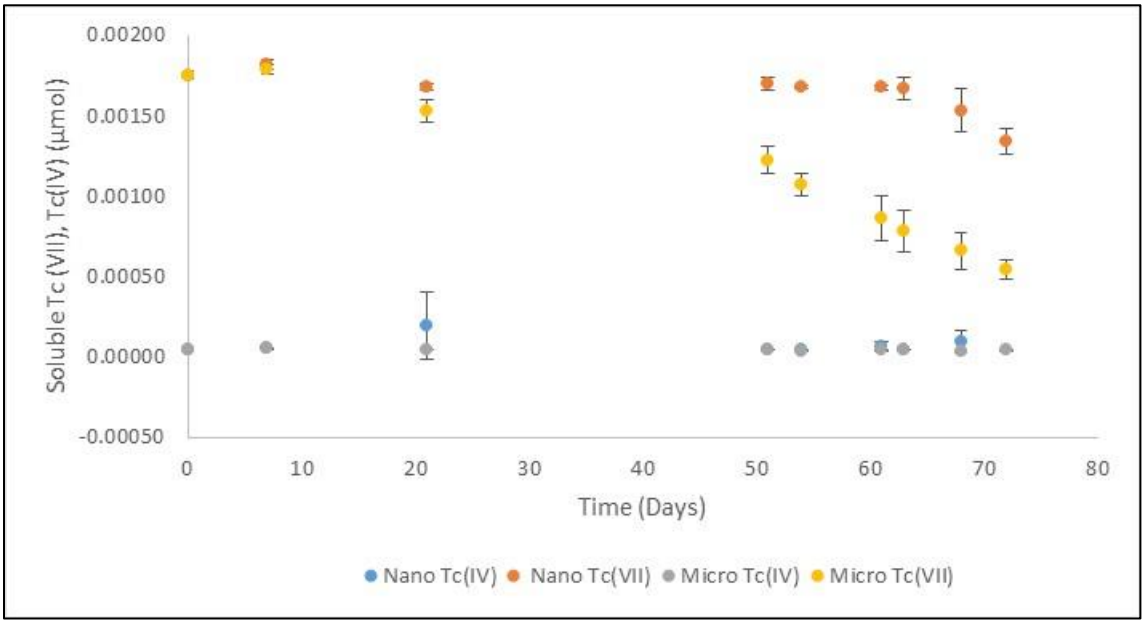


**Figure 43. $Tc(VII)_{aq}$ and $Tc(IV)_{aq}$ as a function of time in the presence of 50 mM bicarbonates at pH 8 for nano- and micro-magnetite.**

The reduction rates of both nano- and micro-magnetite decreased considerably (Table 12) when compared to the rates observed in the controls (bicarbonate-free, not shown). Moreover, micro-magnetite was shown to have better linearity compared to nano-magnetite. The reduced reduction rate suggests that the bicarbonate effect on reduction is greater in the nano-magnetite.

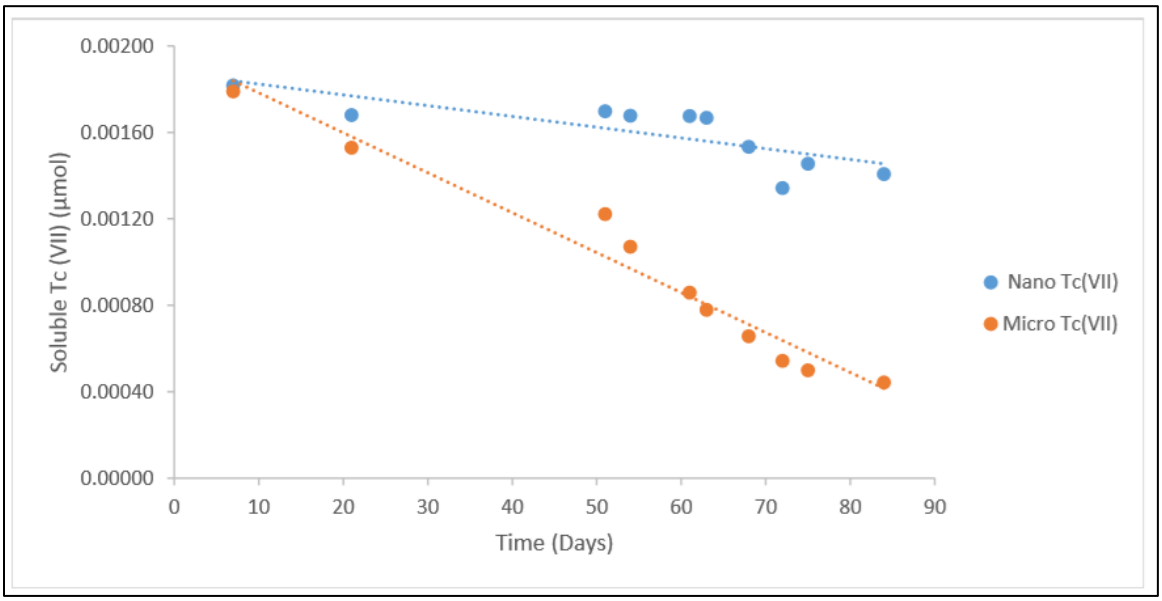


**Figure 44. $Tc(VII)_{aq}$ as a function of time in the presence of 50 mM bicarbonates at pH 8 for nano- and micro-magnetite.**

**Table 12. Reduction Rates in Bicarbonate Free and Bicarbonate Solution.**

| Mineral phase | pH | Bicarbonate free | | Bicarbonate | |
|---|---|---|---|---|---|
| | | k (nmol $d^{-1}$) | $R^2$ | k (nmol $d^{-1}$) | $R^2$ |
| **Micro - magnetite** | 8 | 0.046 ± 0.002 | 0.97 | 2E-5 ± 0.002 | 0.96 |
| **Nano - magnetite** | 8 | 0.058 ± 0.003 | 0.98 | 5E-6 ± 0.003 | 0.63 |
| **Nano - magnetite** | 6 | 0.049 ± 0.003<br>0.15 ± 0.004 | 0.97<br>0.99 | | |

## 4. Magnetite Characterization

XRD analysis of samples containing approximately 500 mg of nano-magnetite in 30 mL of DI water with no pertechnetate was also conducted. The results are a perfect fit for magnetite. As XRD will not able to detect changes smaller than 1% in the solid, there could be a small amount of secondary mineral formation in the solid even though this is not evident in Figure 45.

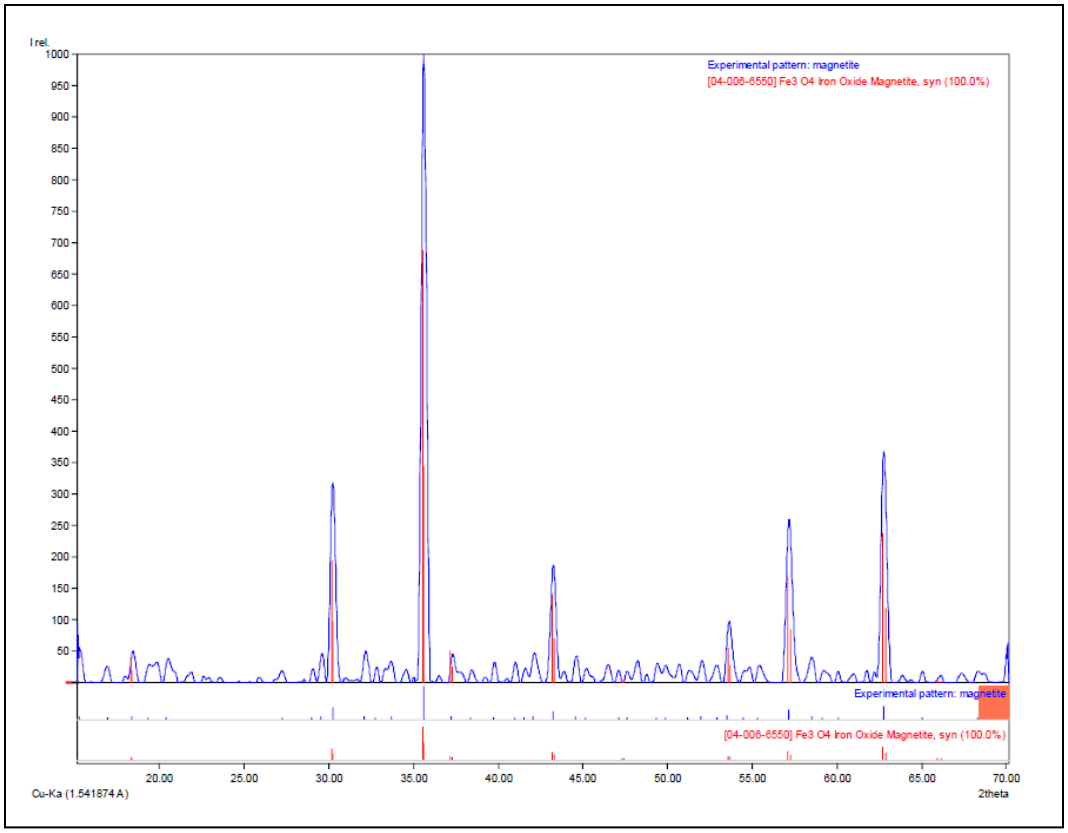


**Figure 45. XRD results of 500 mg of nano-magnetite in with 30 mL of DI water under anaerobic conditions.**

## Subtask 1.4: Future Work

Study the reduction of Tc-99 in the presence of pure minerals, ilmenite, siderite and biotite, in the absence and presence of bicarbonates under identical pH conditions. Determine potential re-oxidation of prior immobilized Tc(IV) in the presence of ferrous-iron-containing minerals in a media with and without bicarbonate.

## Subtask 1.4: Acknowledgements

Funding for this research was provided by U.S. DOE Cooperative Agreement DE-EM0000598. We truly appreciate Dr. Nik Qafoku from PNNL for support of this research.

## Subtask 1.4: References

Cornell R.M., Schwertmann U. (2003). The iron oxides. Structure, Properties, Reactions, Occurrences and Uses. Wiley-VCH Verlag GmbH & Co., Weinheim

Cui D., Eriksen T.E. (1996). Reduction of pertechnetate by ferrous iron in solution: influence of sorbed and precipitated Fe(II), *Environmental Science and Technology*, 30, 2259-2262

Icenhower, J. P., W. J. Martin, N. P. Qafoku & J. M. Zachara. 2008. The geochemistry of technetium: a summary of the behavior of an artificial element in the natural environment. Richland, WA: PNNL.

Husler J, Ferriss E.D.A., Helean K.B., Bryan C.R., Brady P.V. (2010). Optimized ferrozine micro-method for the determination of ferrous and ferric iron in rocks and minerals. Geostandards and Geoanalaytical Research 35(1), 39-44

Jaisi D.P., Dong H.L., Plymale A.E., Fredrickson J.K., Zachara J.M., Heald S., Liu C.X. (2009). Reduction and long term immobilization of technetium by Fe(II) associated with clay mineral nontronite. *Chemical Geology* 264, 127-138

Peretyazhko, T., Zachara J.M., Kukkadapu R.K., Heald S.M., Kutnyakov I.V., Resch C.T., Arey B.W., Wang C.M., Kovarik L., Phillips J.L., Moore D.A. (2012). Pertechnetate ($TcO_4^-$) reduction by reactive ferrous iron forms in naturally anoxic, redox transition zone sediments from the Hanford Site, USA. *Geochimica et Cosmochimica Acta*, 92, 48-66

Peretyazhko T., Zachara J.M., Heald S.M., Jeon B.-H., Kukkadapu R.K., Liu C., Moore D., Resch C.T., (2008). Heterogeneous reduction of Tc(VII) by Fe(II) at the solid–water interface. *Geochimica et Cosmochimica Acta*, 72, 1521–1539.

Rard J.A., Rand M.H., Anderegg G. Wanner H., 1999. Chemical thermodynamics of technetium, Elsevier, Amsterdam, The Netherlands.

Silvester E., Charlet L., Tournassat C., Gehin A., Greneche J.M., Liger E. (2005). Redox potential measurements and Mossbauer spectroscopy of Fe(II) adsorbed onto Fe(III) (oxyhrdr)oxides. *Geochimica et Cosmochimica Acta*, 69, 4801-4815

Zachara J.M., Heald S.M., Jeon B.H., Kukkadapu R.K., Liu C.X., McKinley J.P., Dohnalkova A.C., Moore D.A., (2007). Reduction of pertechnetate [Tc(VII)]by aqueous Fe(II) and the nature of solid phase redox products. *Geochimica et Cosmochimica Acta*, 71, 2137-2757

## Subtask 1.5: Stability of Contaminants in Carbonate Precipitates

## Subtask 1.5: Introduction

Plutonium production at the U.S. Department of Energy Hanford Site resulted in the generation of iodine isotopes. Radioactive waste containing the long half-life $^{129}I$ was discharged to liquid disposal locations such as cribs and trenches or stored in single-shell and double-shell tanks. Accidental releases of $^{129}I$ to the subsurface have resulted in large dilute plumes that cover an area of over 50 $km^2$. The largest $^{129}I$ plume is associated with the 200 West Area in the 200-UP-1 operable unit (OU). The majority of $^{129}I$ concentrations in the plumes are in the proximity of 10 pCi/L, which is above the drinking water standard (DWS) of 1 pCi/L. The aquifer also contains natural stable iodine ($^{127}I$), which has a similar chemical behavior as $^{129}I$ but is present at much larger concentrations in the groundwater, with $^{127}IO_3^-$ /$^{129}IO_3^-$ ratios ranging from 100 to 300 (Truex et al., 2017). The mobility of iodine depends on many factors, including chemical speciation, pH, redox conditions, sedimentary organic matter, calcium carbonate minerals content, and microbial activities. Speciation measurements show that the majority of the groundwater iodine at the Hanford Site exists as $IO_3^-$ (Zhang et al., 2013) followed by organo-iodine and then a small amount of iodide species with averages of 76%, 22% and 2%, respectively (Xu et al., 2015). Currently, DOE has no approved treatment technologies for subsurface iodine plumes to control its mobility in the vadose zone and groundwater.

Calcium carbonate minerals are abundant in nature and exist primarily as calcite, aragonite and vaterite. The crystallization of $CaCO_3$ usually proceeds through a multi-step pathway involving intermediate phase sequences such as (Kellermeier et al., 2008; Rieger et al., 2007):

$$\text{Amorphous } CaCO_3\,(ACC) \longrightarrow \text{Vaterite} \longrightarrow \text{Calcite}$$

Calcite represents the most thermodynamically stable form under ambient conditions and vaterite is the least stable (Meldrum, 2003). At the Hanford Site, the sediments contain significant calcite, up to 40% by weight. The pH of the Hanford formation sediment in equilibrium with atmospheric carbon dioxide and calcite and approximately 8.3 (Serne et al., 2008).

In nature, calcium carbonate may physically incorporate impurities within the solid during crystal growth (Morse et al., 2007). (Kitano et al., 1975) found that calcium carbonate can incorporate sulfate, chloride and sodium. Calcium carbonate can also incorporate magnesium depending on the nature of the co-anion present in the system (Kontrec et al., 2004). This mineral is also the dominant host of inorganic iodine and is important for the retention and removal of radioactive iodine isotope ($^{129}I$) from contaminated waters (Podder et al., 2017). Studies confirmed that iodine removal from the aqueous phase can occur through incorporation into calcium carbonate, which is assumed to be mainly as the $IO_3^-$group substituting for $CO_3^{2-}$. Sequestration of iodine with calcium carbonate minerals is being considered as a potential remediation method for immobilizing $^{129}I$ (Truex et al., 2017; Zhang et al., 2013).

Silica is one of the most abundant elements in nature and can have an impact on chemical weathering of alkaline-earth carbonates in the environment (Daval et al., 2009). Silica is one of the major elements both in minerals and in the porewater composition; however, there is limited data on how environmental conditions, specifically pH and silica concentrations in vadose zone pore water composition, affect the contaminant-calcium carbonate incorporation process. In previous studies, Si was effective in the removal of uranium from synthetic bicarbonate and calcium bearing solutions mimicking pore water compositions at the Hanford Site vadose zone after pH manipulations via ammonia gas injections (Katsenovich et al., 2018). The presence of silica can slow down the precipitation kinetics of calcium carbonate that would control iodate incorporation into calcium carbonate phases. Previous studies have shown that Hanford vadose zone sediments are dominated by quartz (25 to 95 wt%), potassium feldspar (5 to 40 wt%) and plagioclase feldspar (10 to 20 wt%) with minor amounts of amphibole and mica (Serne et al., 2008). In the alkaline conditions due to the disposal of alkaline wastes, the dissolution of quartz and aluminosilicate can increase silica concentrations in the pore water composition. This could promote deposition of hydrated amorphous silica layers on the precipitated calcium carbonate grains and create a silica coating on the aggregates. This process may result in sequestration of contaminants and decrease long-term iodine mobility, leading to a reduction of contaminant flux to the groundwater.

The behavior of carbonate and silicate species in aqueous media as well as precipitation of silica and carbonate phases is sensitive to the pH. The speciation of carbonate is described by the dissolution of carbonic acid according to the following reactions:

$$H_2CO_3 \overset{K_1}{\longleftrightarrow} HCO_3^- + H^+ \overset{K_2}{\longleftrightarrow} = CO_3^{2-} + 2H^+ \quad (1)$$

Where $K_1$ and $K_2$ are the first and second dissociation constants of carbonic acid.

Carbonate ions coexist with bicarbonate in the solution and precipitation of calcium carbonate induces the release of protons as bicarbonate dissociate (García-Ruiz et al., 2009; Kellermeier et al., 2010):

$$HCO_3^- \longleftrightarrow CO_3^{2-} + H^+ \xrightarrow{Ca^{2+}} CaCO_3\downarrow \quad (2)$$

This results in a decrease of pH in the vicinity of calcium carbonate particles that in turn reduce the solubility of silica due to protonation of silicate species and polymerization reactions of silicic acid to form silica solids (Kellermeier et al., 2010).

$$\text{-Si-O}^- + H^+ \longleftrightarrow \text{-Si-OH} + \text{HO-Si} \xrightarrow{-H_2O} \text{-Si-O-Si-} \rightarrow (SiO_2)_n\downarrow \quad (3)$$

The pH of a solution that contains silica is one of the most important characteristics. A slight increase in the pH to 10.5 can convert a silica sol to a solution of sodium silicate ($Na_4SiO_4$), which is soluble in water, unlike many insoluble silicates. When $Na_4SiO_4$ is dissolved in water, it has a tendency to increase the pH of the resulting solution, which is mainly due to its dissociation into $SiO_4^{4-}$ containing four negatively charged oxygen atoms that are capable of scavenging $H^+$ ions (protonation) from the solution. The point of zero charge of polymerized silica is reported to be from pH 0.5 to 3.7 (Iler, 1979) and the silica surface is negatively charged at the pH range tested for these experiments. The divalent ions such as calcium can be adsorbed on the negative surface of silica acting as a positive site. Calcium can also coagulate and precipitate silica and these coagulation reactions could potentially lead to co-precipitation of contaminants.

The purpose of this research is threefold: (1) investigate co-precipitation of iodine with calcium carbonate and study the effect of silica content in the synthetic porewater composition on the co-precipitation process; (2) investigate the pH effect on the iodine co-precipitation with calcium carbonate, and (3) characterize surface morphology and composition of produced solids via SEM/EDS analysis.

## Subtask 1.5: Methodology

*Preparation of samples for various pH and silica concentrations*

The starting materials for preparation of the calcium carbonate-forming solution included certified grade sodium meta-silicate nonahydrate ($Na_2SiO_3$, Fisher Scientific), calcium chloride dehydrate OmniPur ($CaCl_2.2H_2O$; 99.0%,), sodium bicarbonate (99.7%, Sigma Aldrich), sodium hydroxide solution 0.1N, Fisher Scientific, iodate standard ion chromatography (1000 ppm in $H_2O$, Ricca Chemical) and Milli-Q water (18.2 MΩ cm at 25°C). Stock solutions were prepared in 500 mL of deionized water for each chemical (Table 13).

**Table 13. Stock Solution Preparations for Calcium Carbonate-Forming Solutions**

| Stock Solution | Salt Used | Molecular Weight of Salt (g/mol) | Stock Solution Concentration (mM) | Amount to prepare 50 mL (g) | Targeting Concentrations in Samples (mM) | | | |
|---|---|---|---|---|---|---|---|---|
| **Carbonate** | $NaHCO_3$ | 84.01 | 400 | 16.802 | 100 | 100 | 100 | 100 |
| **Metasilicate** | $Na_2SiO_3 \cdot 9H_2O$ | 284.196 | 100 | 14.2098 | 0.5 | 2 | 5 | 20 |
| **Calcium** | $CaCl_2.H_2O$ | 147.01 | 400 | 29.402 | 100 | 100 | 100 | 100 |
| **Iodate, mg/L** | | | 1000 | | 0.250 (as iodine) | 0.250 | 0.250 | 0.250 |

**Table 14. Amount of Stock Solutions and DIW to Prepare 20 mL of Mixed Sample**

| # Sample | Sample | $NaHCO_3$ (µL) | DIW(µL) | $Na_2SiO_3 9H_2O$ (µL) | $CaCl_2.2H_2O$ (uL) | $IO_3$ (µL) (100 ppm stock) |
|---|---|---|---|---|---|---|
| 1 | 100mM $NaHCO_3$, 100mM Calcium, 0.5mMSi | 5000 | 9,831 | 100 | 5000 | 68.9 |
| 2 | 100mM $NaHCO_3$, 100mM Calcium, 2mMSi | 5000 | 9,531 | 400 | 5000 | 68.9 |
| 3 | 100mM $NaHCO_3$, 100mM Calcium, 5mMSi | 5000 | 8,931 | 1,000 | 5000 | 68.9 |
| 4 | 100mM $NaHCO_3$, 100mM Calcium, 20mMSi | 5000 | 5,931 | 4,000 | 5000 | 68.9 |
| 5 | 100mM $NaHCO_3$, 100mM Calcium, no Si, control | 5000 | 9,931 | 0 | 5000 | 68.9 |

Preparation of synthetic calcium carbonate solids were initiated by mixing an appropriate amount of sodium bicarbonate solution in the 50-mL vial to have 0.1M concentration, and with a metasilicate stock aliquot while stirring the solution. The solution was then mixed with an iodate standard to a target concentration of 250 µg/L followed by pH adjustment to the required levels by addition of a NaOH 0.1M solution. The solution was then amended with the calcium chloride stock to have 0.1M in the mixture (Table 14) and pH was readjusted again to the required levels by the addition of a NaOH 0.1M solution. The formulation was completed by the addition of the remaining DIW to bring the final volume to 20 mL (Table 14). All samples were prepared in the pH range between 7 and 11 at the stoichiometric ratio of $Ca^{2+}/CO3^{2-} = 1$. The procedures were repeated with silica concentrations in the solution of 0 mM, 0.5 mM, 2 mM, 5 mM and 20 mM. Samples were kept in the incubator-shaker at 20°C and 70 rpm and sampled after 1, 3, and 7 days from the beginning of the experiment. At each sampling, 1 mL of solution was filtered using 0.2 µm syringe filters (Fisherbrand) and then kept in the refrigerator until the time of analysis. Two controls were prepared: 1) iodate in DIW to track the initial concentration of iodate added to the

sample; and 2) carbonate-silicate mixture with iodate but without the addition of $CaCl_2$. Three sets were prepared for these experiments.

Triplicate samples were prepared using a "late spike" approach where calcium carbonate forming stock solutions were mixed in the presence of sodium silicate (sodium bicarbonate, metasilicate, and calcium chloride solutions) to create a calcium carbonate precipitate. Then, a day later, iodine in the concentration of 250 µg/L was added to reach 20 mL of solution in the vial. For this experiment, five sets of samples were prepared using 0, 0.5, 2, 5, and 20 mM of silica. Each sample contained 100 mM of sodium carbonate and 100 mM of calcium chloride. For each set, four vials were prepared for each silica concentration with pH adjusted to 8, 9, 10, and 11. In order to adjust pH, 1 M of sodium hydroxide and 0.1 M hydrochloric acid was used and followed with the addition of deionized water to reach a final sample volume of 20 mL. The vials were kept in an incubator at 120 rpm and 20°C. After day 1, day 3, and day 7, 2 mL of the supernatant solution was filtered using 0.2 um syringe filters to the 2 mL centrifuge vials that were capped and stored in the refrigerator at 5°C until the time of analysis.

### *Samples preparation for SEM/EDS*

Preparation of a synthetic solution to conduct SEM/EDS analysis followed the same procedures with the exception of using a higher concentration of iodine (500 ppm). Samples prepared using environmental concentrations have much lower iodine concentrations than the detection limits of this analytical method. Two samples were prepared in duplicate with 20 mM of Si at pH 7 and pH 11. Solutions with calcium carbonate precipitates were vacuum filtered via a 0.45µm filter and the recovered precipitates were kept for three days in an incubator at 35°C for drying. The dried precipitates were mounted on a sample holder and coated with gold and palladium to prepare for SEM/EDS analysis (SEM, Jeol JSM-5900LV, 15 keV accelerating voltage). The chemical compositions were analyzed by EDS (IXRF Systems, USA). The EDS analysis of the samples containing lower concentrations of iodine have not detected any iodine presence in the samples.

### *Analysis of iodine samples*

The total iodine as mass 127 was quantitatively measured using a ThermoFisher Scientific iCAP QR inductively coupled plasma-mass spectrometer (ICP-MS). The sample solutions were pumped by a peristaltic pump and aspirated into the argon plasma. The calibration standards were prepared from commercially available stock solutions (1000 ppm in $H_2O$, Ricca Chemical). The concentrations of the calibration standards (0.1, 0.5,1.5, 5, and 10 µg/L) were prepared in 0.1% tetramethylammonium hydroxide (TMAH), 25% w/w aq. soln., electronic grade, 99.9999% (metals basis) obtained from Fisher Scientific. Rhenium and tellurium at 10 µg/L were selected as internal standards to correct for signal drift during the analytical run. All samples and standards were diluted with the same solution of 0.1% TMAH and deionized water with a resistivity of 18.0 MΩ-cm. All instrument blanks used the same solution. For instrument calibration and standardization, FIU used 3 replicates, a dwell time of 0.1s, a wash time of 90s, and delay time a minimum of 30s.

The limit of detection (LOD) was calculated from the slope of the calibration curve; three times the standard deviation of a repeated analysis (n=10) of blank counts was 0.004µg/L. This LOD is sufficiently sensitive for the direct determination of iodine and is superior to ion chromatography or any other traditional analytical method (Julshamn et al., 2001; Takaku et al., 1995; Watts and Mitchell, 2009).

## Subtask 1.5: Results and Discussion

The results suggested that the removal of iodate from the solution occurs by sorption and co-precipitation with calcium carbonate. The experimental data indicated that the highest removal of iodine via co-precipitation with calcium carbonate occurs at pH 7 at all silica concentrations tested and the higher Si concentrations correlated with greater removal of iodine (Figure 46). At silica concentrations of 0 to 2 mM, iodine removal was at the level of 45-55% at pH 7. However, iodate removal increased up to 70-75% at silica concentrations of 5 mM to 20 mM.

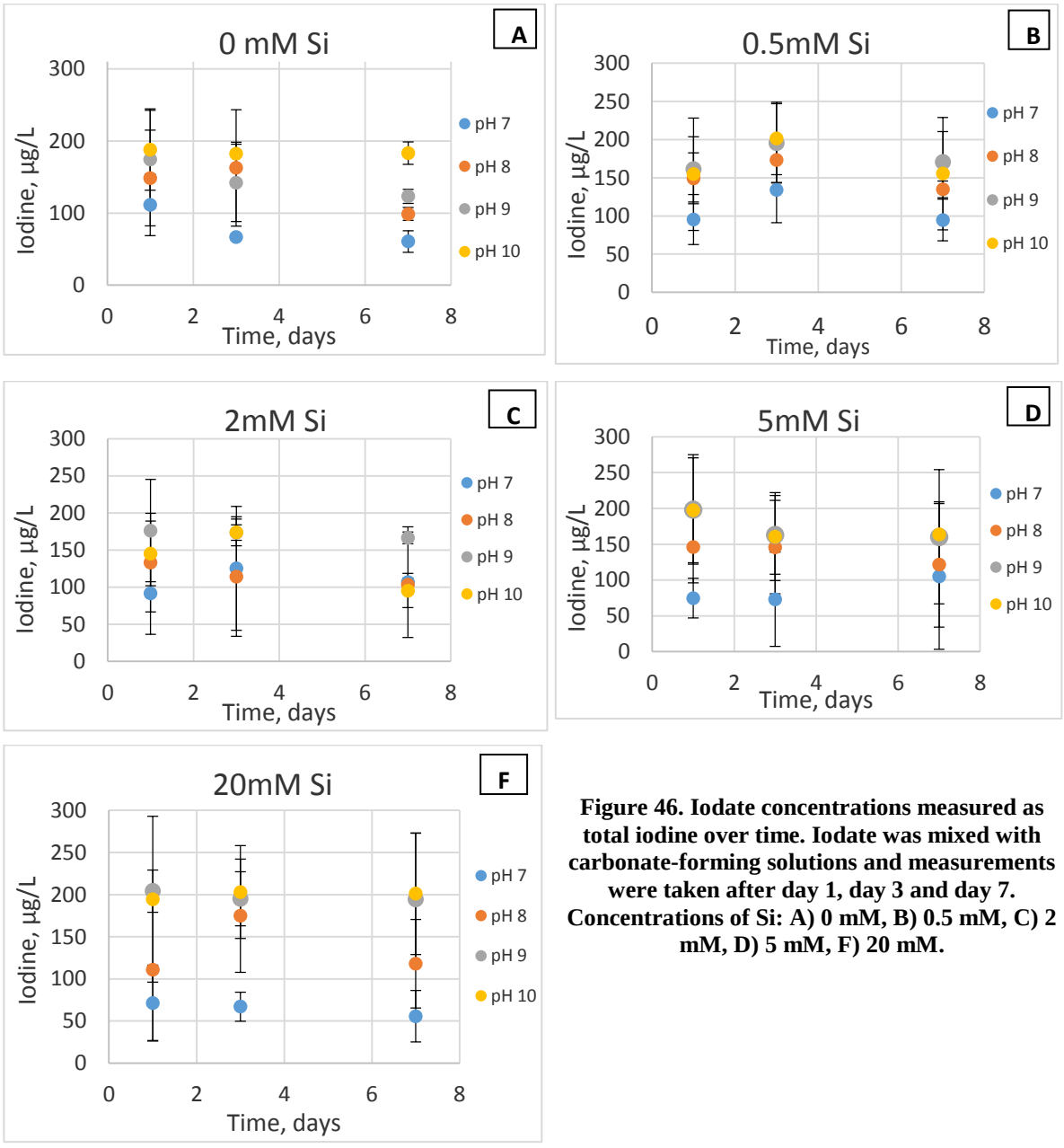


**Figure 46. Iodate concentrations measured as total iodine over time. Iodate was mixed with carbonate-forming solutions and measurements were taken after day 1, day 3 and day 7. Concentrations of Si: A) 0 mM, B) 0.5 mM, C) 2 mM, D) 5 mM, F) 20 mM.**

"Late spike" experiments were conducted to determine the extent of $IO_3^-$ adsorption to freshly precipitated calcium carbonate in the presence of silica at different pH values (Figure 47).

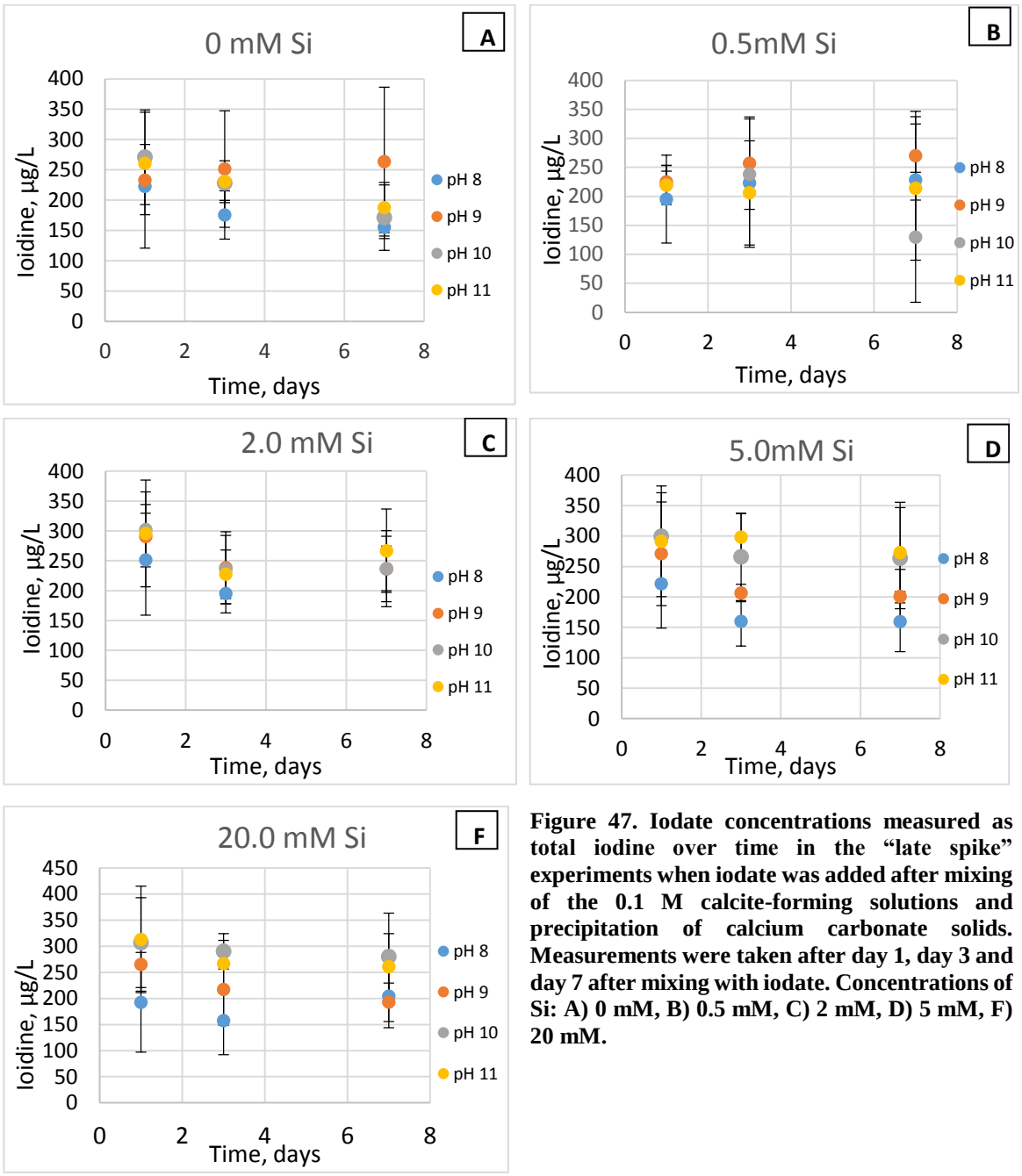


**Figure 47. Iodate concentrations measured as total iodine over time in the "late spike" experiments when iodate was added after mixing of the 0.1 M calcite-forming solutions and precipitation of calcium carbonate solids. Measurements were taken after day 1, day 3 and day 7 after mixing with iodate. Concentrations of Si: A) 0 mM, B) 0.5 mM, C) 2 mM, D) 5 mM, F) 20 mM.**

"Late spike" experiments showed less iodine removal compared to iodine co-precipitation with calcium carbonate. This indicates that iodate removal by sorption is lower than the removal by the co-precipitation process. The data also suggested that the highest removal of iodine occurs at lower pH (7 to 8) at all silica concentrations tested. The increase in pH values reduced the amount of iodine removed from the solution. It's known that the oxidized form of iodine, $IO_3^-$, has a great affinity for geomedia at neutral pH and is retained strongly on phyllosilicates, metals oxyhydroxide

surfaces at near neutral pH. At higher pH conditions, iodate sorption is decreased because the surface of silica particles become negative and repels ionic iodate species in the solution (Cox and Arai, 2014; Kaplan et al., 2000; Nagata and Fukushi, 2010). So, at higher pH, less iodine was incorporated into calcium carbonate precipitates or absorbed on precipitated calcite particle surfaces. In addition, the presence of Si in the solution did not increase the removal of iodine due to the adsorption on precipitates.

*Speciation modeling results*

The speciation modeling to predict the distribution of uranyl aqueous species and formation of uranium solid phases likely to be present in tested SPW was performed using the Geochemist Workbench (GWB) version 10.0.04 with an LLNL database (thermo.comV8.R6+) containing many radionuclides. The concentrations of iodine (250 µg/L), carbonate (100 mM) and calcium (100 mM) were kept constant in all modeling solutions. Simulations to predict the aqueous speciation and the formation of solid phases were conducted using two silica concentrations (0.5 and 20 mM). Dissolved oxygen (DO) was set at 9.0 mg/L at a constant temperature of 20°C. In the GWB Reactants pane, experimental conditions were simulated by sliding pH from 7 to 11 and the speciation modeling was performed for a system open to the exchange of $CO_2$ with the atmosphere. The aqueous iodide species were not considered in this study. The iodine aqueous species and saturation indexes (SI) of mineral phases for samples amended with 0.5 mM and 20 mM of Si were calculated and graphed as a function of pH (Figure 48, Figure 49 ).

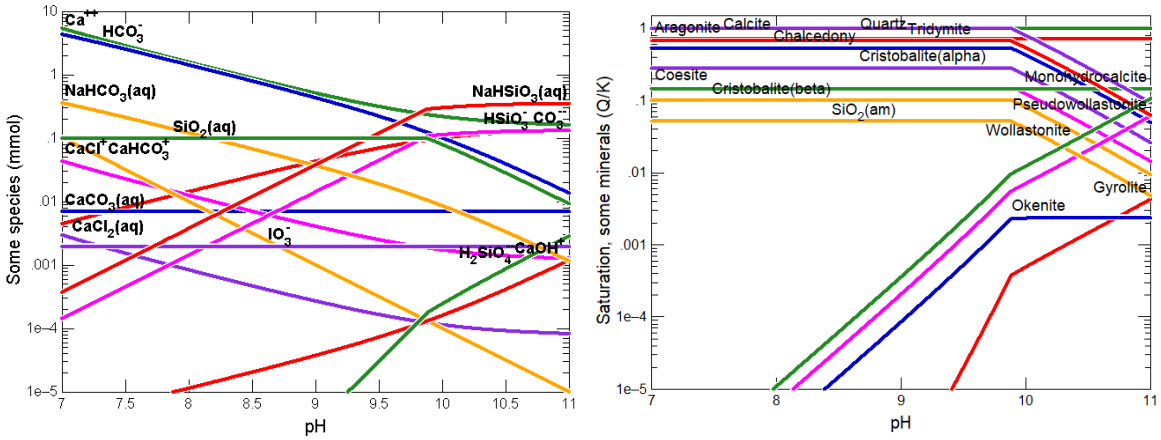


**Figure 48. Diagrams of carbonate and silicate aqueous species (left) and saturation indices of some of the carbonate and silicate mineral phases (right) plotted as a function of pH. Sample composition includes 0.1M of NaHCO3and CaCl2, 0.5mM silicate and 250ppb of iodine as iodate.**

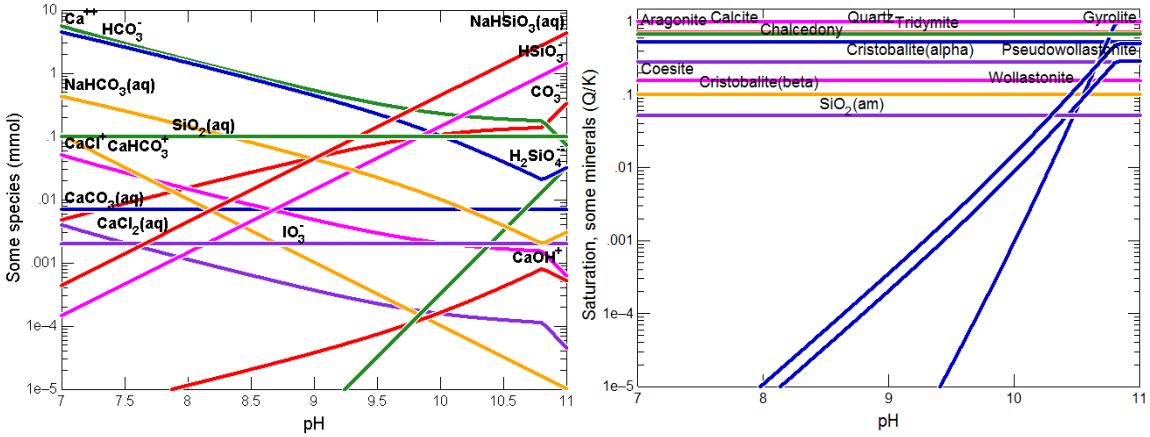


**Figure 49. Diagrams of carbonate and silicate aqueous species (left) and saturation indices of some of the carbonate and silicate mineral phases (right) plotted as a function of pH. Sample composition includes 0.1M of NaHCO3 and CaCl2, 20mM silicate and 250 ppb of iodine as iodate.**

According to the speciation modeling predictions, carbonate ions at pH 7-11 are mainly distributed between $HCO_3^-$, $NaHCO_3$, $CaCO_{3(aq)}$ and $CaHCO_3^+$ species. From those species, only the precipitation of calcite and aragonite can control the removal of inorganic carbon from the aqueous solution.

Modeling calculations on the distribution of silicate species suggested the presence of $SiO_2(aq)$; however, its concentration started to decrease at pH 9.8 for samples amended with 0.5 mM of Si but remained unchanged for samples amended with 20 mM of Si. The concentration of other predicted silicate species in 0.5 mM Si samples ($NaHSiO_3$ and $HSiO_3^-$) increased from 0.002 mmol and 1e-4 mmol at pH 7 to 0.2 mmol and 0.1 mmol at pH 9.8, respectively, and then remained unchanged when pH increased to 11. For samples composed of 20 mM of Si, the concentrations of $NaHSiO_3$ and $HSiO_3^-$ were predicted to increase up to 8 mM and 1 mM, respectively, at pH 11.

The aqueous speciation of iodate was not predicted to change. The content of inorganic carbon and calcium in the fluid composition was reduced as pH of the solution increased up to 11. However, the silica concentration increased from 0.1 mM at pH 7 to 0.5 mM for samples amended with 0.5 mM of Si and to almost 10 mM in the samples amended with 20 mM of Si at pH 11 (Figure 50).

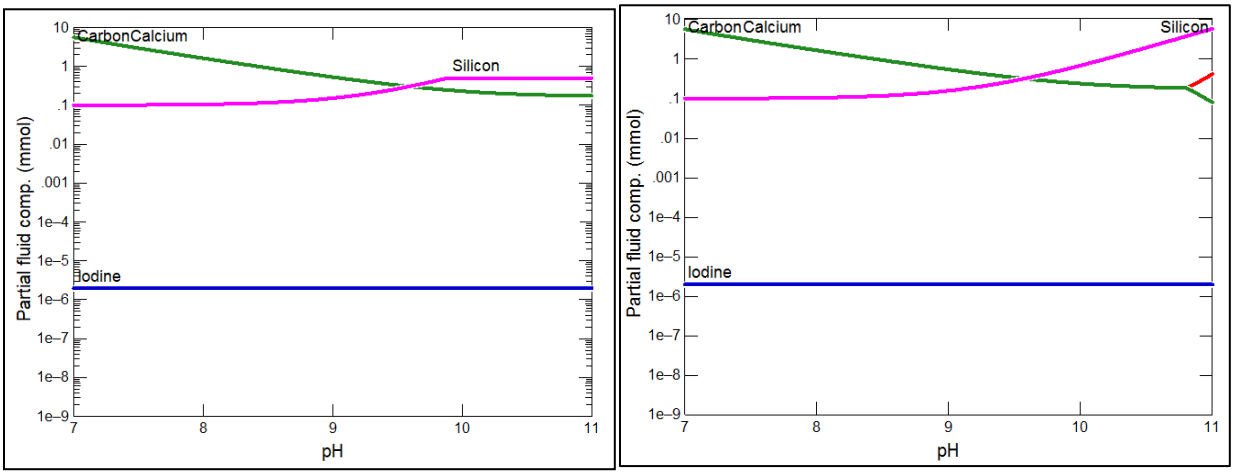


**Figure 50. Element concentrations in solution composition with pH: 0.5 mM Si (left) and 20 mM of Si (right).**

The speciation modeling also predicted the formation of relevant carbonate and silicate mineral phases. The speciation predicted the formation of calcite and quartz (SI=1). The formation of aragonite, chalcedony and quartz polymorphs such as tridymite, coesite and cristobalite, as well as calcium inosilicate wollastonite ($CaSiO_3$) was also predicted. At higher pH conditions, starting from pH 9.8, all silica-bearing minerals except quarts were predicted to be close to saturation, which coincided with the increase in the concentration of silicate species in the aqueous solution (Figure 48, Figure 49). This effect is due to increased solubility of silica species at higher pH conditions (Iler, 1979). The saturation indices of calcium carbonate solid phases remained unchanged in the studied pH range.

*SEM-EDS analyses*

SEM/EDS analysis is unable to detect elements with a mass fraction percentage below 0.1-0.2%. The low total iodine content in the samples (~250 µg/L) prevented the identification of iodine in the surface elemental composition via SEM/EDS. Thus, higher iodine concentrations up to 500 mg/L were added to the samples to detect and quantify the iodine weight percentage in the surface composition via SEM/EDS. Similar experimental limitations were discussed in other studies (Wellman et al., 2007) where the authors investigated the formation of uranium mineral phases in simulated uranium-spiked concrete. Speciation modeling suggested that there was no effect from 500 mg/L iodate on the state of saturation of various silicate and calcium carbonate minerals phases compared to diagrams presented in Figure 49 for 250 µg/L of iodine as iodate.

Literature also reports that the morphology of calcite crystals is modified in the co-presence of potassium and sodium ions (Falini et al., 2009). The morphology of calcite precipitates is also changed in the presence of silica in the solution (Kellermeier et al., 2010; Zhang et al., 2017). SEM-EDS analyses were performed to observe the solid phase surface morphology (Figure 51) and to select representative samples for future EPMA and XRD analysis. In the samples prepared with Si at 20 mM and pH 7, SEM analysis identified two distinct precipitate morphologies that showed different weight percentages of iodine.

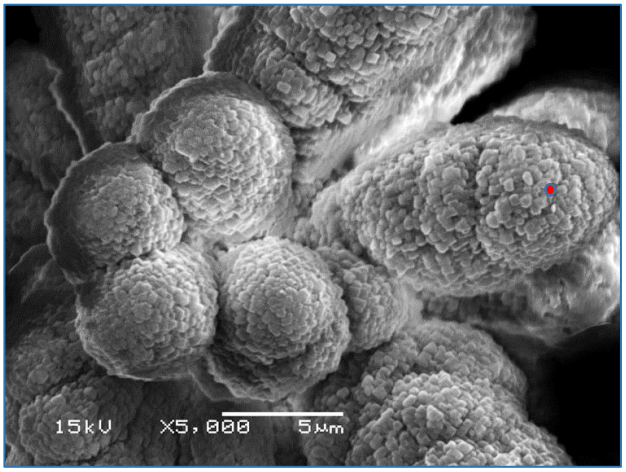


| Elt. | Line | Intensity (c/s) | Conc | Units | Error 2-sig |
|---|---|---|---|---|---|
| C | Ka | 38 | 8.71 | wt.% | 0.487 |
| O | Ka | 69 | 45.11 | wt.% | 1.647 |
| Na | Ka | 2 | 0.36 | wt.% | 0.216 |
| Si | Ka | 3 | 0.35 | wt.% | 0.153 |
| Ca | Ka | 259 | 44.74 | wt.% | 0.805 |
| I | La | 1 | 0.731 | wt.% | 0.906 |
| Total | | | 100.0 | wt.% | |

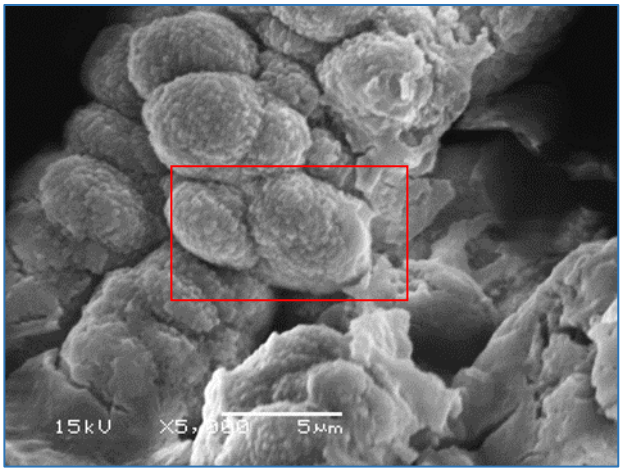


| Elt. | Line | Intensity (c/s) | Conc | Units | Error 2-sig |
|---|---|---|---|---|---|
| C | Ka | 128 | 8.44 | wt.% | 0.247 |
| O | Ka | 264 | 45.39 | wt.% | 0.827 |
| Na | Ka | 10 | 0.49 | wt.% | 0.100 |
| Si | Ka | 70 | 2.13 | wt.% | 0.098 |
| Ca | Ka | 926 | 42.98 | wt.% | 0.408 |
| I | La | 2 | 0.58 | wt.% | 0.441 |
| Total | | | 100.0 | wt.% | |

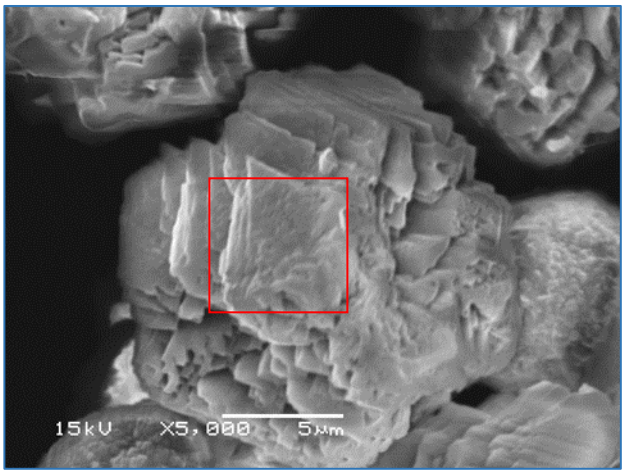


| Elt. | Line | Intensity (c/s) | Conc | Units | Error 2-sig |
|---|---|---|---|---|---|
| C | Ka | 193 | 10.47 | wt.% | 0.244 |
| O | Ka | 433 | 49.43 | wt.% | 0.702 |
| Na | Ka | 23 | 0.88 | wt.% | 0.096 |
| Si | Ka | 106 | 2.65 | wt.% | 0.093 |
| Ca | Ka | 866 | 32.72 | wt.% | 0.322 |
| I | La | 19 | 3.86 | wt.% | 0.439 |
| Total | | | 100.0 | wt.% | |

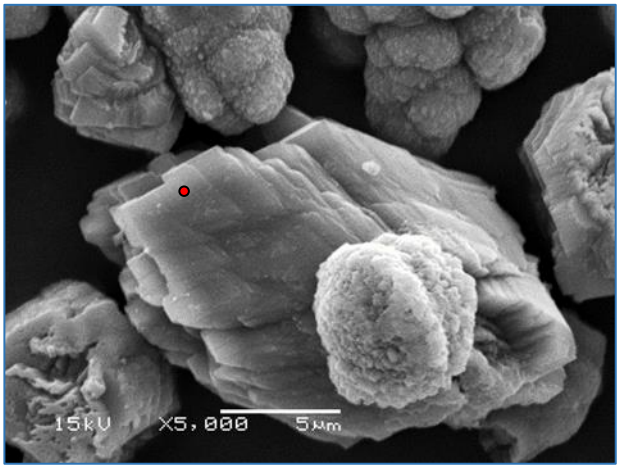


| Elt. | Line | Intensity (c/s) | Conc | Units | Error 2-sig |
|---|---|---|---|---|---|
| C | Ka | 55 | 9.97 | wt.% | 0.428 |
| O | Ka | 106 | 48.17 | wt.% | 1.374 |
| Na | Ka | 5 | 0.75 | wt.% | 0.195 |
| Si | Ka | 3 | 0.3 | wt.% | 0.130 |
| Ca | Ka | 261 | 36.76 | wt.% | 0.659 |
| I | La | 6 | 4.18 | wt.% | 0.929 |
| Total | | | 100.0 | wt.% | |

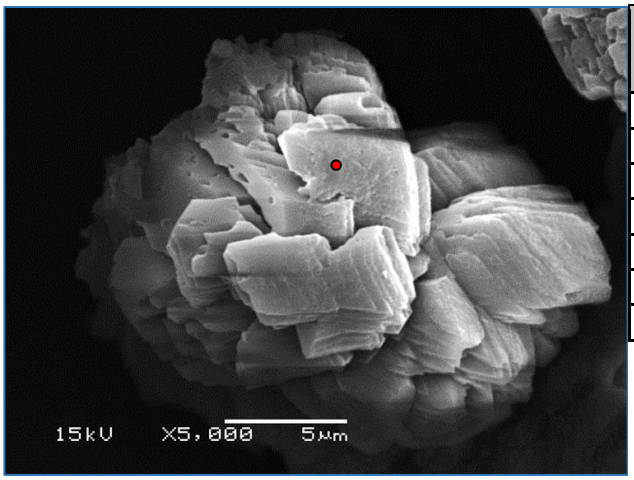


| Elt. | Line | Intensity (c/s) | Conc | Units | Error 2-sig |
|---|---|---|---|---|---|
| C | Ka | 13 | 5.96 | wt.% | 0.562 |
| O | Ka | 25 | 28.96 | wt.% | 1.754 |
| Na | Ka | 2 | 0.62 | wt.% | 0.264 |
| Si | Ka | 39 | 6.79 | wt.% | 0.354 |
| Ca | Ka | 207 | 54.70 | wt.% | 1.109 |
| I | La | 2 | 2.96 | wt.% | 1.538 |
| | | | 100.0 | wt.% | |

**Figure 51. Two different magnifications of calcium carbonate precipitates are reported at pH 7.**

With average values calculated based on the composition analysis of twelve data points, the iodine concentration averaged 0.63±1.3 wt% for the flake-like crystals and 2.46 ±1.7 wt% for the rhombohedral-shaped calcite crystals. At pH 7, the fraction of Si was generally rather small: approximately 0.08 (calculated as Si/Ca molar ratio) in the flake-like particles and 0.04 in the rhombohedral-shaped particles. These values were calculated as the average of 12-14 data points.

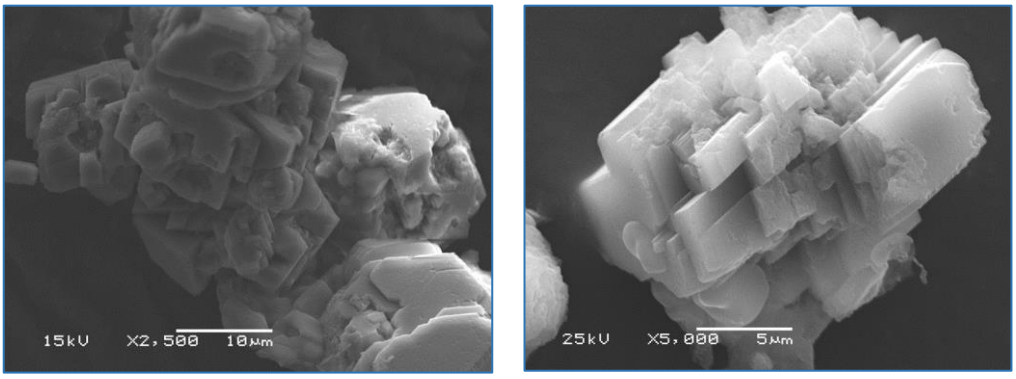


**Figure 52. Precipitate at pH 8 showing rhombohedral calcite crystals covered with amorphous Si floccules.**

At pH 7, iodine was detected on the surface of rhombohedral calcite crystals at a higher weight percentage compared to the flake-like precipitate morphologies. Precipitates prepared at pH 10 showed a more uniform morphology with lower average weight percentages for iodine (0.19 wt%) based on the average composition of ten data points (Figure 53).

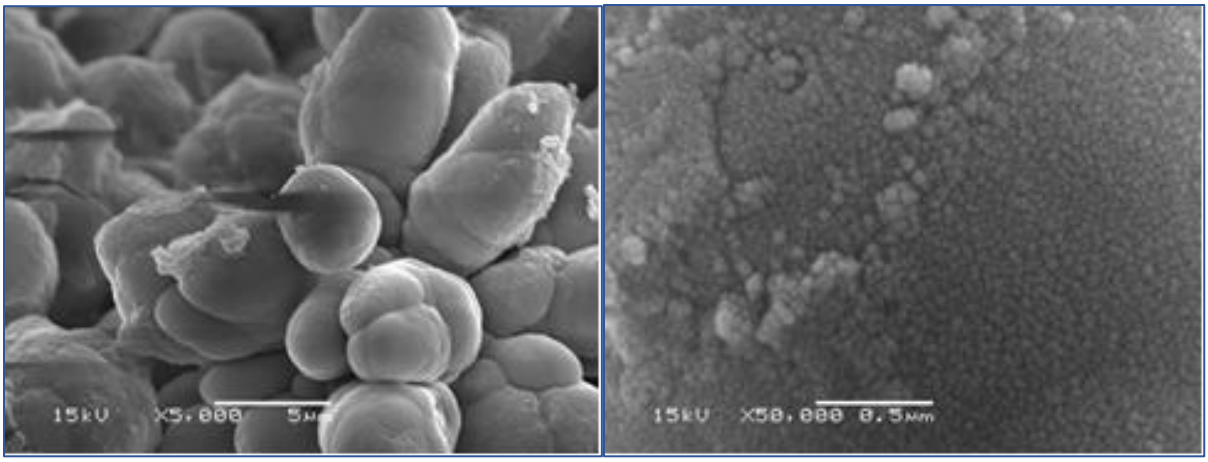


**Figure 53. Precipitate formed at pH 10 with an average iodine concentration of 0.19 wt% (left). Silica coating present on the surface of calcium carbonate precipitate at x50,000 magnification (right).**

The presence of siliceous skin around growing amorphous calcium carbonate particles was reported by Kellermeier who observed that the presence of sodium silicate during precipitation of $CaCO_3$ from supersaturated solutions at elevated pH delayed gradual transformation to crystalline polymorphs due to the spontaneous deposition of siliceous skins around growing ACC particles (Kellermeier et al., 2010). As detected by EDS analysis, silica covers amorphous $CaCO_3$ particles and the Si/Ca molar ratio of 0.96 based on the average composition of ten data points.

## Subtask 1.5: Conclusion

The experiments suggested that iodate can be removed from the solution, occurring by sorption and co-precipitation with calcium carbonate. The highest removal of iodine via co-precipitation with calcium carbonate occurred at pH 7 at all silica concentrations tested and higher Si concentrations correlated with greater iodine removal. Future experiments will be conducted to improve the accuracy of the results by minimizing the standard deviation values between the triplicate samples and to investigate the effect of comingled chromate on the removal of iodine by co-precipitation with calcium carbonate.

## Subtask 1.5: Acknowledgements

Funding for this research was provided by U.S. DOE Cooperative Agreement DE-EM0000598. We truly appreciate Dr. Nik Qafoku from PNNL for his support of this research.

## Subtask 1.5: References

Cox, E. M., and Arai, Y., 2014, Environmental Chemistry and Toxicology of Iodine, Advances in Agronomy, Volume 128, Elsevier, p. 47-96.

Daval, D., Martinez, I., Corvisier, J., Findling, N., Goffé, B., and Guyot, F., 2009, Carbonation of Ca-bearing silicates, the case of wollastonite: experimental investigations and kinetic modeling: Chemical Geology, v. 265, no. 1-2, p. 63-78.

Falini, G., Fermani, S., Tosi, G., and Dinelli, E., 2009, Calcium carbonate morphology and structure in the presence of seawater ions and humic acids: Crystal Growth and Design, v. 9, no. 5, p. 2065-2072.

García-Ruiz, J. M., Melero-García, E., and Hyde, S. T., 2009, Morphogenesis of self-assembled nanocrystalline materials of barium carbonate and silica: Science, v. 323, no. 5912, p. 362-365.

Iler, R. K., 1979, The chemistry of silica: solubility, polymerization, colloid and surface properties, and biochemistry: Canada: John Wiley &Sons Inc.

Julshamn, K., Dahl, L., and Eckhoff, K., 2001, Determination of iodine in seafood by inductively coupled plasma/mass spectrometry: Journal of AOAC International, v. 84, no. 6, p. 1976-1983.

Kaplan, D. I., Serne, R. J., Parker, K. E., and Kutnyakov, I. V., 2000, Iodide sorption to subsurface sediments and illitic minerals: Environmental Science & Technology, v. 34, no. 3, p. 399-405.

Katsenovich, Y. P., Cardona, C., Szecsody, J., Lagos, L. E., and Tang, W., 2018, Assessment of calcium addition on the removal of U (VI) in the alkaline conditions created by NH3 gas: Applied Geochemistry, v. 92, p. 94-103.

Kellermeier, M., Glaab, F., Garcia, E. M., Klein, R., Kunz, W., and Ruiz, J. G., 2008, Co-precipitation of calcium carbonate and silica, DESY Annual Report.

Kellermeier, M., Melero-García, E., Glaab, F., Klein, R., Drechsler, M., Rachel, R., García-Ruiz, J. M., and Kunz, W., 2010, Stabilization of amorphous calcium carbonate in inorganic silica-rich environments: Journal of the American Chemical Society, v. 132, no. 50, p. 17859-17866.

Kitano, Y., Okumura, M., and Idogaki, M., 1975, Incorporation of sodium, chloride and sulfate with calcium carbonate: Geochemical Journal, v. 9, no. 2, p. 75-84.

Kontrec, J., Kralj, D., Brečević, L., Falini, G., Fermani, S., Noethig-Laslo, V., and Mirosavljević, K., 2004, Incorporation of inorganic anions in calcite: European Journal of Inorganic Chemistry, v. 2004, no. 23, p. 4579-4585.

Marshall,T., Morris,T., Law, G. T. W., Mosselmans, J. F W., Bots, P., Parry S.A., and S.Shaw, 2014. Incorporation and Retention of 99-Tc(IV) in Magnetite under High pH Conditions. | *Environ. Sci. Technol*. 48, 11853−11862

Meldrum, F., 2003, Calcium carbonate in biomineralisation and biomimetic chemistry: International Materials Reviews, v. 48, no. 3, p. 187-224.

Morse, J. W., Arvidson, R. S., and Lüttge, A., 2007, Calcium carbonate formation and dissolution: Chemical reviews, v. 107, no. 2, p. 342-381.

Nagata, T., and Fukushi, K., 2010, Prediction of iodate adsorption and surface speciation on oxides by surface complexation modeling: Geochimica et Cosmochimica Acta, v. 74, no. 21, p. 6000-6013.

Podder, J., Lin, J., Sun, W., Botis, S., Tse, J., Chen, N., Hu, Y., Li, D., Seaman, J., and Pan, Y., 2017, Iodate in calcite and vaterite: Insights from synchrotron X-ray absorption spectroscopy and first-principles calculations: Geochimica et Cosmochimica Acta, v. 198, p. 218-228.

Rieger, J., Frechen, T., Cox, G., Heckmann, W., Schmidt, C., and Thieme, J., 2007, Precursor structures in the crystallization/precipitation processes of CaCO 3 and control of particle formation by polyelectrolytes: Faraday discussions, v. 136, p. 265-277.

Serne, R. J., Last, G. V., Gee, G. W., Schaef, H. T., Lanigan, D. C., Lindenmeier, C. W., Lindberg, M. J., Clayton, R. E., Legore, V. L., and Orr, R. D., 2008, Characterization of vadose zone

sediment: Borehole 299-E33-45 near BX-102 in the B-BX-BY waste management area: Pacific Northwest National Laboratory (PNNL), Richland, WA (US).

TAKAKU, Y., SHIMAMURA, T., MASUDA, K., and IGARASHI, Y., 1995, Iodine determination in natural and tap water using inductively coupled plasma mass spectrometry: Analytical sciences, v. 11, no. 5, p. 823-827.

Truex, M., Lee, B., Johnson, C., Qafoku, N., Last, G., Lee, M., and Kaplan, D., 2017, Conceptual Model of Iodine Behavior in the Subsurface at the Hanford Site. PNNL-24709, Rev. 2: Pacific Northwest National Laboratory, Richland, WA.

Watts, M., and Mitchell, C., 2009, A pilot study on iodine in soils of Greater Kabul and Nangarhar provinces of Afghanistan: Environmental geochemistry and health, v. 31, no. 4, p. 503.

Wellman, D. M., Mattigod, S. V., Arey, B. W., Wood, M. I., and Forrester, S. W., 2007, Experimental limitations regarding the formation and characterization of uranium-mineral phases in concrete waste forms: Cement and Concrete Research, v. 37, no. 2, p. 151-160.

Xu, C., Kaplan, D. I., Zhang, S., Athon, M., Ho, Y.-F., Li, H.-P., Yeager, C. M., Schwehr, K. A., Grandbois, R., and Wellman, D., 2015, Radioiodine sorption/desorption and speciation transformation by subsurface sediments from the Hanford Site: Journal of environmental radioactivity, v. 139, p. 43-55.

Zhang, G., Morales, J., and García-Ruiz, J. M., 2017, Growth behaviour of silica/carbonate nanocrystalline composites of calcite and aragonite: Journal of materials Chemistry B, v. 5, no. 8, p. 1658-1663.

Zhang, S., Xu, C., Creeley, D., Ho, Y.-F., Li, H.-P., Grandbois, R., Schwehr, K. A., Kaplan, D. I., Yeager, C. M., and Wellman, D., 2013, Iodine-129 and iodine-127 speciation in groundwater at the Hanford Site, US: Iodate incorporation into calcite: Environmental science & technology, v. 47, no. 17, p. 9635-9642.

# TASK 2: REMEDIATION RESEARCH AND TECHNICAL SUPPORT FOR SAVANNAH RIVER SITE

## Task 2: Executive Summary

Approximately 1.8 billion gallons of acidic waste containing radionuclides and dissolved heavy metals were disposed of in SRS F/H Area seepage basins, which led to the unintentional creation of highly contaminated groundwater plumes consisting of radionuclides and chemicals with an acidic pH of 3 to 5.5. The acidity of the plumes enhances the mobility of several constituents of concern (COC) such as tritium, uranium-238, iodine-129, and strontium-90 for the F-Area plume and tritium, strontium-90 and mercury for the H-Area plume. Task 2 research is focused on uranium (VI), which is a key contaminant of concern in the F-Area groundwater plume.

During FIU Performance Year 8, the scope of work under Task 2 included three (3) technical subtasks conducted in collaboration with scientists at SRNL to support groundwater remediation at the SRS F/H Area. These subtasks focused on the evaluation of remediation techniques for contaminated groundwater, as well as on the role of different environmental factors on the fate and transport of the contaminants of concern.

Iodine-129 and technetium-99 are among the most common contaminants related to radiological waste disposal sites. At SRS, radionuclides previously disposed of within the F-Area, including Tc-99 and I-129, are moving towards the Four Mile Branch Wetland with the natural groundwater flow, where they are subsequently interacting with organic materials present in the wetland. This task investigated the impact of reductive oxygen species on the fate of uranium, technetium and iodine at SRS wetland. These anions interact relatively weakly with inorganic minerals above pH 4, but strong interactions are being reported with organic matter likely due to changes in oxidation and speciation (Emerson et al. 2014, Icenhower et al. 2008). Experiments were conducted with natural wetland sediments varying the exposure time to light, pH, nitrate, and time of addition of Tc, U, and I.

This task also involves expansion of FIU's research in the SRS F/H Area to investigate the possible synergy between colloidal silica and humic acid that may have an effect on the removal of uranium from contaminated groundwater. The research also evaluated the effects of different environmental variables such as pH and uranium concentrations on the process. Additional study included batch and column sorption experiments with humic acid, which simulated the creation of a sorbed humate treatment zone in the acidic groundwater contaminated with uranium. This data will be used for the modeling of the migration and distribution of natural organic matter injected into subsurface systems.

## Subtask 2.1: Impact of free radicals on the fate of Tc, I, and U in wetlands at SRS

## Subtask 2.1: Introduction

The following subtask is a new project begun in the spring of 2018 with collaborators at Savannah River National Laboratory. The goal is the better understand interactions of risk-driving radionuclides with the wetland environment at the Savannah River site. This will contribute to DOE Office of Environmental Management (EM) plans to quantify the effect of co-mingled contaminant plumes (McCabe, D., *et al*., 2017) and is relevant to SRS remediation needs. Specifically, these data will supplement ongoing activities at SRS pertaining to the Area

Completion Project (ACP) and associated permit requirements including Phase 2 strategy to 'Evaluate the performance of Phase 1 including…downgradient of the F-Area inactive process sewer line and at Four Mile Branch.' Further, this proposed research specifically addresses needs identified in the DOE-EM Innovation and Technology: Charting the Path for Fiscal Years 2017-2021 report, including: (1) the high impact Tc-99 challenge for DOE-EM's technology development office (*treatment options for waste processing and environmental remediation*, specific goals that this research may benefit based on the report include FY18 – *develop Tc-99 biogeochemical remediation approaches* and FY21 – *quantify retention/release mechanisms for in situ remediation*), (2) incremental technologies (*gain a better understanding…in the subsurface and hydrogeologic and biogeochemical processes that influence contaminant behavior)*, and (3) fundamental knowledge gaps in basic research.

This sub-task currently supports the training and mentoring of DOE Fellow Silvia Garcia. During FIU Year 8, the major focus of this sub-task was the development of methods to quantify the impact of both light and nitrate on both the degradation of natural organic matter in a wetland environment and its impact on the fate of risk-driving radionuclides. This project produced results that were presented in two invited seminars by Dr. Emerson and that were submitted by DOE Fellow Silvia Garcia in an abstract for the 2019 Waste Management Symposia's student poster competition entitled "Impact of photodegradation of SRS wetland sediments on radionuclide mobility."

## Subtask 2.1: Objectives

To understand I, Tc, and U interactions with reactive oxygen species (ROS) and NOM impacted by ROS due to nitrate and UV interactions. This is applicable due to the high concentrations of nitrates released with the waste and may impact interactions of Tc/I/U with NOM in the SRS wetland. Previous work has shown that nitrate is a major contributor to hydroxyl radical formation in the natural environment due to photochemical reactions which may alter NOM or directly participate in redox reactions with contaminants of concern (Brezonik and Fulkerson-Brekken, 1998; Gligorovski *et al.*, 2015). This research will determine whether these interactions affect the fate of Tc, I, and U and which processes are controlling their behavior (i.e. direct interaction with free radicals or interactions with altered NOM).

Research Questions:

1. How do hydroxyl radicals and other ROS impact organic matter when formed under relevant conditions to Four Mile Branch Wetland (including representative nitrate concentrations)?
2. Do hydroxyl radicals and other ROS or their changes to organic matter impact the fate of the radionuclides of concern?
3. Is there a synergetic effect on radionuclide fate when these processes proceed simultaneously? Including (1) hydroxyl radicals and other ROS formation, (2) organic matter degradation.

## Subtask 2.1: Methodology

Experiments include the following conditions: both 0 and 100 mM $NO_3^-$, the presence and absence of light (light flux of approximately 18,000 lux as measured by a Reed instruments R8120 lux meter), variable pH (3, 5, and 7), and constant temperature at 25°C. In addition, samples were

prepared in both polypropylene and glass (50 mL) vials for comparison as some wavelengths of light may be absorbed by propylene. Control samples exclude light by using opaque black centrifuge tubes (CELLTREAT Scientific).

The system was designed to investigate the maximum alteration of organic matter under conditions relevant to SRS by ROS. The maximum $NO_3^-$ concentration measured within the plume is 19 mM at a distance of 100 meters downstream from the source (Wan *et al*., 2012). However, the average concentration within the seepage basin in the F area of SRS where waste was initially released is 87 mM. It should be noted that $NO_3^-$ plumes have been measured in environmental systems across the United States as high as 135 mM (Nolan and Weber, 2015). Therefore, these data are also potentially applicable to other systems. The pH range chosen is also representative of the range of pH values historically measured within the plume (Kaplan *et al.,* 2011). For initial experiments, maximum light will be considered using the highest setting on the environmental chamber (18,000 lux) which is within the range of full daylight but not direct sunlight.

The following wavelengths were measured by UV-vis spectroscopy in previous experiments:

1. 254 nm (E2) (Dobbs et al., 1972; Helms et al., 2008)
2. 280 nm (Chin et al., 1994; Helms et al., 2008; Sharpless et al., 2014)
3. 365 nm (E3) (Amador et al., 1989; Helms et al., 2008)
4. 465 nm (E6)
5. 665 nm (E4)
6. E4/E6 (Chin et al., 1994)
7. E2/E3 (Sharpless et al., 2014)

In previous research, the 254 nm wavelength is the most common for measurement of the concentration of humic substances and is generally the region of maximum absorption (Dobbs et al., 1972; Helms et al., 2008). The greatest losses during photochemical degradation of glycine were observed in the range of 330-370 nm (Amador et al., 1989). The region of 275-295 and 350-500 was also shown to be related to photochemically induced shifts in the molecular weight of dissolved organic matter (Helms et al., 2008). Sharpless *et al*. previously showed that photooxidation was correlated with increases in the ratio of 254:365 absorbances which may correlate with irreversible oxidation of phenols (Sharpless et al., 2014). Decreases in absorbance at 280 nm were also previously used to indicate photooxidation processes and specifically correlated with molecular weights and aromaticity changes (Chin et al., 1994; Sharpless et al., 2014). It should also be noted that a significant absorbance from nitrate did not occur at any of the abovementioned wavelengths. There is a significant absorption, however, at 220 nm in 0.1 M $NaNO_3$ that is negligible with a 50x dilution as in the samples prepared for analysis by UV-vis.

In addition, a total heterotrophic plate count (HPC) was conducted for all batch samples to investigate the potential for microbial growth as humic acid is degraded to compounds which are more readily available. Yeast-tryptone-dextrose agar was prepared according to the *Standard Methods for the Examination of Water and Wastewater* (Association and Association, 1989). Agar was autoclaved at 121°C for 15 minutes and poured into standard microbial plates after the solution reached approximately 60°C. 100 µL was spread onto each plate with sterile plastic loops and incubated at 21°C for seven days. The spread plate method was chosen because it reduces heat shock and the longer incubation time was chosen because it favors growth of water-based bacteria (Allen et al., 2004; Reasoner and Geldreich, 1985). All manipulations were conducted within a sterile biosafety cabinet with autoclaved pipette tips to reduce additional contamination of samples.

Experiments were also conducted on autoclaved Everglades peat samples under the following conditions: 0.5 g/L peat, 100 mM $NaNO_3$, 100 µg/L $^{99}TcO_4^-$, $^{238}UO_2^{2+}$ and $^{127}IO_3^-$ in a 10 mL volume in quartz vials (triplicate). One set was prepared with and without Tc, U, and I so that UV-vis analysis could be conducted in quartz cuvettes without contaminating the cuvettes. Further, one set both with and without the radionuclides of concern were exposed to full light in the environmental chamber (25°C and 18,000 lux) for approximately 24 hours while the others were placed into 50-mL black centrifuge tubes and carried through the same analysis.

Sampling for total organic carbon was conducted as described previously for humic acid with one exception. Instead of filtration, the dissolved fraction was estimated by centrifugation for 20 minutes at 8000 rpm. This centrifugation step is expected to remove particles >100 nm according to Stoke's law. A 1:10 dilution in 0.001 M NaOH was analyzed for each sample at the following wavelengths: 254, 280, 365, 465, and 665 nm and comparisons were made for the E2/E3 and E4/E6 ratios. For analysis of Tc and U, a 1:50 dilution was prepared in 2% $HNO_3$ and analyzed on ICP-MS with detection limits of 0.036 and 0.018 µg/L, respectively. For iodine, samples were prepared in 0.1% tetramethylammonium hydroxide (TMAH) and are still awaiting analysis on ICP-MS.

## Subtask 2.1: Results and Discussion

### *Preliminary results for experiments monitoring degradation of humic acid*

Figure 54 summarizes the oxidation-reduction potential (ORP) for each of the samples at 25 or 0.5 g/L of humic acid for both of the summer sampling events (71 and 55 days are shown as solid lines, 100 and 84 days are shown as diagonal lines). There is a significant fluctuation for the 0.5 g/L humic acid samples exposed to full sunlight outside possibly due to the added effect of temperature and its impact on microbial growth. Figure 55 represents a summary of temperature fluctuations in the sample placed in full sunlight as measured with a K-type thermocouple taped to the glass vial and connected to a power source with 30 minute continuous collection through LabViewer software. At select times, the temperature was monitored with a glass laboratory thermometer and showed ±10% accuracy of the thermocouple. As shown in Figure 55, temperature fluctuated from 24 to 54°C.

Over the time span of these experiments, significant alterations of humic acid with exposure time have not been observed based on the total concentration of humic acid as measured at 254 nm with recoveries of 92±8% recoveries for all 25 g/L samples. However, for the 0.5 g/L humic acid samples at pH 5, there is a decrease in recovery to 66% for samples with full sun exposure outdoors, and a slight decrease in recovery for samples in the environmental chamber with laboratory UV exposure (85-94%). Moreover, there is significantly less dissolved humic acid at pH 3, potentially due to aggregation of these substances especially at the relatively high concentration of 25 g/L (as measured by passing through a 450 nm PTFE filter) (Figure 56). Further, the differences between the percent dissolved for 0.5 versus 25 g/L humic acid at pH 5 highlights that some enhanced aggregation of humic acid occurs at the elevated concentration.

There are also differences in the E4/E6 ratios for the dissolved versus total fractions as shown in Figure 57. The dissolved fraction (< 450 nm) has E4/E6 ratios < 1.0, while the total fraction exhibits ratios > 1.0. However, there are not clear trends with respect to treatment and tube materials. A comparison of the % difference from the control sample in a black tube for the 0.5 mg/L humic acid samples at pH 5 suggests some effect of treatment along the trend of Glass + 100

mM nitrate – full sun > Glass + 100 mM nitrate > Plastic + 0 mM nitrate > Plastic + 100 mM nitrate (Figure 58).

Although humic substances are not expected to be highly degraded by microbes due to their extensive copolymerization and crosslinking, as shown by previous research suggesting a 1000 year residence time in sediments (Amador et al., 1989), microbial growth may occur as humic substances are degraded to lower molecular weight, more bioavailable compounds (Lindell et al., 1995). Further, although microbial breakdown can occur, it is significantly slower than comparable photochemical reactions. Initial results for five days and without dilution are too numerous to count for all of the plates. However, they do show significantly different microbial populations with different pH and the sample exposed to the natural environment is very different from those stored in the environmental chamber as shown in Figure 59. This could be caused by the significant fluctuations in temperature or greater degradation of humic acid in natural sunlight versus the environmental chamber. Additional plates were be prepared at a 1:100 and 1:1000 dilution to quantify microbial contamination in samples.

Total heterotrophic plate counts for most of the 25 g/L of humic acid samples were still too numerous to count (TNTC) with greater than 300 colonies per plate and those that were able to be quantified did not represent a clear trend (Table 15). However, the 0.5 g/L humic acid samples were all within an appropriate range for counting. Because multiple spread plates were not prepared with serial dilutions in a quantifiable range, most probable number (MPN) tables could not be used to provide adequate confidence intervals. Therefore, these results and trends are compared qualitatively, noting that the differences may not be statistically different. The trend is as follows: clear plastic + $NaNO_3$ > clear plastic > glass + $NaNO_3$ > black plastic > glass + $NaNO_3$ + natural conditions. Based on the temperature fluctuations summarized in the July monthly report, FIU suggests that the microbial population in the glass vial exposed to natural conditions (full sun, outdoors, fluctuating temperature) may have: (1) reached high enough temperatures in the full sun to kill much of the bacteria population, or (2) there was a die-off due to consumption of all available nutrients in the humic acid after exponential growth at the elevated temperatures. Figure 60 shows the HPC plates with a 1:100 dilution. The bacterial population in the sample exposed to full sun outside looks different from the population in the other samples stored in the environmental chamber at constant light and temperature.

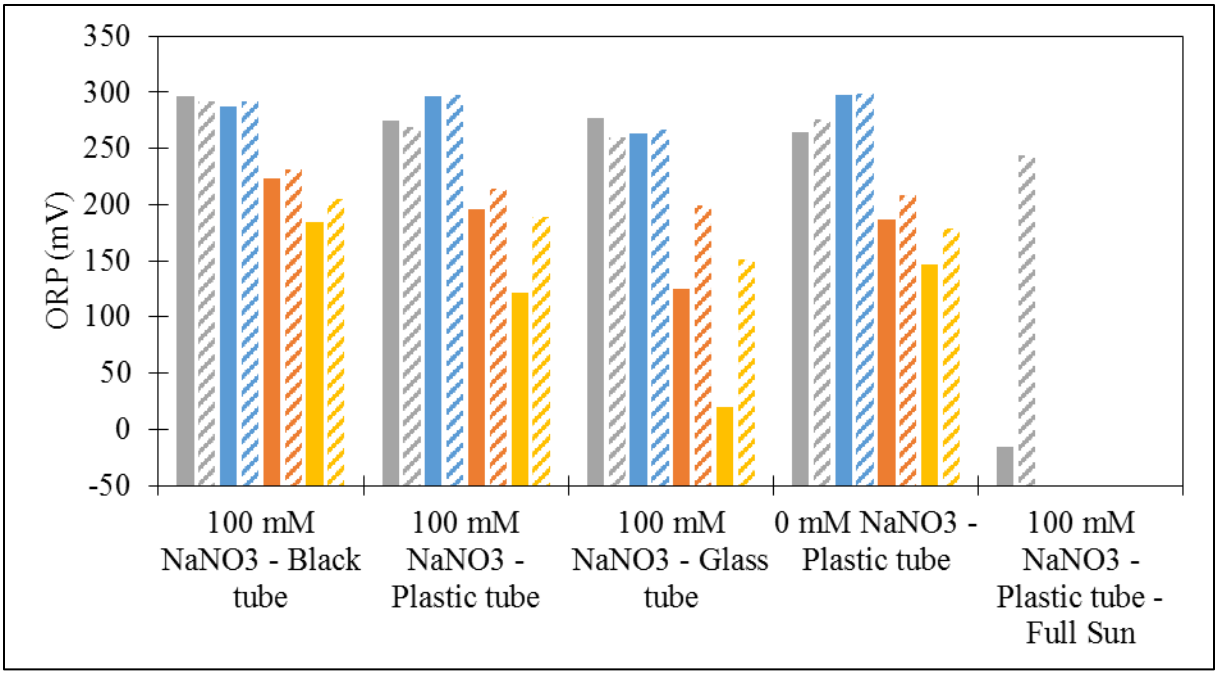


**Figure 54. ORP measurements for samples following exposure to 18,000 lux in the environmental chamber at 25°C for the first four sample types and natural conditions outside for the last sample, under the following concentrations: 0.5 g/L humic acid at pH 5 (gray), 25 g/L humic acid at pH 3 (blue), 25 g/L humic acid at pH 5 (orange), and 25 g/L humic acid at pH 7 (yellow), solid lines are measured at 71 and 55 days of reaction time for 25 and 0.5 g/L humic acid, respectively, dashed lines are measured at 100 and 84 days for 25 and 0.5 g/L humic acid, respectively.**

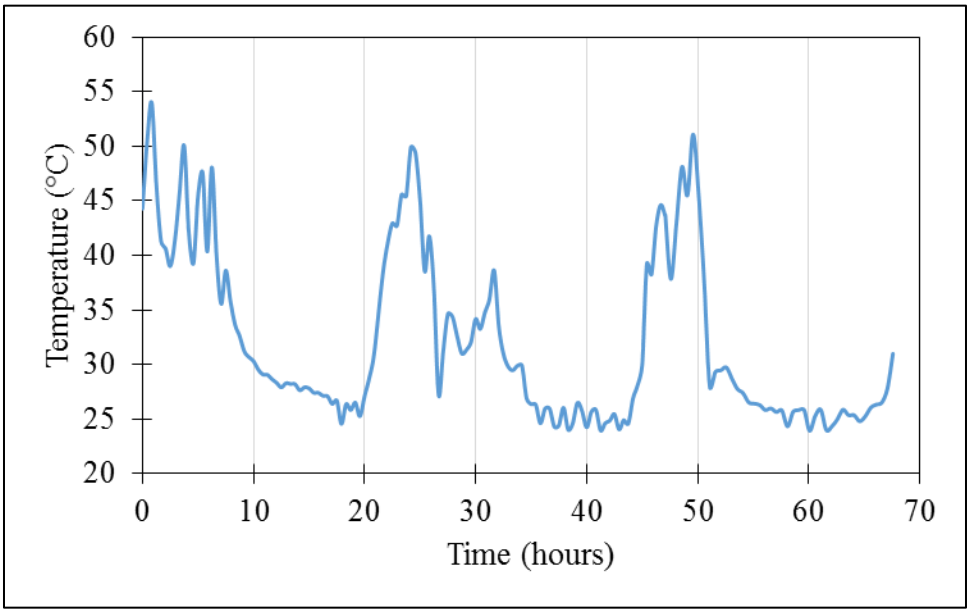


**Figure 55. Temperature fluctuations in 0.5 g/L humic acid sample exposed to full sunlight outdoors with respect to time (hours).**

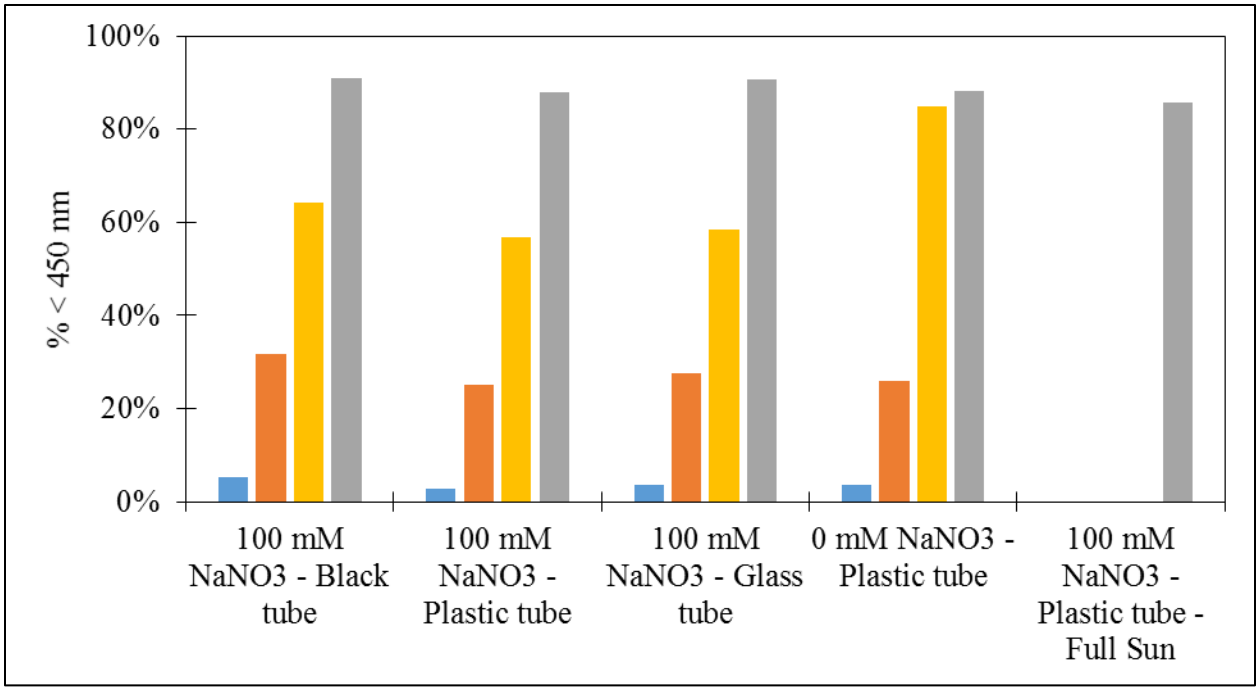


**Figure 56. Fraction dissolved for pH 3 (blue), 5 (orange), and 7 (yellow) at 25 g/L initial humic acid and pH 5 at 0.5 g/L humic acid (gray) with variable treatment conditions as measured after 100 and 84 days of reaction for 25 and 0.5 g/L humic acid concentrations, respectively.**

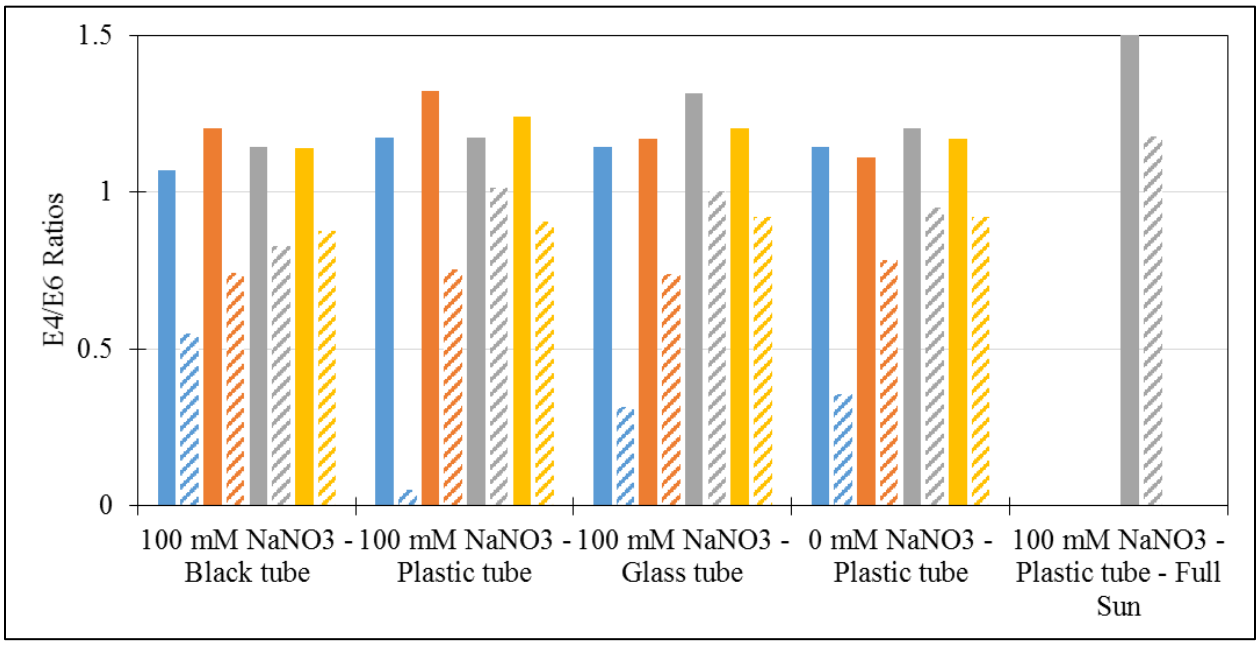


**Figure 57. E4/E6 ratios for total (solid) and dissolved (diagonal lines) humic acid for pH 3 (blue), 5 (orange), and 7 (yellow) at 25 g/L initial humic acid and pH 5 at 0.5 g/L humic acid (gray) with variable treatment conditions for 100 and 84 days of interaction for 25 and 0.5 g/L humic acid concentrations, respectively.**

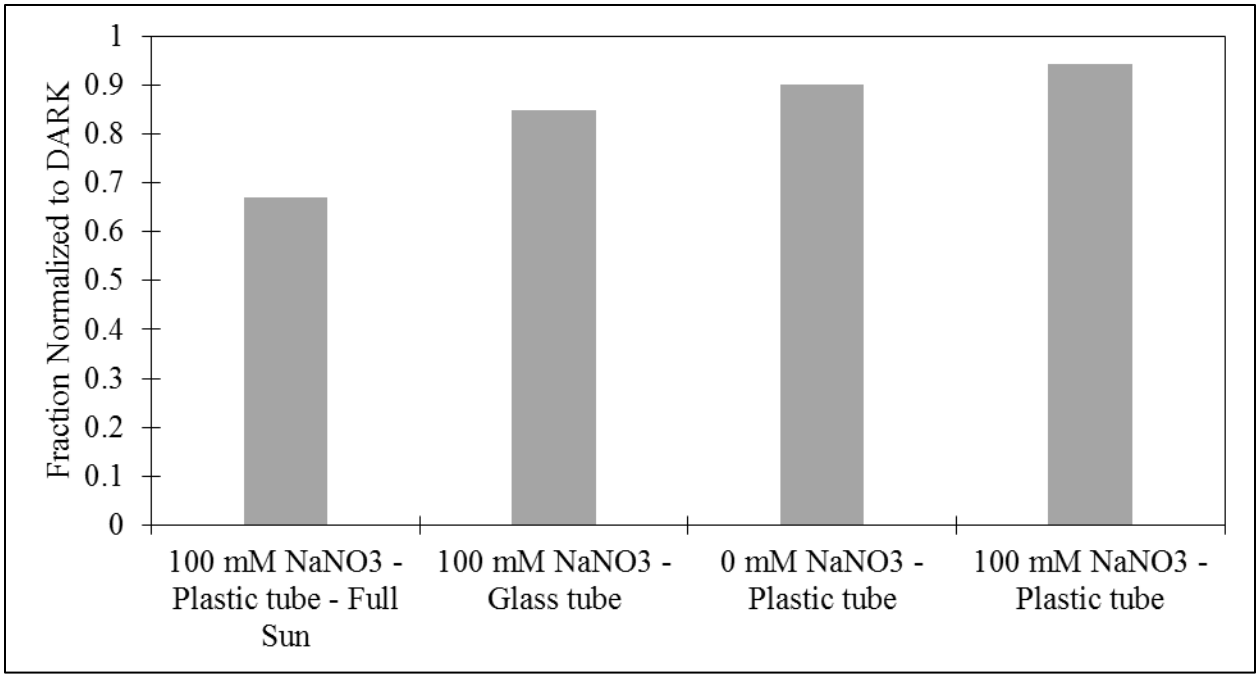


**Figure 58. Fraction of humic acid measured at 254 nm as normalized to the control sample in a black tube for 0.5 g/L initial humic acid concentration at pH 5 after 84 days of reaction time under variable conditions.**

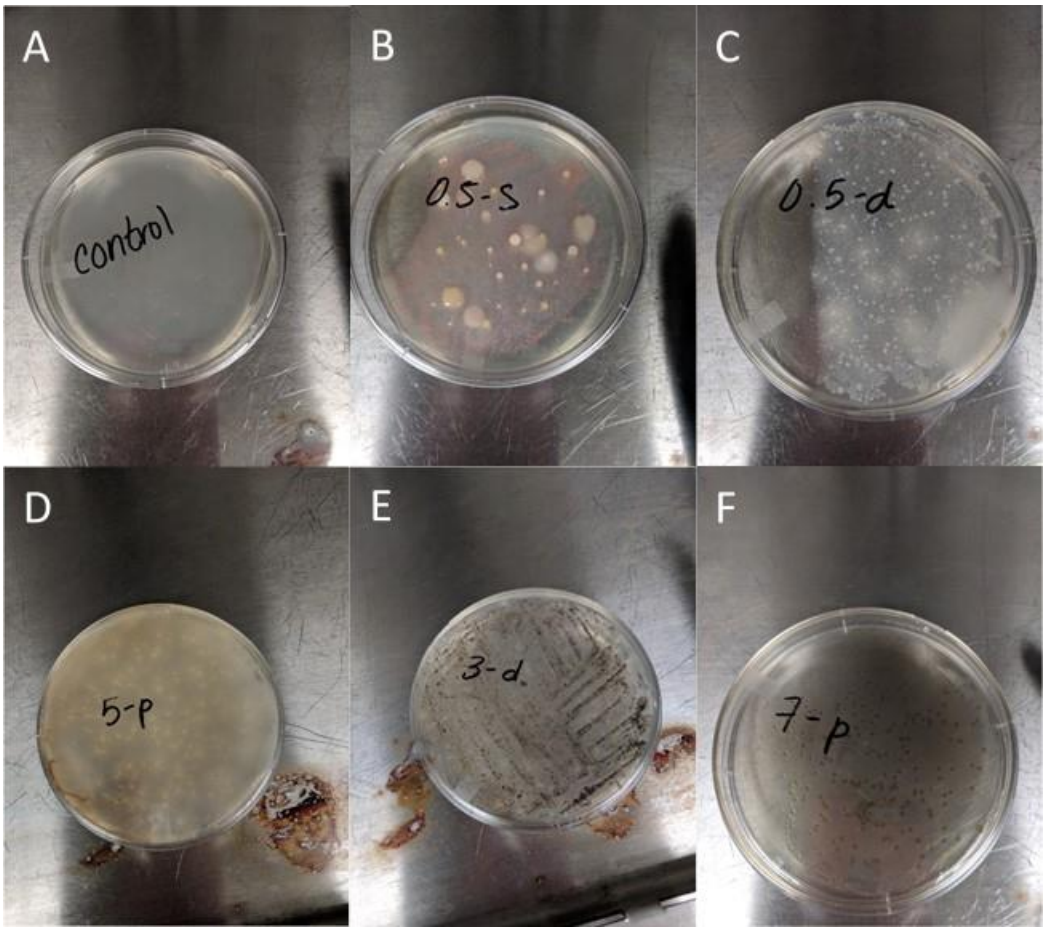


**Figure 59. Qualitative comparison of microbial populations in HPC spread plates after five days of incubation at 20°C where (A) is the control plate used to check for contamination during preparation, (B) 0.5 g/L humic acid at pH 5 exposed to the natural environment, (C) 0.5 g/L humic acid at pH 5 in the environmental chamber, (D) 25 g/L humic acid at pH 5 in the environmental chamber, (E) 25 g/L humic acid at pH 3 in the environmental chamber, and (F) 25 g/L humic acid at pH 7 in the environmental chamber.**

**Table 15. Summary of HPC Results as Compared with the Conditions in each Batch Sample**
*Note: bacteria counts reported in colony forming units (CFU) per milliliter and plates with > 300 reported as too numerous to count (TNTC)*

| Tube | Solution | Treatment | Humic Acid (g/L) | HPC (CFU/mL) |
|---|---|---|---|---|
| Black Plastic | pH3, 0.1 M $NaNO_3$ | 25°C, 18,000 lux | 25 g/L | 230 |
| Clear Plastic | pH3, 0.1 M $NaNO_3$ | 25°C, 18,000 lux | 25 g/L | TNTC |
| Glass | pH3, 0.1 M $NaNO_3$ | 25°C, 18,000 lux | 25 g/L | 380 |
| Clear Plastic | pH3, Ultrapure $H_2O$ | 25°C, 18,000 lux | 25 g/L | TNTC |
| Black Plastic | pH5, 0.1 M $NaNO_3$ | 25°C, 18,000 lux | 25 g/L | TNTC |
| Clear Plastic | pH5, 0.1 M NaNO3 | 25°C, 18,000 lux | 25 g/L | 470 |
| Glass | pH5, 0.1 M NaNO3 | 25°C, 18,000 lux | 25 g/L | TNTC |
| Clear Plastic | pH5, Ultrapure $H_2O$ | 25°C, 18,000 lux | 25 g/L | TNTC |
| Black Plastic | pH7, 0.1 M $NaNO_3$ | 25°C, 18,000 lux | 25 g/L | TNTC |
| Clear Plastic | pH7, 0.1 M $NaNO_3$ | 25°C, 18,000 lux | 25 g/L | TNTC |
| Glass | pH7, 0.1 M $NaNO_3$ | 25°C, 18,000 lux | 25 g/L | TNTC |
| Clear Plastic | pH7, Ultrapure $H_2O$ | 25°C, 18,000 lux | 25 g/L | TNTC |
| Black Plastic | pH5, 0.1 M $NaNO_3$ | 25°C, 18,000 lux | 0.5 g/L | 270 |
| Clear Plastic | pH5, 0.1 M $NaNO_3$ | 25°C, 18,000 lux | 0.5 g/L | 680 |
| Glass | pH5, 0.1 M $NaNO_3$ | 25°C, 18,000 lux | 0.5 g/L | 390 |
| Clear Plastic | pH5, Ultrapure $H_2O$ | 25°C, 18,000 lux | 0.5 g/L | 420 |
| Glass | pH5, 0.1 M $NaNO_3$ | Full Sun, Outside | 0.5 g/L | 90 |
| Clear Plastic | Ultrapure $H_2O$ | None | Control | 0 |

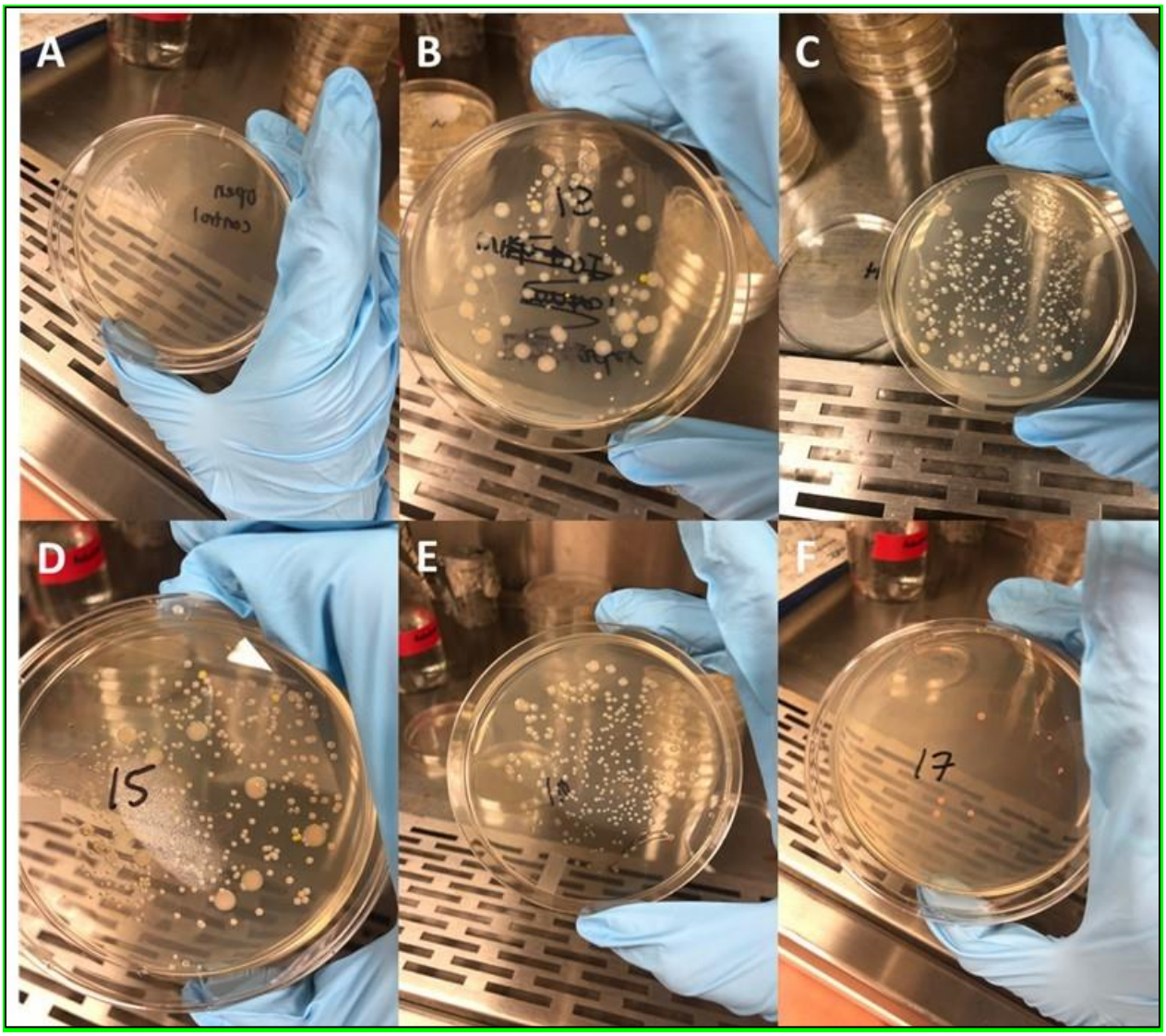


**Figure 60. Qualitative comparison of microbial populations in HPC spread plates after seven days of incubation at 21°C where (A) is the control plate used to check for contamination during preparation, (B) 0.5 g/L humic acid at pH 5 exposed to the natural environment, (C-F) 0.5 g/L humic acid at pH 5 in the environmental chamber for all conditions.**

### *Photodegradation of natural organic matter and interactions with U, Tc, and I*

Results show that there is not a significant difference in total organic carbon and dissolved organic carbon between the two treatments (light and dark) at the major wavelength for analysis of organic matter (254 nm): total 193±15 mg/L, dissolved 35±5 mg/L, and fraction dissolved 18±2%. However, when the E2/E3 ratios are compared, there is a significant difference in the total and dissolved fractions in light versus dark as shown in Table 16. FIU suggests that the error is greater in the dissolved fraction due to pipetting error. Further, insignificant removal of Tc from the aqueous phase occurred for both treatments (93±7 µg/L measured in the aqueous phase via ICP-MS for the six samples). However, there is a significant difference for aqueous U with light versus dark treatment (27±3 and 15.1±0.4 µg/L, respectively). The greater dissolved U with light treatment may be due to formation of small organic compounds which are complexing U.

**Table 16. Comparison of E2/E3 Ratios Suggesting Degradation of Natural Organic Matter after 24 hours of Exposure to Full Light or Dark Conditions and 100 mM $NaNO_3$**

| Exposure | Total NOM | Dissolved NOM |
|---|---|---|
| Dark | 5.8±0.8 | 5.8±1.9 |
| Light | 3.6±0.3 | 3.2±0.8 |

## Subtask 2.1: Future Work

During FIU Performance Year 9, FIU continue batch experiments with commercially available, well-characterized organic matter and background soil from Tim's Branch and/or Four Mile Branch Wetlands with U, $^{99}Tc$, and $^{125}I$. During Year 8, experimental methods were developed in order to conduct experiments in the absence of microbes to rule out competing effects from their degradation of NOM. Preliminary data from Year 8 shows that there is a significant effect of light exposure on degradation of natural organic matter. However, there is a need to conduct experiments with variable conditions in the presence of the radionuclides of concern. The team will conduct experiments with uncontaminated wetland sediments from the Savannah River site.

Experiments will be conducted at variable pH (3 – 7) and ionic strength (as $NaNO_3$) in order to determine the impact of light and nitrate on reactive oxygen species formation and the potential effects on NOM and fate of the contaminants of concern. Nitrate concentrations will be varied from 0 to 135 mM as these are similar to the concentrations that have been released at the Savannah River Site within the F-area plume and average plume concentrations in environmental systems across the U.S. (Wan *et al*., 2012; Nolan and Weber, 2015). Experiments will be conducted in the presence and absence of light (via UV lightbulbs or natural sunlight with quantification of light exposure using a quantum meter) and with addition of the contaminants of concern either before or after light exposure at trace contaminant concentrations (up to 100 µg/L). The effects of various ROS will also be evaluated in the presence and absence of quenching and scavenging materials based on previous work (Buschmann *et al*., 2005).

The residual $^{99}Tc$ in the aqueous phase will be determined by means of liquid scintillation counting (LSC) or inductively coupled plasma mass spectrometry (ICP-MS). In the case of iodine, iodate and iodide speciation will be determined through column separation using an ion chromatograph (IC, Dionex Aquion) coupled to ICP-MS for total iodine quantification. The organo-iodine fraction will be determined based on the difference with measurements of total aqueous iodine. Aqueous U concentrations will be measured by either kinetic phosphorescence analysis (KPA) or inductively coupled plasma mass spectrometry (ICP-MS). Humic substances will be characterized by means of potentiometric titrations, UV-vis, total organic carbon analyzer (TOC), Fourier-transform ion cyclotron resonance mass spectrometry (FT-ICR-MS), and Fourier-transform infrared spectroscopy (FTIR) in order to identify qualitatively and quantitatively the major surface functional groups before and after exposure to free radicals and the contaminants of concern.

## Subtask 2.1: Acknowledgements

Funding for this research was provided by U.S. DOE Cooperative Agreement DE-EM0000598. We truly appreciate Drs. Brian Looney and Daniel Kaplan for their invaluable feedback in the design of these experiments.

## Subtask 2.1: References


1. Allen, M.J., Edberg, S.C., Reasoner, D.J., 2004. "Heterotrophic plate count bacteria—what is their significance in drinking water?," *International Journal of Food Microbiology*, **92**(3): 265-274.
2. Amador, J.A., Alexander, M., Zika, R.G., 1989. Sequential photochemical and microbial degradation of organic molecules bound to humic acid. *Applied and Environmental Microbiology*, **55**(11): 2843-2849.
3. Association, A.P.H., Association, A.W.W., 1989. Standard methods for the examination of water and wastewater. American public health association.
4. Brezonik, P.L. and Fulkerson-Brekken, J. (1998) Nitrate-induced photolysis in natural waters: controls on concentrations of hydroxyl radical photo-intermediates by natural scavenging agents. *Environmental Science and Technology* **32**, 19, 3004-3010.
5. Chin, Y.-P., Aiken, G., O'Loughlin, E., 1994. Molecular weight, polydispersity, and spectroscopic properties of aquatic humic substances. *Environmental Science and Technology*, **28**(11): 1853-1858.
6. Dobbs, R.A., Wise, R.H., Dean, R.B., 1972. The use of ultra-violet absorbance for monitoring the total organic carbon content of water and wastewater. *Water Research*, **6**(10): 1173-1180.
7. Gligorovski, S., *et al*. (2015) Environmental implications of hydroxyl radicals. *Chemical Reviews* **115**, 24, 13051-13092.
8. Helms, J.R. et al., 2008. Absorption spectral slopes and slope ratios as indicators of molecular weight, source, and photobleaching of chromophoric dissolved organic matter. *Limnology and Oceanography*, **53**(3): 955-969.
9. Kaplan, D.I., Roberts, K.A., Schwehr, K.A., Lilley, M., Brinkmeyer, R., Denham, M.E., Diprete, D.P., Li, H.P., Powell, B., Xu, C., Yeager, C., Zhang, S., Santschi, P.H., 2011. Evaluation of a Radioiodine Plume Increasing in Concentration at the Savannah River Site. *Environmental Science and Technology* **45**, 489-495.
10. Lindell, M.J., Granéli, W., Tranvik, L.J., 1995. Enhanced bacterial growth in response to photochemical transformation of dissolved organic matter. *Limnology and Oceanography*, **40**(1): 195-199.
11. Nolan, J., Weber, K.A., 2015. Natural Uranium Contamination in Major US Aquifers Linked to Nitrate. *Environmental Science and Technology Letters* **2**, 215-220.
12. Reasoner, D.J., Geldreich, E., 1985. A new medium for the enumeration and subculture of bacteria from potable water. *Applied and Environmental Microbiology*, **49**(1): 1-7.
13. Sharpless, C.M. et al., 2014. Photooxidation-induced changes in optical, electrochemical, and photochemical properties of humic substances. *Environmental Science and Technology*, **48**(5): 2688-2696.
14. Wan, J., Tokunaga, T.K., Dong, W., Denham, M.E., Hubbard, S.S., 2012. Persistent Source Influences on the Trailing Edge of a Groundwater Plume, and Natural Attenuation Timeframes: The F-Area Savannah River Site. *Environmental Science and Technology* **46**, 4490-4497.

## Subtask 2.2: The Synergistic Effect of Humic Acid and Colloidal Silica on the Removal of Uranium (VI)

### Subtask 2.2: Introduction

Uranium is one of the key contaminants of concern in groundwater as a result of past nuclear processing activities at the Department of Energy (DOE) facilities such as the Savannah River Site (SRS) in Aiken, South Carolina. SRS was one of the major nuclear processing facilities during the Cold War where plutonium was produced (Evans et al., 1992). Beginning with the implementation of the environmental cleanup program in 1981, SRS has become a hazardous waste management facility responsible for the storage and remediation of contaminated soil and groundwater from radionuclides. Approximately 1.8 billion gallons of acidic waste containing radionuclides and dissolved heavy metals was disposed in the F/H Area seepage basins. This led to the unintentional creation of highly contaminated groundwater plumes, consisting of radionuclides with an acidic pH between 3 and 5.5. The acidity of the plumes contributed to the mobility of several constituents of concern (COC) such as tritium ($^{3}H$), uranium-238 ($^{238}U$), iodine-129 ($^{129}I$), and strontium-90 ($^{90}Sr$) for the F-Area plume and $^{3}H$, $^{90}Sr$ and mercury for the H-Area plume (Denham and Vangelas, 2008). This investigation will focus on uranium in the oxidation state +6 (U(VI)), which is a key contaminant of concern in the groundwater plume of the F-Area.

Initially, the pump-treat-reinject system was implemented from 1997 to 2003 to remove contaminants from polluted groundwater. Downgrade groundwater within the system would be pumped to the water treatment facility and re-injected upgrade within the aquifer. The effectiveness and sustainability of this process diminished over time. Therefore, it was discontinued and replaced with a funnel-and-gate process in 2004. This new process injects sodium hydroxide directly into the gates of the F-Area groundwater to effectively raise pH levels. By raising the pH of the groundwater, a treatment zone is created by reversing the acidic nature of the contaminated sediments and producing a negative net charge on the surface of sediment particles. As a result, the adsorption of cationic contaminants is expected to be enhanced. So far, this process has resulted in a decrease of $^{90}Sr$ and $^{238}U$ concentrations, though the concentration of iodine has been unaffected by this treatment (Denham and Vangelas, 2008). The solution used for the injections contains a high carbonate alkalinity in order to overcome the surface acidic conditions and natural partitions in the groundwater system. To maintain the neutral pH in the treatment zone, systematic injections are required. The continuous use of high concentrations of a carbonate solution to raise pH could re-mobilize uranium previously adsorbed within the treatment zone, though this has not been observed in the monitoring data.

Humic substances (HS) are major components of soil organic matter. HS are polyfunctional organic macromolecules formed by the chemo-microbiological decomposition of biomass or dead organic matter. These substances are usually divided into three main fractions: humin (insoluble at all pH values), humic acid (soluble at pH greater than 3.5), and fulvic acid (soluble at all pH values) (Chopping, et al.1992).

Humic acid carries a large number of functional groups such as aromatic rings, carboxyl groups, phenols, aliphatic chains, etc. (Tipping, 2002). Humic acid is an important ion exchange and metal complexing ligand with a high complexation capacity. The ability of humic acid to chemically bind to metals influences in their migration behavior and fate in natural systems (Davis, 1982; Plancque et al., 2001). Various studies have suggested that the retention of U(VI) via sorption in the presence of humic acid is a complex process. For instance, humic acid can form an organic

coating at the surface of minerals, which can enhance the sequestration of metals (Davis, 1984; Zachara et al., 1994; Labonne-Wall et al., 1997; Perminova et al., 2002). Ivanov et al. (2012) studied the sorption of U(VI) sorption onto bentonite in the presence and absence of humic acid. The study found that uranium sorption in the presence of humic acid was enhanced at low pH (below 3.8) while at moderate pH (3.8 and 6.5) uranium sorption was reduced compared to the absence of humic acid. At high pH (7 and 9), uranium sorption was reduced for both the presence and absence of humic acid (Ivanov et al., 2012). Also, Krepelova et al. (2007) not only found that U(VI) sorption onto kaolinite was influenced by pH, U(VI) concentration, the presence of inorganic carbon species, and humic acid but also that U(VI) preferred to be adsorbed onto kaolinite as a uranyl-humate complex (Krepelova et al., 2007).

This investigation analyzed the mechanisms of the synergetic interactions of humic acid and colloidal silica on the removal of uranium in the presence of pure minerals such as quartz, kaolinite and goethite which are characteristic of the F/H area.

## Subtask 2.2: Methodology

### Materials

In this study, sediment samples (FAW1 70-90 ft) collected from the F-Area were used. Sediment was sieved through a 2-mm sieve to remove gravel and larger sediment particles. Fumed colloidal silica, silicon (IV) oxide 99%, and humic acid sodium salt (50-60% as humic acid) were obtained from Fisher Scientific. Stocks of Si and HA were prepared in DIW at 2000 ppm and 100 ppm, respectively. A commercial 1000 ppm uranyl nitrate stock solution in 2% nitric acid (Fisher Scientific) was used as a source of U(VI).

### Experimental Procedure

Batch experiments were conducted by bringing quartz (400 mg), kaolinite (400 mg), a mix of quartz (380 mg, 95%) and kaolinite (20 mg, 5%) and mix of quartz (378 mg, 94.5%), kaolinite (20 mg, 5%) and goethite (2 mg, 0.5%) in contact with 20 mL of aqueous suspension in deionized water spiked with U (VI) ($C_i$ = 0.5 mg $L^{-1}$), silica (3.5 mM), and humic acid (HA) (30 mg $L^{-1}$) at different pH values (3, 5, and 8) following the sets of experiments below:

Set #1: Batch 1: Quartz + U(VI)

Batch 2: Quartz + U(VI) + HA

Batch 3: Quartz + U(VI) + HA + Si

Set #2: Batch 1: Kaolinite + U(VI)

Batch 2: Kaolinite + U(VI) + HA

Batch 3: Kaolinite + U(VI) + HA + Si

Set #3: Batch 1: Quartz + Kaolinite + U(VI)

Batch 2: Quartz + Kaolinite + U(VI) + HA

Batch 3: Quartz + Kaolinite + U(VI) + HA + Si

Set #4: Batch 1: Quartz + Kaolinite + Goethite + U(VI)

Batch 2: Quartz + Kaolinite + Goethite + U(VI) + HA

Batch 3: Quartz + Kaolinite + Goethite + U(VI) + HA + Si

Samples were mixed with a vortex mixer for 30 seconds and placed on a platform shaker for 7 days at 100 rpm. The pH was monitored daily and adjusted with 0.1 M HCl or 0.1 M NaOH for all of the samples (Figure 61). After 7 days, the samples were centrifuged for 30 minutes at 2700 rpm (Figure 62). Unfiltered samples were prepared by simply taking an aliquot of the supernatant from the centrifuged samples while filtered samples were prepared by filtering an aliquot of the supernatant through 0.45 µm syringe filters. The samples were analyzed by kinetic phosphorescence analyzer.

**Figure 61. Experimental setup.**


**Figure 62. Shaker and centrifuge experimental setup.**

## Subtask 2.2: Results and Discussion

Figure 63 shows the data obtained for set #1 experiments conducted with pure quartz mineral. At pH 3, uranium removal for Batch 1 was negligible for unfiltered and filtered samples (Figure 63). Dong & Wan (2014) reported that the sorption capacity of quartz is negligible at acidic pH, and the sorption increases with an increase in pH to pH 6 and then later decreases. Also, the point of zero charge of quartz (PZC) is between 2.5 and 3.5. This means that at pH 3, the quartz surface is net positively charged. However, with an increase in pH, the quartz surface becomes increasingly negative, and this enhances the sorption of positively charged U(VI) species by electrostatic attraction (Kenney et al., 2017). Uranium removal in the presence of humic acid at pH 3 (Batch 2) was observed to be 30% for unfiltered and 50% for filtered samples. At acidic pH, humic acid tend to precipitate, so any uranium that is bound to humic acid will be removed from the aqueous phase. In addition, humic acid can be sorbed to the quartz surface, and this could enhances the U(VI)

removal. Filtered samples indicated that there is a fraction of uranium associated with humic acid in the colloidal state. When colloidal silica was included (Batch 3), little effect was seen compared to Batch 2 for unfiltered and filtered samples. This means that U(VI) has a stronger binding affinity to humic acid compared to Si.

At pH 5, uranium removal for Batch 1 was 80% for unfiltered and almost 100% for filtered samples. With an increase in pH, the charge of the quartz surface becomes increasingly negative, which favors the sorption of positively charged U(VI) species (Kenney et al., 2017). Some studies have observed that uranium sorption reaches a maximum sorption edge close to pH 6 in the presence of quartz. This is attributed to the formation of aqueous U (VI) hydroxyl complexes such as $(UO_2)_3\ (OH)^{5+}$, enhancing the sorption of U(VI) onto quartz minerals (Prikryl et al., 2001; Du et al., 2017). Uranium removal for Batch 2 (35% for unfiltered and 50% for filtered samples) was less than Batch 1. Humic acid probably reduces uranium removal due to the formation of aqueous humic-U(VI) complexes. Colloidal silica (Batch 3) had little effect on uranium removal when compared to Batch 2 for unfiltered and filtered samples. At low pH values, silanol groups in the silica particle are protonated and will carry positive charges. As a result, there is very little sorption of uranium to the surface of the silica particles due to electrostatic repulsion.

At pH 8, uranium removal for Batch 1 decreased to 60% due to the formation of uranyl-carbonate species such as $UO_2(CO_3)_3^{4-}$. Electrostatic repulsion between uranyl carbonate species and the negatively charged quartz surface probably contribute to the decrease of uranium removal. For Batch 2, uranium removal in the presence of humic acid decreased to less than 20%. At basic conditions, humic acid is soluble, so it can form aqueous humic-U(VI) complexes. As a result, the removal of U(VI) is decreased. Colloidal silica showed a slightly higher uranium removal compared to Batch 2.

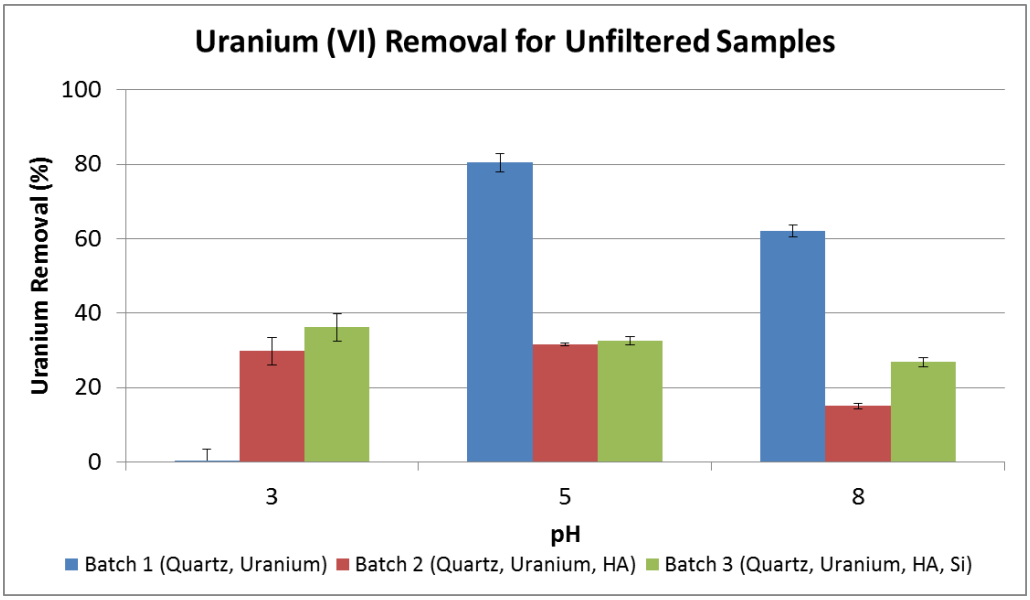

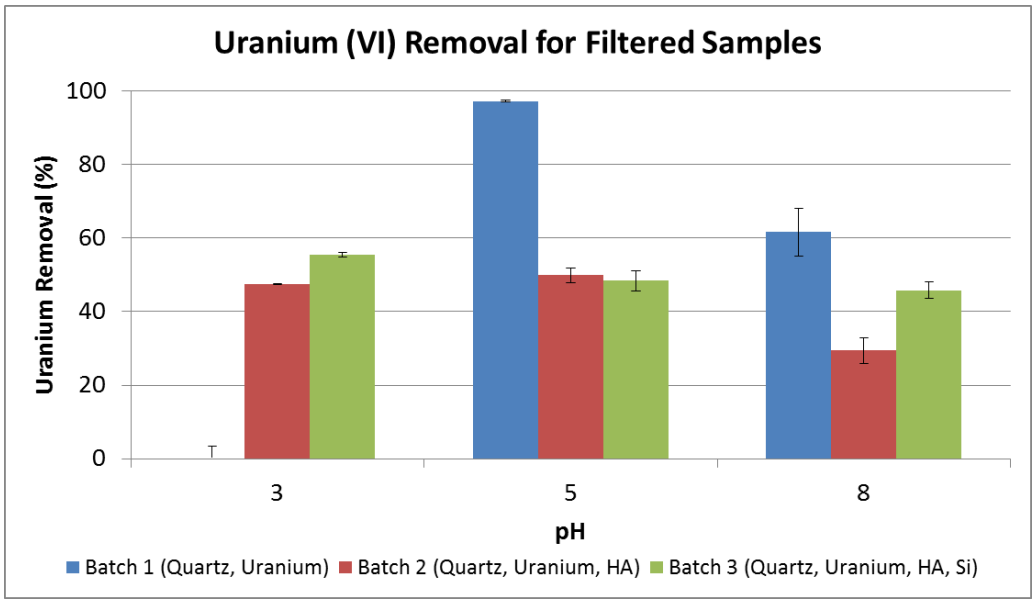


**Figure 63. Uranium removal for unfiltered and filtered samples (quartz, Set #1).**

In the case of kaolinite (set 2) at pH 3, uranium removal for Batch 1 was 60% for unfiltered and filtered samples (Figure 64). The reason for this is that kaolinite has the PZC at pH ≈ 4.0−5.0. Thus, kaolinite surfaces should be net positively charged at pH 3, and this can result in a decrease of uranium removal due to electrostatic repulsion between the kaolinite surface and positively charged U(VI) species. Uranium removal in the presence of humic acid at pH 3 (Batch 2) was observed to be close to 80% for unfiltered and filtered samples. Kaolinite contributes to the sorption of HA. The binding mechanism between humic molecules and hydroxyl groups on the surface of kaolinite is believed to be through ligand exchange, where the $-OH_2^+$ and $-OH$ groups at the surface are exchanged with the anionic groups (carboxyl groups) in humic molecules. Humic acid sorbed to the surface of kaolinite provides additional reactive sites for uranium to bind. Colloidal silica (Batch 3) has little effect on uranium removal when compared to Batch 2 for unfiltered and filtered samples.

At pH 5, uranium removal for Batch 1 increased to 85% for unfiltered and 95% for filtered samples. With an increase in pH, the charge of the kaolinite surface starts to become negative and positive uranium species could interact more with binding sites. In the case of Batch 2, uranium removal was found similar to pH 3. Colloidal silica (Batch 3) has little effect on uranium removal when compared to Batch 2 for unfiltered and filtered samples.

At pH 8, uranium removal for Batch 1 decreased slightly compared to pH 5. Several studies have found that uranyl carbonate species can sorb onto montmorillonite and imogolite surfaces (Catalano and Brown, 2005; Arai et al, 2006). It is believed that similar surface complexes are formed on the kaolinite surface. For Batch 2, uranium removal in the presence of humic acid decreased to less than 60% for unfiltered and 65% for filtered samples. As the pH is increased, fewer $-OH_2^+$ and $-OH$ groups are available for the binding of humic molecules due to deprotonation, which causes a decrease in humic acid sorption. Since less humic acid is sorbed, a fraction of uranium bound to humic acid also remains in the aqueous phase, thus decreasing the efficiency of uranium removal. Colloidal silica showed a similar uranium removal as compared to Batch 2.

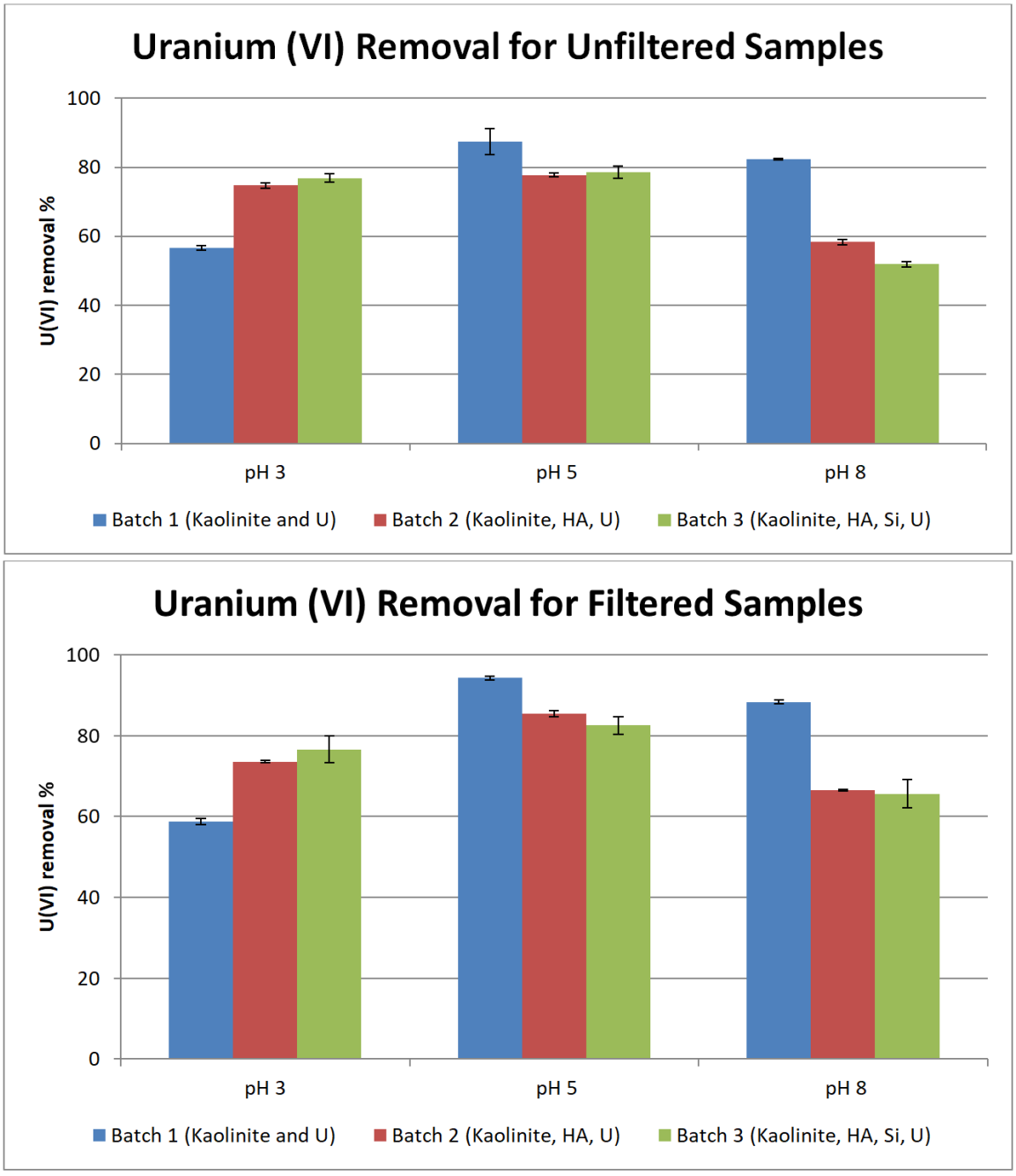


**Figure 64. Uranium removal for unfiltered and filtered samples (kaolinite, Set #2).**

For mixed mineral samples (quartz + kaolinite, set 3), the uranium removal results demonstrated behavior similar to the pure quartz samples. (Figure 65); quartz makes up 95% of the mineral mixture composition. At pH 3, uranium removal for batch 1 is negligible for both filtered and unfiltered samples. This is due to the zero charge of quartz at pH 3 and a net positively charged surface on kaolinite, which decreases the sorption of uranium. For batch 2, close to 40% of uranium was removed in the presence of humic acid. This is attributed to the sorption of humic acid onto the kaolinite and quartz surfaces, which provides additional reactive sites for U(VI) to bind. Very little contribution from colloidal silica was observed when it was added (batch 3). Silanol groups in the silica particle are protonated at low pH and will carry a positive charge while uranium

species are in the form of uranyl cation, carrying a positive charge as well, which cause electrostatic repulsion and hinders uranium removal.

For pH 5, batch 1 (quartz + kaolinite + U (VI)) had about 80% uranium removal for both unfiltered and filtered samples. When compared to quartz, the presence of kaolinite decreased the removal of U(VI). This is probably due to blocking of some reactive sites in quartz by kaolinite. Batch 2 (adding humic acid) demonstrated about 40% uranium removal for unfiltered and 55% for filtered. When colloidal silica was added (batch 3), the sorption was barely effected.

At pH 8, unfiltered and filtered batch 1 samples had approximately 80% uranium removal; this indicates an increase in uranium removal of about 20% compared to quartz samples due to the presence of kaolinite, which allows the sorption of uranyl carbonate species due to the presence of neutral aluminol groups at the kaolinite surface. Addition of humic acid reduced the uranium removed since humic acid is soluble at basic pH and forms aqueous complexes with U(VI).

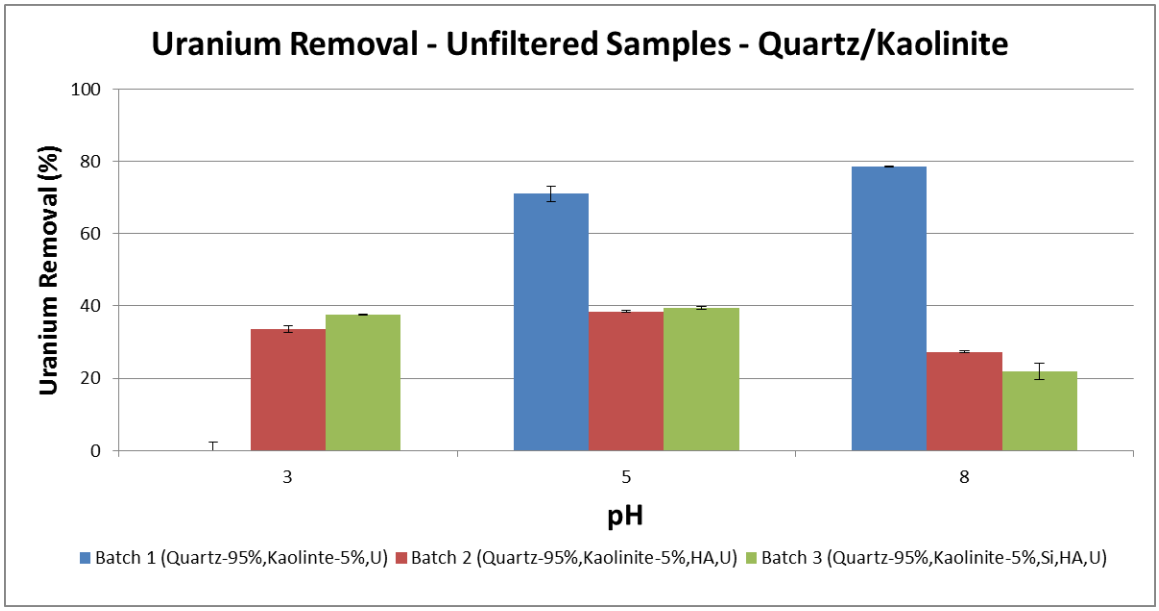

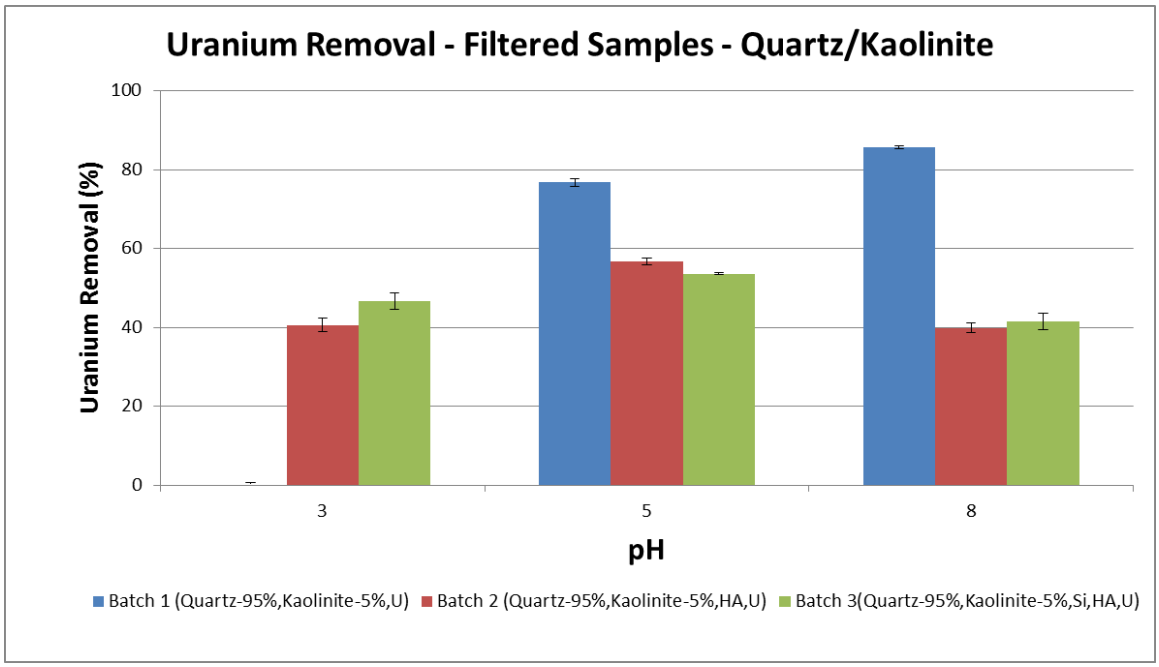


**Figure 65. Uranium removal for unfiltered and filtered samples (quartz and kaolinite, Set #3).**

As shown in Figure 66, goethite slightly aids in the sorption of U (VI) at pH 3; however, it is expected to contribute more at pH > 6. With an increase of pH and in the presence of $CO_2$, U(VI) sorption is enhanced thorough the formation of ternary complexes such as $\equiv FeOCO_2UO_2$ and $(\equiv FeOH)_2UO_2CO_3$ on the goethite surface. At pH 3 for batch 1, uranium removal for unfiltered samples and filtered samples is 25% and 18% respectively. Batch 2 and 3 from pH 3 to pH 8 has similar trends for the unfiltered samples at about 58% uranium removal. When compared to quartz and quartz + kaolinite, it was observed that the mixed minerals quartz + kaolinite + goethite had a higher U(VI) removal. In this case, the presence of goethite enhances the sorption of humic acid, and this contributes to the removal of U(VI) by providing additional binding sites. Figure 6 also shows that colloidal silica in the solution mixture has little contribution on the removal of uranium.

At pH 5, batch 1 had close to 100% uranium removal, with the addition of goethite contributing to higher sorption of uranium at pH > 4. Sherman et al. (2008) suggested that U (VI) sorption is enhanced in the presence of $CO_2$ because of the formation of ternary complexes on the surface of goethite. Batches 2 and 3 still correlated and have no major differences but uranium removal did decrease to about 60%, compared to batch 1 which showed almost 100% removal.

At pH 8, a slight decrease in sorption was observed at 85% uranium removal for batch 1, due to the formation of strong uranyl-carbonate complexes in solution. Batch 2 had sorption of uranium at 50% for unfiltered samples and 60% for filtered samples while batch 3 showed 45% removal for unfiltered samples and 70% for filtered.

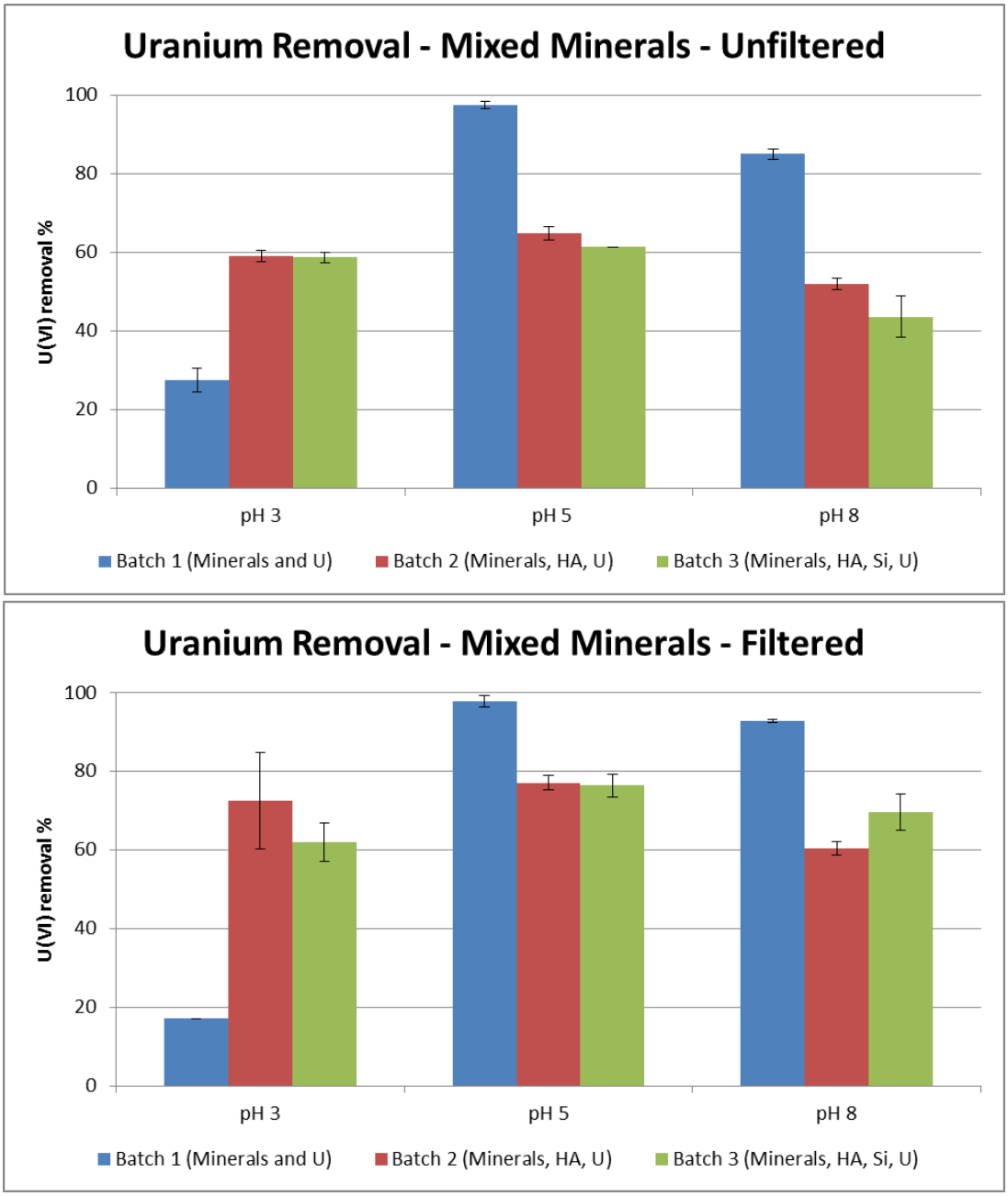


**Figure 66. Uranium removal for unfiltered and filtered samples (quartz, kaolinite, and goethite, Set #4).**

In FIU Performance Year 8, FIU completed experiments to investigate the possible synergy between colloidal silica and humic acid that may have an effect on the removal of uranium from contaminated groundwater.

## Subtask 2.2: Acknowledgements

Funding for this research was provided by U.S. DOE Cooperative Agreement DE-EM0000598. We truly appreciate Dr. Miles Denham and Dr. Brian Looney from SRNL for their valuable input and support of this research. XRD analyses were conducted at FIU AMERI facilities.

## Subtask 2.2: References

Arai, Y.; McBeath, M.; Bargar, J. R.; Joye, J.; Davis, J. A., 2006. Uranyl adsorption and surface speciation at the imogolite-water interface: Self consistent spectroscopic and surface complexation models. *Geochim. Cosmochim. Acta* 70, 2492-2509.

Catalano, J. G.; Brown, Jr., G. E., 2005. Uranyl adsorption onto montmorillonite: Evaluation of binding sites and carbonate complexation. *Geochim. Cosmochim. Acta* 69, 2995-3005.

Chen, C., and X. Wang, 2007. Sorption of Th (IV) to silica as a function of pH, humic/fulvic acid, ionic strength, electrolyte type. *Applied Radiation and Isotopes* 65, 155-163.

Choppin, G.R., 1992. The role of natural organics in radionuclide migration in natural aquifer systems. *Radiochim. Acta* 58/59, 113.

Davis, J.A., 1982. Adsorption of natural dissolved organic matter at the oxide/water interface. *Geochim. Cosmochim. Acta* 46, 2381-2393.

Davis, J.A., 1984. Complexation of trace metals by adsorbed natural organic matter. *Geochim. Cosmochim. Acta* 48, 679-691.

Denham, M., Vangelas, K.M., 2008. Biogeochemical gradients as a framework for understanding waste-site evolution. Remediation. 19, 5-17.

Dong, W; Wang, J. 2014. Additive surface complexation modeling of uranium (VI) adsorption onto quartz-sand dominated sediments. Environ. Sci. Technol, 48, 6569-6577.

Du, L; Li, S; Li, X; Wang, P; Huang, Z; Tan, Z; Liu, C; Liao, J; Liu, N. (2017). Effect of humic acid on uranium(VI) retention and transport through quartz columns with varying pH and anion type. Journal of Environmental Radioactivity, 177, 142-150.

Evans, A.G., Bauer, L.R., Haselow, J.S., Hayes, D.W., Martin, H.L., McDowell, W.L., Pickett, J.B., 1992. Uranium in the Savannah River Site environment. Westinghouse Savannah River Co., Aiken, SC (United States), p. 95.

Ivanov, P., Griffiths, T., Bryan, N.D., Bozhikov, G. and S. Dmitriev, 2012. The effect of humic acid on uranyl sorption onto bentonite at trace uranium levels. *J. Environ. Monit.,* 14, 2968 -2975.

Kenney P. L. Janice, Kirby E. Matthew, Cuadrosb Javier, and Weissa J. (2017). A conceptual model to predict uranium removal from aqueous solutions in water–rock systems associated with low- and intermediate-level radioactive waste disposal. Royal Society of Chemistry.

Kobayashi M., Juillerat F., Galletto P., Bowen P., and Borkovec M., 2005. Aggregation and Charging of Colloidal Silica Particles: Effect of Particle Size, Langmuir, 21 (13), 5761-5769 DOI: 10.1021/la046829z

Koopal, LK, Y. Yang, A.J. Minnaard, P.L.M. Theunissen, W.H. Van Riemsdijk, 1998. Chemical immobilisation of humic acid on silica. Colloids and Surfaces A: Physicochemical and Engineering Aspects 141, 385-395.

Krepelova, A., 2007. Influence of Humic Acid on the Sorption of Uranium(VI) and Americium(III) onto Kaolinite (Dissertation).

Krepelova, A., Brendler, V., Sachs, S., Baumann, N., Bernhard, G., 2007. U(VI)-Kaolinite Surface Complexation in Absence and Presence of Humic Acid Studied by TRLFS. Environ. Sci. Technol. 2007, 41, 6142-6147.

Krestou A., Panias D., 2004, Uranium (VI) speciation diagrams in the $UO_2^{2+}/CO_3^{2-}/H_2O$ system at 25ºC, The European Journal of Mineral Processing and Environmental Protection, Vol.4, No.2, 1303-0868, 2004, pp. 113-129.

Labonne-Wall, N., Moulin, V., Vilarem, J.P., 1997. Retention properties of humic substances onto amorphous silica: consequences for the sorption of cations. *Radiochim. Acta,* 79, 37-49.

Lagos, L., Katsenovich, P., Gudavalli, R., et al., 2014. Rapid Deployment of Engineered Solutions for Environmental Problems at Hanford. Yearend Technical Report, June 30, 2014, U.S. Department of Energy Office of Environmental Management Office of Science and Technology under Grant No. DE-EM0000598.

Perminova, I.V, Hatfield, K., Hertkorn, N., 2002. Use of humic substances to remediate polluted environments: from theory to practice. In the proceedings of the NATO Advance Research Workshop, Springer, P.O Box 17, 3300 AA Dordrech, The Netherland.

Plancque, G., Amekraz, B., Moulin, V., Toulhoat, P., Moulin, C., 2001. Molecular structure of fulvic acids by electrospray with quadrupole time-of-flight mass spectrometry. *Rapid Commun. Mass Spectrom*. 15, 827-835.

Prikryl, J; Jain, A; Turner, D; Pabalan, R. (2001). Uranium$^{VI}$ sorption behavior on silicate mineral mixtures. Journal of Contaminant Hydrology, 47, 241-253.

Sherman, D., Peacock, C. and Hubbard, C. (2008). Surface complexation of U(VI) on goethite (α-FeOOH).

Tipping, E., 2002. Cation Binding by Humic Substances. Vol. 12. Cambridge UP, p. 266.

Wang, X. K.; Dong, W. M.; Dai, X. X.; Wang, A. X.; Du, J. Z.; Tao, Z. Y. 2000, Sorption and desorption of Eu and Yb on alumina: mechanisms and effect of fulvic acid. Appl. Radiat. Isot. 52, 165-173.

Zachara, J.M., Resch, C.T., Smith, S.C., 1994. Influence of humic substances on $Co^{2+}$ sorption by a subsurface mineral separate and its mineralogical components. *Geochim. Cosmochim. Acta* 58, 553-566.

## Subtask 2.3: Humic Acid Batch Sorption and Column Experiments with SRS Soil

## Subtask 2.3: Introduction

Savannah River Site (SRS), located 13 miles south of Aiken in South Carolina, was a defense nuclear processing facility owned by the U.S. government. During the Cold War, from 1953 to 1988, SRS produced a large amount of radioactive and hazardous acidic waste from the production of plutonium and irradiated fuel (Dong, Tokunaga et al. 2012). The acidic waste solutions containing low-level radioactivity from numerous isotopes were discharged into a series of unlined seepage basins in the F/H Area. At that time, it was believed that most of the radionuclides present in the waste solution would bind to the soil, precluding the migration of the radionuclides. However, sufficient quantities of uranium isotopes, $^{129}I$, $^{99}Tc$, and tritium migrated into the groundwater, creating an acidic plume (Denham and Vangelas 2008). For many years, efforts have been made by the Department of Energy to clean up the site and remediate the groundwater. Groundwater contaminated by operation of the F-Area Seepage Basins remains acidic with a pH as low as 3.2 near the basins and increasing downgradient to 5, and has concentrations of uranium

and other radionuclides that exceed the Environmental Protection Agency (EPA) designated Maximum Contaminant Levels (Wan et al., 2011).

Remediation of SRS has been an ongoing effort since the U.S. nuclear program was established. Techniques such as the pump-and-treat and the funnel and gate system have been applied; however, the pH remains acidic with radionuclide concentrations that remain above the allotted maximum contaminant level (MCL). In an effort to remove the contaminants from the groundwater, pump-and-treat and re-inject systems were implemented in 1997. Down gradient contaminated groundwater was pumped to a water treatment facility, treated to remove metals (through osmosis, precipitation/flocculation, and ion exchange), and then re-injected up gradient within the aquifer. The pump-and-treat water treatment unit eventually became less effective, generated large amounts of radioactive waste and was expensive to maintain, prompting research for new remedial alternatives. In 2004, the pump-and treat system was replaced by a funnel and gate system in order to create a treatment zone via injection of a solution mixture composed of two components, sodium hydroxide and carbonate. The injections were done directly into the gates of the F-Area groundwater to raise pH levels. Treatment zone were implemented to reverse the acidic nature of the contaminated sediments by creating a more negative net charge on the surface of sediment particles and enhancing adsorption of cationic contaminants. To raise the pH to near neutral values, a systematic re-injection of the base was required. However, the continuous use of high concentrations of a carbonate solution to raise pH creates a concern of possible re-mobilization of uranium that was previously adsorbed within the treatment zone since U (VI) in the presence of bicarbonate ions forms soluble aqueous uranyl-carbonate complexes.

In search of a solution, Savannah River National Laboratory (SRNL) has been experimenting with humic substances. Humic substances (HS) occur naturally in soil, water, and sediment of the ecosystem by biochemical and chemical reactions during decay and transformation of plant and microbial remains. Along with being abundant (50-80%) in soil and sediment, humic substances also have a significant complexing capacity with metals. Three main fractions of HS are identified based on their solubility in dilute acids and bases. Their size, molecular weight, elemental composition, structure, and the number and position of functional groups vary.

> ***Humic acids:*** the fraction of humic substances that is not soluble in water under acidic conditions (pH < 2) but is soluble at higher pH values. They can be extracted from soil by various reagents, which are insoluble in dilute acid. Humic acids are the major extractable component of soil humic substances. They are dark brown to black in color.
>
> ***Fulvic acids:*** the fraction of humic substances that is soluble in water under all pH conditions. They remain in solution after removal of humic acid by acidification. Fulvic acids are light yellow to yellow-brown in color.
>
> ***Humin:*** the fraction of humic substances that is not soluble in water at any pH value or in alkali. Humin is black in color.

A blended material, humate (HA), contains both humic and fulvic acids. Humate is the initial/raw product of an alkaline extraction of natural materials that are rich in organic matter. Based on desirable properties, various humate materials, specifically raw potassium humate (referred as Huma-K in this report) and a chemically modified humate (KW15 modified humics or Mod-HA) are being tested for remediation purposes to reduce the mobility of uranium (VI) and other radionuclides in the subsurface at SRS. Injecting humate into the contaminated plumes augment sorption of uranium, sr-90, I-129 by increasing ion exchange and increasing/stabilizing pH.

Florida International University's (FIU) Applied Research Center (ARC) assists SRNL in research by conducting flow through column experiments to investigate sorption/desorption properties of humic acid along with its correlation to the mobility of uranium through humic acid sorbed sediment. Modeling the effect of sorbed HA on the mobility of uranium administers Mod-HA and Huma-K as remediation technology that can be used for employment on DOE sites. Three tests were conducted per HA of interest (Mod-HA and Huma-K): 1) a rhenium tracer test, which set parameters, 2) a humate injection test, and 2) uranium injection through humate loaded sediment. This research is also determine if the low cost unrefined humate solution known as Huma-K can be used to facilitate uranium adsorption to control the mobility of uranium in acidic groundwater. Huma-K is an organic fertilizer used by farmers to stimulate plant growth and facilitate nutrient uptake. It is a water soluble potassium salt of humic and fulvic acids that comes from the alkaline extraction of leonardite (a low-rank coal). Leonardite has a very high content of humic substances due to decomposition by microorganisms. Also, compared to other sources of humic substances, Leonardite has a higher humic/fulvic acid content. The extraction of humic/fulvic acid from Leonardite is performed in water with the addition of potassium hydroxide (KOH), and the resulting liquid is freeze-dried to produce the amorphous crystalline black powder/shiny flakes as seen in Figure 67

**Figure 67. Huma-K**

## Subtask 2.3: Methodology

### 1. Batch Experiments

### Sorption Experiment of Uranium onto SRS Sediment with and without Huma-K Amendment

Huma-K (Land and Sea Organics), a commercially available humic material extracted from Leonardite, was used in these experiments. Clean SRS sediment used in the sorption experiments (field borehole sampling FAW-1, depth interval 70-90 ft) was collected from the aquifer near the F-Area seepage basins. This particular background sediment was selected because of similarities in mineral composition with the uranium contaminated aquifer sediment. The SRS sediment was sieved (U.S. Standard Testing Sieves, Fisher Scientific), and the sediment fraction with diameter $\leq$ 2 mm was retained and used throughout the experiments. For comparison, reference quartz (Ottawa Sand Standard 20-30 mesh, Fisher Scientific), kaolinite (Alfa Aesar), and goethite (Alfa Aesar) were used as reference minerals.

For the sorption experiments, a Huma-K stock solution of 1000 mg $L^{-1}$ was prepared by dissolving 1000 mg of Huma-K in 1 L of deionized (DI) water (Barnstead Nanopure Diamond Water Purification System, resistivity $\geq$ 18 MΩ·cm). A commercial 1000 mg $L^{-1}$ uranyl nitrate stock

solution in 2% nitric acid (Fisher Scientific) was used as a source of U(VI). All batch experiments were conducted in triplicate under normal atmospheric conditions ($P_{CO2} = 10^{-3.5}$ atm and 25°C).

In the first step, SRS sediment amended with Huma-K was prepared by bringing the sediment into contact with a Huma-K solution (Figure 68). The batch sorption experiments were conducted with 20 mL of aqueous suspension in DI water using 50 mL polypropylene centrifuge tubes, containing 200 mg of SRS sediment (10 g $L^{-1}$) spiked with a fixed concentration of Huma-K (20 mg $L^{-1}$) at constant ionic strength (I = 0.01 M $NaClO_4$) at pH 4. The samples were mixed with a vortex mixer (Maxi Mix Plus, Barnstead Thermolyne) for 30 sec and then rotated for 5 days on a platform shaker at 100 rpm (New Brunswick Scientific Innova 2000) to ensure thorough fluid-mineral contact throughout the sorption period (Figure 70). All samples were centrifuged for 30 min at 2700 rpm (Thermo Scientific Sorvall ST 16R centrifuge), and the supernatant was withdrawn (Figure 69).

In the second step, the samples containing 200 mg of sediment (with and without Huma-K amendment) were brought into contact with a 20-mL solution of DI water (I = 0.01 M $NaClO_4$) spiked with an initial U(VI) concentration specified below. The samples were vortex mixed, placed on a platform shaker, and centrifuged in a similar procedure as described above. Aqueous U(VI) concentration was measured by kinetic phosphorescence analyzer (KPA-11, Chemchek) (Figure 71). For the kinetic studies, an initial U(VI) concentration of 0.5 mg $L^{-1}$ was allowed to equilibrate with the sediment for different time periods at pH 4. For the equilibrium studies, the initial U(VI) concentration ranged from 0.025 to 1 mg $L^{-1}$, and the samples were reacted at pH 4 for a period of 7 days (based on the kinetic study). The effect of pH on U(VI) sorption onto sediment was studied at a pH range of 3-8 for 7 days and an initial U(VI) concentration of 0.5 mg $L^{-1}$. The pH was adjusted with 0.1 M HCl or 0.1 M NaOH during the reaction period.

**Figure 68. Sample with SRS sediment.**

**Figure 69. Centrifugation**

**Figure 70. Shaker table with samples**


**Figure 71. Kinetic phosphorescence analyzer**

**Desorption Experiment of Uranium from SRS Sediment with and without Huma-K Amendment**

Batch desorption experiments were conducted at a range of pH values (3-8). First, the sorption of U(VI) onto SRS sediment with and without Huma-K amendment at pH 4 was done in a similar procedure as described in section 3.2.2. At the end of the sorption procedure, U(VI) desorption was carried out by replacing the supernatant with an equal volume of DI water at different pH values (3-8) and constant ionic strength (I = 0.01 M $NaClO_4$). The pH was monitored daily and adjusted with 0.1 M HCl or 0.1 M NaOH. The samples were rotated for 7 days and centrifuged as previously described, and the desorbed U(VI) concentration in the aqueous phase was determined.

## 2. Flow Through Column Experiments

### a. Sediment Characterization

Sediment previously obtained from SRS and characterized by FIU during 2014 was used in the experiments. The sediment was obtained from FAW-1 at a depth of 60'-70'. The sediment was disaggregated with minimal force to avoid creating new mineral surfaces due to fracturing and abrasion using a 2-mm sieve to collect sediment of particle size ≤2 mm.

### b. Column Experiments

Glass columns (25 mm x 300 mm) obtained from Ace Glass Inc. were used to conduct the flow-through column experiment to study the sorption/desorption of humate onto SRS sediment and to study the mobility of uranium through humate sorbed sediment. The columns, fitted with Teflon® adapters containing 350 micron screen support and a layer of glass wool (Figure 72), was filled with a known mass of oven-dried sediment obtained from SRS (Figure 73).

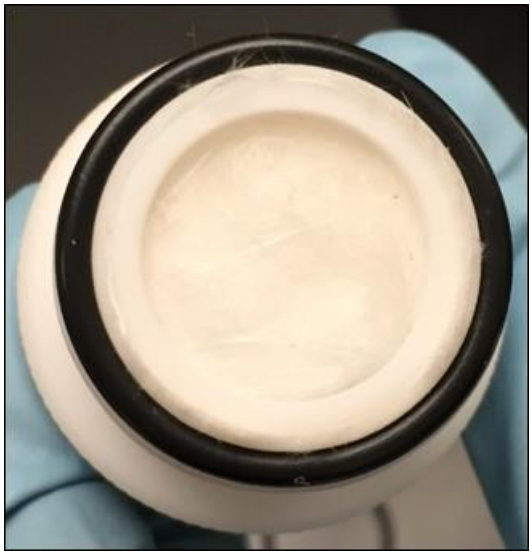

**Figure 72. Teflon ® adapter with layer of glass wool.**

**Figure 73. Column with SRS sediment post DIW saturation.**

### c. Column Tracer Test

A rhenium tracer test was performed to obtain transport parameters. The columns were first saturated with deionized water (DIW) from the bottom of the column to the top in order to remove air bubbles. The flow of DIW was continued until an effluent flow rate of 2.0 ml/min was achieved. After flow was equilibrated, 2.93 ml of a 250 ppm rhenium solution was injected from the base of the column. Samples of the effluent were collected in pre-weighed containers at regular intervals. After each interval, the sample containers were re-weighed and the rhenium concentration was analyzed using ICP-OES. Samples were collected until all of the rhenium was recovered. The data collected was used to determine the mean residence time, the pore volume, and the peclet number. The residence distribution function, E(v), as a function of volume fractions (Levenspiel, 1972) was calculated using Eq. 2:

$$E(v) = \frac{C(v)}{\int_0^\infty C(v)\,dv} \qquad \text{Eq. (2)}$$

Where:
v - Volume of effluent
C(v) - Concentration of rhenium

The mean residence time ($t_m$), and pore volume ($V_p$) (Shook et al., 2005) were estimated using Eq. 3 and Eq. 4:

$$t_m = \frac{\int_0^\infty t\,E(t)\,dt}{\int_0^\infty E(t)\,dt} = \int_0^\infty t\,E(t)dt \qquad \text{Eq. (3)}$$

$$V_p = \frac{\int_0^\infty v\,E(v)\,dv}{\int_0^\infty E(v)\,dv} = \int_0^\infty v\,E(v)dv \qquad \text{Eq. (4)}$$

Where:
t - Time
E(t) - Residence distribution function in terms of time
v - Volume of effluent
E(v) - Residence distribution function in terms of volume

Variance and the dimensionless Peclet number ($P_e$), which represents the ratio of the rate of transport by convection to the rate of transport by diffusion or dispersion, were determined by solving the 1D dispersion/advection equation (Bischoff et al., 1963; Fogler et al., 1992; Mibus et al., 2007):

$$Variance\ (\sigma^2) = \int_0^\infty (v - v_p)^2\ E(v)\,dv \qquad \text{Eq. (5)}$$

$$\frac{\sigma^2}{t_m^2} = \frac{2}{P_e^2}\left(P_e - 1 + e^{-P_e}\right) \qquad \text{Eq. (6)}$$

Where:
v - Volume of effluent
$v_p$ - Pore volume
E (v) - Residence distribution function in terms of volume

### d. Sorption/Desorption of Humate

After the tracer test, the column was preconditioned using pH adjusted artificial groundwater (AGW). Artificial groundwater that mimics SRS groundwater characteristics was prepared according to Strom and Kabak (Strom & Kaback, 1992) by dissolving 5.4771 g $CaCl_2$, 1.0727 g $Na_2SO_4$, 3.0943 g $MgCl_2$, 0.3997 g KCl, and 2.6528 g NaCl in 1 L of deionized water (Barnstead NANOpure water purification system). 0.84995 g $NaNO_3$ was dissolved to obtain a 0.01M $NaNO_3$ solution. One (1) mL of the stock solution was diluted into 1 L of deionized water acidified to the desired pH to create a working solution. AGW pH adjusted to 3.5 was pumped from the bottom of the column until the pH of the effluent solution reached equilibrium (approximately pH 3.5). Once the pH of the effluent reached equilibrium, approximately 1/2 pore volume (PV) of 10,000 ppm humic acid solution was injected at an effective flow rate of 2 mL/min. Following the humic acid solution, AGW solution adjusted to pH 3.5 was injected into the column until the effluent concentration reached approximately 2% of the initial concentration; effluent samples were collected to measure the change in pH and concentration of humic acid. The concentration of humic acid in the effluent was measured immediately after collecting the sample to ensure the desired end point of the desorption phase was achieved. Samples were analyzed using a Thermo Scientific Genesys 10S UV-Vis Spectrophotometer. Figure 74 and Figure 75 shows the calibration curves developed at wavelength 254 nm of Mod-HA and Huma-K respectively.

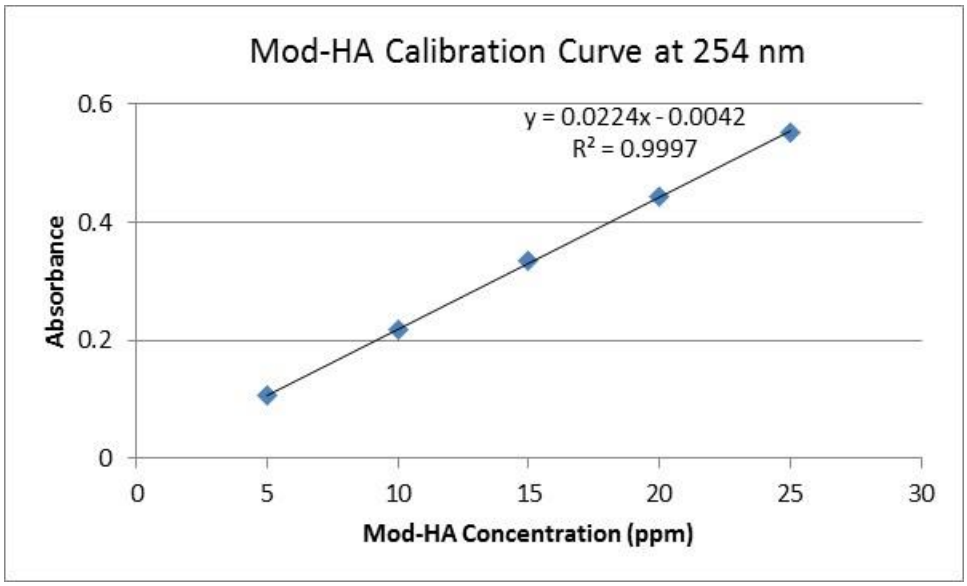


**Figure 74. Mod-HA calibration curve**

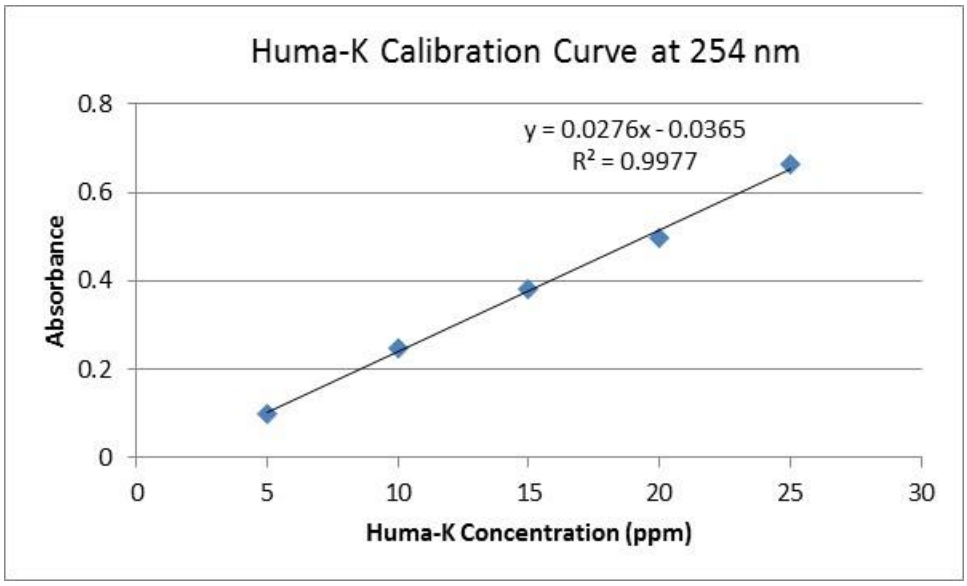


**Figure 75. Huma-K calibration curve**

e. **Sorption of Uranium**

After sorption and desorption of humic acid, uranium sorption was studied using the control, Mod-HA, and the Huma-K column. 500 ppb uranium solution prepared with AGW at pH 3.5 was injected until the effluent concentration was half of the initial concentration ($C/C_0 = 0.5$). Using columns containing humic acid sorbed sediment facilitated the investigation of the effect humic acid has on the mobility of uranium. Effluent samples were collected 4 and 7 min intervals then analyzed to determine the uranium concentration present in the effluent. The collected samples were analyzed via KPA to measure the concentration of uranium.

## Subtask 2.3: Results and Discussion

### Kinetic Studies of Uranium Sorption onto SRS Sediment with and without Huma-K Amendment

Kinetics experiments were conducted using SRS sediment with and without Huma-K amendment (Figure 76). The sorption of U(VI) onto SRS sediment in the absence of Huma-K was characterized by a fast initial uptake, reaching equilibrium within 8 hours (0.33 days). This behavior is typical of many metal-mineral systems, in which the rapid initial sorption step is associated with reaction-controlled sorption. Then, it follows a slower sorption step attributed to diffusion-controlled sorption, sorption on sites of low reactivity, and surface precipitation (Bruemmer, Gerth et al. 1988, Scheinost, Abend et al. 2001). For SRS sediment amended with Huma-K, a much slower U(VI) sorption was observed, reaching equilibrium within 7 days. The slow U(VI) sorption could be attributed to the formation of a surface coating on sediment by Huma-K, which might act as a diffusional barrier to active binding sites. The sorbed Huma-K alters the characteristics of the SRS sediment particles. On the other hand, the removal of U(VI) by Huma-K was higher (30.5 mg $kg^{-1}$) compared to plain sediment (4.6 mg $kg^{-1}$).

The experimental data were evaluated on the basis of various nonlinear kinetic models including pseudo-first (Eq. 7) and pseudo-second (Eq. 8) order models. The results from the nonlinear kinetic models for SRS sediment with and without Huma-K amendment showed that neither pseudo-first

nor pseudo-second order models were able to provide a good fit with the experimental data (Figure 77). This is because of the kinetic models being developed to describe binary systems (one sorbing compound and one sorbent). In this study, the system is more complex, consisting of a mixture of different minerals in the SRS sediment and different organic compounds in the Huma-K. For that reason, the kinetic models were not able to provide a good fit with the experimental data.

$$F = \frac{q_t}{q_e} = 1 - e^{-k_1 t} \quad [7]$$

$$F = \frac{q_t}{q_e} = \frac{k_2^* t}{1 + k_2^* t} \quad [8]$$

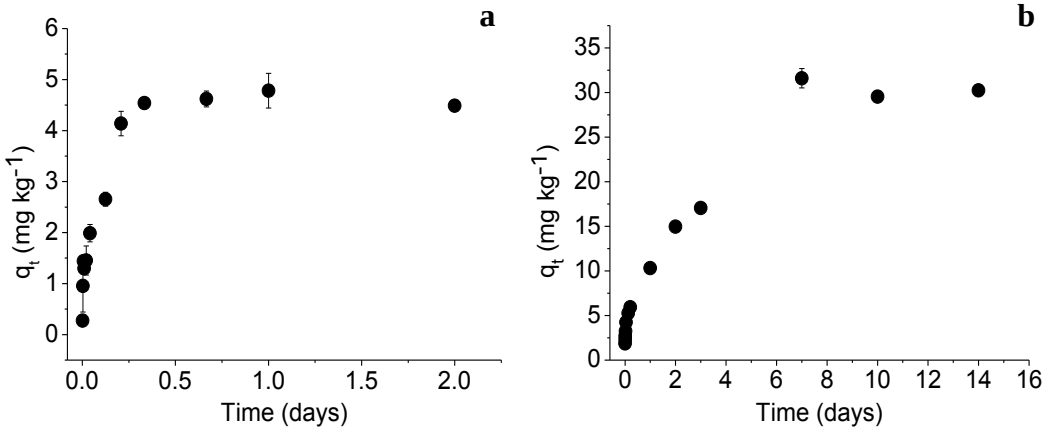


**Figure 76. Kinetic study of U(VI) ($C_i$ = 0.5 mg L$^{-1}$) sorption on (a) SRS sediment and (b) SRS sediment amended with Huma-K (10 g L$^{-1}$ of sediment, pH 4, I = 0.01 M $NaClO_4$, and T = 25°C).**

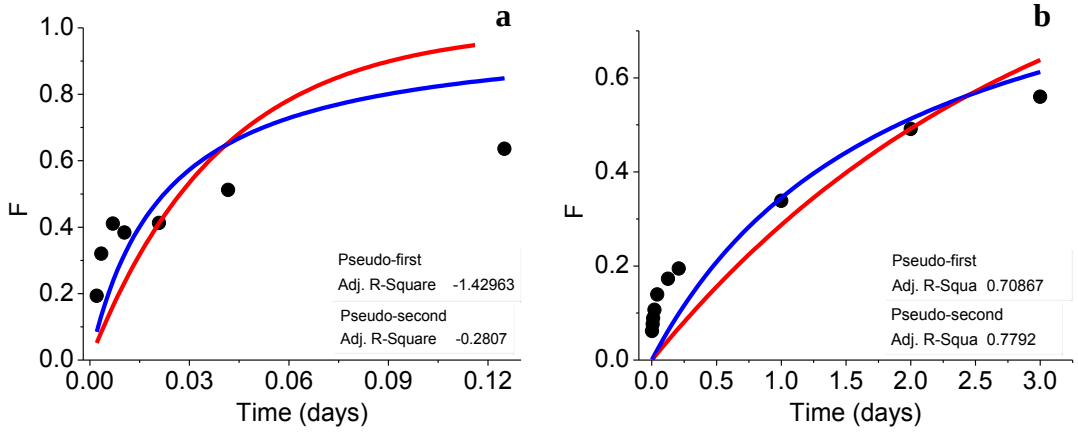


**Figure 77. Non-linear fit of F data for (a) SRS sediment (t ≤ 0.125 days) and (b) SRS sediment amended with Huma-K (t ≤ 3 days). Circle points = experimental data; red line = results of fit with pseudo-first order; blue line = result of fit with pseudo-second order.**

## Equilibrium Studies of Uranium Sorption onto SRS Sediment with and without Huma-K Amendment

Equilibrium studies of U(VI) sorption onto SRS sediment with and without Huma-K amendment were investigated to determine the sorption capacity for both systems in acidic conditions (Figure 78). The experimental data showed that SRS sediment amended with Huma-K (39.2 mg $kg^{-1}$) has a significantly higher sorption capacity compared to plain sediments (3.76 mg $kg^{-1}$) for the range of U(VI) concentrations studied. The increased sorption capacity in sediments amended with Huma-K could be attributed to the presence of carboxyl and phenolic OH groups, which are considered to be mainly responsible for the complexation of U(VI) (Pompe, Schmeide et al. 2000, Kremleva, Krüger et al. 2009). Complexation of humic substances with U(VI) can occur in monodentate, bidentate, and chelate form (Sundararajan, Rajaraman et al. 2011). Extended X-ray absorption fine structure (EXAFS) spectroscopy studies have shown that the complexation between uranyl ions and the carboxyl groups of humic acid occurs in a monodentate fashion at low pH (Denecke, Pompe et al. 1997, Schmeide, Sachs et al. 2003). On the other hand, the low sorption capacity of plain sediment is attributed to a low abundance of binding sites available in acidic conditions.

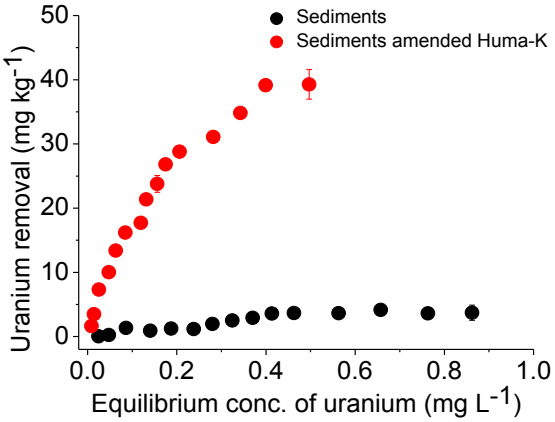


**Figure 78. Sorption isotherm of U(VI) ($C_i$ = 0.025 – 1 mg $L^{-1}$) on SRS sediment with and without Huma-K amendment for 7 days (10 g $L^{-1}$ of sediment, pH 4, I = 0.01 M $NaClO_4$, and T = 25°C).**

In order to describe the sorption equilibrium, the Langmuir and Freundlich sorption isotherm models were applied. The Langmuir isotherm was proposed by Langmuir (1918). The assumptions of the Langmuir model are: monolayer sorption, uniform sorption across the surface, finite sorption sites, and no interactions between already sorbed molecules. This means that once all the sorption sites have been occupied, sorption ceases. The nonlinear form (Eq. 9) of the Langmuir model is expressed as:

$$q_e = \frac{q_m K_L C_e}{1+K_L C_e} \quad [9]$$

The Freundlich isotherm model was proposed by Freundlich (1906), and it is usually considered as an empirical equation that describes both multilayer and heterogeneous sorption. The nonlinear form (Eq. 10) is expressed as:

$$q_e = K_F C_e^{1/n} \quad [10]$$

For SRS sediment, the Langmuir and Freundlich nonlinear models were not able to describe the sorption process of U(VI) (Figure 10a). This is attributed to the fact that sediments are

intrinsically heterogeneous, having a composition of different minerals such as quartz, kaolinite and goethite. In the case of SRS sediment amended with Huma-K, the Langmuir model better described the sorption of U(VI) compared to the Freundlich model (Figure 79b). This indicates that U(VI) might be interacting with a single class of binding sites (e.g., carboxyl groups), resulting in the good fit with the Langmuir model. Once all the binding sites in Huma-K are occupied, no further sorption should take place.

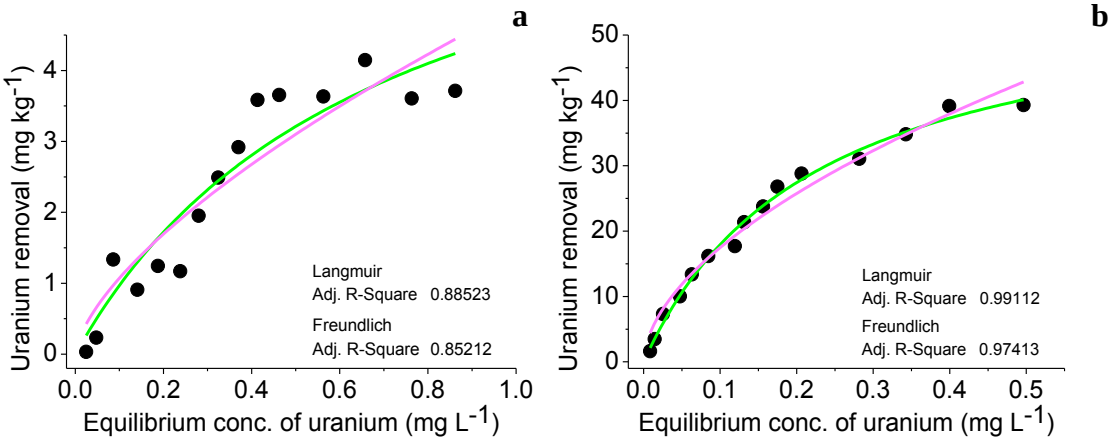


**Figure 79. Non-linear fit adsorption isotherm for (a) SRS sediment and (b) SRS sediment amended with Huma-K. Circle points = experimental data; green line = results of fit with Langmuir model; magenta line = result of fit with Freundlich model.**

## Effect of pH on Uranium Sorption on SRS Sediment with and without Huma-K Amendment

The interactions between U(VI) and SRS sediment with and without Huma-K amendment was investigated as a function of pH (Figure 80). In the case of U(VI) sorption onto SRS sediment, a three pH-dependent region can be distinguished. For pH ≤ 4, the sorption of U(VI) was very low (~10%). At low pH, there is a competition between $H^+$ and $UO_2^{2+}$ for the binding sites, thus limiting the sorption of U(VI). For 4 ≤ pH ≤ 7, the sorption of U(VI) increased up to ~88%. This indicates an increase in the chemical affinity between U(VI) species and SRS sediment. For pH > 7.5, the sorption of U(VI) seemed to start to decrease. In this region, carbonate ions compete for the complexation with U(VI) in solution, hindering its sorption.

SRS sediment amended with Huma-K showed a strong influence in the sorption of U(VI), and a three pH-dependent region could be distinguished (Figure 80). For 3 ≤ pH ≤ 5, U(VI) sorption increased from 26% up to ~74%. When compared to plain sediment, the sediment amended with Huma-K showed a higher U(VI) sorption capacity. One could think that the amendment of SRS sediment with Huma-K would block the binding sites at the sediment surface, causing a reduction in U(VI) sorption. However, the number of binding sites that may have been lost at the sediment surface from the amendment are overcompensated by the additional binding sites from the Huma-K. In this pH region, several studies have identified the formation of the binary complex between U(VI) and humic acid (HA) (Eq. 11) (Pashalidis and Buckau 2007, Steudtner, Müller et al. 2011). For 5 ≤ pH ≤ 7, the sorption of U(VI) remained relatively the same (~70%). In this region, the ternary complexes between U(VI) with humic acid and inorganic ligands such as $OH^-$ start to form (Eq. 12). Above pH 7, U(VI) sorption started to decrease. In this pH region, carbonate species compete with humic molecules for the complexation of U(VI). According to Steudtner,

Sachs et al. (2011) ternary carbonato humate complexes can also form (Eq. 13). However, the ternary carbonato humate complexes might form slowly because of the direct interaction between negative charged species, resulting in electrostatic repulsion (Efstathiou and Pashalidis 2017).

$$UO_2^{2+} + HA \rightleftarrows UO_2HA \qquad \log \beta = 6.2 \text{ l mol}^{-1} \qquad [11]$$

$$UO_2OH^{+} + HA \rightleftarrows UO_2(OH)HA \qquad \log \beta = 6.94 \text{ l mol}^{-1} \qquad [12]$$

$$UO_2(CO_3)_3^{4-} + HA \rightleftarrows UO_2(CO_3)_2HA^{4-} + CO_3^{2-} \qquad \log \beta = 2.83 \text{ l mol}^{-1} \qquad [13]$$

Aliquots of the supernatant of the samples containing SRS sediment with Huma-K amendment were filtered using a 0.45 µm PTFE filter. It was found that filtration increased the removal of U(VI) for the range of pH studied (Figure 80). This indicates that there is a fraction of humic molecules either in the colloidal form or associated with colloidal mineral particles that was desorbed, and it is forming aqueous complexes with U(VI). With an increase of pH, humic molecules become more ionized, and this enhances the desorption of humic molecules from sediments.

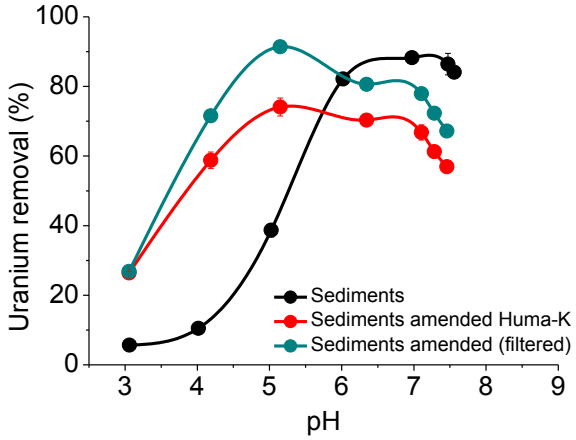


**Figure 80. Percent removal of U(VI) ($C_i$ = 0.5 mg $L^{-1}$) from the aqueous phase as a function of pH (10 g $L^{-1}$ of sediment, 7 days, I = 0.01 M $NaClO_4$, and T = 25°C).**

## Comparison of Uranium Sorption onto Quartz, Kaolinite, Goethite, and SRS Sediment

SRS sediment is composed of quartz (93.2%), kaolinite (5.1%), and goethite (1.1%). Therefore, the sorption of U(VI) onto SRS sediment was compared with reference minerals (Figure 81a). For quartz, the sorption of U(VI) was low at pH $\leq$ 4 (~10%). Since silanol groups (≡ SiOH) at the quartz surface are going to be protonated (p$K$ = 4), outer-sphere complexation should be favored. With an increase of pH, there was a sharp increase in the sorption of U(VI). The deprotonation of the silanol groups at the quartz surface and the formation of aqueous U(VI) hydroxyl complexes contribute to the formation of surface complexes between quartz and U(VI) (Prikryl, Jain et al. 2001). Above pH 6, a significant decline in the sorption of U(VI) was observed. The formation of uranium-carbonate complexes can suppress the sorption onto quartz because of electrostatic repulsion between negatively charged species.

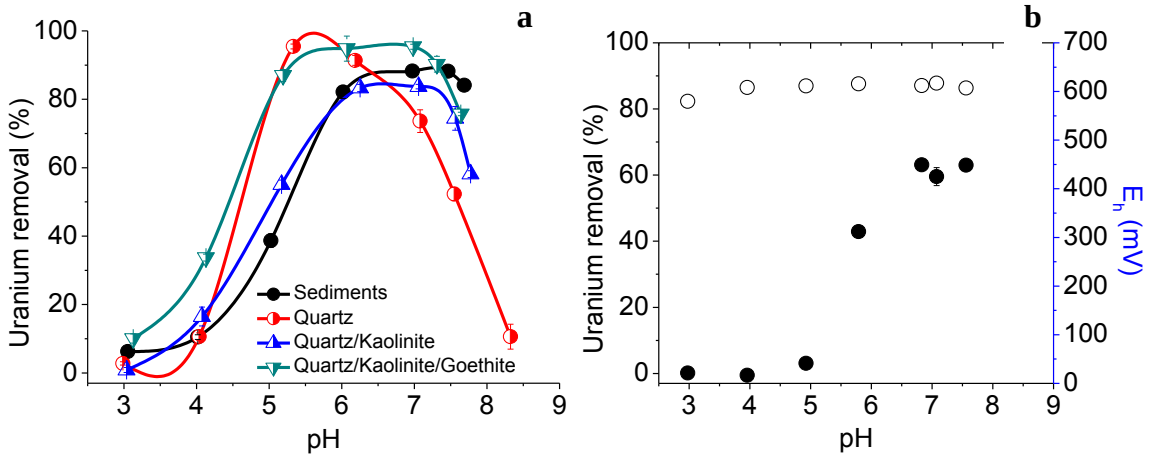


**Figure 81. (a) Comparison of U(VI) ($C_i$ = 0.5 mg $L^{-1}$) removal for SRS sediment, quartz (100%), quartz/kaolinite (95%:5%), quartz/kaolinite/goethite (94%:5%:1%). (b) Control samples with no sediment (closed circles) and Eh (open circles). (7 days, I = 0.01 M $NaClO_4$, and T = 25°C).**

When compared to SRS sediment, quartz did not follow the same pH-dependent trend on U(VI) removal. This indicates that other minerals might be contributing to the removal of U(VI) in the range of pH studied.

Gabriel, Charlet et al. (2001) investigated the sorption of U(VI) onto amorphous silica by laser-induced time-resolved fluorescence spectroscopy. The study distinguished three surface complexes: $\equiv SiO_2UO_2$, $\equiv SiO_2UO_2OH^-$, and $\equiv SiO_2UO_2OHCO_3^{3-}$ dominating at pH 5, 7.7, and 8.6, respectively (Eq. 14-16). It is suggested that similar surface complexes might form at the surface of quartz. In addition, molecular dynamic studies have been carried out to describe the interactions between uranium and quartz. The studies suggest the formation of an outer-sphere surface complexation characterized by hydrogen bonding between a coordinated water molecule from $UO_2^{2+}$ ion and the protonated surface of quartz. For a partially deprotonated quartz surface, the $UO_2^{2+}$ ion forms an inner-sphere complex involving one or two surface oxygen atoms. In the presence of carbonate ions, an inner-sphere surface complex is formed only when one carbonate ion is coordinated to $UO_2^{2+}$. On the other hand, the dicarbonato complex $(UO_2(H_2O)(CO_3)_2)^{2-}$ is only found to form hydrogen bonding with the surface (Greathouse, O'Brien et al. 2002).

$$\equiv Si(OH)_2 + UO_2^{2+} \rightleftarrows \equiv SiO_2UO_2 + 2H^+ \quad [14]$$

$$\equiv Si(OH)_2 + UO_2^{2+} + H_2O \rightleftarrows \equiv SiO_2UO_2OH^- + 3H^+ \quad [15]$$

$$\equiv Si(OH)_2 + UO_2^{2+} + H_2CO_3 + H_2O \rightleftarrows \equiv SiO_2UO_2OHCO_3^{3-} + 5H^+ \quad [16]$$

For the mix quartz/kaolinite, the U(VI) sorption was also low at pH ≤ 4 as in the case of quartz. Silanol groups from the quartz surface contribute only to negative charges, so sorption of $UO_2^{2+}$ through electrostatic attraction should be favorable to the silanol surface sites. Kaolinite possesses both silanol ($\equiv SiOH$) and aluminol ($\equiv AlOH_2OH$) groups with p*K* values of 6.9 and 5.7, respectively (Liu, Lu et al. 2013). It is suggested that protonated aluminol groups ($\equiv AlOH_2^+$) should not contribute to $UO_2^{2+}$ sorption because of electrostatic repulsion. With an increase of pH, the sorption of U(VI) increased, reaching a saturation at pH ~ 6. The formation of U(VI) hydrolyze species and the deprotonation of both silanol and aluminol surface functional groups facilitates the sorption of U(VI). Above pH 7, U(VI) sorption started to decline. The formation of negatively charged uranyl-carbonate species decreases the U(VI) onto the negatively charged

surface of kaolinite. When compared to SRS sediment, the quartz/kaolinite mix followed a very similar pH-dependent trend for U(VI) removal. Above pH 6, there is a slight difference in U(VI) for both systems, probably caused by the presence of goethite in SRS sediment.

Kremleva et al. (2008) studied the U(VI) sorption on the surface of kaolinite by using density functional calculations, and the study found that $UO_2^{2+}$ sorption is thermodynamically favored at the $Al(O,OH)_6$ octahedral surface and unfavorable at the $Si(O,OH)_4$ tetrahedral surface (Kremleva, Krüger et al. 2008). Martorell et al. (2010) suggested two possible binding sites where $UO_2^{2+}$ ions can form surface complexes on kaolinite. The first site is composed of two surface oxygen atoms connected to one Al atom (AlOO) designated short-bridge site. The second site consists of two surface oxygen atoms attached to two neighboring Al atoms (AlO–AlO) designated long-bridge site. The study concluded that the sorption to a short-bridge site requires less energy than a long-bridge site, so $UO_2^{2+}$ ions prefer to sorb at the short bridge site (Martorell, Kremleva et al. 2010). In the presence of carbonate species, uranyl carbonate surface complexes are unfavorable at the surface of kaolinite because of steric hindrance caused by the carbonate ions (Kerisit and Liu 2014).

For the mix quartz/kaolinite/goethite mix, the sorption of U(VI) followed a similar pH-dependent trend compared to SRS sediment. However, the sorption of U(VI) for the quartz/kaolinite/goethite mix was higher. With an increase of pH, the sorption of U(VI) increased and reached a maximum at pH ~6 in spite of the fact that both uranyl species and the surface of goethite are positively charged. Goethite has a pzc of ~8–9.5, so the surface charge remains positive in the range of pH studied. Above pH 7, the sorption of U(VI) started to decline.

Sherman et al. (2008) investigated the interactions between U(VI) and goethite using extended X-ray absorption fine structure spectroscopy. The study postulated three surface complexes: $(\equiv FeOH)_2UO_2(H_2O)_3$, $\equiv FeOCO_2UO_2$, and $(\equiv FeOH)_2UO_2CO_3$. At low pH and in the absence of $CO_2$, the specie that tends to dominate is the surface bidentate complex $(\equiv FeOH)_2UO_2(H_2O)_3$. At higher pH, the presence of $CO_2$ enhances the sorption of $UO_2^{2+}$ either through sorption of $CO_3^{2-}$ on the surface or the formation of ternary complexes $\equiv FeOCO_2UO_2$ and $(\equiv FeOH)_2UO_2CO_3$ (Sherman, Peacock et al. 2008).

Taking into consideration the contributions of quartz, kaolinite, and goethite to U(VI) removal, it becomes clear that these minerals enhance the U(VI) removal much more in the circumneutral pH compared to SRS sediment amended with Huma-K.

In Figure 82, it is shown the concentration of ions that were dissolved from SRS sediment during the course of the experiment. Dissolved Al was detected at pH < 4 and at pH > 6. The presence of Al might decrease the sorption of U(VI) through binding competition. Dissolved silica was observed to occur at pH > 6. However, the effects of Si on U(VI) sorption are still not well understood. Dissolved Fe was not detected in solution.

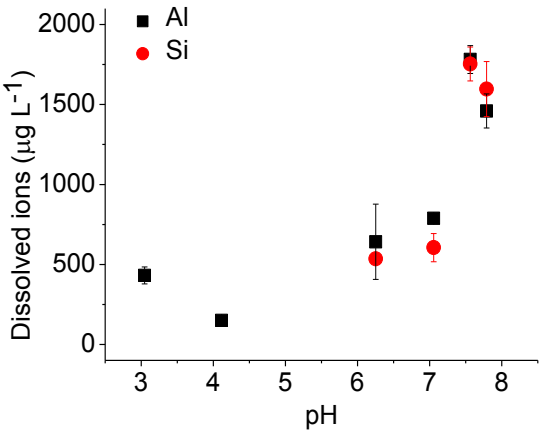


**Figure 82. Dissolution of Al and Si from SRS sediment**

In addition, control experiments using sediment-free batches were conducted to monitor U(VI) loss in the range of pH studied. It was observed that at pH ≤ 5, U(VI) loss was minimal (~3%). On the other hand, U(VI) loss (~60%) started to become significant at pH ≥ 6 (Figure 81b). This indicates that the mechanism of U(VI) removal not only involves sorption and surface complexation but also precipitation in the experimental conditions of this study. In the pH range where precipitation occurred, U(VI) becomes increasingly hydrolyzed and forms oligomeric species that might have led to precipitation of U(VI) as schoepite ($UO_3 \cdot 2.25H_2O$) (Eq. 17). Precipitation of U(VI) is favored in the absence of $CO_2$ while in the presence of $CO_2$, U(VI) precipitation is suppressed because of the high metal-complexing ability of carbonates, which results in the increased solubility of U(VI). In this study, the samples were likely not in complete equilibrium with atmospheric $CO_2$ even though the samples were open to atmospheric $CO_2$ daily. The failure to achieved full equilibration with $CO_2$ might have caused the precipitation of U(VI).

$$UO_2^{2+} + 3H_2O \rightleftarrows UO_3 \cdot 2.25H_2O_{(s)} + 2H^+ \quad [17]$$

Thermodynamic modeling calculations were performed with Geochemist's Workbench 12.0 for mineral saturation by using the experimental conditions in this study in the presence and absence of $CO_2$. The model uses the mineral saturation index $\left(SI = \log\left(\frac{Q}{K}\right)\right)$ to predict the tendency of a mineral to dissolve or form. If $\frac{Q}{K}$ is less than 1, the system is undersaturated, so the mineral is not formed. If $\frac{Q}{K}$ is greater than 1, the system is supersaturated, favoring the precipitation and formation of the mineral. The results of the modeling shown in Figure 83 indicate that, in the presence of $CO_2$, no precipitation and formation of minerals occur. On the other hand, in the absence of $CO_2$, the mineral $UO_2OH_2$ (beta) is formed at pH 8-9. In this study, most of the U(VI) lost in the control samples were at pH 7-8, very close to the region were mineral saturation occurs.

In addition, the redox potential ($E_h$) of the samples was measured at the end of the experiment to verify that reducing conditions had not developed, which could favor the reduction of U(VI) to U(IV), a less soluble form. The samples in Figure 81b show a constant $E_h$ value (~600 mV). This indicates that uranium in the experimental conditions of the study was in the oxidation state (VI).

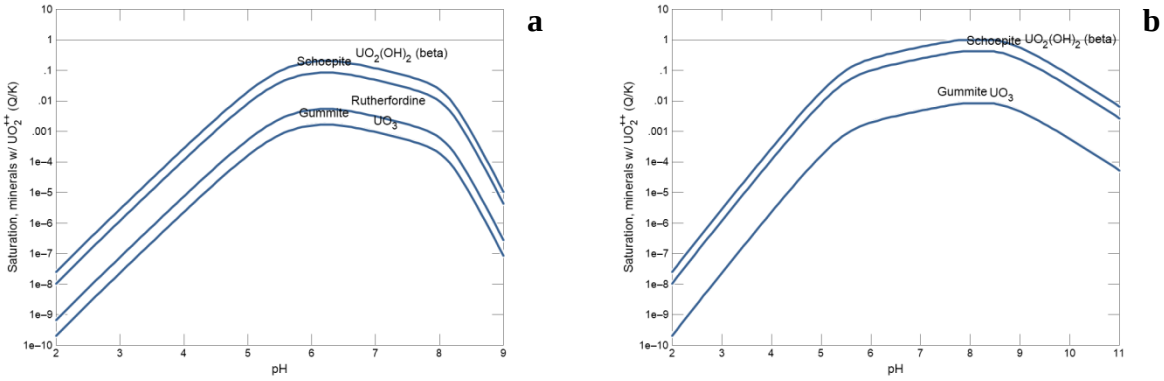


**Figure 83. Diagram for U(VI) mineral saturation in the (a) presence and (b) absence of CO2 ($P_{CO2} = 10^{-3.5}$ atm) was created in Geochemist's Workbench (thermo-minteq database).**

## Desorption of Uranium from SRS Sediment with and without Huma-K Amendment

Desorption is a very important parameter in the understanding of the mobility, bioavailability and fate of metals in the environment. Desorption studies were conducted by first sorbing U(VI) onto SRS sediment with and without Huma-K amendment at pH 4. To evaluate the desorption process, DI water adjusted to different pH values was used (Figure 84a). For SRS sediment, the maximum desorption of U(VI) (100%) was observed at pH 3. Above pH 3, desorption of U(VI) was not detected. In acidic conditions, $H^+$ have the ability to displace cations such as $UO_2^{2+}$ from their binding site and reduce the cation exchange capacity of minerals. Also, metals are more soluble under acidic conditions. In the case of SRS sediment amended with Huma-K, a similar maximum desorption of U(VI) (71.4%) was observed at pH 3. At pH 4, desorption had a sudden decrease (12.5%), and then desorption continued to increase with an increase of pH, reaching 37.4% desorption at pH 7.5. The high desorption of U(VI) in acidic conditions is related to the displacement uranyl ions by $H^+$. On the other hand, when the pH is increased, humic molecules in Huma-K become more soluble, and this enhances the desorption of U(VI) that is associated to Huma-K. This is attributed to the deprotonation of functional groups in humic molecules and the increase in negative charges that leads to their repulsion from the surface of the sediment. However, the amount of U(VI) that remained sorbed to the SRS sediment amended with Huma-K was higher than in plain sediments for the pH range studied (Figure 84b). This indicates that although an increase in pH promotes the soil-bound Huma-K to be released, remobilizing uranium, the SRS sediment amended with Huma-K performs better at the sequestration of U(VI).

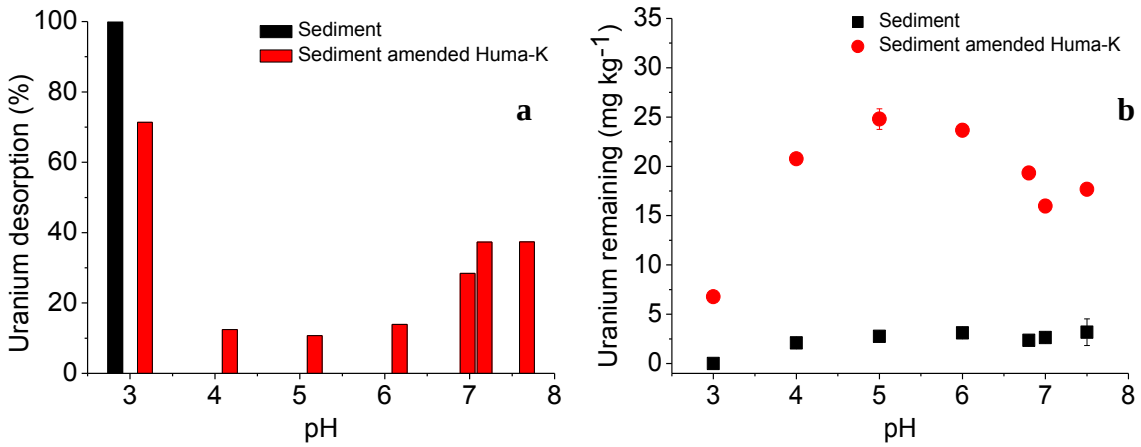


**Figure 84. (a) Desorption of U(VI) from SRS sediment with and without Huma-K amendment removal (10 g $L^{-1}$ of sediment, 14 days, I = 0.01 M $NaClO_4$, and T = 25°C). (b) Uranium remaining sorbed in SRS sediment after desorption.**

## Flow Through Column Experiments

Three flow through column experiments (control, Mod-HA, Huma-K) were conducted to investigate HA effects on the mobility of uranium. Parameters of each column were determined via rhenium tracer test then applied to study the sorption and desorption of humate along with study the sorption of uranium on humate loaded sediment. Each column was evaluated and compared to determine the relative performance of the tested HA substances, Mod-HA or Huma-K, to assess potential deployment performance, and how well they immobilize uranium. The results of each test phase for each column are conveyed below.

### Rhenium Tracer Test

Three 4" long columns (the control, Mod-HA, and Huma-K) were filled with 106.87g, 103.34 g, and 102.60 g of oven-dried SRS sediment that was sieved through a 2-mm sieve. After columns were filled and saturated with DI water, a rhenium tracer test was performed by following the procedure detailed in the methodology section. 3.03 mL (0.227 mg), 2.88 mL (0.216 mg), and 2.94 mL (0.220 mg) of 75 ppm rhenium solution was injected into the individual columns at an effective flowrate of approximately 2.0 mL/min. Thirty to fifty samples were collected in pre-weighed centrifuged tubes at 4 and 7 minute intervals. After each interval, tubes containing samples were re-weighed and analyzed to determine rhenium concentration. Upon completing data analysis, rhenium recovered from the Control, Mod-HA, and Huma-K column was found to be 0.229 mg, 0.206 mg and 0.186 mg; therefore, giving a percent recovery of 101%, 95%, and 84%. The data obtained from the tracer test is presented in Figure 85 and Table 17. Figure 85 shows the change in concentration of rhenium versus the collection time for each tracer test performed. The pore volume, variance and Peclet number were calculated using equations 1-5 as described in the methodology section. Tracer test data is presented below in Table 17 while Table 18 presents the column parameters calculated. The results indicate the pore volume of each column to be approximately 80 ml, 67 mL, and 54 mL respectively for the control, Mod-HA and Huma-K columns.

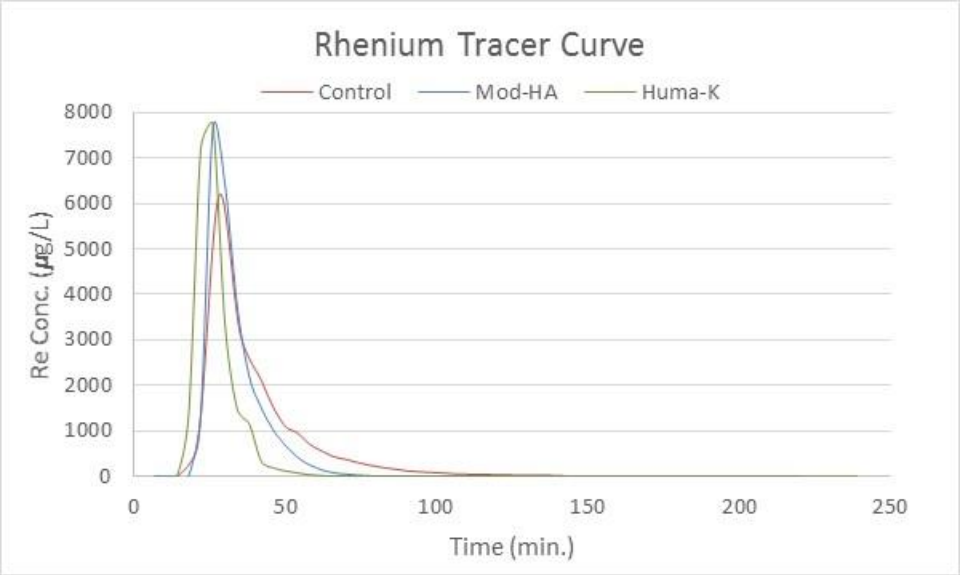


**Figure 85. Concentration of measured rhenium vs collection time**

**Table 17. Tracer Test Results**

| Column Type | Sediment weight (g) | Flow Rate (mL/min) | Rhenium Injected (mg) | Rhenium Recovered (mg) | Percent Recovery (%) | Total Fluid Collected (mL) | Pore Volume (mL) |
|---|---|---|---|---|---|---|---|
| **Control** | 106.9 | 2.01 | 0.227 | 0.229 | 101.11 | 285.3 | 79.9 |
| **Mod-HA** | 103.3 | 2.02 | 0.216 | 0.206 | 95.5 | 443.7 | 67.1 |
| **Huma-K** | 102.6 | 1.99 | 0.221 | 0.186 | 84.49 | 476.4 | 54.2 |

The dimensionless Peclet number (Pe) is defined as the ratio of the rate of transport by convection to the rate of transport by diffusion or dispersion (Eq. 18). Pe, found experimentally from the tracer test, was used to calculate effective dispersion (Table 18); the values of the Peclet number were used to correlate the effect of dispersion on the effluent tracer concentration.

$$Pe = \frac{rate\ of\ transport\ by\ convection}{rate\ of\ transport\ by\ diffusion\ or\ dispersion} = \frac{UL}{D_a} \qquad \text{Eq. (18)}$$

Where:

L - characteristic length term (m)

$D_a$ - effective dispersion coefficient ($m^2/s$)

U - average interstitial velocity (m/s)

**Table 18. Column Transport Parameters Determined by Rhenium Tracer Injection**

| Column Type | U (m/s) | Variance, $\sigma^2$ | Pe | Dispersion ($m^2/s$) | 1/Pe=D/uL |
|---|---|---|---|---|---|
| **Control** | 6.82E-05 | 302.41 | 9.36 | 7.40E-07 | 0.107 |
| **Mod-HA** | 6.85E-05 | 148.88 | 13.78 | 5.05E-07 | 0.073 |
| **Huma-K** | 6.77E-05 | 585.38 | 13.13 | 5.24E-07 | 0.076 |

## Sorption and Desorption of Humate

Following the rhenium tracer test of each column, AGW with pH adjusted to 3.5 was injected from the base of the column to equilibrate the effluent solution at pH of approximately 3.5. Mod-HA and Huma-K columns were injected with half (1/2) PV of 10,000 ppm of humate at an approximate flowrate of 2.0 mL/min. In order to avoid the humic acid from settling during injection, solution was continuously stirred during injection. After the humate injection, AGW at pH 3.5 was injected into the column until the concentration of humic acid reached approximately 2% of the initial concentration. The concentration of humic acid in the effluent samples were measured immediately, after collecting samples at 4 minute intervals, in order to ensure that the desired end point of the desorption phase was achieved. The pH of each effluent sample was also measured and recorded. Figure 86 shows the breakthrough curve of humic acid sorption and desorption for the Mod-HA and Huma-K column along with the change in pH. It is evident from the curve that most of the humic acid injected into the column was retained until 0.48 PV and 0.74 PV where humic acid was finally observed in the effluent. The concentration of humic acid increased to a peak value of approximately 7,971 ppm for Mod-HA and 7,668 ppm for Huma-K. As fresh humic acid passed through the column and interacted with the soil conditioned with pH 3.5 AGW, pH of the humate decreased, this could facilitate the precipitation of Humic acid. As the humic acid continued to flow, the column pH steadily increased which could cause the re-solubilization of humate. Because of precipitation and re-dissolution, the amount of HA sorbed is inconclusive and the term “retained” is used over “sorbed” in this report. At 0.76 PV and 1.3 PV, the concentration of HA started to decrease. The concentration of Mod-HA in the effluent reached 205 ppm and 210 ppm after injecting approximately 1.14 PV and 1.49 PV of AGW at pH 3.5. Table 19 shows the results obtained from sorption and desorption of humic acid. The pH of the Mod-HA column changed from 3.37 to 6.99 while retaining 313.29 mg of Mod-HA per kg of sediment. Whereas the Huma-K column’s pH changed from 3.5 to 7.4 while retaining 426.64 mg of Huma-K per kg of sediment.

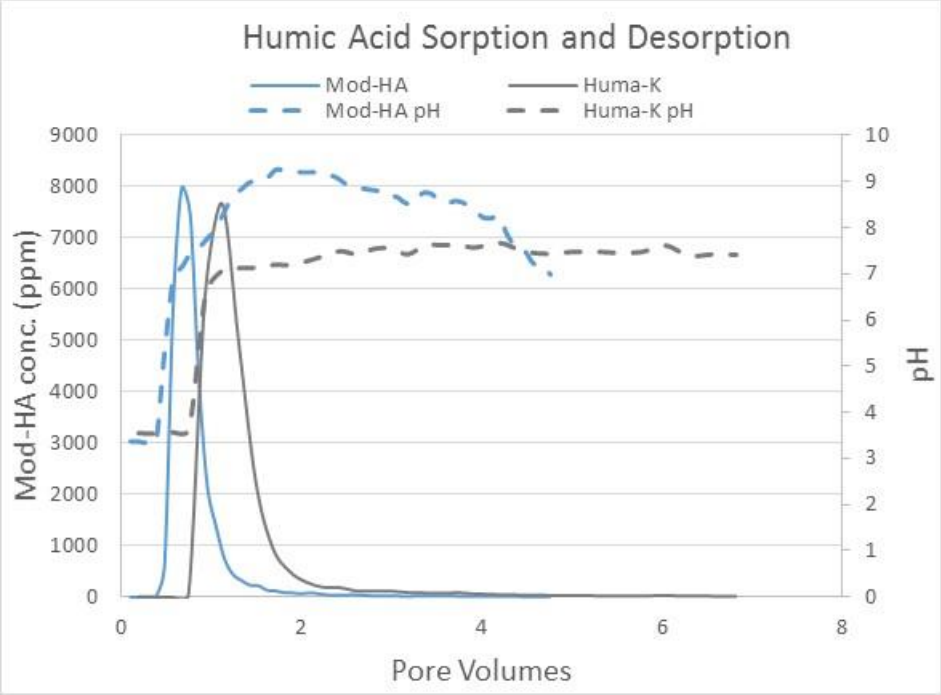


**Figure 86. Concentration profile of HA in the effluent of the column**

**Table 19. Soprtion/Desorption of modified humic acid**

| Column Type | Sediment Weight (g) | pH | | Humic acid | | | |
|---|---|---|---|---|---|---|---|
| | | Initial | Final | Volume Injected (ml) | Injected (mg) | Recovered (mg) | Retained (mg/kg) |
| **Mod-HA** | 103.3 | 3.37 | 6.99 | 34.18 | 341.84 | 309.47 | 313.29 |
| **Huma-K** | 102.6 | 3.54 | 7.4 | 28.14 | 281.44 | 243.81 | 366.89 |

## Sorption of Uranium

Sorption of uranium was studied by injecting 500 ppb uranium solution prepared with SRS AGW at pH 3.5 into three separate columns (the control, Mod-HA, and Huma-K). Solution was injected until the ratio of the effluent concentration (C) reached half of the initial concentration ($C_0$). This resulted in $C/C_0$ equaling 0.5. Figure 87 displays the behavior of uranium mobility through each column. It was observed that the uranium control column reached $C/C_0 = 0.5$ after injecting a total volume 249 mL while the columns containing humic acid used a larger volume of uranium solution to reach the same point. The Mod-HA and Huma-K column reached 0.5 after injecting 2382 mL and 1809 mL. However, when comparing the PV of each column they are similar.

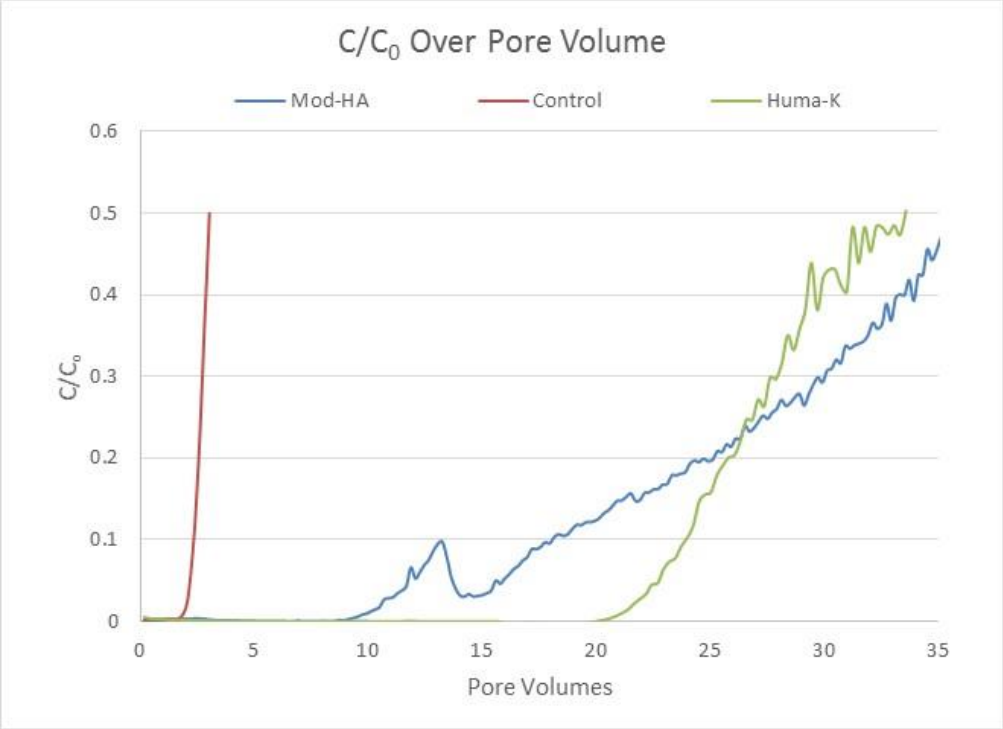


**Figure 87. $C/C_0$ Over Pore Volume**

As shown in Figure 87, sediment treated with mod-HA and the Huma-K column retained/removed more uranium from the solution than the control column. Figure 88 depicts how the uranium retained correlates with $C/C_0$. As shown all three columns have a similar trend. However, when compared to the control Mod-HA has retained 9x the amount of uranium with 9951.74 ug per kg of sediment. While Huma-K retained 8x the amount of uranium with 7963.06 ug per kg of sediment, Table 20..

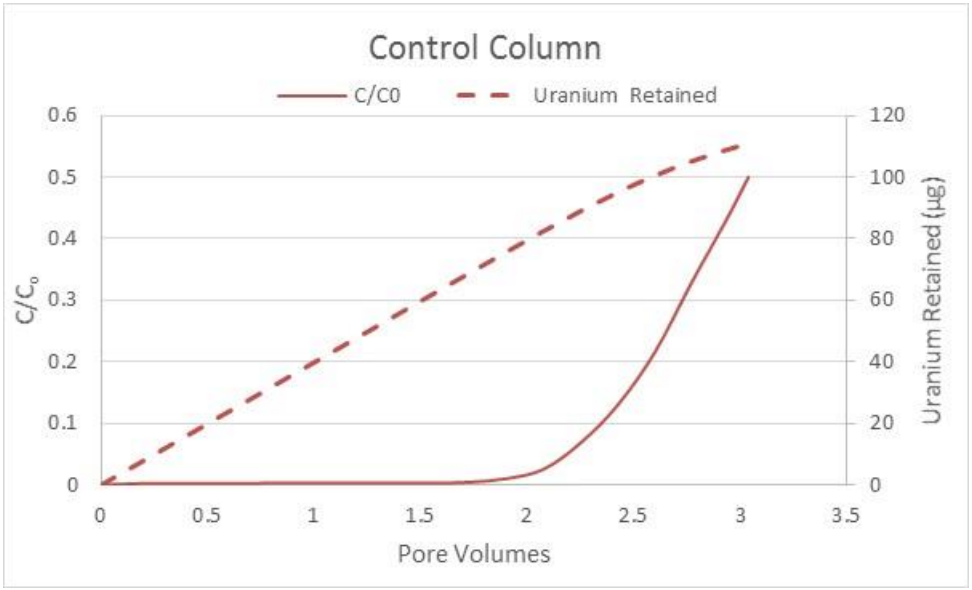


**Figure 88. $C/C_0$ and Uranium Retained for the Control Column**

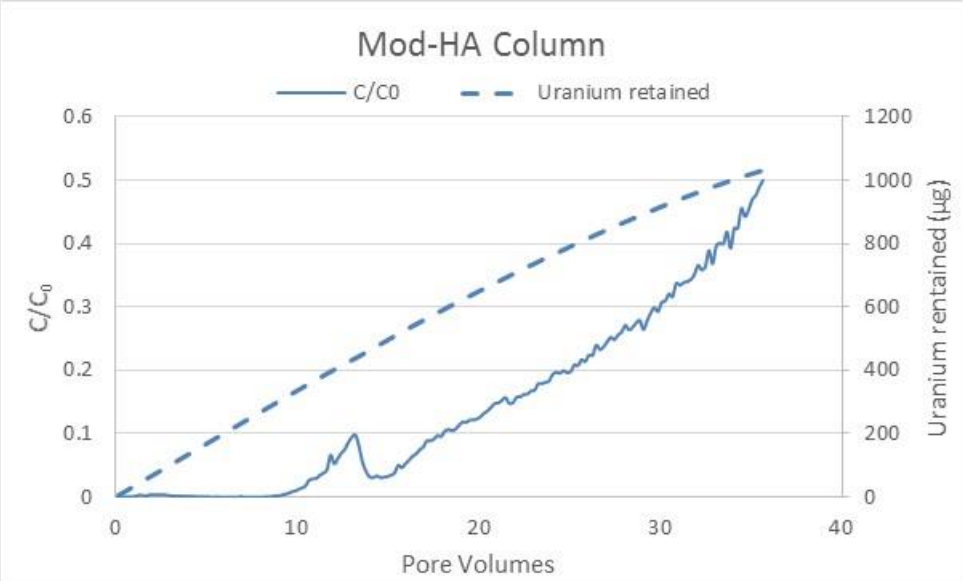


**Figure 89. $C/C_0$ and Uranium Retained for the Mod-HA Column**

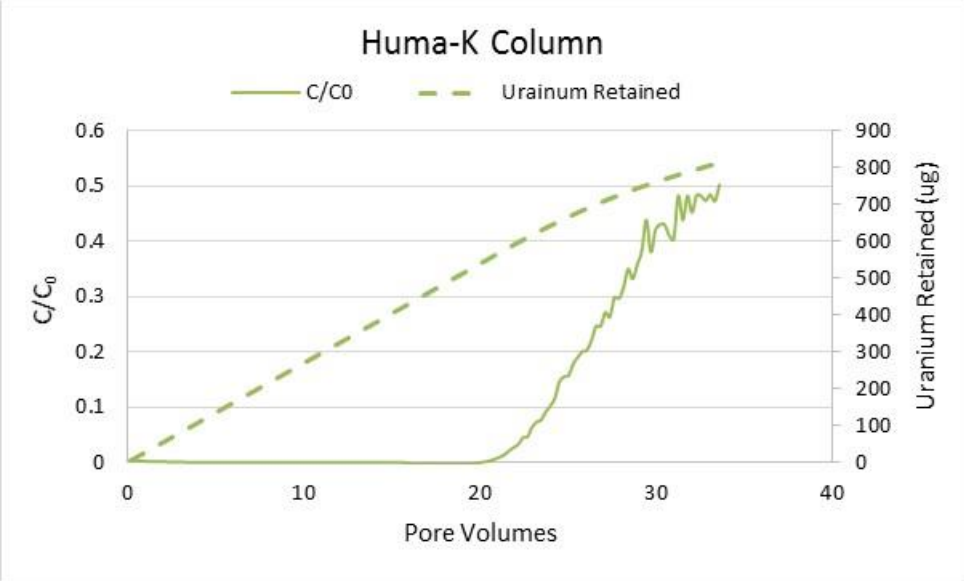


**Figure 90. $C/C_0$ and Uranium Retained for the Huma-K Column**

**Table 20. Soprtion of Uranium**

| | Sediment weight (g) | pH | | Injected (ml) | Injected (µg) | Recovered (µg) | Retained (µg /kg) |
|---|---|---|---|---|---|---|---|
| | | Initial | Final | | | | |
| **Control** | 106.9 | 3.35 | 3.15 | 249.19 | 124.59 | 10.46 | 1067.99 |
| **Mod-HA** | 103.3 | 6.99 | 3.65 | 2391.77 | 1195.89 | 167.47 | 9951.74 |
| **Huma-K** | 102.6 | 7.4 | 3.47 | 1819.48 | 909.74 | 92.97 | 7963.06 |

### Comparison Modified Humic Acid to Huma-K

In summary, sediments retained less Mod-HA compared to Huma-K, yet the Mod-HA loaded sediments retained more uranium than Huma-K loaded sediment. Using comparable injection quantities (approximately 30 mL of 10,000 mg/L humate), the Huma-K loaded column retained 366.89 mg/kg while the Mod-HA loaded column retained 313.29 mg/kg. Retention of the HA substances was the net result of sorption, precipitation and re-dissolution of HA as the pH of the solution changed. The lower sorption of Mod-HA resulted in more distribution throughout the column creating a larger treatment zone. This difference would impact potential deployment designs in terms of zone of influence and the total quantity of amendment needed to treat a target volume.

On a unit basis, each mg of Mod-HA sorbed more U than each mg of Huma-K. Sediments loaded with Mod-HA retained 9951.74 μg/kg of uranium while sediments loaded with Huma-K retained 7963.06 μg/kg of uranium.

In evaluating the results, both HA amendments immobilized and retained significantly more uranium compared to the control column. The degree of improvement was similar for both materials (i.e., the uranium retention capacity increased by 8x to 9x). Either material could be incorporated into an in-situ immobilization strategy. The lower sorption and broader distribution of the Mod-HA would support wider deployment spacing and potentially a reduced amendment quantity in a real-world remedial design.

## Subtask 2.3: Future Work

In continuation of studying the sorption of uranium on humic acid sorbed sediment, uranium sorbed to the sediment will be measured by taking soil sample from each column and analyzing them via X-Ray Fluorescence (XRF) Spectrometer.

## Subtask 2.3: Acknowledgements

Funding for this research was provided by U.S. DOE Cooperative Agreement DE-EM0000598. We truly appreciate Dr. Miles Denham and Dr. Brian Looney from SRNL for their valuable contributions and support of this research.

## Subtask 2.3: References

Bear, Jacob, Hydraulics of Groundwater, McGraw-Hill Book Company, New York 1979.

Bischoff K., Levenspiel O., (1963) Adv. Chem. Eng. 4, p. 95.

Blake, G.R., and Hartge, K.H., (1986). Bulk Density. In: Klute, A. (Ed.), Methods of Soil Analysis. Part 1. Physical and Mineralogical Methods. American Society of Agronomy-Soil Science Society of America, 677 South Segoe Road, Madison, WI, 363-375.

Blake, G.R., and Hartge, K.H., (1986). Particle Density. In: Klute, A. (Ed.), Methods of Soil Analysis. Part 1. Physical and Mineralogical Methods. American Society of Agronomy-Soil Science Society of America, 677 South Segoe Road, Madison, WI, 377-382.

Bruemmer, G. W., et al. (1988). Reaction kinetics of the adsorption and desorption of nickel, zinc and cadmium by goethite. I. Adsorption and diffusion of metals. Journal of Soil Science **39**(1): 37-52.

Choppin Gregory, R. (1988). Humics and radionuclide migration. Radiochimica Acta. **44-45:** 23.

Danielson, R.E., and Sutherland, P.L., (1986). Porosity. In: Klute, A. (Ed.), Methods of Soil Analysis. Part 1. Physical and Mineralogical Methods. American Society of Agronomy-Soil Science Society of America, Madison, WI, 443-450.

Denecke, M. A., et al. (1997). "Measurements of the structural parameters for the interaction of uranium(VI) with natural and synthetic humic acids using EXAFS." Radiochimica Acta **79**(3): 151-159.

Denham, M. and K. M. Vangelas (2008). "Biogeochemical gradients as a framework for understanding waste-site evolution." Remediation **19**(1): 5-17.

Dong, W., Tokuanga, T. K., Davis, J. A., Wan, J., (2012). Uranium(VI) Adsorption and Surface Complexation Modeling onto Background Sediments from the F-Area Savannah River Site. Environ. Sci. Technol. 46, 1565-1571.

Efstathiou, M. and I. Pashalidis (2017). "A comparative study on the sorption of tri- and hexavalent actinides on sea sediments." Journal of Radioanalytical and Nuclear Chemistry **312**(2): 181-185.

Fogler, H., S., (1992). Elements of Chemical Reaction Engineering, PTR Prentice-Hall, Inc., 837p.

Freundlich, H. M. F. (1906). "Over the adsorption in solution." The Journal of Physical Chemistry **57**: 385-471.

Gabriel, U., et al. (2001). Uranyl surface speciation on silica particles studied by time-resolved laser-induced fluorescence spectroscopy. Journal of Colloid and Interface Science **239**(2): 358-368.

Greathouse, J. A., et al. (2002). "Molecular dynamics study of aqueous uranyl interactions with quartz (010)." The Journal of Physical Chemistry B **106**(7): 1646-1655.

Ivanov, P., et al. (2012). "The effect of humic acid on uranyl sorption onto bentonite at trace uranium levels." Journal of Environmental Monitoring **14**(11): 2968-2975.

Kerisit, S. and C. Liu (2014). "Molecular dynamics simulations of uranyl and uranyl carbonate adsorption at aluminosilicate surfaces." Environmental Science & Technology **48**(7): 3899-3907.

Killops, S., et al. (2004). Long-term fate of organic matter in the geosphere. Introduction to organic geochemistry, Blackwell Publishing Ltd.**:** 117-165.

Kremleva, A., et al. (2008). "Density functional model studies of uranyl adsorption on (001) surfaces of kaolinite." Langmuir **24**(17): 9515-9524.

Kremleva, A., et al. (2009). "Role of aliphatic and phenolic hydroxyl groups in uranyl complexation by humic substances." Inorganica Chimica Acta **362**(8): 2542-2550.

Křepelová, A., et al. (2006). "Uranium(VI) sorption onto kaolinite in the presence and absence of humic acid." Radiochimica Acta **94**(12): 825-833.

Langmuir, I. (1918). "The adsorption of gases on plane surfaces of glass, mica and platinum." Journal of the American Chemical Society **40**(9): 1361-1403.

Levenspiel, O., Chemical Reaction Engineering, 2nd Ed., (1972), John Wiley &Sons.

Liu, X., et al. (2013). "Acidity of edge surface sites of montmorillonite and kaolinite." Geochimica Et Cosmochimica Acta **117**: 180-190.

Martorell, B., et al. (2010). "Density functional model study of uranyl adsorption on the solvated (001) surface of kaolinite." Journal of Physical Chemistry C **114**(31): 13287-13294.

Mibus, J., Sachs, S., Pfingsten, W., Nebelung, C., Bernhard, G., (2007). Migration of Uranium (IV)/(VI) in the Presence of Humic Acids in Quartz Sand: a Laboratory Column Study, Journal of Contaminant Hydrology, Volume 89, Issues 3-4, Pages 199-217.

Milling, M. R., Amidon, M. B., Denham M. E., Looney B. B., (2013). Preliminary Data Report: Humate Injection as an Enhanced Attenuation Method at the F-Area Seepage Basins, Savannah River Site (U). (SRNL-STI-2013-00514).

Pashalidis, I. and G. Buckau (2007). "U(VI) mono-hydroxo humate complexation." Journal of Radioanalytical and Nuclear Chemistry **273**(2): 315-322.

Pompe, S., et al. (2000). "Investigation of humic acid complexation behavior with uranyl ions using modified synthetic and natural humic acids." Radiochimica Acta **88**(9-11): 553.

Prikryl, J. D., et al. (2001). "UraniumVI sorption behavior on silicate mineral mixtures." Journal of Contaminant Hydrology **47**(2): 241-253.

Ptak, T., Piepenbrink, M., Martac E. (2004). Tracer Tests for the Investigation of Heterogeneous Porous Media and Stochastic Modelling of Flow and Transport - a Review of some Recent Developments, Journal of Hydrology, 122 - 163.

Scheinost, A. C., et al. (2001). "Kinetic controls on Cu and Pb sorption by ferrihydrite." Environmental Science & Technology **35**(6): 1090-1096.

Schmeide, K., et al. (2003). "Interaction of uranium(VI) with various modified and unmodified natural and synthetic humic substances studied by EXAFS and FTIR spectroscopy." Inorganica Chimica Acta **351**: 133-140.

Sherman, D. M., et al. (2008). "Surface complexation of U(VI) on goethite (α-FeOOH)." Geochimica Et Cosmochimica Acta **72**(2): 298-310.

Shook, G. M., Forsmann, J. H., (2005). Tracer Interpretation Using Temporal Moments on a Spreadsheet (INL/EXT-05-00400).

Steudtner, R., et al. (2011). "Binary and ternary uranium(VI) humate complexes studied by attenuated total reflection Fourier-transform infrared spectroscopy." Dalton Transactions **40**(44): 11920-11925.

Steudtner, R., et al. (2011). "Ternary uranium(VI) carbonato humate complex studied by cryo-TRLFS." Radiochimica Acta **99**(11): 687-692.

Strom, R.N., Kaback, D.S. 1992. SRP Baseline Hydrogeologic Investigation: Aquifer Characterization, Groundwater Geochemistry of the Savannah River Site and Vicinity (U). Westinghouse Savannah River Company, Savannah River Laboratory.

Sundararajan, M., et al. (2011). "Speciation of uranyl ions in fulvic acid and humic acid: A DFT exploration." Physical Chemistry Chemical Physics **13**(40): 18038-18046.

Tipping, E. (2002). Cation binding by humic substances. New York, USA, Cambridge University Press.

Wan, J., Dong, Wenming, and Tokunaga T. K., (2011) Method to Attenuate U(VI) Mobility in Acidic Waste Plumes Using Humic Acids, Environ. Sci. Technol. 2011, 45, 2331–2337

Wan, J., et al. (2012). "Persistent source influences on the trailing edge of a groundwater plume, and natural attenuation timeframes: The F-Area Savannah River Site." Environmental Science & Technology **46**(8): 4490-4497.

# TASK 3: SURFACE WATER MODELING OF TIMS BRANCH

## Task 3: Executive Summary

This task involves the development of an integrated, fully distributed hydrology and transport model to be used as a tool for assessment, evaluation and long-term monitoring of the fate and transport of sediment and contaminants in the Tims Branch watershed, the major portion of which is located within the Savannah River Site (SRS) in Aiken, SC. The Tims Branch watershed is a small stream-scale ecosystem that lies within the larger Upper Three Runs watershed, which is a sub-basin of the lower Savannah River Basin. Two major tributaries of Tims Branch, referred to as the A-014 and A-011 outfall tributaries, extend into the SRS A and M Areas and have received direct discharges of wastewater through the A-014 and A-011 outfalls from on-site process and laboratory facilities which, at various times, has contained uranium, nickel, aluminum, mercury, other metals and radionuclides, as well as organic solvents. Innovative treatment methods were deployed to limit the contaminant flux to Tims Branch, including a wetland treatment system in 2000, and a mercury removal system in 2007 that uses a tin (II) reagent and air stripping. These treatments effectively eliminated all local anthropogenic mercury inputs to Tims Branch; however, the tin-based treatment resulted in the controlled discharge of low-levels of inorganic tin oxide into the ecosystem. The controlled discharge of tin to Tims Branch has provided high quality records on the quantity and timing of the release which provides a unique opportunity for the released tin to serve as a potential tracer for sedimentation and particle transport processes in the stream. This makes Tims Branch an ideal testbed to study complex systems science in a relatively well defined ecosystem that has experienced controlled changes in boundary conditions. Results from this study are key to evaluating the effectiveness of wetland treatment and tin (II) - based mercury treatment at the SRS site, and are also relevant to evaluating the potential of using water treatment and novel remediation technologies in other mercury-contaminated stream systems.

The principal objective of this task is to develop and test a comprehensive transport model using available hydrology software and geographical information systems (GIS) tools to examine the response of Tims Branch to historical discharges and environmental management remediation actions. A rigorous calibration and validation exercise is necessary to increase confidence in the models' ability to estimate spatial distribution of flow depth and velocity, and contaminant concentration over time. The main challenges in hydrological modeling, however, are finding observed/measured timeseries data for the model calibration and validation process. A secondary objective of this task, therefore, is to identify data gaps and, where necessary, attempt to collect additional field data to support model validation. The field work conducted under this task has been incorporated as part of student summer internships in coordination with SRNL and SREL, with periodic follow-up by FIU researchers to conduct routine maintenance on deployed remote monitoring systems.

## Subtask 3.1: Modeling of Surface Water and Sediment Transport in the Tims Branch Ecosystem

## Subtask 3.1: Introduction

The overall objective of this subtask is to support SRS and DOE EM's Office of Subsurface Closure goals by developing an integrated hydrology and contaminant transport model to be used as a long-term monitoring tool for studying the sedimentation and particle transport processes in

the Tims Branch ecosystem at SRS. The Tims Branch ecosystem represents an important applied science opportunity as a result of significant past research by SRNL and SREL. Recent innovative cleanup technologies developed by DOE EM have eliminated anthropogenic mercury sources from Tims Branch watershed; however, a known quantity of relatively inert tin oxide tracer was introduced to the ecosystem. DOE EM has highlighted the need to track the tin and to understand the impact of frequent or extreme atmospheric events on its redistribution in Tims Branch. FIU will utilize the data available from the tin-based remediation technology to develop a model that can not only be extended to investigate other contaminants of concern (e.g., mercury, uranium, nickel, aluminum and other metals and radionuclides), but also be applicable to other nearby watersheds.

## Subtask 3.1: Methodology

The Tims Branch model development is being executed in phases. The preliminary phase has involved the development of an integrated surface water/groundwater model capable of simulating the Tims Branch watershed hydrology and examining its response to extreme hydrological events. Subsequent phases involve development and integration of the contaminant transport component in order to create a fully comprehensive, distributed contaminant fate and transport model that can be used as a tool to estimate the potential movement and redistribution of contaminants of concern in the Tims Branch watershed.

The software used by FIU in Performance Years 6 & 7 to develop the existing hydrology models has provided the flexibility to simulate overland flow and stream flow in either a stand-alone or coupled fashion, which can each provide significant results. Work for this year (FIU Performance Year 8) has been focused on completing sensitivity analyses and calibration of the stand-alone 1-D stream flow and 2-D overland flow models already developed, and then integrating/coupling these models to create a fully comprehensive distributed surface water model that can be used as a tool to estimate hydrological components of the surface water under different scenarios. The main activities in Year 8 have included the following:

- Sensitivity analysis of the MIKE SHE overland flow model.
- Addition of existing man-made hydraulic control structures to the MIKE 11 stream flow model of the A-014 outfall tributary, and subsequent sensitivity analysis of this model with and without the hydraulic structures implemented.
- Development and sensitivity analysis of the MIKE 11 stream flow model of the main Tims Branch stream.
- Coupling of the overland flow and stream flow hydrological models.

Calibration of the coupled hydrology model is still in progress, utilizing historical as well as recently acquired field observation timeseries data. In FIU Performance Year 9, FIU plans to complete the calibration of the hydrology model and implement the contaminant transport module. FIU will implement specific rainfall scenarios in each model to understand the models' behavior under various atmospheric conditions. Atmospheric scenarios will be determined based upon historical rainfall events and data provided by federal/state online databases or data provided by SRNL/SRNS. MIKE and ArcGIS tools will be used for data analysis and visualization of model results.

## Subtask 3.1: Results and Discussion

### MIKE SHE Overland Flow Model

*Sensitivity analysis of the MIKE SHE overland flow model.*

The MIKE SHE model includes a wide range of parameters that represent the major processes in the hydrologic cycle and includes process models for evapotranspiration, overland flow, unsaturated flow, groundwater flow, stream flow and their interactions. Each parameter can be considered as a calibration factor. Performing a model calibration for the entire range of MIKE SHE parameters would not only require a substantial amount of field data, but also a significant computer runtime that would make this approach impractical. Performing a sensitivity analysis limits the number of parameters to only those that have a significant impact on the simulation results. Sensitivity analyses have revealed that there are a few dominant parameters such as vegetation and root depth, as well as empirical parameters that influence evapotranspiration and recharge. The type of the soil plays a role in the infiltration/evapotranspiration and recharge functions in the unsaturated zone, while at the saturated zone level, the hydraulic conductivity is of primary significance.

In this model development process, the focus was on parameters that had the greatest impact on the hydrology and characteristics of the overland flow in Tims Branch watershed. Table 21 shows the initial parameter values used in the MIKE SHE Evapotranspiration (ET) module which were based either upon experimental/field data if available, or from the literature.

**Table 21. Initial Parameter Values Used in the MIKE SHE – ET Module**

| Parameter | Value | Unit |
|---|---|---|
| Detention Storage | 2.5 | mm |
| Surface-Subsurface Leakage Coefficient | 0.0001 | 1/sec |
| Reference Evapotranspiration | 2.22 | mm/day |
| Leaf Area Index | 1.3 – 6.3 | $m^2/ m^2$ |
| Root Depth | 0.0 – 4000 | mm |

Sensitivity analysis was initiated in Performance Year 7 by first changing the values of the detention storage (DS) and reference evapotranspiration (RET). A series of MIKE SHE overland flow simulations were performed for a period of 9 months from 1/1/2014 to 9/30/2014. Two peak rainfall events were selected as the point for visual comparison. The rain events occurred on 2/14/2014 and 6/1/2014. No Saturated Zone (SZ) module was included in these simulations.

This year, FIU continued the MIKE SHE overland flow model focusing on the model's sensitivity to changes in the surface-subsurface leakage coefficient (SSLC). Several simulations were performed with ±5% changes in SSLC. Also, the simulations were performed under wet and dry land conditions. Dry conditions refer to simulations starting with zero initial water depth and wet conditions refer to simulations where an initial depth of water is imposed. The initial depth was taken from the final time step in previous overland flow simulations. These simulations were performed for the time period of 2010 through 2012. A total of 16 simulations were conducted with ±5% changes in SSLC. The initial value of SSLC was set to 0.0001. No obvious errors were

found; however, the results show inconsistency in water balance and depth of overland flow at both monitoring locations (A-014 outfall and downstream Tims Branch). The results of overland flow water depth consist of missing values which may be the result of numerical errors because of initial values of the depth of water and SSLC. Further investigation is in progress to evaluate the numerical stability of the model while calibration is in progress. Additional efforts to improve the model performance and stability have included the modification of initial and boundary conditions in the saturated and unsaturated zone modules.

### MIKE 11 Stream Flow Model (A-014 Outfall Tributary)

*Sensitivity analysis and calibration of the MIKE 11 stream flow model of the A-014 outfall tributary and addition of existing man-made infrastructures to the A-014 model.*

The MIKE 11 stream flow model of the A-014 outfall tributary was completed by generating model files such as the stream network, cross sections, boundary conditions, and hydrodynamic parameters including initial water depth and simulation characterization. Each file has undergone several revisions with modifications based on the model's performance and available data.

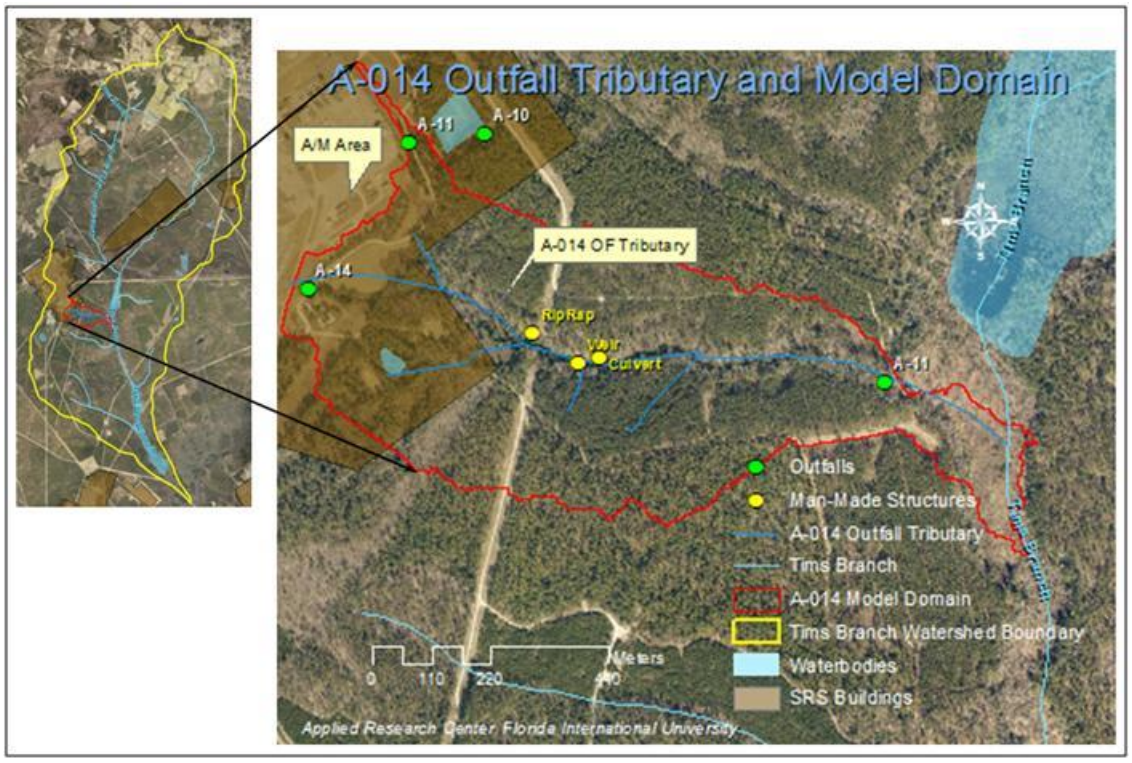


**Figure 91. A-014 outfall tributary and model domain.**

Existing hydraulic structures (i.e., weir, culvert, and riprap) were incorporated in the network file using weir specifications from a weir in South Florida, assuming the weir in crested board and based on personal observation during FIU's past visits to the SRS study site. The culvert was assumed to act as a weir as it was installed vertically, which differs from regular culverts. The diameter was estimated to be 1.0 m. The engineering design specifications of these hydraulic control structures were requested from SRNL and the data derived from the drawings provided have been included in the steam network module.

A sensitivity analysis was then perfomed as follows:

1. Several MIKE 11 simulations were implemented to understand the model's sensitivity to various parameters. The first set of simulations was completed for a period of 9 months, from 01/01/2014 through 09/29/2014. Next, the flow in the A-014 outfall tributary was simulated for a period of 3 years from 10/01/1993 to 9/30/1996.
2. Several adjustments were made to the original model input parameters in order to achieve the steady state flow in the stream. Major adjustments were applied to the river network. The river network shapefile was simplified by eliminating all the minor tributaries so only one major stream was left to represent the A-014 outfall tributary. It was assumed that the small tributaries within the A-014 domain would have minimal contribution to the flow in the A-014 outfall tributary because of the fact that they stay dry most of the year. Other adjustments were made to the cross sections at the stream banks. The cross sections were modified to reflect the natural trapezoidal shape characteristic of the stream.
3. Boundary conditions were also modified. It was assumed that flow was constant at the rate of 450 GPM (0.03 $m^3/s$). Field measurements taken by FIU in 2016 and 2017 also indicated a 0.03 $m^3/s$ flow rate in the stream. An open boundary condition was assumed at the downstream end of the A-014 outfall tributary.
4. A channel roughness coefficient (Manning's value) was assumed to be 0.04. This value is recommended by various water resources handbooks. The Manning's coefficient was used as a calibration parameter.
5. Significant man-made structures, including a weir and a culvert, were incorporated into the existing A-014 stream network. Due to the lack of engineering design specifications, the dimensions of similar weirs and culverts in other streams were used. The weir type was assumed to be crusted, with dimensions similar to weirs installed in most streams in the region. The culvert was assumed to be 1.00 m diameter.
6. In order to include rainfall data, the MIKE 11 stream flow model was coupled with the MIKE SHE overland flow model. The domain in MIKE SHE was modified from the Tims Branch watershed to the A-014 sub-watershed. Other parameters such as the horizontal and vertical hydraulic conductivities in both the unsaturated and saturated zones were also adjusted. The vegetation file was also modified based on the simulation time period.

The following figures illustrate a one year (1993) flow simulation at various cross sections along the A-014 outfall tributary. The results were processed and visualized using MIKE VIEW. Figure 92 shows the results of a flow simulation in the A-014 outfall tributary in 1993. The results indicate that after approximately one month of warm up, the system reaches to a steady state flow of 0.03 m3/s. Each peak in the graph refers to a rainfall event that occurred in 1993. A comparison between the observed rainfall data (Figure 93) and the simulated discharge (Figure 92) indicates that the model correlates well with the rainfall events.

Figure 94 and Figure 95 illustrate the flow depth in cross sections and the water levels along the A-014 outfall tributary. Both figures show that the flow depth and water level reach a steady state with approximate 10-20 cm of water depth along the stream, except for the areas where there are ponds between the weir and culvert.

Overall, at this stage, the model corresponds to rainfall and produces steady state flow depth and discharge along the stream. The model will continue to be calibrated and refined as flow data

becomes available from stage gauges that were deployed along Tims Branch and the A-014 outfall tributary in February 2018.


**Figure 92: Simulated discharge for 1993 at various cross section locations along A-014 outfall tributary. Each color refers to a cross section location. The locations of the simulated cross sections along A-014 are shown.**

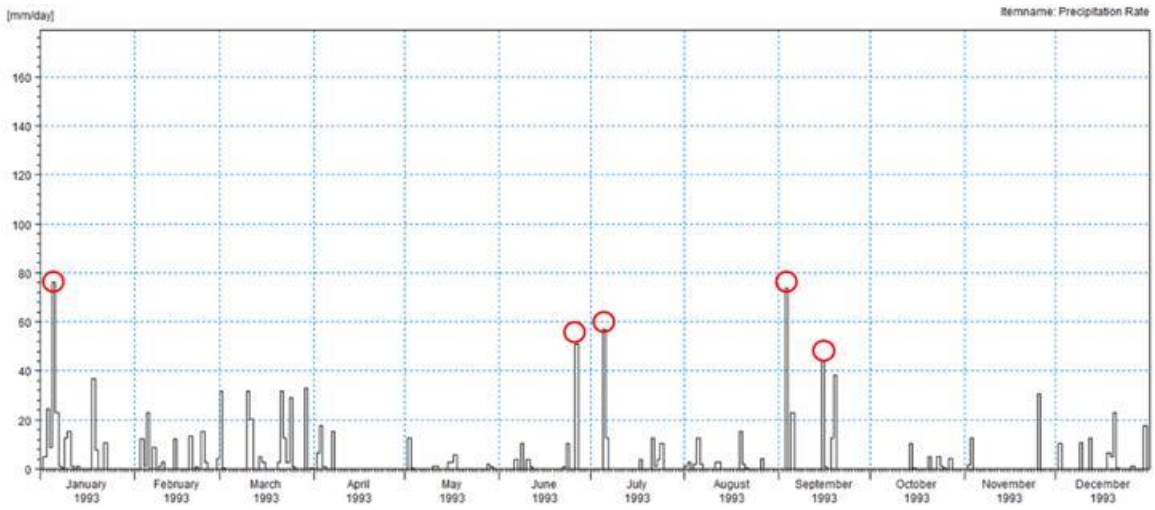


**Figure 93: Daily rainfall data for 1993. The red circles correlate with the peaks seen in the discharge graph (Figure 92).**

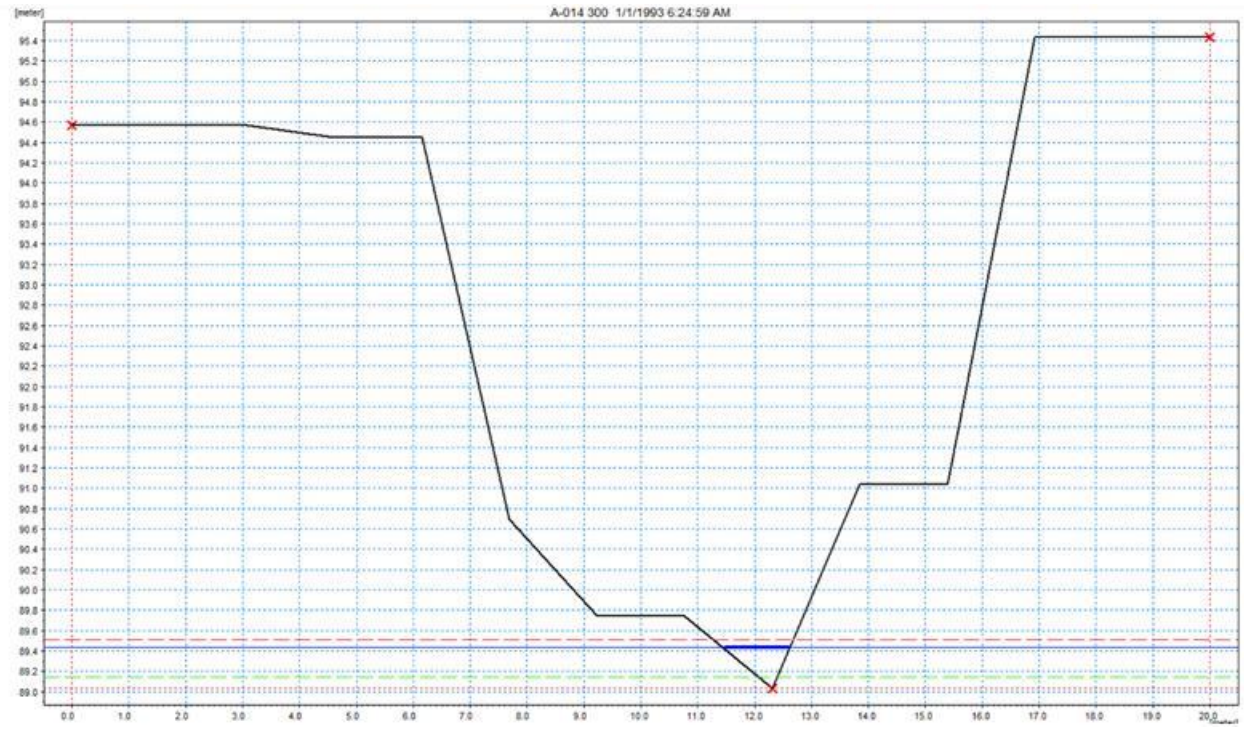


**Figure 94. Discharge at cross section 300. The blue line indicates the value of depth of water.**

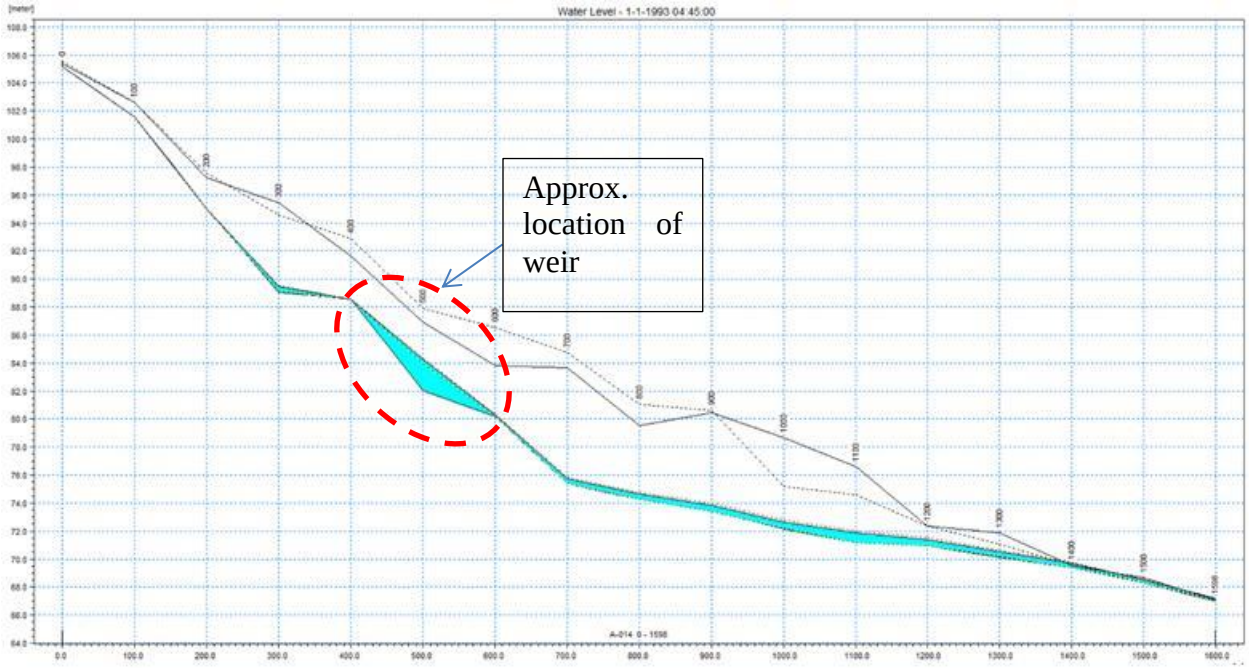


**Figure 95. Simulation of water level along A-014. As it shows, cross section 500 is in the proximity of the weir location.**

In April, the sensitivity analysis of the MIKE 11 stream flow model of the A-014 outfall tributary (milestone 2017-P2-M7) was completed. A memo was sent to all of the relevant collaborators on 4/5/2018, one day ahead of the milestone due date.

Simulations were run after modifying the MIKE 11 boundary conditions, changing them from constant discharge to time series using available historical data.

The model simulations at this stage of development have shown acceptable performance. Flow data from recently installed stage gauges in Tims Branch by FIU's DOE Fellows is being used at the A-014 downstream location for model calibration.

This model has served as the basis for DOE Fellow Mohammed Albassam's Master's thesis topic entitled "The effect of Frequent Atmospheric Events and Hydrologic Infrastructure on Flow Characterization in Tims Branch and Its Major Tributary, SC". Mohammed was assisted by his mentor, Dr. Mahmoudi, in completing his thesis research and by Ms. Angelique Lawrence in his thesis write-up, which was approved by his graduation committee during the summer. Mohammed successfully defended his research before his thesis review committee at FIU's Department of Civil and Environmental Engineering on June 15, 2018 and has since graduated with a Master's in Civil Engineering.

**Figure 96. DOE Fellow, Mohammed Albassam, with his Master's thesis review committee: (from left to right) Dr. Leonel Lagos (Applied Research Center Director of Research and the DOE Fellows Program Director), Dr. Shonali Laha, Mohammed Albassam and Dr. Walter Tang.**

## MIKE 11 Stream Flow Model (Tims Branch)

### *Development and sensitivity analysis of the MIKE 11 stream flow model of the main Tims Branch stream.*

In May 2018, FIU began development of the MIKE 11 stream flow model of the main Tims Branch stream using the same methodology employed for the A-014 outfall tributary model. This model

is an exclusive stream flow model that simulates the flow characteristics within the Tims Branch stream. Tims Branch is highly affected by runoff, therefore it is very important to develop an exclusive flow model to estimate the flow depth and velocity after heavy rainfall occurs.

FIU delineated the main Tims Branch stream network using MIKE 11 and ArcGIS tools. A simplified shapefile of the Tims Branch stream network was imported into MIKE 11, and MIKE Hydro tools were used to generate the cross sections and chainages along the main Tims Branch stream and tributaries as seen below (Figure 97). Details of the Tims Branch network simplification are described under Subtask 3.2.

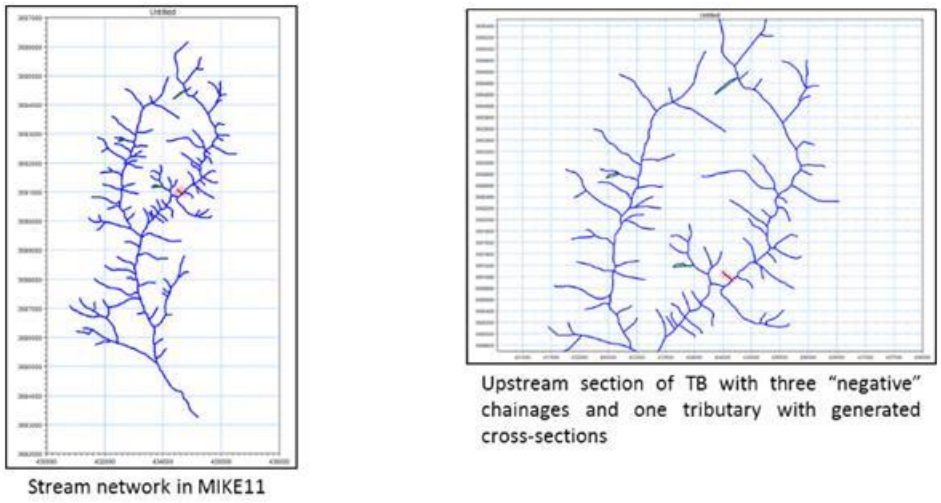


**Figure 97. MIKE Hydro tools being used to generate the cross sections and chainages of the modified stream network.**

Once modification of the stream network was completed, the network file was imported into MIKE Hydro to first auto generate the chainages and then the cross sections. The modified stream network file consisted of 101 branches and 1522 points/nodes. After generating the chainages in MIKE Hydro, the file was modified manually to eliminate unwanted and unnecessary chainages. Finally, the network file was used to generate the cross sections which required extensive manual modification along each branch. Duplicate points within the network file were also removed. The figure below shows a tabular view of the points in the network file. There were 1,522 duplicate points that were eliminated from the file.

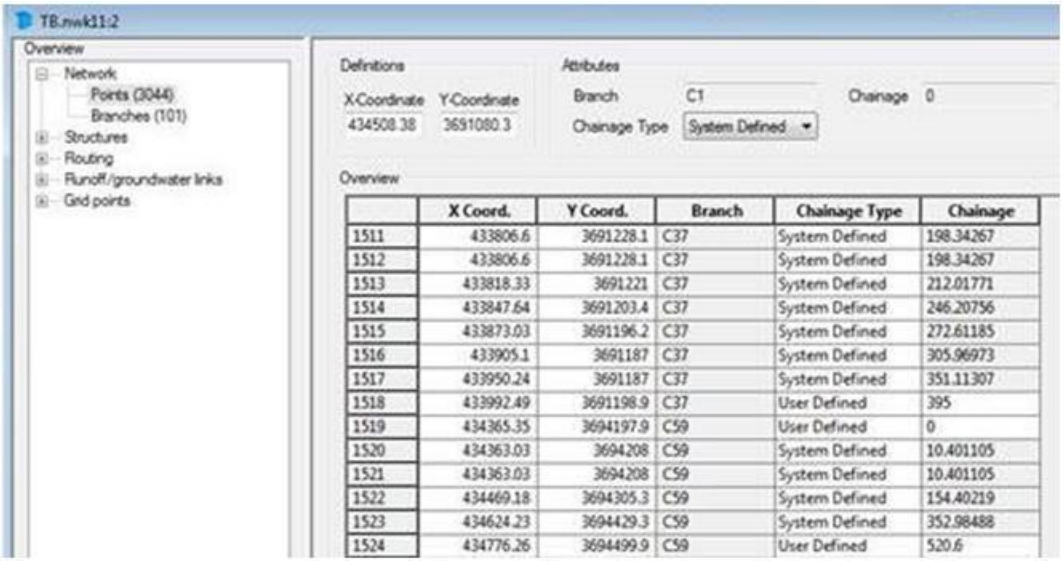


| | X Coord. | Y Coord. | Branch | Chainage Type | Chainage |
|---|---|---|---|---|---|
| 1511 | 433806.6 | 3691228.1 | C37 | System Defined | 198.34267 |
| 1512 | 433806.6 | 3691228.1 | C37 | System Defined | 198.34267 |
| 1513 | 433818.33 | 3691221 | C37 | System Defined | 212.01771 |
| 1514 | 433847.64 | 3691203.4 | C37 | System Defined | 246.20756 |
| 1515 | 433873.03 | 3691196.2 | C37 | System Defined | 272.61185 |
| 1516 | 433905.1 | 3691187 | C37 | System Defined | 305.96973 |
| 1517 | 433950.24 | 3691187 | C37 | System Defined | 351.11307 |
| 1518 | 433992.49 | 3691198.9 | C37 | User Defined | 395 |
| 1519 | 434365.35 | 3694197.9 | C59 | User Defined | 0 |
| 1520 | 434363.03 | 3694208 | C59 | System Defined | 10.401105 |
| 1521 | 434363.03 | 3694208 | C59 | System Defined | 10.401105 |
| 1522 | 434469.18 | 3694305.3 | C59 | System Defined | 154.40219 |
| 1523 | 434624.23 | 3694429.3 | C59 | System Defined | 352.98488 |
| 1524 | 434776.26 | 3694499.9 | C59 | User Defined | 520.6 |

**Figure 98. Simplification of the stream network into fewer polylines.**

Several startup simulations were executed to evaluate model runtime and errors. Sources of errors were identified and corrective actions were taken to remove the errors. Most of the errors originated from cross sections and elevations at the grid level. Each error related to the cross sections was carefully studied and modified.

Existing hydraulic structures were included into the Tims Branch network file which required additional modification of the cross sections upstream and downstream of the structures.

### Coupling of the overland flow and stream flow hydrological models

This year FIU completed the coupling of the MIKE 11 stream flow model of the A-014 outfall tributary with the MIKE SHE overland flow model of the Tims Branch watershed, which marked the completion of milestone 2017-P2-M9. FIU also completed the development of the MIKE 11 stream flow model of the main Tims Branch stream and coupled it with the MIKE SHE overland flow model. Sensitivity analysis and model calibration will follow in future scope. At this stage, the model is ready for execution of preliminary simulations. Several short term simulations will be conducted to understand and eliminate numerical instabilities and errors. Corrective actions will be taken to remove the numerical errors associated with the duration of the time steps and river network cross sections. Once numerical stability has been achieved and the errors corrected, long term simulations will be performed. Activities related to the model development included:

- Completion of the cross section modifications.
- Archiving of flow data from SRS A/M Area outfalls:
- A-01 – daily flow for 2016 (used in model as a boundary condition).
- A-011 – monthly flow for 2016 (used in model as discharge to A-014).
- Utilization of a MS Excel converter tool which converts water level data to flow data.
- Update of the vegetation files for 2018.
- Change of the overland flow computation control parameters to explicit.

- Computational error analysis to find source of simulation errors.
- Corrective actions to time steps and numerical stability to eliminate errors.
- Simulations to find optimal time steps for overland flow, unsaturated flow, and saturated flow (0.5, 2, and 4 hours).
- Preparation of a technical report deliverable which was submitted in August 2018.
- Preparation of a draft manuscript for submission to a peer reviewed journal to be determined.

Figure 99 and Figure 100 show the non-calibrated overland flow simulation results for Tims Branch watershed using the integrated hydrology model. The simulation was performed for the months of January through September 2014. It should be taken into consideration that the model is in its calibration stage and the results presented are only to exhibit the model capability, visualize the results, and present the efforts behind the model development. Note that these results are from a startup simulation and they only represent the model output.

Figure 99 represents simulated water level along Tims Branch for the period of January through September 2014. The horizontal and vertical axes represent the distance from the original reference point (m) and the simulated water level (m) along Tims Branch. The blue areas refer to changes in flow depth along the stream.

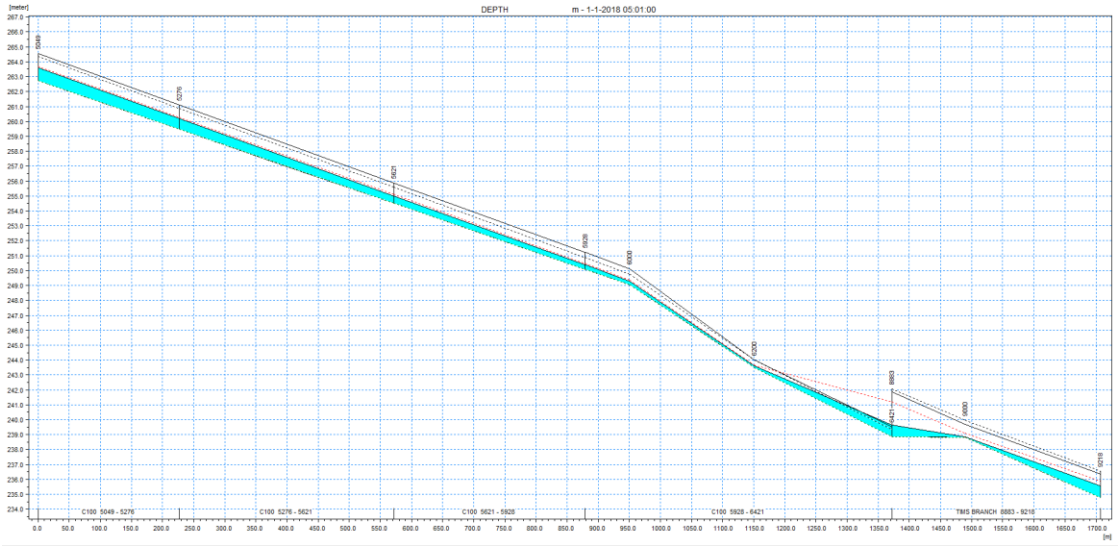


**Figure 99. Simulated water level along Tims Branch. The x axis refers to the distance from the original reference point along Tims Branch and the y axis refers to water level. The blue area indicates how water level varies along Tims Branch.**

Figure 100 represents results of simulated discharge at two locations along Tims Branch stream from January to September 2014. The x-axis represents the flow rate Q in $m^3/s$ and the y-axis represents the month.

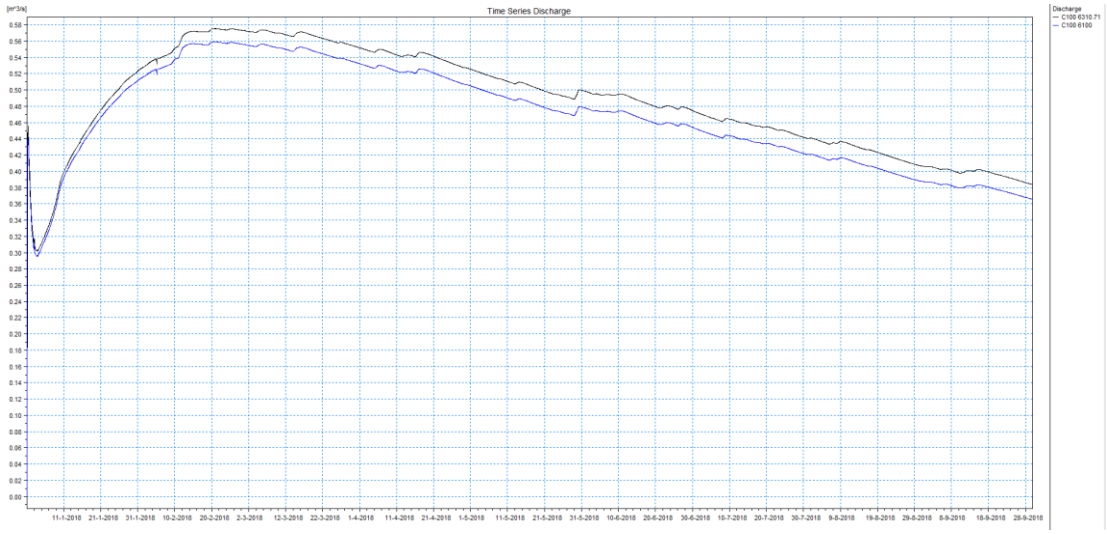


**Figure 100.Simulated discharge over time at two locations along Tims Branch. The x axis refers to the time step (month), and the y axis refers to discharge rate (m3/s).**

### *Generating points and branches*

MIKE 11 was used to generate points and branches from the Tims Branch stream network shapefile. A total of 1522 points and 101 branches were generated. The new network file was exported as a shapefile to GIS for further modifications.

The exported stream network file was first modified in GIS to remove branches smaller than 200 m in length. It was assumed that small branches have little impact on the hydrodynamic stream model, and can therefore be eliminated from the main Tims Branch stream network.

The second modification to the stream network file was to reposition the vertices of the tributaries further away from the main stream line. This helps to avoid complexities during cross section development at the locations where tributaries are connected to main streams. The ArcGIS ArcMap Editor tool was used to reposition the vertices.

The modified stream network was imported into MIKE 11. Branches were then connected using "auto-connect branches" in the network editor. This process creates a new stream network file which requires an extensive manual review to assure the all the branches are connected. The new stream network file was then used to generate the cross sections.

### *Generating cross sections*

Generating points, chainages, and cross sections are the most time consuming and labor intensive part of hydrology model development, particularly in areas with topographic variation and complex hydro-networks. Cross section development involves:

- Location modification,
- Bank modification, and
- Bathymetry modification (according to DEM).

The MIKE HYDRO tool was used to generate cross sections from the network file. Depending on the length of the branch, the number of cross sections at each branch varied. A minimum of two

cross sections were generated on each branch. A total of 320 cross sections were generated for the entire stream network. The cross sections were 75 m in width and placed at 100 m intervals. The cross section file was then imported into the MIKE 11 model.

The next step was to modify the cross sections based on elevation and the natural width of the streams and tributaries. Each cross section was edited through the MIKE 11 cross section editor to resemble the natural width and bathymetry of Tims Branch and its tributaries. Several in situ site measurements of the width of Tims Branch and depth of water were taken during the field work conducted in June 2017. These data were also used to edit the cross sections.

*Boundary Conditions:* Open boundary conditions at the upstream and downstream ends of Tims Branch were assigned.

*Initial Depth:* An initial uniform depth of 10 cm was assumed for the main Tims Branch stream.

The completed MIKE 11 simulation file was imported into the MIKE SHE overland flow model to complete the coupling process.

## REVIEW AND MODIFICATION OF TIMS BRANCH MODEL PARAMETERS

### *MIKE Goundwater Module and Geological Layers*

FIU also began research that would enable a more detailed representation of the geological layers in the MIKE SHE model. Currently, the groundwater properties specified in MIKE SHE are assumed to be constant with only two layers: shallow aquifer and aquifer. A review of geologic data from SRS reports has revealed that the subsurface of the Tims Branch watershed is more intricate than two aquifers (Van Pelt et al., 1994). As such, FIU will investigate the possibility of modifying the saturated and unsaturated modules in the current model with a more detailed hydrogeology over the next year and how the additional details affect the model's performance. Preliminary work began this month by performing simulations of the groundwater head in the study area to compare simulated groundwater head with observed data from monitoring wells in the Tims Branch watershed. Simulations are in progress to understand the model's response to changes in hydraulic conditions in the root zone. Several errors were encountered with the altered model parameters, and as such, FIU is reviewing the model in an attempt to eliminate the errors. This research will be the basis of DOE Fellow Ron Hariprashad's Master's thesis. Ron, with the help of his mentor Dr. Mahmoudi, has developed a draft of his thesis proposal which is entitled "Quantifying Groundwater/Surface Water Interaction in the Tims Branch Watershed at the Savannah River Site, Aiken, South Carolina". Ron plans to defend his thesis proposal before his graduate committee by November 2018.

### *Reference Evapotranspiration*

FIU also worked on processing new data received from the SRNL Atmospheric Technologies Group following their fieldtrip and meeting in August 2018 at SRS. The data consists of evaporation time series from 2013 through 2018 in 15 minute intervals. The data was collected from a station within close vicinity to SRNL that is equipped with Class A pan evaporation bucket. The data is considered to be raw and requires extensive modification (conversion into daily pan evaporation rate, estimating actual evapotranspiration rate, and reference evapotranspiration, etc.) before incorporation into the Tims Branch model. The current version of the model assumes a uniform reference evapotranspiration (ET) at a constant rate of 2.22 mm/day which may limit model accuracy. The Tims Branch watershed is densely vegetated and ET is considered to be an

important factor affecting the hydrology and water balance in this region with such a high vegetation density. Understanding the change in ET will enhance model performance and calculation of the water balance in the watershed. Figure 101 shows a graph of the raw rainfall and pan evaporation data for the year 2016 derived from the gauge station near SRNL Graphs of this nature will help to estimate the initial water depth in the pan bucket before evaporation occurs when no rainfall was recorded. The Class A pan should always sustain 10 in. of water. Any decrease in depth will be considered as evaporation in the pan. From the graph, the data below the 10 in. line is considered evaporation, while above the 10 in, line is considered the rainfall contribution.

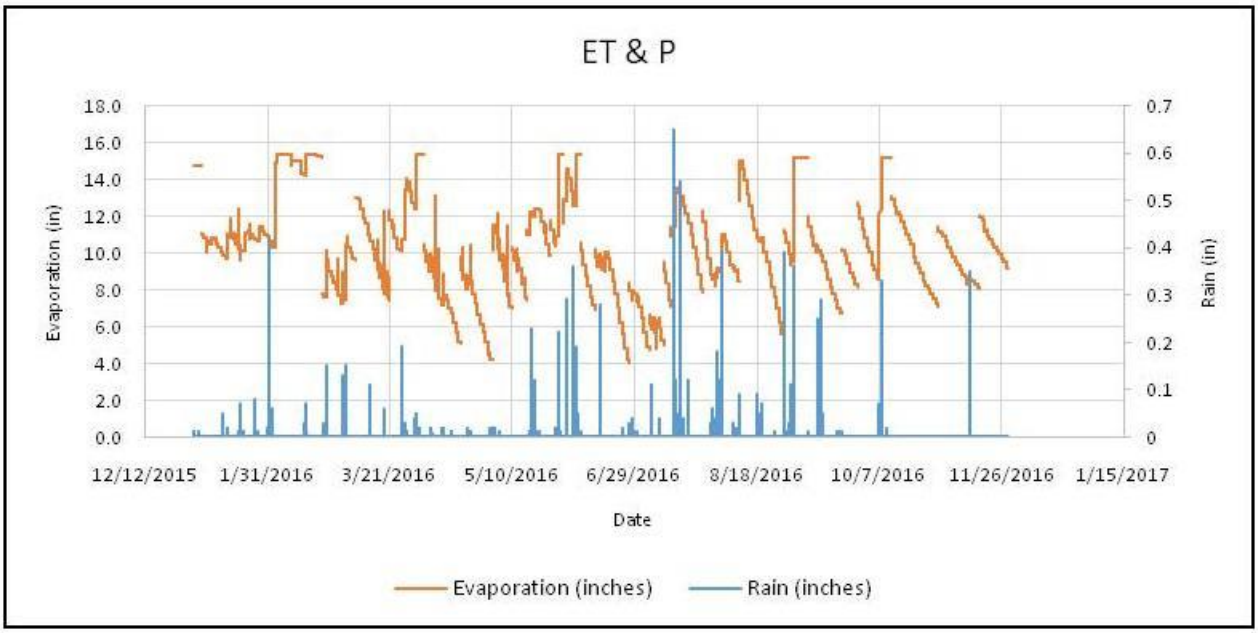


**Figure 101. Graph depicting raw rainfall and pan evaporation data in 2016 from gauge station neat SRNL.**

### *Leaf Area Index (LAI) and Root Depth (RD)*

The current version of the MIKE SHE overland flow model includes a vegetation file that consists of average Leaf Area Index (LAI) and average Root Depth (RD) values for each vegetation class. According to (Wijesekara et al., 2014), the leaf area index (LAI) and root depth (RD) define the vegetation properties of the model domain. These components govern the precipitation interception on leaves and the evapotranspiration through roots and they both vary through time in a year. In reality, LAI and RD vary throughout the year. Seasonal fluctuations occur as vegetation growth is maximized over the summer with highest leaf and root production, and minimized during winter with lowest leaf and root growth. LAI values vary from 1 to 6 in the Tims Branch study area. Root depth values are average depths of the actual root zone of the vegetation. Forest areas are usually defined with a higher root depth which is considered a constant. Root depth values for agricultural areas begin at 0, peak when the crops are fully grown, and drop down to 0 when the crops are harvested.

To improve the model performance, a MIKE SHE vegetation file (*.etv) was generated that includes seasonal changes in both LAI and RD. LAI and RD increase as vegetation grows faster during spring and summer (the peak) while the growth slows down during fall. During winter there is no vegetation growth and therefore no increase in LAI or RD.

This year, FIU began work to support the modification of the MIKE SHE ET by gathering information on vegetation leaf area index (LAI) and root depth. The time series data of LAI became available through Oak Ridge National Laboratory Distributed Active Archive Center (ORNL DAAC), and is expected to improve the ET module performance in the Tims Branch hydrology model. The current model uses the Richard's equation as a means of estimating ET over time which requires time series data of LAI. In addition, the vegetation crop coefficient will be modified for each vegetation class.

The downloaded LAI data was used to generate a GIS point shapefile of the measurement locations in the eastern region of the US. The shapefile was then used to perform an inverse distance weighted (IDW) linear interpolation using the LAI values at each point location as the z-value to generate a gridded surface representing a spatially distributed LAI. The LAI data will be used in the MIKE SHE model for a more detailed spatiotemporal representation.

### Subtask 3.1: Conclusion

FIU has successfully set up the coupled MIKE SHE/MIKE 11 hydrology model of the Tims Branch watershed, however model sensitivity and calibration is still required. FIU will perform the model calibration and validation over the next year after modifying the parameters for which recent timeseries data was acquired (i.e., RET, RD and LAI). Incorporation of this data will help to improve the model's accuracy and performance. Over the next year, FIU will also begin development of the contaminant transport component and couple it with the hydrology model for a completely integrated and spatially distributed contaminant fate and transport model of the Tims Branch watershed.

### Subtask 3.2: Application of GIS Technologies for Hydrological Modeling Support

### Subtask 3.2: Introduction

Application of GIS technology is a key component in hydrological modeling that helps to prepare data, display results and conduct further spatial analyses. The use of GIS technology has supported the MIKE SHE and MIKE 11 hydrology model development. The ArcGIS platform has provided a geodatabase to store and manage model-specific geospatial and timeseries data, and GIS modeling tools to prepare, analyze and visualize model input data and model results.

### Subtask 3.2: Methodology

GIS tools were used for delineation of the stream network and generation of cross-sections and profiles of the major and minor tributaries of Tims Branch. Advanced geospatial and statistical analyses were also conducted for the Tims Branch watershed. This included an extreme hydrological event analysis to determine hyetographs for Tr = 2, 5, 10, 25, 50, 100 and 200 years for use in the integrated surface water model in future to simulate the spatiotemporal distribution of flow depth and velocity in Tims Branch under extreme hydrologic scenarios. FIU graduate and undergraduate DOE Fellow students were mentored and trained on how to perform geoprocessing tasks, conduct geospatial analyses and generate maps and graphs for reporting purposes.

## Subtask 3.2: Results and Discussion

*Data Pre-Processing and Automation*

FIU has created several GIS process flow models to automate repetitive tasks required for processing and formatting of the field data into model-specific formats. The ArcGIS platform has helped with assimilation and formatting of the data collected during FIU's field trips to SRS. The data was incorporated into the existing SRS geodatabase, and converted to MIKE model-specific formats where necessary. GIS point shapefiles were generated to map the locations where the HOBO remote monitoring units were deployed, as well as where the water samples were taken. The flow and chemical analysis data were appended to the attribute tables of these shapefiles in order to map the spatial variation of these parameters.

ArcGIS ModelBuilder was used to automate the process of interpolating the concentration data for several heavy metals and radionuclides and clipping the gridded surfaces generated using 50 m and 100 m buffers along the length of the A-014 outfall tributary and Tims Branch study areas. The preliminary model was only capable of automating the interpolation and clipping processes for a single parameter ($^{238}U$); however, FIU refined the model so that several parameters could be processed simultaneously to create delineated contaminant distribution rasters datasets for each parameter. Below is a snapshot of the updated model. The model can now iterate through a spreadsheet of chemical analysis data and process several parameters simultaneously to create delineated contaminant distribution rasters datasets for each parameter. The model also gives the user the option to customize the input parameters (i.e., the input table of laboratory/field data, the sample location shapefile, the buffer width (50 m/100 m, and the total number of chemical parameters). This provides broader use of the model for varying site locations and types of data collected. The model also automatically loads the raster datasets generated for each parameter in ArcMap. The benefit of this model lies in its ability to process large amounts of field and laboratory data in a very short period of time and generate maps which depict the spatial distribution of the collected parameters in the Tims Branch watershed. The data and maps can be then used for further geospatial analysis. ArcGIS ModelBuilder also provides a nice way of documenting the process work flow for reporting purposes as shown below.

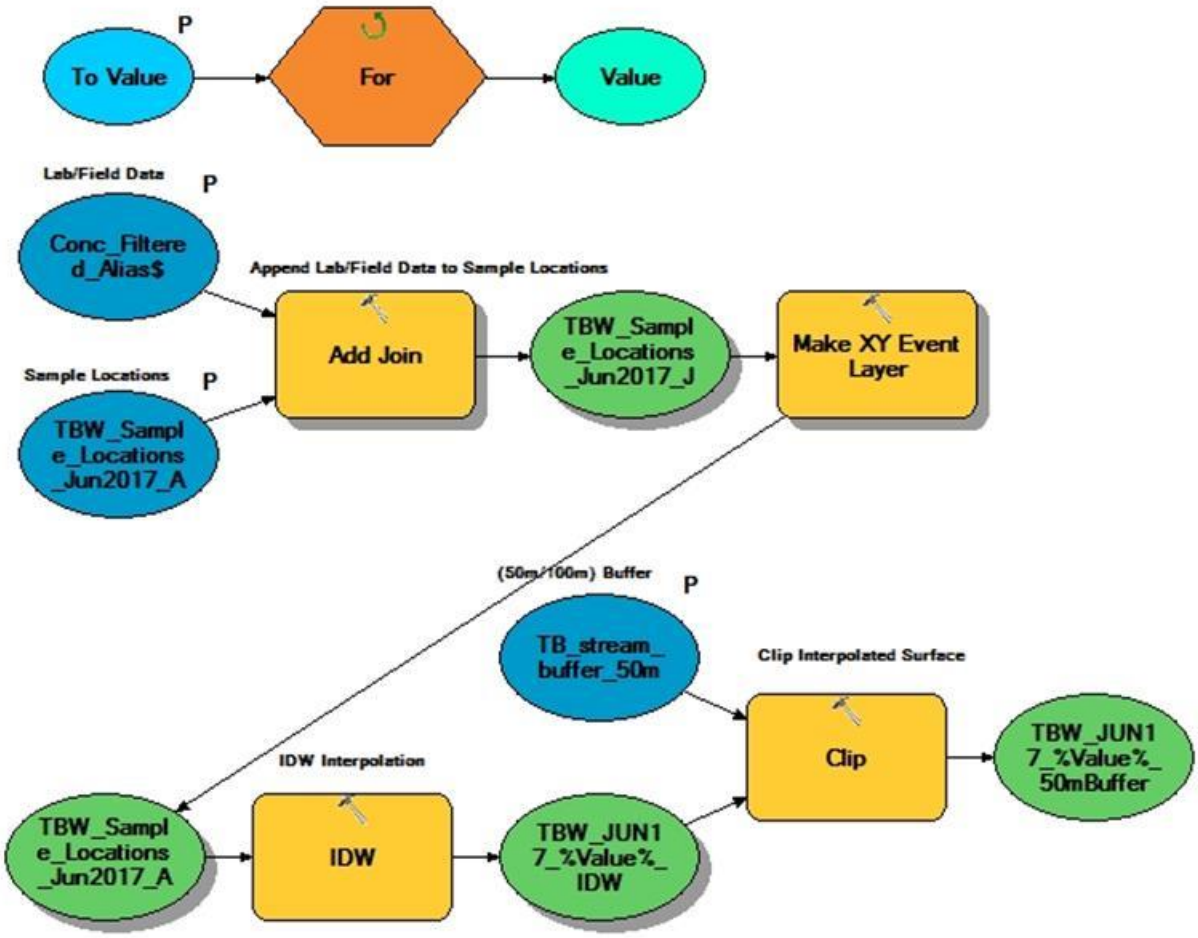


**Figure 102. Refined process flow model generated in ArcGIS ModelBuilder for interpolating heavy metal and radionuclide concentrations in water samples collected in June 2017 to show their spatial distribution in the Tims Branch study area.**

A second process flow model was also created to automate the delineation of the A-014 Outfall tributary study area from a 3 m resolution digital elevation model (DEM) of the Tims Branch watershed. This model utilizes ArcHydro tools to delineate the drainage lines and catchments in the small study area. The files were generated for use in the MIKE 11 stream flow model. Below are screenshots of the process flow model as well as the output shapefiles viewed in ArcMap.

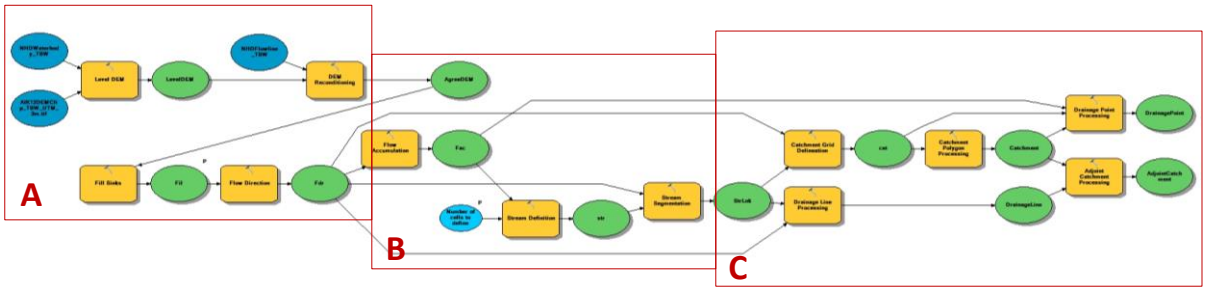


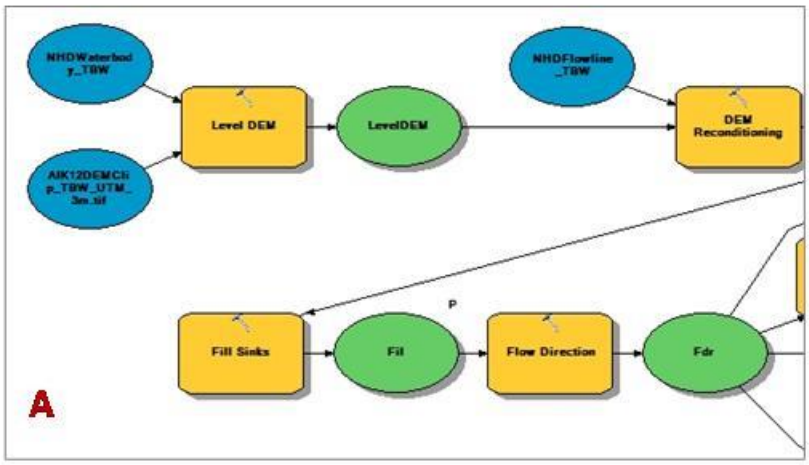


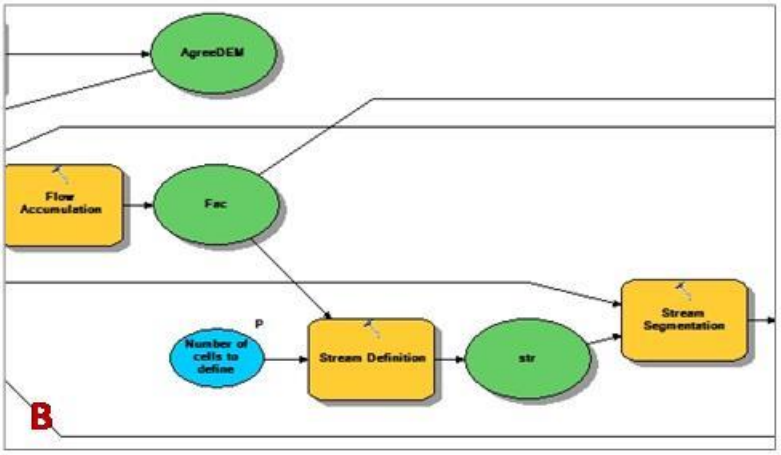


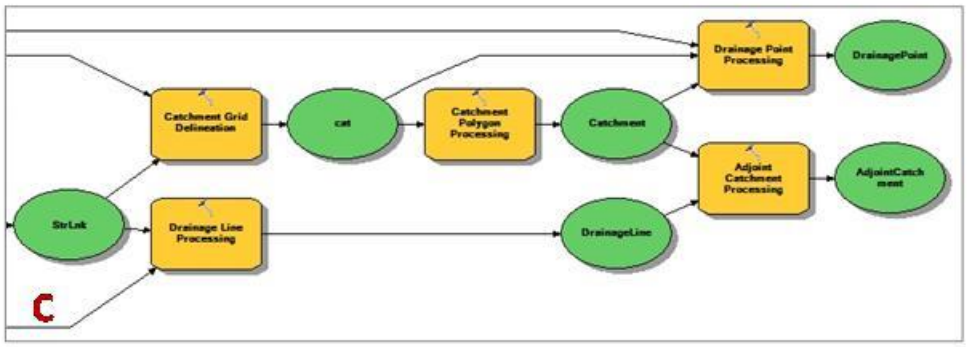


**Figure 103. Process flow model generated in ArcGIS ModelBuilder to automate the delineation of the drainage lines and catchments of the smaller A-014 Outfall tributary study area.**

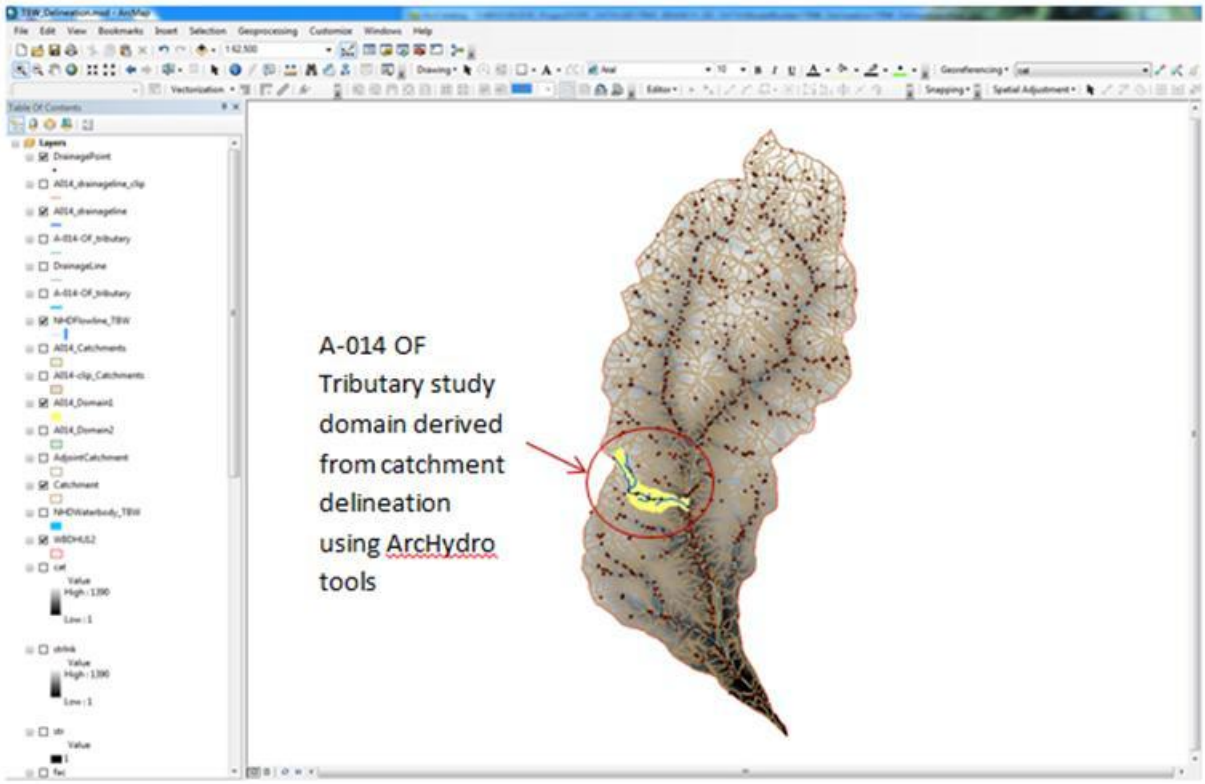


**Figure 104. (1) Delineated drainage line, drainage points and catchments in the Tims Branch watershed generated from a 3m DEM using ArcHydro tools, and (2) the A-014 Outfall tributary study domain.**

FIU also used ArcGIS tools to perform a simplification process of the extremely dendritic Tims Branch stream network. The stream shapefile was modified by eliminating several of the very small tributaries and merging the line segments of the larger ones to create single polylines that are readable by MIKE Hydro. This process was very time consuming as it required intricate attention to detail with respect to the line segments, which in many cases had to be modified manually. The number of features was decreased from approximately 500 to 100 polylines.

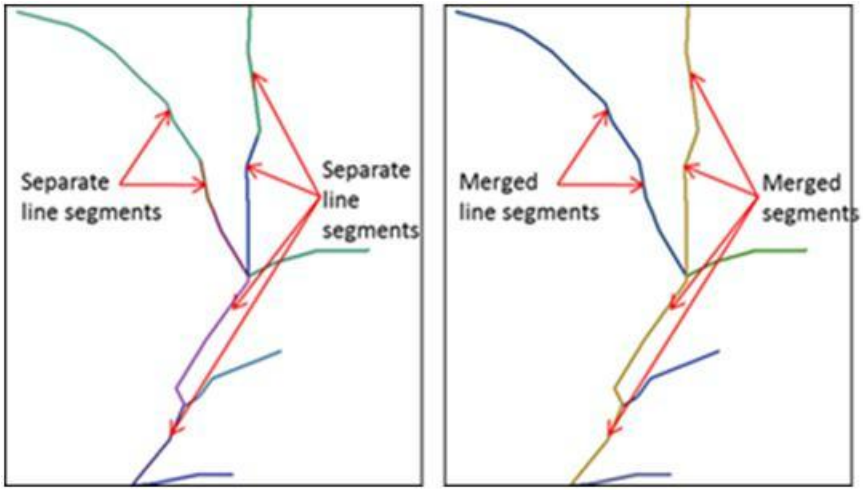


**Figure 105. Simplification of the stream network by merging small line segments to generate single polylines.**

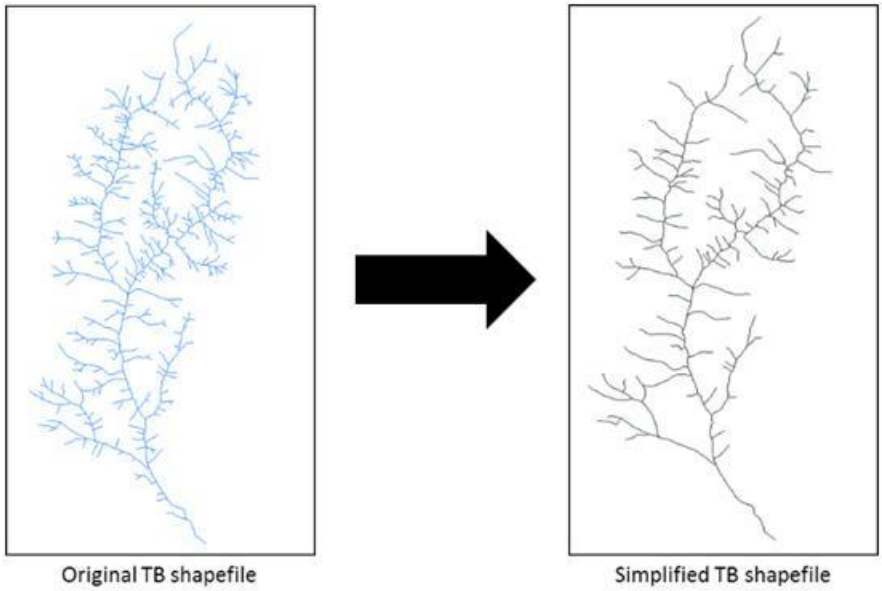


**Figure 106. Simplification of the stream network into fewer polylines.**

The simplified network file was imported into MIKE 11 in order to generate the branches and nodes and then re-exported to GIS (using the MIKE export tool) in order to modify the connection of tributaries to the main branches. The ArcMap editor tool was used to move the point of each tributary where it connects to the main branch away from the main branch (as seen below). This procedure is recommended to help with the auto generation of the cross sections in MIKE 11 and avoids complication as to whether the generated cross section should be assigned to the main stream or the connected tributary.

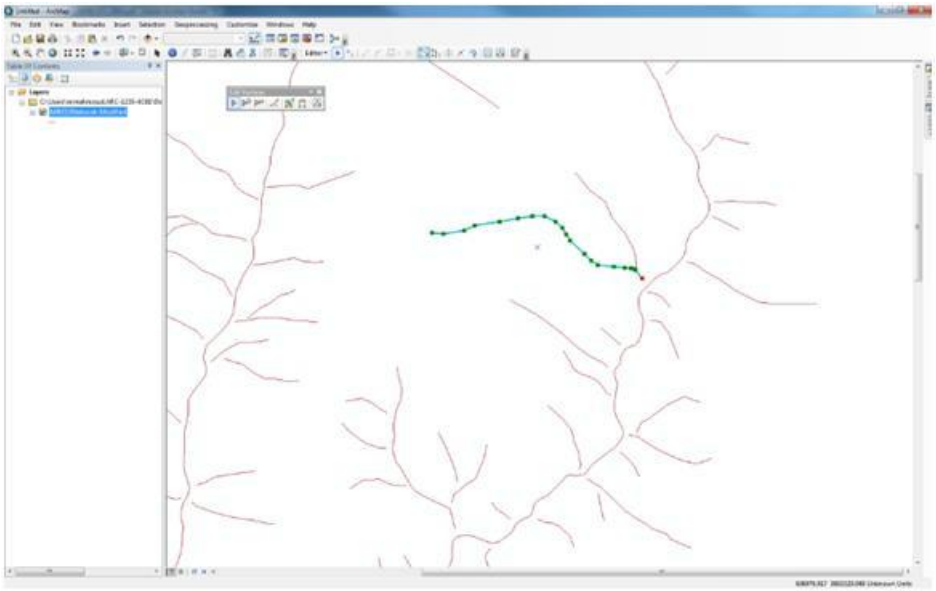

**Figure 107. Modification of the stream network intersection points using editor tools in ArcMap.**

The modified stream network shapefile was then imported into MIKE HYDRO in order to auto generate the cross-sections as described under Subtask 3.1 above. Each cross-section was then

modified manually based on comparative measurements taken during the field exercise conducted at SRS in June 2017.

*Big Data Analytics*

In July 2018, FIU initiated communication with Dr. Richard Koehler to discuss a methodology he developed using GIS for visualization of large timeseries datasets, which FIU plans to use in the next fiscal year to generate raster hydrographs of the data being used for the hydrological model development. Dr. Koehler's work was showcased as a poster and oral presentation entitled "Using a Temporal Information System for Visualization and Analysis of Hydrologic Time-Series Data" at the recent 2018 AWRA Spring Specialty Conference - GIS and Water Resources X held in Orlando in April 2018.

FIU also began formatting the rainfall and timeseries data spreadsheets in order to conduct an extreme hydrological event analysis to determine hyetographs for return periods (TR) = 2, 5, 10, 25, 50, 100 and 200 years. The Log-Pearson Type III distribution was used for fitting frequency distribution data and predicting the design storm. Statistical parameters such as mean values, standard deviations, skewness, probabilities and recurrence intervals were calculated from the daily rainfall data. Preliminary analysis results can be seen in the table and graph below.

**Table 22. Maximum Rainfall Calculations for Different Recurrence Times for SRS Station 700A Data**

| **Station 700A; Lat= 33.33431; Lon= -81.73379** | | | | | | |
|---|---|---|---|---|---|---|
| TR (years) | LogTR (log year) | K Lower (0.5) | K Upper (0.6) | Slope | K Calculated (0.5782) | MaxRain (mm) |
| **1.0101** | 0.00 | -2.00 | -1.88 | 0.75 | -1.89634 | 42.29 |
| **2** | 0.30 | -0.10 | -0.10 | -0.16 | -0.09551 | 75.98 |
| **5** | 0.70 | 0.81 | 0.80 | -0.08 | 0.80174 | 101.74 |
| **10** | 1.00 | 1.32 | 1.33 | 0.05 | 1.32691 | 120.70 |
| **25** | 1.40 | 1.91 | 1.94 | 0.29 | 1.93268 | 147.00 |
| **50** | 1.70 | 2.31 | 2.36 | 0.48 | 2.34854 | 168.30 |
| **100** | 2.00 | 2.69 | 2.76 | 0.69 | 2.73997 | 191.15 |
| **200** | 2.30 | 3.04 | 3.13 | 0.91 | 3.11218 | 215.76 |

*NOTE: Calculations based on rainfall records from 1/1/1964 to 9/29/2014; K values are frequency factors based on a calculated skew coefficient.*

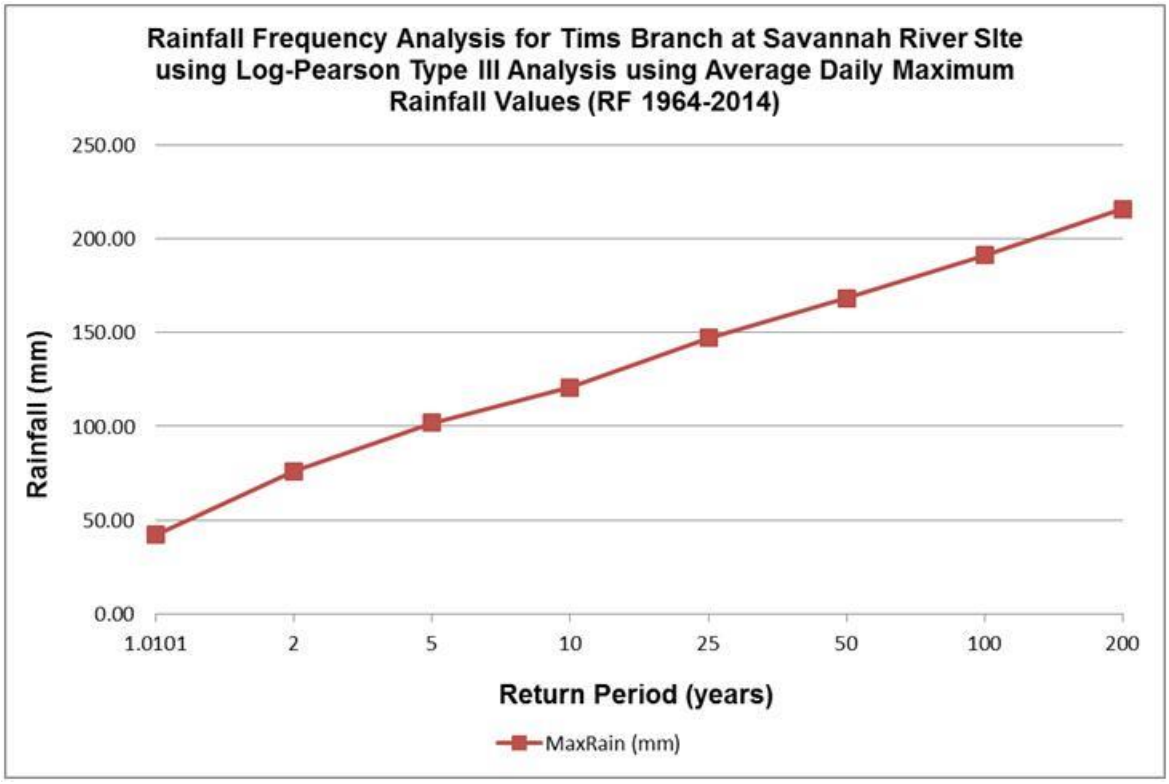


**Figure 108. Correlation between recurrence time and maximum rainfall for Tims Branch rainfall data.**

The analysis to date has been conducted for data derived from the 700A, BARR2 and SRTC weather stations at SRS. Calculations using data from other on-site weather stations at SRS still need to be computed. Data derived from more than one location will provide a more spatially distributed analysis of the hydrological conditions in the study area.

## Subtask 3.2: Conclusion

The ArcGIS process flow models developed by FIU have significantly reduced the processing time required for the preparation of hydrological model input parameters through the automation of repetitive geoprocessing tasks. The MIKE SHE/MIKE 11 hydrological modeling package being used has a GIS user interface built into its system that can directly use spatial GIS databases (geodatabases) for model input parameters. The use of GIS data is significant not just for the spatial representation of hydrologic features, but particularly because of its integration with timeseries data attributes such as flow rates and directions, contaminant concentrations, water levels, precipitation, etc. Availability of data in this format shortens the time for model-specific data preparation and ultimately model development. GIS tools have also assisted in the analysis of hydrological model data and production of maps for visualization of the surface water hydrology of the Tims Branch watershed. The extreme hydrological event analysis using the Log-Pearson Type III distribution method will also provide projected maximum rainfall values and determine hyetographs for return periods (TR) = 2, 5, 10, 25, 50, 100 and 200 years, which will be used for future extreme event scenario analyses. Throughout the year, FIU graduate and undergraduate DOE Fellow students were mentored and trained on how to perform geoprocessing tasks, conduct geospatial analyses and generate maps and graphs for reporting purposes.

## Subtask 3.3: Data Collection, Sampling and Analysis in Tims Branch Watershed

### Subtask 3.3: Introduction

Calibrating a numerical model of stream flow requires real-time data of rainfall and flow velocity/depth. Such data is essential for hydrological model development for calibration and validation as the final steps to maximize model certainty in estimating overland flow depth and velocity over time in an entire watershed. It is also important to collect real-time data as part of post remediation monitoring. Conducting numerical simulations with real-time data will provide a better understanding of the system's response to clean-up activities. Collecting real-time data, however, is one of the most challenging parts of any study as it becomes cumbersome and sometimes impossible due to limited site accessibility. Tims Branch and the A-014 outfall tributary at SRS are examples where collection of field data is challenging due to various field constraints such as physical inaccessibility due to dense vegetation or other environmental conditions, or restricted areas which require site permits and adherence to specific safety protocols before they can be accessed. For this reason, in addition to sampling along Tims Branch and the A-014 outfall tributary, FIU collaborated with researchers at SRNL and SREL to mentor and train an FIU graduate student (DOE Fellow) to deploy remote monitoring devices in Tims Branch to assist in collecting real-time data which is essential in both model calibration and monitoring water quality and the fate and transport of contaminants in Tims Branch.

### Subtask 3.3: Methodology

The first quarter of FIU Performance Year 8 was spent training FIU DOE Fellow graduate students supporting this research project on field data collection techniques, particularly the operation of the remote monitoring system stage gauge/data logger (HOBO RX3000 Remote Monitoring System) purchased over the summer of 2017. The equipment was assembled and tested at a nearby canal along Tamiami Trail just west of SW 109th Ave in Miami, for eventual deployment in Tims Branch. The stage gauge collects water depth timeseries data which can be used to calculate flow rate. Below are photos of the assembled unit, the DOE Fellows conducting a field test, and screenshots of the HOBOlink web-enabled software platform through which the data collected can be accessed via the Internet. The remote monitoring device transmits data wirelessly in customized time intervals and stores it in a cloud where it can then be downloaded.

**Figure 109.Assembled HOBO RX3000 Remote Monitoring System.**

**Figure 110. DOE Fellows conducting a field test of the HOBO RX3000 Remote Monitoring System.**

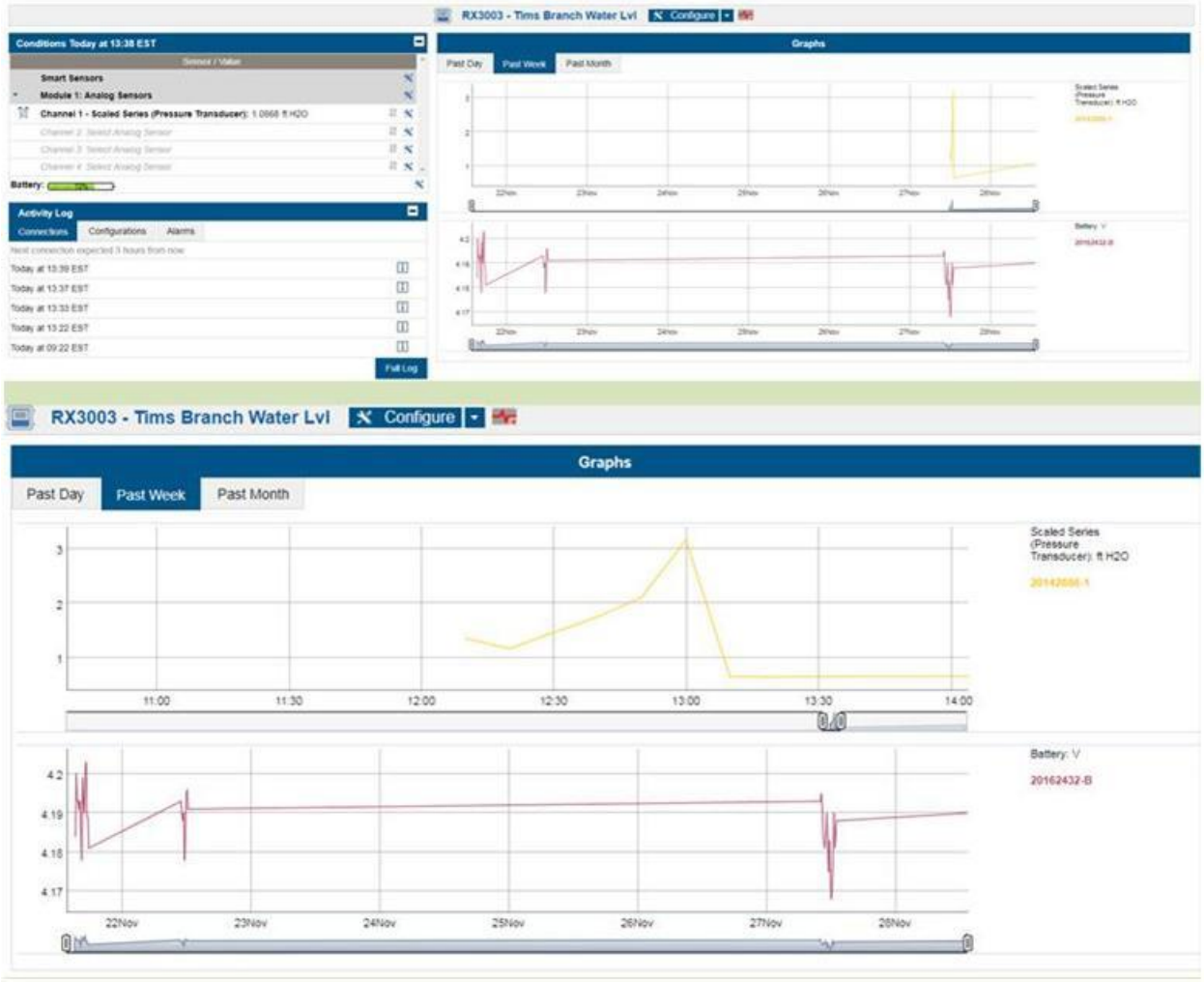


**Figure 111. Screen shots of the HOBOlink web-enabled software platform used to access data from the HOBO RX3000 Remote Monitoring System.**

FIU's field trip to Savannah River Site scheduled for January 21-24, 2018 to deploy the HOBO remote monitoring system in Tims Branch was cancelled due to the federal government shutdown, which would have made DOE badging and Radiological Control (RADCON) support unavailable. FIU therefore rescheduled the trip for February 4-7, 2018 and graduate students (DOE Fellows), Ron Hariprashad and Juan Morales, travelled to Savannah River Site to deploy two remote monitoring systems in Tims Branch. The necessary security clearances and permits were acquired with the aid of Dr. Seaman and his team at SREL.

The FIU field work was a continuation of efforts to collect timeseries data to support the ongoing development of the Tims Branch surface water flow and contaminant transport model. Although historical data was available for preliminary development of the flow model, several data gaps were encountered. In order to improve the accuracy of the model, FIU has deployed the HOBO units which will provide near real-time data in an attempt to capture the effect of extreme hydrological events on the stream flow and pollutant transport. The two HOBO RX3000 3G Remote Monitoring Stations were installed in one location along the A-014 outfall tributary near

its confluence with the main Tims Branch stream, and at a second location downstream of Steed Pond along Tims Branch near its confluence with Upper Three Runs.

Water samples for water quality analysis were also collected which will support ongoing monitoring of the Tims Branch system following the implementation of a tin-based remediation technology to address historical low-level mercury contamination in the stream. The water quality data will be used for development and calibration of the contaminant transport component of the model being developed by FIU.

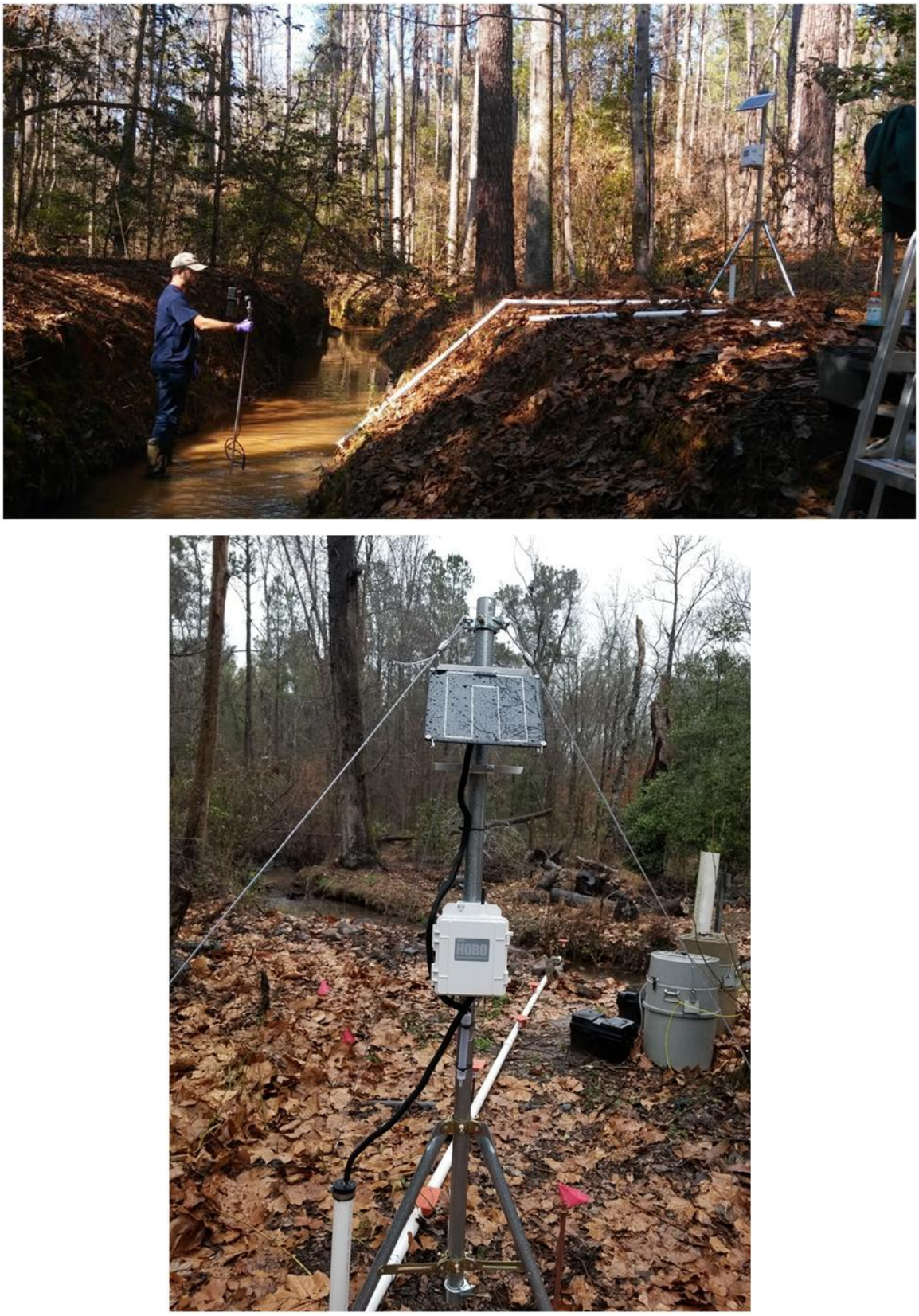


**Figure 112. DOE Fellows installing HOBO RX3000 3G Remote Monitoring Stations in the A-014 Outfall tributary and Tims Branch study areas.**

In August 2018, Dr. Noosha Mahmoudi and DOE Fellow Ron Hariprashad revisited the Tims Branch area to deploy a third HOBO RX3000 remote monitoring device along Tims Branch upstream of Steed Pond., which will provide an additional water level/flow data point to be used as a calibration parameter for the surface water hydrology model being developed. As with the other formerly installed HOBO stage gauges, the data from this device will be transmitted to a web-based cloud service from which it can be downloaded at FIU.

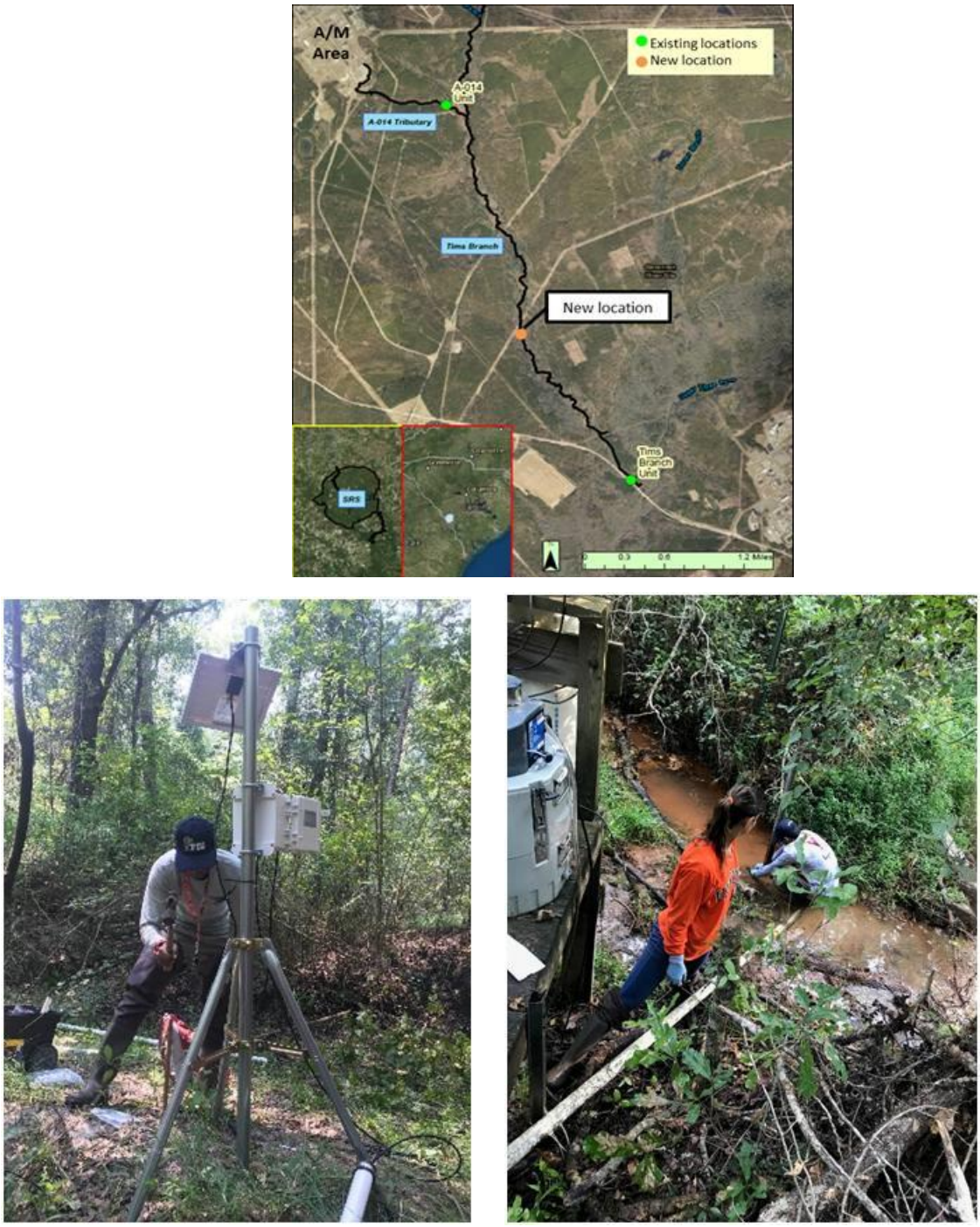


**Figure 113. FIU graduate student installing the HOBO RX3000 remote monitoring device in Tims Branch at SRS (left); (right) FIU researcher and student calibrating and testing the device (right).**

While at SRS from August 12-16, 2018, FIU also performed an inspection and routine maintenance of the first two HOBO devices that were installed during the previous SRS site visit in February 2018. Unusual flow oscillations were observed from the cloud data of the stage gauge installed downstream of the A-014 outfall tributary. After field inspection of the device, it was noted that the probe was covered by sediment. After several observations over the duration of the trip, it was apparent that the sediment is very loose and mobile and covers the probe when the flow rate increases. Measures to counteract this issue are being investigated.

During the SRS site visit in August, FIU was also able to assist SREL in completing the installation and calibration of an ISCO water quality monitoring device located downstream of Steed Pond. Installation of the ISCO unit was initiated in summer 2017 during a DOE Fellow internship. The unit is now fully functional. Data from this device will be collected manually by SREL researchers.

FIU also held meetings with SRNL and SRNS personnel to acquire additional data to support model calibration and improve overall communication and coordination with SRS site personnel and DOE contractors with respect to sharing of data that assists in DOE EM's long-term monitoring goals. FIU met with the SRNL Atmospheric Technologies Group to determine the availability of 15-minute timeseries precipitation data that can be used for calibration of the Tims Branch hydrology model. The data will assist in capturing extreme rainfall events which are generally short-term intermittent phenomena. Although several rain gauge stations exist on-site at SRS, only one station was identified within the vicinity of the Tims Branch study area that records precipitation data in 15-minute increments. FIU also met with an SRNS field officer who is involved in research being conducted in the A/M Area, specifically in the vicinity of the A-01 outfall, who may be able to provide timeseries discharge data in Tims Branch upstream of the wetland treatment system. There was also discussion of obtaining timeseries data of the water table from monitoring wells within the Tims Branch study area.

### Subtask 3.3: Results and Discussion

In March 2018, the students began the process of monitoring and downloading the data being recorded by the HOBO units: Unit 1 (Tims Branch) Lat/Long: 33.287105 -81.697206; Unit 2 (A-014) Lat/Long: 33.331748, -81.721641.

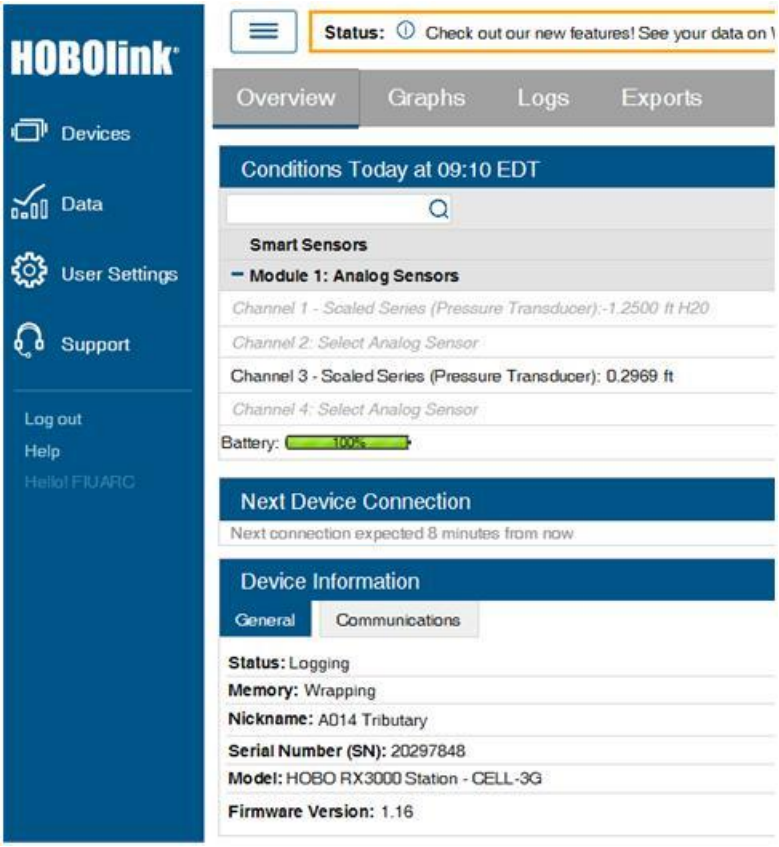


**Figure 114. Screenshot of the HOBO Unit 2 device information viewed via the HOBOlink online user interface.**

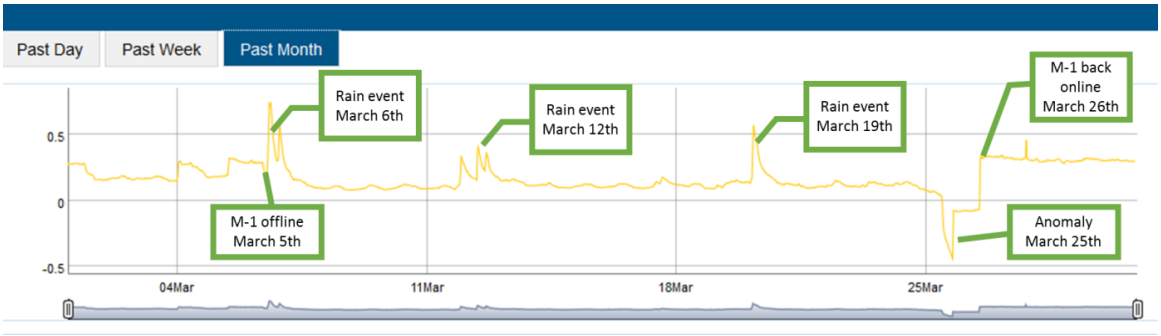


**Figure 115. Screenshot of HOBOlink interface showing data from Unit 2 for the month of March 2018.**

| | A | B | C | D | E | F | G | H | I | J | K |
|---|---|---|---|---|---|---|---|---|---|---|---|
| 1 | Date | Raw (ft) | Actual (ft) | $y_{open}$ (ft) | Area ($ft^2$) | Wetted Perimeter (ft) | Hydralic Radius R (ft) | Hydralic Radius (m) | | Area ($m^2$) | Flow ($m^3/s$) |
| 2 | 3/5/2018 0:00 | 0.1790 | 0.3840 | 1.199 | 0.899 | 5.681 | 0.158 | 0.048 | | 0.0835 | 0.0334 |
| 3 | 3/5/2018 0:15 | 0.1778 | 0.3828 | 1.201 | 0.892 | 5.679 | 0.157 | 0.048 | | 0.0829 | 0.0330 |
| 4 | 3/5/2018 0:30 | 0.1778 | 0.3828 | 1.201 | 0.892 | 5.679 | 0.157 | 0.048 | | 0.0829 | 0.0330 |
| 5 | 3/5/2018 0:45 | 0.1792 | 0.3842 | 1.199 | 0.900 | 5.682 | 0.158 | 0.048 | | 0.0836 | 0.0335 |
| 6 | 3/5/2018 1:00 | 0.1800 | 0.3850 | 1.198 | 0.905 | 5.684 | 0.159 | 0.049 | | 0.0841 | 0.0338 |
| 7 | 3/5/2018 1:15 | 0.1814 | 0.3864 | 1.197 | 0.913 | 5.687 | 0.161 | 0.049 | | 0.0848 | 0.0343 |
| 8 | 3/5/2018 1:30 | 0.1817 | 0.3867 | 1.197 | 0.915 | 5.688 | 0.161 | 0.049 | | 0.0850 | 0.0344 |
| 9 | 3/5/2018 1:45 | 0.1814 | 0.3864 | 1.197 | 0.913 | 5.687 | 0.161 | 0.049 | | 0.0848 | 0.0343 |
| 10 | 3/5/2018 2:00 | 0.1819 | 0.3869 | 1.196 | 0.916 | 5.688 | 0.161 | 0.049 | | 0.0851 | 0.0344 |
| 11 | 3/5/2018 2:15 | 0.1810 | 0.3860 | 1.197 | 0.911 | 5.686 | 0.160 | 0.049 | | 0.0846 | 0.0341 |
| 12 | 3/5/2018 2:30 | 0.1802 | 0.3852 | 1.198 | 0.906 | 5.684 | 0.159 | 0.049 | | 0.0842 | 0.0339 |
| 13 | 3/5/2018 2:45 | 0.1800 | 0.3850 | 1.198 | 0.905 | 5.684 | 0.159 | 0.049 | | 0.0841 | 0.0338 |
| 14 | 3/5/2018 3:00 | 0.1800 | 0.3850 | 1.198 | 0.905 | 5.684 | 0.159 | 0.049 | | 0.0841 | 0.0338 |
| 15 | 3/5/2018 3:15 | 0.1800 | 0.3850 | 1.198 | 0.905 | 5.684 | 0.159 | 0.049 | | 0.0841 | 0.0338 |
| 16 | 3/5/2018 3:30 | 0.1810 | 0.3860 | 1.197 | 0.911 | 5.686 | 0.160 | 0.049 | | 0.0846 | 0.0341 |
| 17 | 3/5/2018 3:45 | 0.1807 | 0.3857 | 1.198 | 0.909 | 5.685 | 0.160 | 0.049 | | 0.0844 | 0.0340 |
| 18 | 3/5/2018 4:00 | 0.1814 | 0.3864 | 1.197 | 0.913 | 5.687 | 0.161 | 0.049 | | 0.0848 | 0.0343 |
| 19 | 3/5/2018 4:15 | 0.1800 | 0.3850 | 1.198 | 0.905 | 5.684 | 0.159 | 0.049 | | 0.0841 | 0.0338 |
| 20 | 3/5/2018 4:30 | 0.1800 | 0.3850 | 1.198 | 0.905 | 5.684 | 0.159 | 0.049 | | 0.0841 | 0.0338 |

**Figure 116. Spreadsheet showing some of the data downloaded from Unit 2 on March 5, 2018. Data is recorded in HOBOlink every 15 minutes. (Note: The M-1 Air Stripper located in the SRS A/M Area was turned off at this time).**


**Figure 117. Screenshots of graphs generated in HOBOlink of data collected by Unit 2. Graphs can be generated for recorded data on a daily, weekly or monthly basis.**

The following is the procedure and algorithms implemented to convert the raw water level data being recorded by the units to flow rates.

Converting water level data to flow data for Unit 2 (A-014):

1. To calculate the actual water level, 0.205 ft was added to the raw water level due to displacement and error.

$$y_{actual} = y_{raw} + 0.205\ ft$$

2. All variables for Manning's equation are given or solved for except S, slope factor. S is solved for by back calculating based on field measurements taken during the field trip in February.

$$*Q = VA = \left(\frac{1.00}{n}\right) AR^{\frac{2}{3}}\sqrt{S}$$

Q = Flow Rate

V = Velocity

A = Flow Area

n = Manning's Roughness Coefficient

R = Hydraulic Radius

S = Channel Slope

*This equation is for S.I. units.

The equation is rearranged for S and area was not needed because flow velocity was measured, not flow volume.

$$S = \left(\frac{Vn}{R^{\frac{2}{3}}}\right)^2$$

S was calculated to be 0.0185.

3. The flow area and wetted perimeter are the only changing variables at each time step. With a detailed cross section taken, the flow area and wetted perimeter are estimated using the trapezoid method.

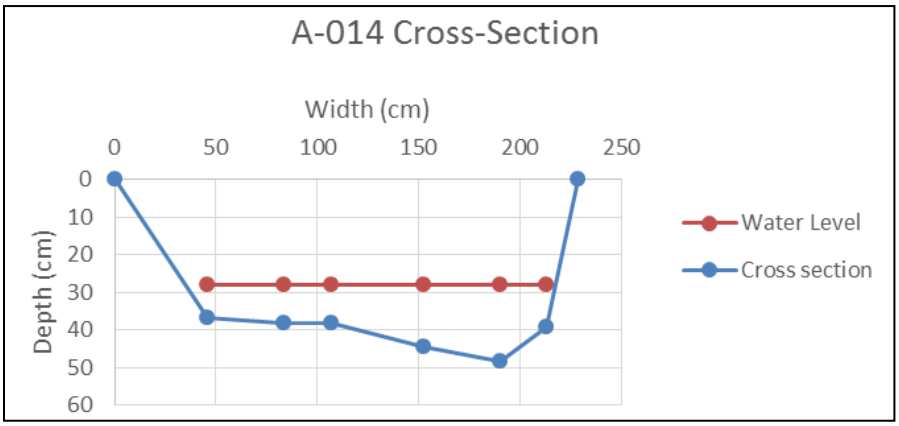


**Figure 118. A-014 cross-section taken in February 2018 while installing the HOBO units. As the flow changes, the flow area can be calculated as the cross-section is constant.**

4. After area and wetted perimeter is calculated, flow can be calculated. A simple calculation is below for 3/5/2018 at 4:00 am.

$$Q = \left(\frac{1.00}{n}\right) AR^{\frac{2}{3}}\sqrt{S}$$

$$Q = \left(\frac{1.00}{0.04}\right)(0.0848\ m^2)(0.049\ m)^{\frac{2}{3}}\sqrt{0.0146}$$

$$\boxed{Q = 0.0343\ \frac{m^3}{s}}$$

The figure below shows a screenshot of the online HOBOlink GUI showing the recorded and graphed water level data where high rainfall events have been highlighted. Also significant to note was the difference in the water levels when the M-1 air striper was off versus when it was turned back on.


**Figure 119. Recorded and graphed water level data as viewed from the HOBOlink GUI.**

A-014 with M-1 online

| Date | A-014 water height (ft) |
|---|---|
| 3/26/2018 13:00 | 0.3008 |
| 3/26/2018 13:15 | 0.3179 |
| 3/26/2018 13:30 | 0.3304 |
| 3/26/2018 13:45 | 0.3387 |

A-014 with M-1 offline for a few hours

| Date | A-014 water height (ft) |
|---|---|
| 3/25/2018 0:00 | 0.0811 |
| 3/25/2018 0:15 | 0.0828 |
| 3/25/2018 0:30 | 0.0813 |
| 3/25/2018 0:45 | 0.0782 |

**Figure 120. Pictures and tabular data showing the difference in water levels in the A-014 outfall tributary when the M-1 air stripper was on versus when it was turned off.**

The water level data downloaded from the HOBOlink website was converted to the appropriate SI units (i.e., from ft to m) for use in the hydrology models. This data was then imported into MIKE 11 to assist in the calibration process of the stream flow model of the main Tims Branch.

FIU continuously monitors and periodically downloads the water level data for implementation in the hydrology models. Below is a graph of the water levels recorded for the month of June 2018. There are two distinct peaks observed from the data that may correspond to possible rainfall events that occurred in June 2018. The graph shows that the water level dropped from approximately 27 cm (0.9 ft) to 10 cm (0.35 ft) between June 1 and June 22. Further investigation may be required to understand the reason for the decrease in water level in Tims Branch during this period.

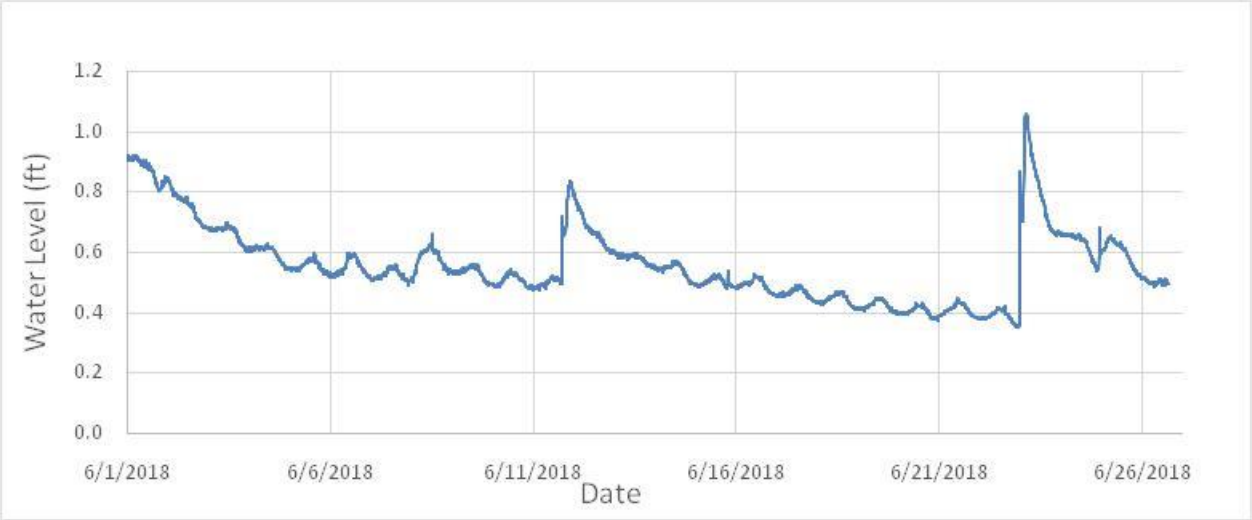


**Figure 121. Water level data recorded in June 2018 by the HOBO RX3000 stage gauge located downstream in Tim Branch.**

FIU is currently processing the pan evaporation data retrieved from the SRNL Atmospheric Technologies Group during a field trip in August 2018 in order to convert it to reference evapotranspiration for improvement of the MIKE SHE model. The details are described under Subtask 3.1.

## Subtask 3.3: Conclusion

Watershed models are fundamental to water resources assessment, development, and management. Watershed models are employed to understand dynamic interactions between climate and land-surface hydrology. The Tims Branch hydrological model allows users to input relevant hydrologic parameters to simulate flow in the subsurface (saturated and unsaturated zones) and surface sub-domains (overland and river). This model can be used as a tool for long-term monitoring of post remediation efforts through hydrological modeling of the Tims Branch watershed in order to examine the response of the system to historical contaminant discharges and environmental management remediation actions.

Dai et al. (2010) developed and evaluated the MIKE SHE model for a forested coastal area in South Carolina. They calibrated the model using a bi-criteria approach and concluded that the MIKE SHE model could be a good candidate for simulating streamflow and water table in forested areas. This approach may be used in the next step of calibrating the Tims Branch model as the area is similar to the study area in their research.

Utilization of Tims Branch as a test bed to develop a numerical modeling tool to evaluate hydrological impacts on the fate and transport of major contaminants of concern (e.g., Hg, U, Ni, radionuclides) will be beneficial to SRS, particularly if the tool developed can be applied to other streams at SRS as well as other DOE EM sites.

### *Conference Participation, Publications & Awards*

The A-014 hydrology model development process and preliminary results have been presented at local and national conference proceedings. In April, Dr. Noosha Mahmoudi presented a poster titled "Development of an Integrated Hydrology Model to Monitor Flow in Tims Branch Watershed" (Figure 122) during a poster session at the recent American Water Resources Association (AWRA) 2018 Spring Specialty Conference (GIS & Water Resources X: Spatial Analysis of Watersheds: Ecological, Hydrological, and Societal Responses) held from April 22-25, 2018 in Orlando, FL. The poster described the MIKE SHE and MIKE 11 model results derived from this research.

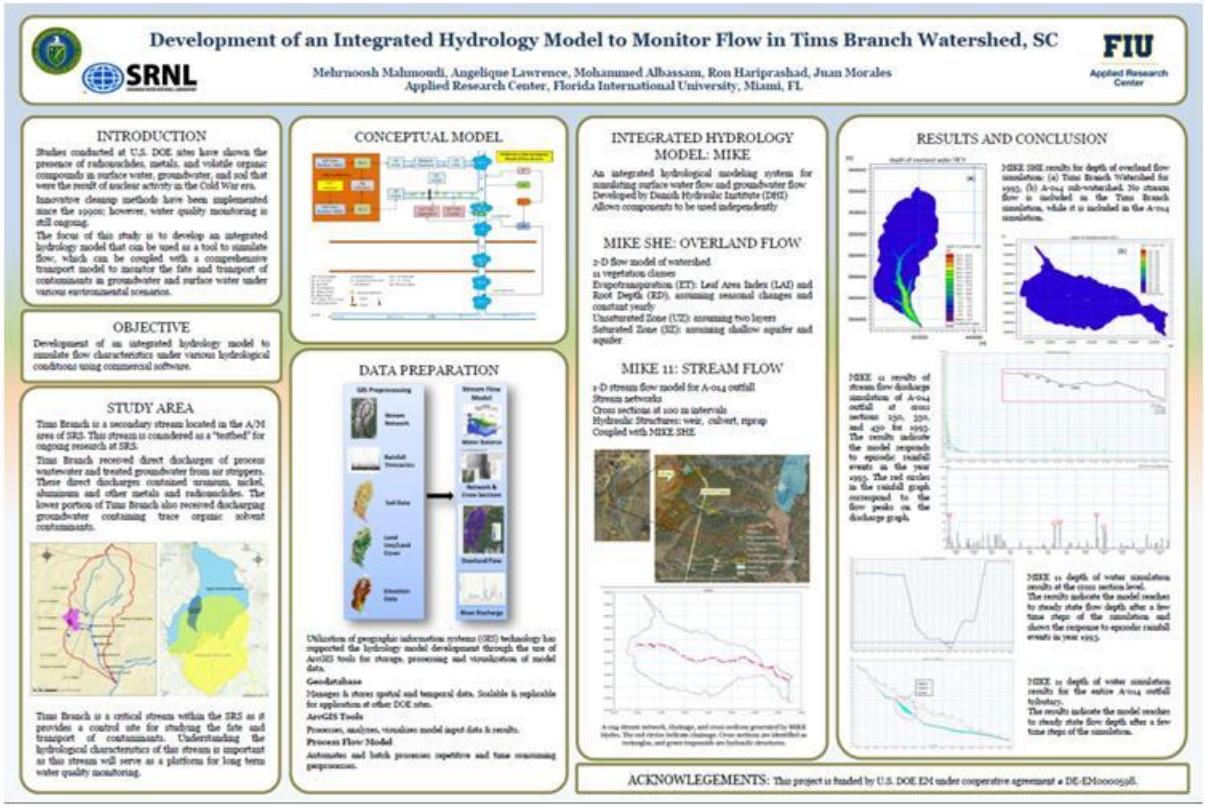


**Figure 122. Poster presented at the AWRA 2018 Spring Specialty Conference in Orlando, FL.**

An abstract was also submitted to the 2019 WM Symposia to be held in Phoenix, AZ in March, 2019, which was accepted as a poster presentation. The abstract was entitled "An Integrated Hydrological Model for Long-Term Monitoring in Tims Branch Watershed, SC," and will be related to the Tims Branch model development over the past few years. DOE Fellow Ron Hariprashad's abstract entitled "Quantifying groundwater/surface water interaction in the Tims Branch Stream, Savannah River Site, South Carolina", was also accepted and will be presented as a poster in the student track.

The Tims Branch hydrology model was presented at the AWRA annual conference which was held on November 4 -7, 2018 in Baltimore, MD. Dr. Noosha Mahmoudi presented the topic "Development of an Integrated Hydrology Model for Tims Branch Watershed, SC" under the hydrology and monitoring oral session.

A draft manuscript is being prepared for submission to a relevant peer reviewed journal, and due to the site specific nature of the research, the publication will be presented as a case study.

### Task 3: Future Work

Future work will include calibration and validation of the integrated hydrology model of the Tims Branch watershed. Specific rainfall scenarios will also be implemented in each model to understand the models' behavior under various atmospheric conditions. Atmospheric scenarios will be determined based upon historical rainfall events and data provided by federal/state online databases or data provided by SRNL/SRNS. The contaminant transport component will also be developed and incorporated to complete the development of a fully integrated flow and contaminant transport model of the Tims Branch watershed.

### Task 3: Acknowledgements

Funding for this research was provided by U.S. DOE Cooperative Agreement DE-EM0000598. We would like to acknowledge and thank Dr. Brian Looney and Dr. Daniel Kaplan from SRNL, Dr. John Seaman and his staff and students from SREL, SRS RADCON personnel, the SRNL Atmospheric Technologies Group and the SRNS NPDES SMEs. We sincerely appreciate their input and consistent support, and we look forward to and value their continued participation.

### Task 3: References

Aadland, R. K., Gellici, J. A., Thayer, P. A., and Carolina, S., 1995, Hydrogeologic framework of west-central South Carolina, State of South Carolina, Department of Natural Resources.

Abbott, M. B., and Ionescu, F., 1967, On The Numerical Computation Of Nearly Horizontal Flows: Journal of Hydraulic Research, v. 5, no. 2, p. 97-117.

Batson, V. L., Bertsch, P., and Herbert, B., 1996, Transport of anthropogenic uranium from sediments to surface waters during episodic storm events: Journal of Environmental Quality, v. 25, no. 5, p. 1129-1137.

Beven, K., and Kirkby, M., 1979, A physically based, variable contributing area model of basin hydrology: Hydrological Sciences Journal, v. 24, no. 1, p. 43-69.

Conrads, P. A., Roehl, E. A., Daamen, R. C., and Kitchens, W. M., 2006, Simulation of water levels and salinity in the rivers and tidal marshes in the vicinity of the Savannah National Wildlife Refuge, Coastal South Carolina and Georgia: U. S. Geological Survey.

Dai T., A. R., Alvi, K., Wool, T., Manguerra, H., Choski, M., Yang, H., and Kraemer, S., 2005, Characterizing spatial and temporal dynamics: Development of a grid-based watershed mercury loading model. American Society of Civil Engineers Conference Proceedings. Managing Watersheds for Human and Natural Impacts: Engineering: Ecological, and Economic Challenges, Williamsburg, Virginia, USA.

Dai, Z., Li, C., Trettin, C., Sun, G., Amatya, D., and Li, H., 2010, Bi-criteria evaluation of the MIKE SHE model for a forested watershed on the South Carolina coastal plain: Hydrology and Earth System Sciences, v. 14, no. 6, p. 1033-1046.

Feaster, T. D., Benedict, S. T., Clark, J. M., Bradley, P. M., and Conrads, P. A., 2014, Scaling up watershed model parameters: flow and load simulations of the Edisto River Basin, South Carolina, 2007-09: United States Geological Survey.

Feaster, T. D., Golden, H. E., Conrads, P. A., and Bradley, P. M., 2012, Simulation of Streamflow in the McTier Creek Watershed, South Carolina, Using TOPMODEL and GBMM.

Graham, D. N., and Butts, M. B., 2005, Flexible, integrated watershed modelling with MIKE SHE: Watershed models, v. 849336090, p. 245-272.

Hayes, D., 1984, Uranium studies in the Tims Branch and Steed Pond system: Westinghouse Savannah River Co., Aiken, SC (United States).

Hiergesell, R., 2004, An Updated Regional Water Table of the Savannah River Site and Related Coverages: Savannah River Site (US).

Kilgo, J., 2005, Ecology and management of a forested landscape: fifty years on the Savannah River Site, Island Press.

Liu, H.-L., Chen, X., Bao, A.-M., and Wang, L., 2007, Investigation of groundwater response to overland flow and topography using a coupled MIKE SHE/MIKE 11 modeling system for an arid watershed: Journal of Hydrology, v. 347, no. 3, p. 448-459.

Looney, B., Jackson, D., Peterson, M., Mathews, T., Southworth, G., Paller, M., Bryan, L., Eddy-Dilek, C., and Halverson, N., 2010, Assessing Potential Impacts of Stannous Chloride Based Mercury Treatment on a Receiving Stream Using Real-World Data from Tims Branch, Savannah River Site: SRS.

Ma, L., He, C., Bian, H., and Sheng, L., 2016, MIKE SHE modeling of ecohydrological processes: Merits, applications, and challenges: Ecological Engineering, v. 96, no. Supplement C, p. 137-149.

Malek-Mohammadi, S., Tachiev, G., Cabrejo, E., and Lawrence, A., 2012, Simulation of Flow and Mercury Transport in Upper East Fork Poplar Creek, Oak Ridge, Tennessee: Remediation Journal, v. 22, no. 2, p. 119-131.

Mast, M. A., and Turk, J. T., 1999, Environmental characteristics and water quality of hydrologic benchmark network stations in the midwestern United States, 1963-95, US Geological Survey.

Refshaard, J., Storm, B., and Singh, V., 1995, MIKE SHE: Computer models of watershed hydrology., p. 809-846.

Singh, V. P., 1995, Computer models of watershed hydrology, Water Resources Publications Highlands Ranch, CO.

Tu, V. T., and Tingsanchali, T., Flood hazard and risk assessment of Hoang Long River basin, Vietnam2010.

Varlik, B., 2013, Total Maximum Daily Load Document Tims Branch SV-324 and Upper Three Runs SV-325 Hydrologic Unit Codes 030601060501, 030601060502, 030601060503, 030601060504, 030601060505, 30601060506.

Wolock, D., 1993, Simulating the variable-source-area concept of streamflow generation with the watershed model TOPMODEL: US Geological Survey, Water Resources Division; US Geological Survey, Books and Open-File Reports [distributor].

# TASK 5: REMEDIATION RESEARCH AND TECHNICAL SUPPORT FOR THE WASTE ISOLATION PILOT PLANT

## Task 5: Executive Summary

The following task is a collaboration begun in spring 2016 with Los Alamos National Laboratory's field office at the Carlsbad Environmental Monitoring and Research Center (LANL CEMRC) which is a part of New Mexico State University. The goal is to generate accurate sorption data for the actinides to minerals and under conditions relevant to the Waste Isolation Pilot Plant (WIPP) as previous risk assessment models are based on conservative assumptions. This task produced one publication in a peer-reviewed journal, six oral presentations, and four poster presentations during FIU Performance Year 8 (listed below) including two invited seminars and one invited webinar with the National Analytical Management Program funded by the Department of Energy.

In addition, DOE Fellow Frances Zengotita received 1st place for her poster presentation at the McNair conference in October 2018 and received an undergraduate competition award from the Innovations in Nuclear R&D program sponsored by DOE-NE based on her summer 2017 internship report. DOE Fellow Zengotita also spent eight weeks as an intern at LANL CEMRC and completed a project investigating the impact of bacteria on the transport of relevant radionuclides to the WIPP. She is currently finalizing a publication based on her summer internship report; therefore, these results will not be included in the annual report for Performance Year 8.

## Task 5: Objectives

The overall objective of this task is to update the experimental sorption data for the actinides to develop more realistic performance assessment models for the WIPP. These data will improve basic understanding of the interactions of actinides in these complex systems and reduce uncertainty in future performance assessment models.

Research questions:

1. How does ionic strength affect processes like sorption and incorporation in the dolomite – actinide system?
2. How do relevant ligands and chelators impact sorption of the actinides at ionic strengths relevant to the WIPP?
3. Is there potential for ternary complexation of actinides, ligands, and mineral phases in the near field of the WIPP repository and how will they impact the fate of actinides? (e.g. dolomite and iron oxides from corrosion of stainless steel)
4. What is the potential effect of ligands on intrinsic actinide colloids versus dissolved species? (i.e. saturated versus unsaturated actinide systems)

## Task 5: Results and Discussion

### Subtask 5.1: Sorption of neodymium to dolomite in variable ionic strength systems

The following results were finalized during FIU Performance Year 8 and incorporated into a paper published in the *Journal of Environmental Radioactivity* entitled "Retention of neodymium by dolomite at variable ionic strength as probed by batch and column experiments.

## Gran titration results

Gran titrations were conducted based on previous work by Rai *et al*. to estimate correction factors (A) to adjust the measured pH (hydrogen ion activity) to pCH (hydrogen ion concentration) based on equations 19 and 20 below [1]. Titrations were conducted at the ionic strengths of batch experimental data (0.1, 1.0, 2.0, 3.0, and 5.0 M) and a linear regression was fit to measure A. These results are compared with measurements by Rai *et al*. in Figure 123. Experimentally determined correction factors (A) by Rai *et al*. (blue circles) and this study (black circles) with the one sigma of a linear regression based on previous work (blue lines).. The correction factors measured in the FIU laboratory are within the error of the linear regression Rai *et al*.'s data.

$$pC_{H+} = pH_{obs} + A \quad \text{Eqn. 19}$$

$$H^{+}{}_{ob} = 10^{A} C_{H+} \quad \text{Eqn. 20}$$

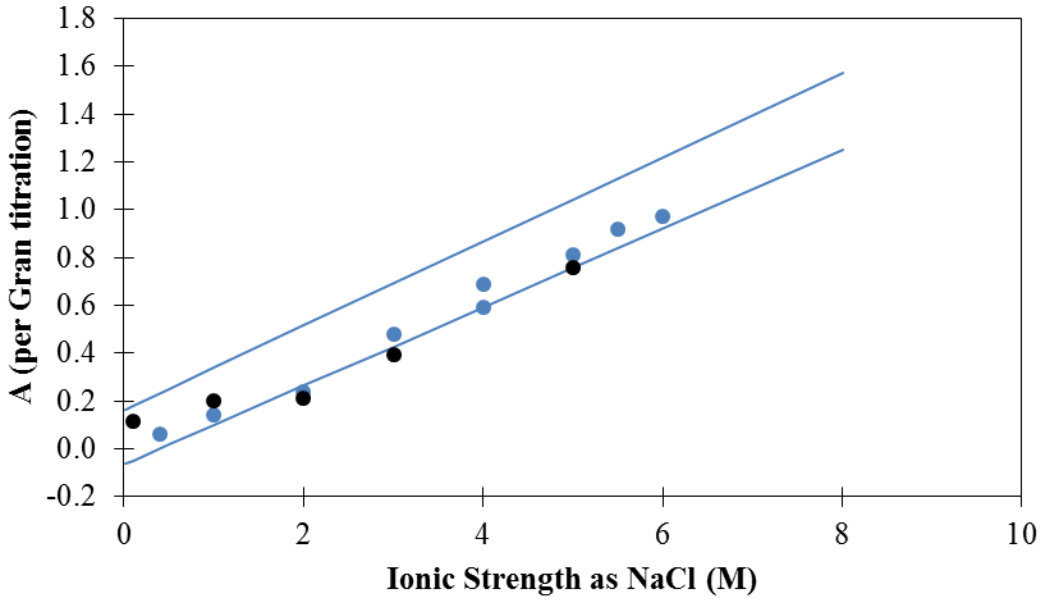


**Figure 123. Experimentally determined correction factors (A) by Rai *et al.* (blue circles) and this study (black circles) with the one sigma of a linear regression based on previous work (blue lines).**

## Tracer column data and model fitting

A one-dimensional, constant dispersivity model for the breakthrough of Nd was developed based on the analytical solution of the advective-dispersive contaminant transport equation assuming a semi-infinite step release and constant dispersivity (Eqn. 21). The column pore volume was estimated based on the difference in a dry, packed column mass and the wet column mass. The dispersion coefficient was estimated from a tracer column conducted at 0.1 M NaCl with 5 ppm $ReO_4^-$. Although Re is not commonly used as a tracer, previous work has shown that perhennate ($ReO_4^-$) does not react with inorganic minerals (montmorillonite, quartz, and iron oxides) and humic substances [2, 3]. Breakthrough curves for Re were fit for dispersion using Stanmod with dimensionless, inverse parameter fitting via the CXTFIT module (Figure 124). The $R^2$ correlation was 0.89 with a dispersion coefficient estimate of 0.102 (dimensionless, i.e. 1/Pe) or 0.000142 $cm^2$/sec.

$$C_{x,t} = \frac{C_0}{2}\left[erfc\left(\frac{Rx-ut}{\sqrt{4Dt}}\right) + exp\left(\frac{xu}{D}\right) erfc\left(\frac{Rx-ut}{\sqrt{4Dt}}\right)\right] \quad \text{Eqn. 21}$$

The model was then used to predict breakthrough of Nd with the range of $K_d$ values used in the WIPP performance assessment (20-400 mL/g) and the minimum $K_d$ measured in batch experiments (500 mL/g) as shown in Figure 125. Figure 126 shows an overlay of experimentally measured Nd breakthrough at 0.1 and 5.0 M ionic strength (datapoints) with the model predicted $K_d$ of 6400 mL/g. It provides a reasonable fit for the data. However, further work must consider whether these values are representative of the WIPP subsurface because the relatively fast flow rates used in column experiments are not likely to occur in the underground.

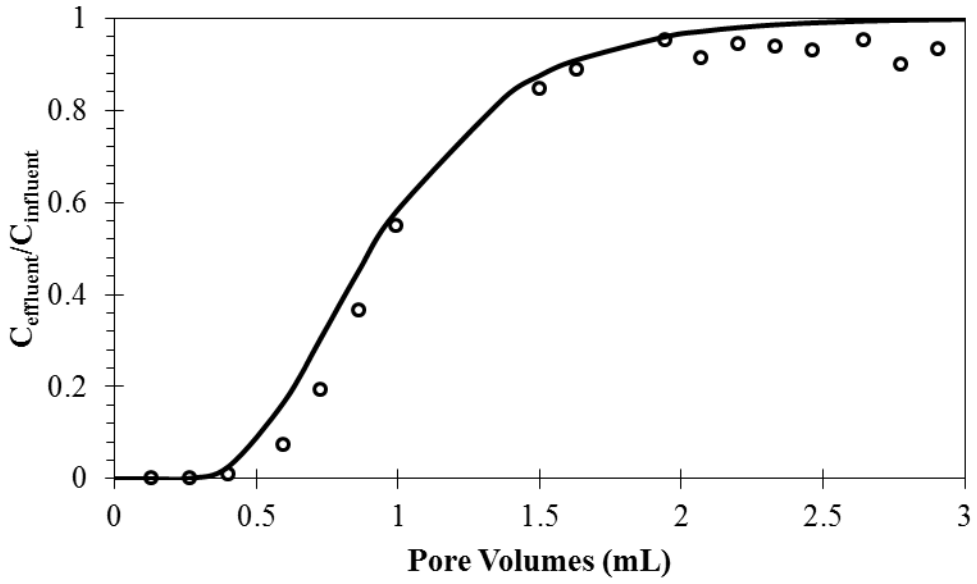


**Figure 124. Recovery of rhenium following step injection of 5 ppm $ReO_4^-$ in 0.1 M NaCl mini column (data points) with best fit for constant dispersivity model fit via StanMod software (line) with CXTFIT module.**

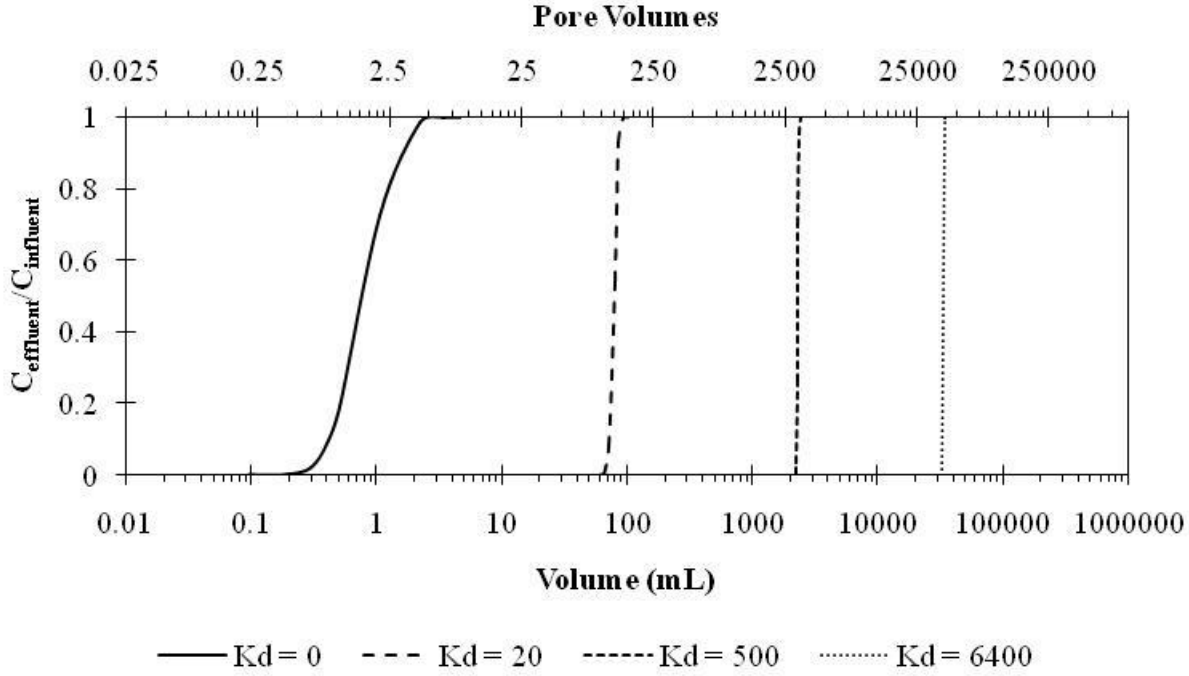


**Figure 125. One-dimensional, constant dispersivity (D=0.00014 $cm^2$/sec) prediction of recovery of contaminant following a continuous step injection into mini columns packed with dolomite for $K_d$=0 (solid line) for a conservative tracer and variable $K_d$ based on the range used previously in performance assessment modeling for the WIPP**

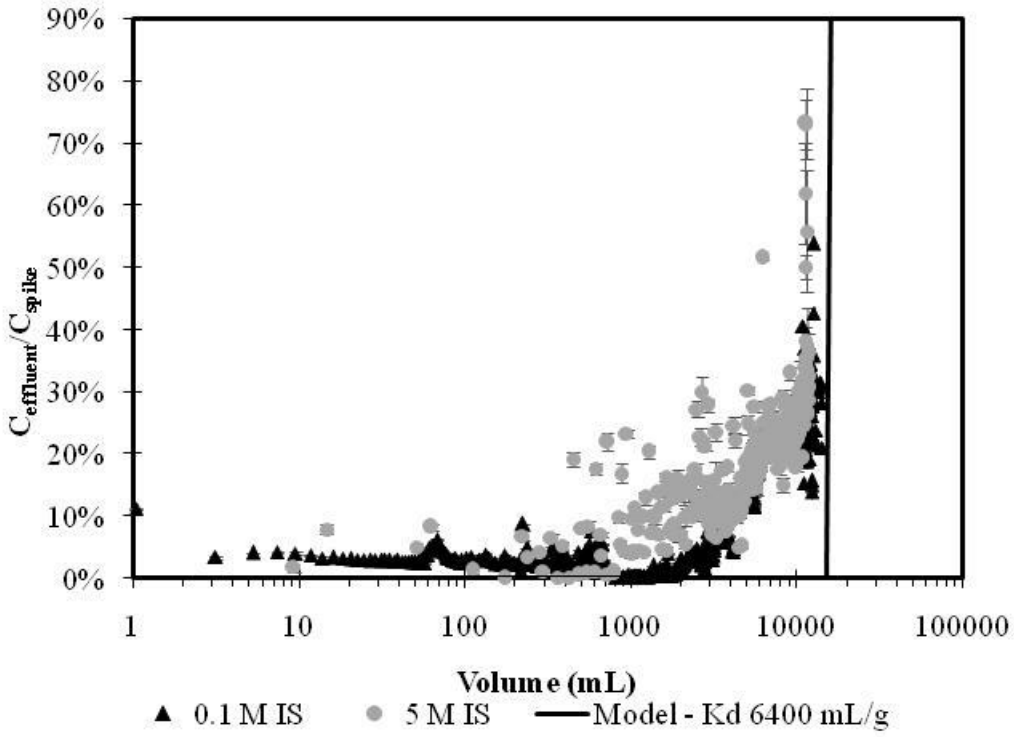


**Figure 126. Results for continuous injection column experiments in the presence of 20 ppb Nd at 0.1 and 5.0 M ionic strength (0.003 M $NaHCO_3$ + NaCl), Note: error bars are based on triplicate analyses via ICP-MS.**

### Dolomite thin section analysis

After reaction of dolomite with solutions at variable ionic strengths and pCH 8.5 in both batch and column experiments, the dolomite particles changed significantly. The average size of dolomite particles decreased significantly after reaction with solutions and porosity appears to increase as shown by samples analyzed on a scanning electron microscope (SEM) in Figure 127 following preparation of thin sections by National Petrographic (Rosenberg, TX). The variability in Ca and Mg content as assessed via point analysis with SEM-EDX increased from 2 and 3% relative standard deviation to 15-30% before and after conducting experiments, respectively. In addition, Nd was detected with a relatively homogenous distribution across particles. These results highlight that secondary Ca and Mg precipitates may have formed and increased the variability in elemental analysis of the surface via SEM-EDX and that Nd interacted strongly with the dolomite minerals.

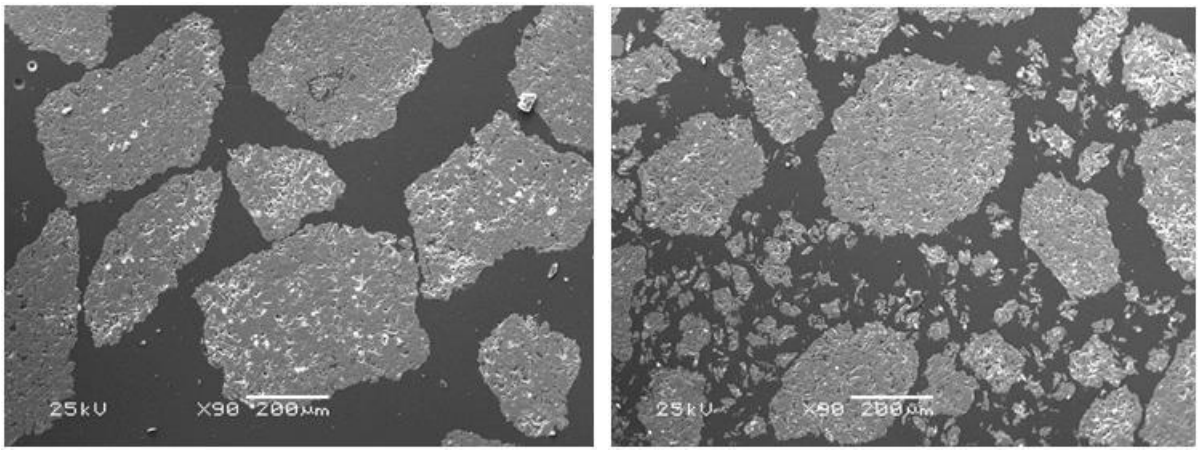


**Figure 127. Comparison of control dolomite (left) not reacted with solutions and dolomite from 5.0 M ionic strength miniature column (right) after approximately one year of exposure.**

## Subtask 5.2: Fate of actinides in the presence of ligands in high ionic strength systems

*Preliminary results for batch experimental controls conducted in the absence of dolomite*

Controls were prepared to consider separations procedures for differentiating between dissolved species and potentially mobile colloidal precipitates with three steps.

1. Settling time of 15 minutes after removal from rotators
2. Filtration through 450 nm PTFE syringe filter (Fisher Scientific)
3. Filtration through 10k MWCO centrifugal filter (Pall Corporation)

Previous experiments likely did not sufficiently separate Th and Nd precipitates from the dissolved phases. A nominal filter pore size of approximately 2 nm was targeted in a previous review (Neck and Kim, 2001), where researchers used filters with a molecular weight cutoff (MWCO) from 2.5k to 25k for separation of Th(IV) colloids (Felmy et al., 1991; Moon, 1989; Ryan and Rai, 1987). The mean diameter reported previously for Th colloids was 16-23 nm (Moon, 1989). Therefore, 10k MWCO filters (Pall Corporation Nanosep) were chosen which list a membrane nominal pore size less than 10 nm (Pall).

Controls were prepared at pH 8.5 in the presence and absence of 5 mg/L of EDTA and with 10 or 1000 µg/L of Th, Nd, and U in 0.1 or 1.0 M ionic strength solutions of NaCl, $CaCl_2$, or $MgCl_2$ for comparison. Samples were analyzed after ten days of equilibration on an Inductively Coupled Plasma Mass Spectrometer (ICP-MS, Thermo Scientific iCAP RQ) with approximate detection limits of 0.006, 0.005, and 0.04 µg/L for Nd, Th, and U, respectively. Figure 128 to Figure 132 summarize the results for Nd, Th, and U.

The speciation of Nd is most impacted by EDTA under these conditions (as compared to Th and U) likely due to its relatively stronger complexation by EDTA (Boukhalfa et al., 2004; Pokrovsky et al., 1998; Thakur et al., 2014). In the presence of EDTA, $Nd(EDTA)^-$ is the major species (>99.9%) predicted at pH 8.5. However, Nd-carbonate species are the major species present at pH 8.5 in NaCl and $MgCl_2$ media while Nd-OH species dominate in $CaCl_2$ media (Table 23 and Table 24). The complexation constant used in the GWB model is based on previous work (Gritmon et al., 1977). It is consistent with previous values measured for other trivalent actinides and lanthanides including Am, Cm, and Eu especially at pH > 8 (Rizkalla et al., 1989). In addition, there is the potential for formation of ternary complexes with Nd-$CO_3$-EDTA as shown previously for the Am and Cm especially in the pH range from 8-11 which are not accounted for in this model (Griffiths et al., 2013).

Significant precipitation of Nd at 1000 ppb initial concentration occurred in the absence of EDTA as shown by Figure 128, with similar concentrations measured in the presence of EDTA for all samples in NaCl and $MgCl_2$. However, significantly greater losses of Nd occurred in the presence of Ca potentially due to precipitation either with calcite or as intrinsic colloids. It should be noted that the pH of $CaCl_2$ solutions was significantly lower (6.9-7.8 depending on ionic strength) upon measurement at ten days potentially due to precipitation of carbonates with Ca and U. GWB models predict precipitation of calcite ($CaCO_3$) and liebigite ($Ca_2(UO_2)_2(CO_3)_3*11H_2O$) (Table 24- Table 25).

Recovery of Nd is generally less in the absence of EDTA due to its strong complexation with the exception of the 1.0 M $MgCl_2$ where recovery is greater for larger filtration sizes but similar to the presence of EDTA for the 10k MWCO filters. In addition, recovery is much greater at the lower concentration (10 µg/L) in NaCl and $MgCl_2$ (Figure 129). However, there are still significant losses, especially in the absence of EDTA. This will be investigated further since the speciation modeling predicts very different species in the presence and absence of EDTA.

**Table 23. Nd speciation in the aqueous phase as predicted by Geochemist's Workbench in variable ionic strength solutions of NaCl, $CaCl_2$, and $MgCl_2$ with 3 mM $NaHCO_3$ and 1000 µg/L Nd at pH 8.5, Note: all similar species aggregated to simplify, i.e. Nd-$CO_3$ represents $Nd(CO_3)^{2-}$ and $NdCO^{3+}$**

| Ionic Strength | Nd-EDTA | Nd-OH | Nd-$CO_3$ | $Nd^{3+}$ |
|---|---|---|---|---|
| 0.1 M NaCl | 0.0% | 0.1% | 99.8% | 0.0% |
| 1.0 M NaCl | 0.0% | 0.2% | 99.6% | 0.0% |
| 0.1 M $CaCl_2$ | 0.0% | 28.0% | 44.6% | 27.4% |
| 1.0 M $CaCl_2$ | 0.0% | 41.4% | 8.3% | 50.2% |
| 0.1 M $MgCl_2$ | 0.0% | 3.8% | 92.6% | 3.7% |
| 1.0 M $MgCl_2$ | 0.0% | 20.4% | 53.7% | 25.9% |

**Table 24. Nd speciation in the aqueous phase as predicted by Geochemist's Workbench in variable ionic strength solutions of NaCl, $CaCl_2$, and $MgCl_2$ with 3 mM $NaHCO_3$ with 5 mg/L of EDTA and 1000 µg/L Nd at pH 8.5, Note: all similar species aggregated to simplify, i.e. Nd-$CO_3$ represents $Nd(CO_3)^{2-}$ and $NdCO^{3+}$**

| Ionic Strength | Nd-EDTA | Nd-OH | Nd-$CO_3$ | $Nd^{3+}$ |
|---|---|---|---|---|
| 0.1 M NaCl | 100.0% | 0.0% | 0.0% | 0.0% |
| 1.0 M NaCl | 100.0% | 0.0% | 0.0% | 0.0% |
| 0.1 M $CaCl_2$ | 98.5% | 0.4% | 0.7% | 0.6% |
| 1.0 M $CaCl_2$ | 92.0% | 3.3% | 0.7% | 4.0% |
| 0.1 M $MgCl_2$ | 99.8% | 0.0% | 0.1% | 0.0% |
| 1.0 M $MgCl_2$ | 99.8% | 0.0% | 0.1% | 0.1% |

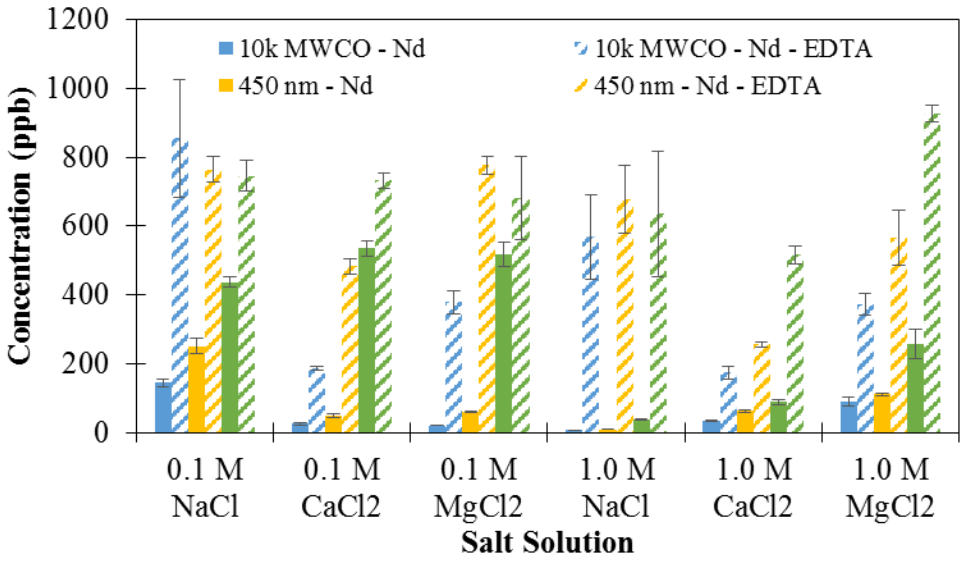


**Figure 128. Measurement of Nd [initial concentration 1000 µg/L] after ten days of equilibration in variable ionic strength solutions of NaCl, $CaCl_2$, or $MgCl_2$ in the presence (diagonal lines) or absence (solid bars) of 5 mg/L of EDTA following settling (green), filtration to remove 450 nm particles (yellow) or <10 nm particles (blue), Note: for $MgCl_2$ and $CaCl_2$ the concentration is 0.033 or 0.33 M to reach 0.1 or 1.0 M ionic strength, respectively.**

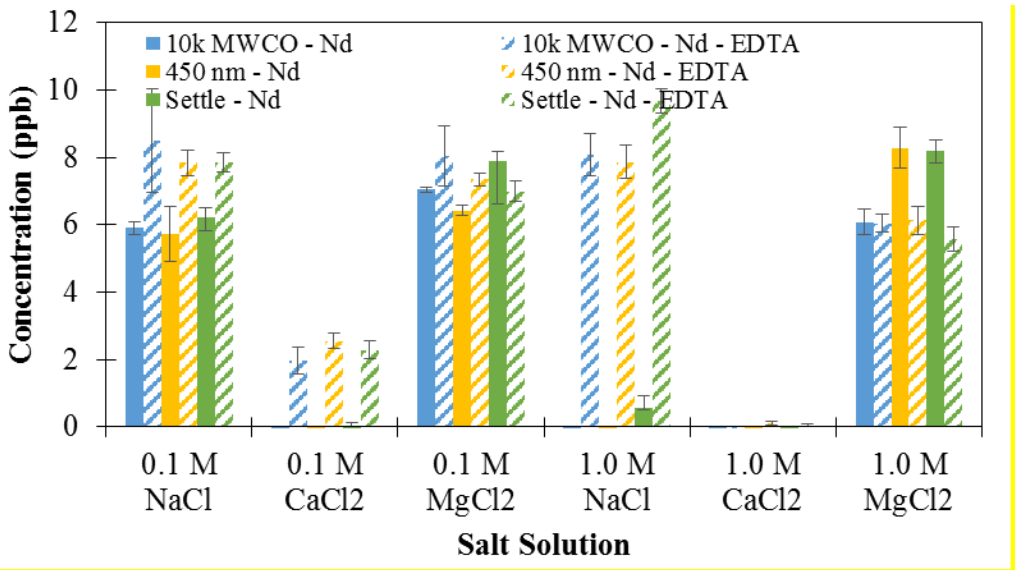


**Figure 129. Measurement of Nd [initial concentration 10 µg/L] after ten days of equilibration in variable ionic strength solutions of NaCl, $CaCl_2$, or $MgCl_2$ in the presence (diagonal lines) or absence (solid bars) of 5 mg/L of EDTA following settling (green), filtration to remove 450 nm particles (yellow) or <10 nm particles (blue), Note: for $MgCl_2$ and $CaCl_2$ the concentration is 0.033 or 0.33 M to reach 0.1 or 1.0 M ionic strength, respectively.**

Control results for U initially at 1000 µg/L (Figure 130) show similar stability of U in the presence and absence of EDTA as expected due to its relatively weak complexation (Note: similar results also for 10 ppb U, not shown). EDTA species compose < 0.1% of the total U above pH 8. The major species at pH 8.5 are $UO_2(CO_3)_3^{-4}$ at ~96% and $UO_2(CO_3)_2^{-2}$ at ~4% in 0.1 M NaCl (with 3 mM $NaHCO_3$). Therefore, EDTA is not expected to play a significant role in sorption and complexation processes of uranium in the WIPP-dolomite system. Previous work also confirms the weak complexation with EDTA above neutral pH and shows that ionic strength does not significantly affect complexation up to 5.0 m (Pokrovsky et al., 1998). In addition, uranyl carbonate species (not uranyl EDTA) have been predicted to interact with calcite when both are present (Rihs et al., 2004). Therefore, uranyl EDTA species are not expected to interact with dolomite either.

GWB models do not predict any uranium minerals forming at the concentrations used in these experiments in the NaCl system at 0.1 or 1.0 M ionic strength. Liebigite ($Ca_2(UO_2)_2(CO_3)_3*11H_2O$) and bayelite ($Mg_2UO_2(CO_3)_3*18H_2O$) are predicted in the $CaCl_2$ and $MgCl_2$ systems, respectively, based on the Geochemist's Workbench models and previously measured thermodynamic parameters (Gorman-Lewis et al., 2008). However, experimental results suggest that the formation of these species is not being observed as similar concentrations of U were measured in control samples across the variable ionic strengths and electrolytes.

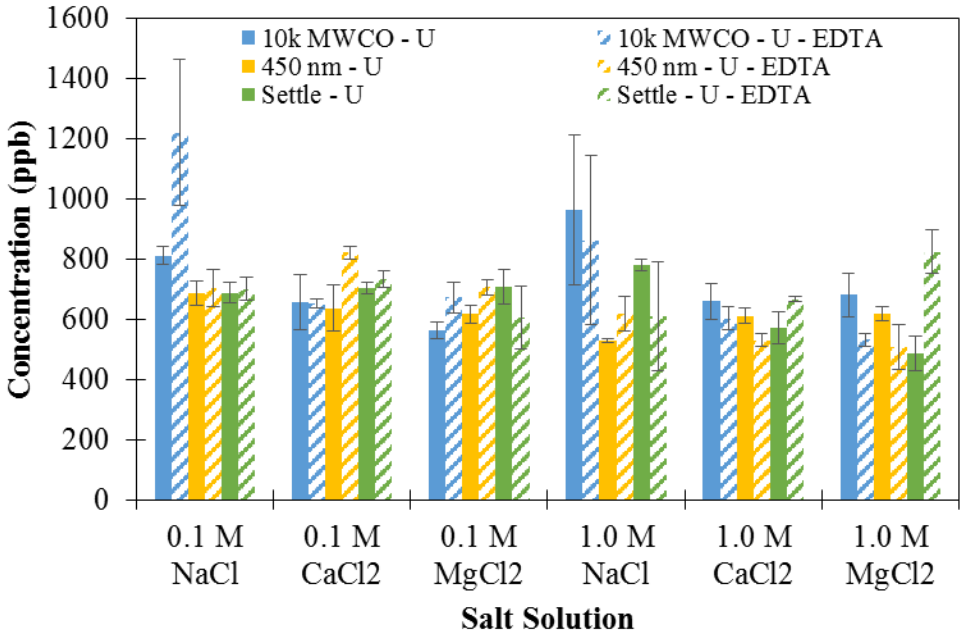


**Figure 130. Measurement of U [initial concentration 1000 µg/L] after ten days of equilibration in variable ionic strength solutions of NaCl, $CaCl_2$, or $MgCl_2$ in the presence (diagonal lines) or absence (solid bars) of 5 mg/L of EDTA following settling (green), filtration to remove 450 nm particles (yellow) or <10 nm particles (blue), Note: for $MgCl_2$ and $CaCl_2$ the concentration is 0.033 or 0.33 M to reach 0.1 or 1.0 M ionic strength, respectively.**

**Table 25. Summary of solid phase species forming (moles) as predicted by Geochemist's Workbench in variable ionic strength solutions of NaCl, $CaCl_2$, and $MgCl_2$ with 3 mM $NaHCO_3$ and 1000 µg/L Nd, Th, and U at pH 8.5**

| Ionic Strength | $ThO_2$ | $Nd_2(CO_3)_3$ | $Nd(OH)_3$ | $Ca_2(UO_2)_2(CO_3)_3$ *11$H_2O$ | $Ca(UO_2)_6O_4(OH)_6$ *8($H_2O$) | $CaCO_3$ | $MgCO_3$ |
|---|---|---|---|---|---|---|---|
| 0.1 M NaCl | 4.3E-06 | 2.7E-06 | - | - | - | - | - |
| 1.0 M NaCl | 4.4E-06 | - | - | - | - | - | - |
| 0.1 M $CaCl_2$ | 4.3E-06 | - | 5.8E-06 | 3.1E-06 | - | 2.9E-03 | - |
| 1.0 M $CaCl_2$ | 4.3E-06 | - | 6.1E-06 | - | 5.81E-07 | 3.0E-03 | - |
| 0.1 M $MgCl_2$ | 4.3E-06 | 2.8E-06 | - | 3.7E-06 | - | - | 2.6E-03 |
| 1.0 M $MgCl_2$ | 4.3E-06 | - | 5.2E-06 | 3.7E-06 | - | - | 2.9E-03 |

Thorium represents the lowest solubility oxidation state (+4) with an approximate solubility of $10^{-8.5}$ M at pH 8.5 in 0.1 M $NaClO_4$ (Neck and Kim, 2001). However, if microcrystalline colloids are forming in this saturated system, the solubility may be several orders of magnitude higher (Rothe et al., 2002). In the absence of EDTA, most Th is removed from the aqueous phase at 1000 µg/L and more than half is lost at 10 µg/L as expected based on solubility (Figure 131 and Figure 132). However, the GWB model predicts a solubility of $4.3x10^{-6}$ M at pH 8.5 in the presence of EDTA if the formation of $Th(OH)_4$ solid species is included but $ThO_2$ is suppressed, as it is expected that this species will control solubility within the timeframe of these experiments. If $ThO_2$ is included, solubility is similar in the presence and absence of EDTA. Therefore, it seems this system is somewhere between the two as it is not in thermodynamic equilibrium.

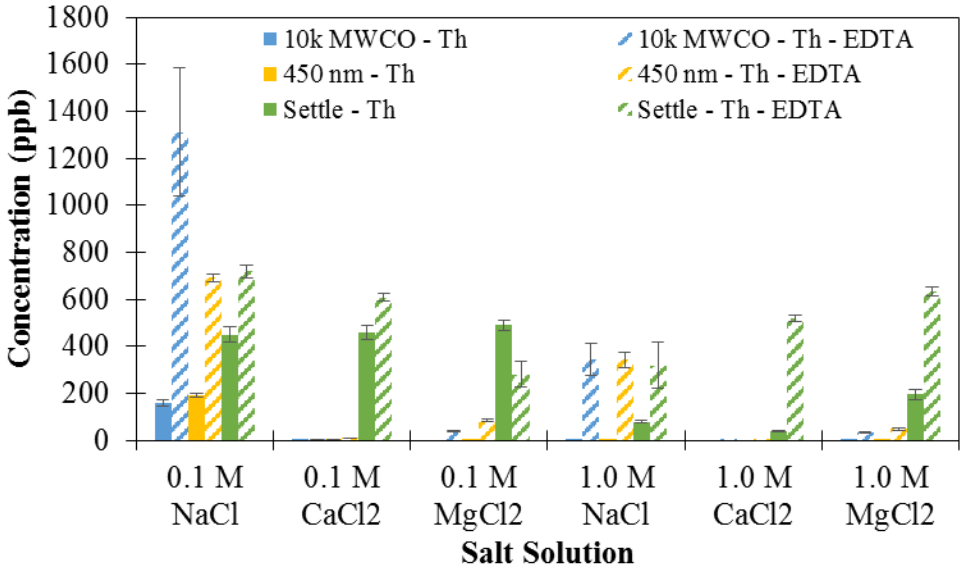


**Figure 131. Measurement of Th [initial concentration 1000 µg/L] after ten days of equilibration in variable ionic strength solutions of NaCl, $CaCl_2$, or $MgCl_2$ in the presence (diagonal lines) or absence (solid bars) of 5 mg/L of EDTA following settling (green), filtration to remove 450 nm particles (yellow) or <10 nm particles (blue), Note: for $MgCl_2$ and $CaCl_2$ the concentration is 0.033 or 0.33 M to reach 0.1 or 1.0 M ionic strength, respectively.**

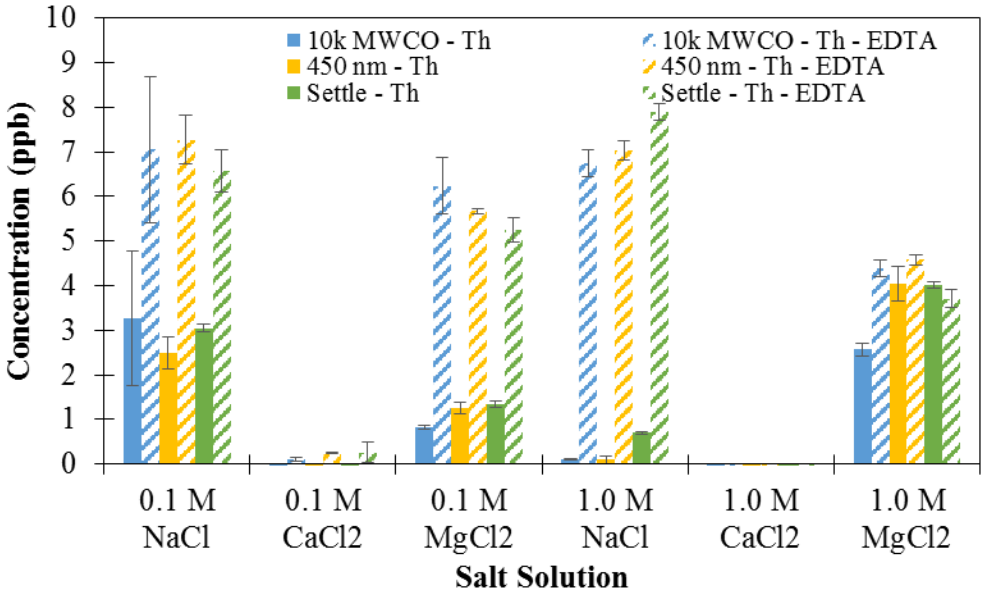


**Figure 132. Measurement of Th [initial concentration 10 µg/L] after ten days of equilibration in variable ionic strength solutions of NaCl, $CaCl_2$, or $MgCl_2$ in the presence (diagonal lines) or absence (solid bars) of 5 mg/L of EDTA following settling (green), filtration to remove 450 nm particles (yellow) or <10 nm particles (blue), Note: for $MgCl_2$ and $CaCl_2$ the concentration is 0.033 or 0.33 M to reach 0.1 or 1.0 M ionic strength, respectively.**

*Preliminary results for dolomite dissolution in the presence and absence of EDTA*

A comparison was made between previous batch experiments with 5 g/L dolomite in 0.1 M NaCl in the presence and absence of 5 mg/L EDTA to compare the dissolution of dolomite via aqueous measurements of Ca and Mg by ICP-OES. Figure 132 shows that the aqueous fraction of Ca and Mg does not change significantly under the conditions of these experiments in the presence and absence of EDTA. Further, all measurements were above detection limits for Ca and Mg (LOD 0.23 and 0.29 µM, respectively) on ICP-OES in a range of 50 - 350 µM.

Previous work suggests that the chelation reaction with Ca that increases dissolution of calcite is limited at concentrations below $10^{-3}$ M (Fredd and Fogler 1998). The concentration of EDTA is 1.7 x $10^{-5}$ M (5 mg/L EDTA) in these experiments. Further, the maximum concentrations predicted in the Waste Isolation Pilot Plant are 3 x $10^{-4}$ M based on the assumption that the maximum brine volume is 17,400 $m^3$ and the inventory reported previously (Van Soest *et. al*. 2005). Therefore, if EDTA interacts similarly with dolomite to calcite, then little effect on mineral dissolution is expected. However, FIU will conduct experiments at variable ionic strength to confirm mineral dissolution rates as the effect of total salt has not been considered previously.

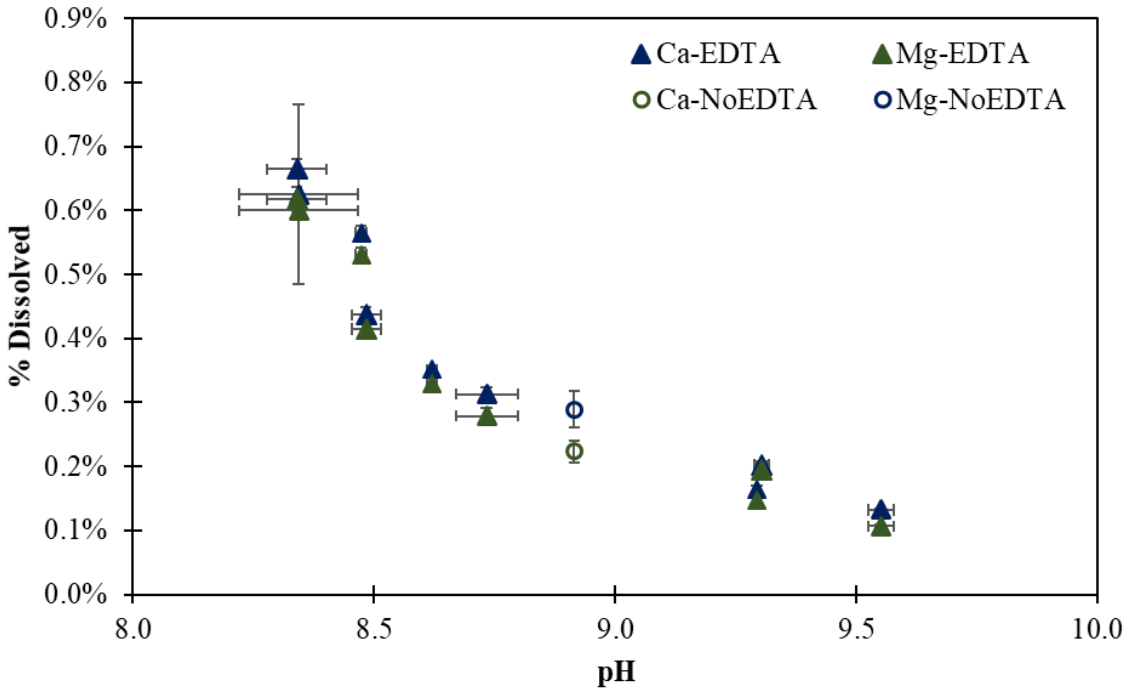


**Figure 133. Aqueous Ca (filled) and Mg (open) following reaction of 5 g/L of dolomite with 0.1 M NaCl and 0 (circles) or 5 (triangles) mg/L of EDTA (1.7 x $10^{-5}$ M) in batch experiments.**

## Task 5: Future Work

Future efforts are in alignment with the DOE Office of Environmental Management (EM) plans to quantify the effect of co-mingled contaminant plumes (McCabe et al., 2017) and is relevant to WIPP performance assessment needs. Proposed research specifically addresses needs identified in the DOE-EM Innovation and Technology: Charting the Path for Fiscal Years 2017-2021 report, including: (1) incremental technologies (*gain a better understanding…in the subsurface and hydrogeologic and biogeochemical processes that influence contaminant behavior)* and (2)

fundamental knowledge gaps in basic research. These experiments are expected to significantly reduce the uncertainty in the fate of the actinides in the presence of WIPP relevant minerals and conditions. These experiments may also lead to the development of more realistic performance assessment models of actinide interactions with WIPP relevant minerals leading to a decrease in uncertainty. There is also synergy between this proposed research and ACRSP efforts including current and future studies by Reed, Yalcintas, and Stanley investigating redox chemistry (including radiolysis effects) and complexation of uranium in the presence of EDTA and carbonate in the absence of minerals. In addition, ongoing research by Swanson and Reed will benefit from these results as microbial communities may be impacted by and capable of influencing the formation and degradation of the ligands (e.g. cellulose degradation products like isosaccharinic acid).

**During FIU Performance Year 9**, mini-column and batch sorption experiments will be continued with stable oxidation state analogs [Nd/Am(III), Th(IV), and U(VI)] and relevant WIPP solids and ligands to establish a baseline comparison for actinides by oxidation state. Analog concentrations will vary from 1 to 1000 µg/L. The +5 oxidation state will not be considered in this work as it is not expected to be a significant risk under the reducing conditions within the repository. Relevant minerals will include dolomite from the Culebra formation above the WIPP and iron oxides (hematite and magnetite) as potential corrosion products from stainless steel. Ligands may include, but are not limited to, EDTA (co-disposed in TRU waste), citrate (common plant and microbial exudate), isosaccharinic acid (ISA, microbial exudate), and gluconate (plasticizer in cement). Total ionic strength in simplified brines will be investigated from 0.01 to 5.0 M ionic strength (as NaCl, $CaCl_2$, or $MgCl_2$) and with WIPP-relevant brines including the U.S. Energy Research and Development Administration Well 6 (ERDA-6, ionic strength of 5.3 M) and generic weep brine (GWB, ionic strength of 7.4 M). The ERDA-6 brine is representative of the fluids in the Castile brine reservoirs while the GWB brine is a representative MgO-impacted brine.

## Task 5: Acknowledgements

Funding for this research was provided by U.S. DOE Cooperative Agreement DE-EM0000598. We truly appreciate Drs. Floyd Stanley, Juliet Swanson, and Don Reed for their invaluable feedback in the design of these experiments and the time given to training and hosting Hilary Emerson and Frances Zengotita as visiting scientists.

## Task 5: References

Boukhalfa, H., Reilly, S.D., Smith, W.H., Neu, M.P., 2004. “EDTA and mixed-ligand complexes of tetravalent and trivalent plutonium.” *Inorganic Chemistry*, **43**(19): 5816-5823.

Brush, L.H. and L.J. Storz, 1996. *Revised Ranges and Probability Distributions of Kds for Dissolved Pu, Am, U, Th, and Np in the Culebra for the PA Calculations to Support the WIPP CCA*, S.N. Laboratories. Albuquerque, NM.

Chao, Y. and T. Zhang, 2011. "Optimization of fixation methods for observation of bacterial cell morphology and surface ultrastructures by atomic force microscopy." *Applied Microbiology and Biotechnology*, **92**(2): 381.

Emerson, H.P., K.A. Hickok, and B.A. Powell, 2016. "Experimental evidence for ternary colloid-facilitated transport of Th (IV) with hematite ($\alpha$-$Fe_2O_3$) colloids and Suwannee River fulvic acid." *Journal of Environmental Radioactivity*, **165**: p. 168-181.

Felmy, A., Rai, D., Mason, M., 1991. "The solubility of hydrous thorium (IV) oxide in chloride media: Development of an aqueous ion-interaction model." *Radiochimica Acta*, **55**(4): 177-186.

Fredd, C. N. and H. S. Fogler (1998). "The influence of chelating agents on the kinetics of calcite dissolution." *Journal of Colloid Interface Science*, **204**(1): 187-197.

Gorman-Lewis, D., Burns, P.C., Fein, J.B., 2008. "Review of uranyl mineral solubility measurements." *The Journal of Chemical Thermodynamics*, **40**(3): 335-352.

Griffiths, T.L. et al., 2013. "Understanding the Solution Behavior of Minor Actinides in the Presence of $EDTA_4^-$, Carbonate, and Hydroxide Ligands." *Inorganic chemistry*, **52**(7): 3728-3737.

Gritmon, T., Goedken, M., Choppin, G., 1977. "The complexation of lanthanides by aminocarboxylate ligands—I: Stability constants." *Journal of Inorganic and Nuclear Chemistry*, **39**(11): 2021-2023.

McCabe, D., Wilmarth, B., Machara, N., Bonczek, R., Chamberlain, S., Cline, M., Denham, M., Freshley, M., Harp, B., Lee, H., Levitskaia, T., Peterson, R., Suggs, P. (2017) Technetium Management Program Plan. Savannah River Site.

Moon, H.-C., 1989. "Equilibrium ultrafiltration of hydrolyzed thorium (IV) solutions." *Bulletin of the Korean Chemical Society*, **10**(3): 270-272.

Neck, V., Kim, J.I., 2001. "Solubility and hydrolysis of tetravalent actinides." *Radiochimica Acta*, **89**: 1-16.

Pall Corporation, Selection Guide: Separation Products for Centrifugal and Tangential Flow Filtration. https://laboratory.pall.com/content/dam/pall/laboratory/literature-library/non-gated/id-7046.pdf.

Pokrovsky, O.S., Bronikowski, M.G., Moore, R.C., Choppin, G.R., 1998. "Interaction of neptunyl (V) and uranyl (VI) with EDTA in NaCl media: Experimental study and Pitzer modeling." *Radiochimica Acta*, **80**(1): 23-30.

Rai, D., et al., 1995. *Estimating the Hydrogen Ion Concentration in Concentrated NaCl and $Na_2SO_4$ Electrolytes*, Sandia National Lab: Albuquerque, NM.

Rihs, S. et al., 2004. "Interaction of uranyl with calite in the presence of EDTA." *Environmental Science and Technology*, **38**(19): 5078-5086.

Rizkalla, E., Sullivan, J., Choppin, G.R., 1989. "Calorimetric studies of americium (III) complexation by amino carboxylates." *Inorganic Chemistry*, **28**(5): 909-911.

Rothe, J., Denecke, M., Neck, V., Müller, R., Kim, J., 2002. "XAFS investigation of the structure of aqueous thorium (IV) species, colloids, and solid thorium (IV) oxide/hydroxide." *Inorganic chemistry*, **41**(2): 249-258.

Ryan, J.L., Rai, D., 1987. "Thorium (IV) hydrous oxide solubility." *Inorganic Chemistry*, **26**(24): 4140-4142.

Takahashi, Y., et al., 1999. "Comparison of adsorption behavior of multiple inorganic ions on kaolinite and silica in the presence of humic acid using the multitracer technique." *Geochimica et Cosmochimica Acta*, **63**(6): p. 815-836.

Thakur, P., Xiong, Y., Borkowski, M., Choppin, G.R., 2014. "Improved thermodynamic model for interaction of EDTA with trivalent actinides and lanthanide to ionic strength of 6.60 m." *Geochimica et Cosmochimica Acta*, **133**: 299-312.

Van Soest, G. and Z. et. al. (2005). Performance Assessment Inventory Report, Savannah River National Laboratory**,** 38.

# APPENDIX

The following documents are included in this report as separate attachments:

1. Appendix 1: Garcia, Alejandro. *The Effect of Microbial Growth on the Spectral Induced Polarization Response in Hanford Vadose Zone Sediment in the Presence of Autunite Mineral*, Thesis, Master of Science in Geoscience, Florida International University, June 2018.
2. Appendix 2: Albassam, Mohammed. *The Effects of Frequent Atmospheric Events and Hydrologic Infrastructure on Flow Characterization in Tims Branch and its Major Tributary, SC,* Thesis, Master of Science in Civil Engineering, Florida International University, June 2018.

The following documents are available at the DOE Research website for the Cooperative Agreement between the U.S. Department of Energy Office of Environmental Management and the Applied Research Center at Florida International University: http://doeresearch.fiu.edu

1. Florida International University, *Project Technical Plan,* Project 2: Environmental Remediation Science and Technology, September 2017.
2. Florida International University, *The Synergistic Effect of Humic Acid and Colloidal Silica on the Removal of Uranium (VI),* Technical Report, June 2018.
3. Florida International University, *The Synergistic Effect of Humic Acid and Colloidal Silica on the Removal of Uranium (VI),* Technical Report, December 2018.
4. Florida International University, *Investigation of the Properties of Acid-Contaminated Sediment and its Effect on Contaminant Mobility*, Final Technical Report, August 2018.
5. Florida International University, *Effect of Bicarbonate on Microbial Autunite Interactions,* Final Technical Report, August 2018.
6. Florida International University, *Sorption Properties of the Humate Injected into the Subsurface System*, Technical Report, May 2018.
7. Florida International University, *Environmental Remediation Technologies: Surface Water Modeling of Tims Branch*, Technical Report, August 2018.